Proceedings of

MMM

Third International Conference

Multiscale Materials Modeling

September 18-22, 2006, Freiburg, Germany

Symposium 4
Microstructural effects on the mechanics of materials

Peter Gumbsch
Editor and Conference Chair

Organized by Fraunhofer-Institute for Mechanics of Materials.
Hosted by University of Freiburg.

IWM
Fraunhofer Institut
Werkstoffmechanik

ALBERT-LUDWIGS-
UNIVERSITÄT FREIBURG

Imprint

Papers published in this volume constitute the proceedings of the Third International Conference on Multiscale Materials Modeling. Papers were selected by the program committee for oral or poster presentation. They are published as submitted, in the interest of timely dissemination.

Contact
Fraunhofer Institute for Mechanics of Materials IWM
Woehlerstraße 11
79108 Freiburg
Germany
Phone + 49 761 5142 0
Fax + 49 761 5142 110

The complete proceedings of the conference are available at

Fraunhofer Information-Centre for Regional Planning and Building Construction IRB
P.O. Box 80 04 69, D-70504 Stuttgart
Nobelstrasse 12, D-70569 Stuttgart
Fon +49 (0) 7 11/9 70-25 00
Fax +49 (0) 7 11/9 70-25 07
E-Mail irb@irb.fraunhofer.de
URL www.irb.fraunhofer.de
ISBN-10: 3-8167-7206-4
ISBN-13: 978-3-8167-7206-4

Foreword

Computational modeling of materials behavior by multiscale materials modeling (MMM) approaches is becoming a reliable tool to underpin scientific investigations and to complement traditional theoretical and experimental approaches of component assessment. At transitional (microstructural) scales continuum approaches begin to break down and atomistic methods reach inherent limitations in time and length scale. Transitional theoretical frameworks and modeling techniques are developed to bridge the gap between the different length scales.

Industrial success in high technology fields relies on the possibility to specifically engineer materials and products with improved performance. The success factor is the ability to make these material related developments timely at relatively low-costs. This demands not only the rapid development of new or improved processing techniques but also better understanding and control of material chemistry, processing, structure, performance, durability, and their relationships. This scenario usually involves multiple length and time scales and multiple processing and performance stages, which are usually only accessible via multi-scale / multi-stage modeling or simulation.

In high-payoff, high-risk technologies such as the design of large structures in the aerospace and nuclear industries, the effects of aging and environment on failure mechanisms cannot be left to conservative approaches. Increasing efforts are now focused on advancing MMM approaches to develop new material systems components and devices. Appropriate validation experiments are crucial to verify that the models predict the correct behavior at each length scale. Thus, one of the advantages of these MMM approaches is that, at each scale, physically meaningful parameters are predicted and used in models for subsequent scales, avoiding the use of empiricism and fitting parameters.

Recent interest in nanotechnology is challenging the scientific community to design nanometer to micrometer size devices for applications in new generations of computers, electronics, photonics or drug delivery systems. These new application areas of multiscale materials modeling require novel and sophisticated science-based approaches for design and performance evaluation. Theory and modeling are playing an increasing role to reduce development costs and manufacturing times. With the sustained progress in computational power and MMM methodologies, new materials and new functionalities are increasingly more likely discovered by MMM approaches than by traditional trial and error approach. This is part of a paradigm shift in modeling, away from reproducing known properties of known materials towards simulating the behavior of hypothetical composites as a forerunner to finding real materials with these novel properties.

The MMM 2006 conference provides an international forum for the scientific advances of multiscale modeling methodologies and their applications.

I would like to thank the members of the international advisory committee, the local program committee and particularly the organizing team, the symposium organizers and the session chairs and the University of Freiburg for their engagement and support. Without their hard work and their devotion of time and ressources, the Third International Conference Multiscale Materials Modeling would not have been possible.

Finally, I would like to thank our conference sponsors for their financial support: The German Research Foundation DFG, Accelrys Inc., Plansee S.E. and the Ministry of Science, Research and Art, Baden-Württemberg.

Peter Gumbsch
Conference Chair

Conference Committee

International Advisory Committee

Prof. Bacon, David	University of Liverpool, UK
Dr. Baskes, Michael	Los Alamos National Laboratory, USA
Prof. Busso, Esteban	Imperial College, London, UK
Prof. Cale, Timothy S.	Rensselaer Polytechnic Institute, Troy, USA
Dr. Diaz de la Rubia, Tomas	Lawrence Livermore National Lab., USA
Prof. Ghoniem, Nasr	University of California, Los Angeles, USA
Prof. Guo, Xiao	Queens College, London, UK
Prof. Iwata, Shuichi	University of Tokyo, Japan
Prof. Kratochvil, Jan	Technical University, Prague, Czech Republic
Prof. Kremer, Kurt	Max Planck Institute, Mainz, Germany
Dr. Kubin, Ladislas	ONERA-LEM, Chatillon, France
Dr. LeSar, Richard	Los Alamos National Laboratory, USA
Prof. Meguid, Shaker	University of Toronto, Canada
Prof. Needleman, Alan	Brown University, Providence, USA
Prof. Odette, Robert	University of California, Santa Barbara, USA
Prof. Ortiz, Michael	California Institute of Technology, USA
Prof. Pettifor, David	Oxford University, UK
Prof. Phillips, Robert	California Institute of Technology, USA
Prof. Raabe, Dierk	Max Planck Institute, Düsseldorf, Germany
Prof. Shibutani, Yoji	Osaka University, Japan
Dr. Soneda, Naoki	Komae Research Laboratory, Tokyo, Japan
Prof. Suresh, Subra	Massachusetts Institute of Technology, USA
Prof. Tomita, Yoshihiro	Kobe University, Japan
Prof. Van der Giessen, Erik	University of Groningen, Netherlands
Prof. Walgraef, Daniel	Free University of Brussels, Belgium
Dr. Wolf, Dieter	Argonne National Laboratory, USA
Prof. Yip, Sidney	Massachusetts Institute of Technology, USA
Dr. Zinkle, Steve	Oak Ridge National Laboratory, USA

Organizing Committee

M. J. Alava	Helsinki University of Technology, Finland
D. Dimiduk	The Ohio State University, USA
M. Dao	Massachusetts Institute of Technology, USA
M. Doi	University of Tokyo, Japan
C. Elsässer	Fraunhofer IWM, Germany
E. v. d Giessen	University of Gronigen, Netherlands
N. Gov	The Weizmann Institute of Science, Israel
H. J. Herrmann	University of Stuttgart, Germany
R. James	University of Minnesota, USA
K. Kremer	Max Planck Institute for Polymer Research, Germany
J. Korvink	IMTEK, University of Freiburg, Germany
J. Li	The Ohio State University, USA
S. Müller	Max Planck Institute for Mathematics in the Sciences, Germany
A. Paxton	Queen’s University, Belfast, UK
M. Payne	University of Cambridge, UK
D. Raabe	Max Planck Institute fuer Eisenforschung, Germany
N. Soneda	Central Research Institute of Electric Power Industry, Japan
M. Zaiser	University of Edinburgh , UK
S. Zapperi	University of Rome, Italy
F. Willaime	Commissariat a l’Energie Atomique (CEA), France
B. Wirth	University of California, Berkely, USA

Contents

Symposium 4

Symposium 4

Microstructural effects on the mechanics of materials

Multi-Scale Modelling for Hot Deformation of Aluminium Alloy

M.F. Abbod[1], **D.A. Linkens**[2], **M. Mahfouf**[2] **and I.C. Howard**[3]

IMMPETUS
Institute for Microstructural and Mechanical Process Engineering: The University of Sheffield
[2]Department of Automatic Control and Systems Engineering,
[3]Department of Mechanical Engineering
University of Sheffield, Sheffield S1 3JD, UK
[1]School of Engineering and Design, Brunel University, Uxbridge UB8 3PH, UK
email: maysam.abbod@brunel.ac.uk

ABSTRACT

The paper presents a systems state framework ϕ-CAFE to model deformation in Aluminium alloys. The proposed framework spatially evolves the relevant microstructure features at two distinct length scales using the scale invariance nature of Cellular Automata (CA). The first length scale is at the micron level where the CA cells hold the information of grain interiors and grain boundaries. The second length scale is at the sub-micron level where the CA cells hold the information as an averaged lumped entity and a periodic function (ϕ) evolves the formation of cells and microbands depending on the initial location and orientation of the CA cells with respect to the global deformation axis. The model is applied to the 2D simulation of plane strain compression of Al-1%Mg. Results from the ϕ-CAFE show the potential to capture local phenomena using simple system state formulations while at the same time reflecting the structural response to the applied deformation.

1. Introduction

The multiscale modelling of material concept is based on predicting the behaviour of complex materials across a range of length and time scales. At the molecular scale, quantum mechanics methods are required to describe the interactions between atoms and electrons. On the other hand, moving from the atomic scale towards the macroscale in solids, for example, the performance at the micrometre scale is governed by the behaviour of misorientations and dislocations. At the next larger scale, the effects of grain boundaries and ensembles of defects become important. Finally, at the macro or continuum scale, the behaviour of materials may be dominated by environmental or loading factors such as applied stresses or temperature gradients.

In this work a hybrid modelling technique that combines cellular automata, finite elements intelligent models and physical equations is used simulate and predict the behaviour of Al-1%Mg aluminium alloy during hot deformation using the commercial finite element software package ABAQUS^{TM}. Hot deformation is a thermo-mechanical process which relies on an accurate identification and precise control of the process variables. These variables are classified into two inter-related groups, namely, interface and intrinsic. The interface variables are identified as friction and heat transfer that affect the surface characteristics and sub-surface metallurgical evolution. The intrinsic variables are the metallurgical features of interest such as dislocation densities, subgrain sizes and subgrain misorientations. This paper addresses the issue of capturing microstructural details and providing macro linkage by two scales. Finite elements is used to simulate the material using a suitable length scale such that numerical models are sufficient in detail and are appropriate in terms of computational time. The second scale is to use Cellular Automata (CA) as an additional technique that can be used in conjunction with a conventional Finite Elements (FE) representation to model material heterogeneity and related properties. This simulation considers an intermediate scale between the micro and macro scales, termed the “mesoscale”. The simulation model benefits from utilisation of the CA technique to represent initial and evolving microstructural features at an appropriate length scale, and consequently linking the macro scale process variables obtained using an overlying FE mesh.

Simulations were conducted on a specimen and tool model using 4-noded quadrilateral elements. Deformation was simulated for aluminium alloy at 400^oC temperature which friction at the tool-stock interface is modelled using the Amonton-Coulomb law with a constant coefficient of friction of 0.1. The deformation was done a constant nominal strain-rate of 3 /s. The stock is thickness reduced by 41% during the deformation. The results of flow stress predictions from the multi-scale model are presented.

2. Multi-Scale Model Design

The paper builds on the work of Zhu and Sellars [1] on plane strain compression of Al-1%Mg alloys to evolve periodic functions (ϕ). These periodic functions are capable of mimicking the different sub-grain features explicitly within a CA cell. Figure 1 illustrates the proposed systems state modelling framework. The macro variables are captured at the finite element integration point. Using the CAFE framework, the micron level information in terms of grain interiors and grain boundaries are captured by CA cells of the size of 40~100 microns. The integration point variables e.g. strain are distributed over the CA cells using a biasing procedure [2]. These are marked as ε_{gb} and ε_{in} for strains at grain boundaries and grain interiors respectively. The effect of the micron level CA strain on the sub-micron is analysed by the periodic function (ϕ) with different cut-off ranges to model the emergence of the sub-CA structures. Outputs from ϕ are the dislocation densities and sub-grain sizes that are integrated to calculate the integration point stress.

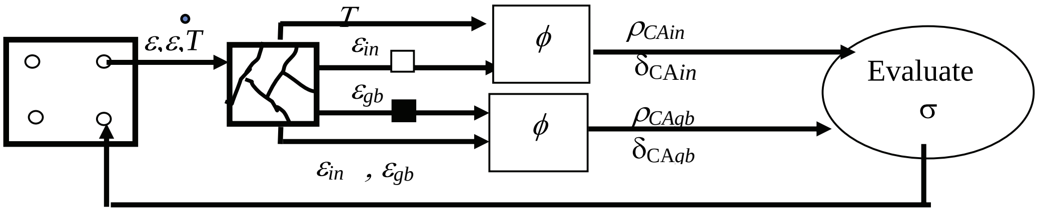

Figure 1 Block diagram of the ϕ-CAFE modelling framework.

Figure 1 illustrated the ϕ-CAFE modelling framework. There are two components: The periodic function ϕ determines the functional form of the events occurring within the 10 by 10 micron material point while the CA holds the information at a 40~100 micron material point. The FE holds the information in terms of local strain, strain rate and temperature at its integration point at a material point of the size of 0.5~1.0 mm.

Figure 2 shows the results of the integration of the sub-micron features with the overlying micron level CA that hold the grain information. The grain structure is deformed and follows the deformation pattern of the overlying finite element.

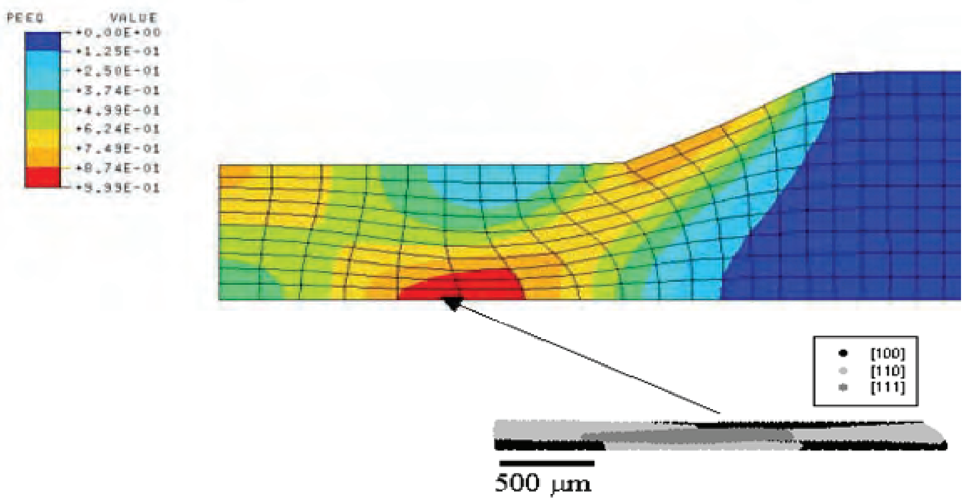

Figure 2: Shape of the PSC sample after a compression of 41%. The insert shows the deformation to the 7 grains associated with the finite element.

3. Conclusions

The paper presented a systems state driven cellular automata based finite element framework to model deformation. The framework is based on observations from micrographs under different deformation conditions and uses periodic functions to mimic the spatial evolution of the micro-features at the sub-micron level. The effect of these are summed up at the micron level and transferred to the integration point of the finite element. The framework is generic in nature and is capable of replicating the local evolution of micro-feature while at the same time reflecting the material response. Further extension to this model is the use of functions that capture the a-periodicity in the observed micrographs in terms of cell size variations.

Acknowledgment

The authors gratefully acknowledge the Engineering and Physical Sciences Research Council, UK for their financial support under grant no. GR/L50198.

References

[1] Q. Zhu and C. M. Sellars. Effect of deformation paths on static recrystallisation behaviour of an Al-2Mg, Recrystallisation and Related Topics (ReX'96), eds. T.R. McNelley et.al, Monterey, California, USA, 195-202 (1996).

[2] S. Das, E. J. Palmiere, and I. C. Howard. CAFE: A Tool for Modelling Thermomechanical Processes. Int. Conf. on Thermomechancial Processing: Mechanics, Microstructure and Control, Sheffield, 23-26 June (2002).

Tensile properties and internal friction study of thermal and athermal dislocation movement in Fe-Cu alloy as a function of Cu precipitation

Abderrahim Al Mazouzi[1], *M. J. Konstantinovic*[1]

[1]*SCK-CEN, Reactor Materials Research Departement, LHMA/ Boeretang 200, 2400 Mol, Belgium*

Fe-Cu model alloys are used to mimic the irradiation damage in Reactor pressure vessel (RPV) steels and to study the kinetics of Cu precipitation in BCC iron. One of the open issues regarding the hardening and the consequent embrittlment of RPV steels, is the role played by copper precipitates on the hardening process. Thus, within the European framework program PERFECT, a substantial effort is dedicated to the evaluation of the strength of all type of irradiation induced obstacles to the movement of dislocations including Cu-preciptates. In this paper, we report on the measurements of the internal friction and tensile properties in Fe-Cu alloys measured in the temperature range between 80 and 450 K to study of the thermal and athermal dislocation movement as a function of Cu precipitation. The formation of different Cu precipitates has been achieved by various thermal aging processes at about 800 K. We analyze the interaction between dislocation and obstacles as a function of their size and distribution on the basis of comparison between experimental results and computer simulations.

Structure-Property Relationships of DIN 22NiMoCr37 Steel in Simulated Coarse-Grained Heat-Affected-Zone

Maria Jose Balart, John F. Knott

Department of Metallurgy and Materials, School of Engineering,
The University of Birmingham, Edgbaston, Birmingham B15 2TT, UK
M.J.BalartMurria@bham.ac.uk J.F.Knott@bham.ac.uk

ABSTRACT

To simulate the microstructures generated in high temperature regions of the heat-affected-zone in thick sections of ferritic steel weldments, samples of as-received (AR) DIN 22NiMoCr37 nuclear reactor pressure vessel steel have been heat treated for 1 h at the austenitising temperature of 1100°C. The samples were then water quenched, tempered for 2 h at 650°C, water quenched and held isothermally at 520°C for 180 h before final air-cooling (QTQE). This heat treatment gave a prior austenite grain size of approximately 100 μm. Fracture toughness tests at –150°C and blunt notch tests at –150°C and –196°C were carried out for the AR steel, which possess a tempered bainite microstructure, and for the 1100-QTQE steel, which possess a tempered martensite microstructure. Compared to the AR steel, the 1100-QTQE steel exhibited improved combinations of strength and fracture toughness, in general, and superior combinations of yield strength and local fracture stress, σ_f, values.

1. Introduction

Alloy steel plates —ASTM A508 MnMoNiCr, ASTM A533B MnMoNi steel, 2 1/4Cr-1Mo, ASTM A543 NiCrMo— quenched and tempered, are widely used for the construction of nuclear reactor pressure vessels (RPV) [1,2]. Thick forgings or plates of such steels usually have a tempered bainite microstructure and are fabricated by welding. Tempered martensite microstructures may be generated in the weld heat-affected-zone (HAZ). Comparing tempered bainite and tempered martensite microstructures in an A533B RPV steel [3], autotempered martensite microstructures had superior combinations of yield strength and fracture toughness values than a lower-and-upper bainite or an upper bainite microstructure. However, a tempered martensitic microstructure was found to be more susceptible to intergranular embrittlement than a bainitic microstructure, in an A533 cl.1 steel having 0.017 wt.% P content and a prior austenite (γ) grain size of 150 μm [4]. The intergranular embrittlement impaired the toughness level. Prior γ grain size is a major factor in determining the brittle and ductile properties of MnMoNi alloys, having a tempered martensitic microstructure and similar strength levels [5]. The effects of austenitizing temperature on prior γ grain size in a specific sample of DIN 22NiMoCr37 steel have been reported [6]. The specific sample was from a forged ring section used to generate the Euro data set for fracture toughness [7]. Fracture toughness data in precracked SE(B)-0.4T specimens and σ_f in blunt notch SE(B)-0.4T specimens in the lower shelf region, in the steel alloy having low levels of trace impurity elements, have been determined for the AR and 1100-QTQE steels [8]. An overview of the main findings on structure-property relationships of DIN 22NiMoCr37 steel in simulated coarse-grained heat-affected-zone (CGHAZ) will be presented here.

2. As-received DIN 22NiMoCr37 steel and experimental procedure

The chemical composition of the DIN 22NiMoCr37 steel, which is said to be equivalent to ASTM A508 Cl.2, is given in Tab. 1. Specimens for mechanical testing were machined from the C(T)-4T broken halves SX25.3, SX25.2 and SX20.1 used in the Euro data set [7]. Details of the specimen location and the mechanical testing procedure are given in Ref. [8].

Table 1. Chemical composition of DIN 22NiMoCr37 steel [6]

C	Si	P	S	Cr	Mn	Ni	Cu	Mo	Sn
0.21	0.22	0.005	0.004	0.41	0.87	0.87	0.06	0.52	0.007
Al	As	B	Sb	Ti	Nb	V	N	O	Fe
0.014	0.006	<0.0005	0.002	0.0004	0.002	0.004	0.008	0.0005	Bal.

3. Results, discussion and conclusions

3.1 Prior austenite grain size

The microstructure of the AR steel consists of tempered bainite whereas that of the 1100-QTQE steel is tempered martensite. The AR sample exhibited a fine-grained microstructure, Fig. 1(a). The 1100-QTQE steel showed a prior γ grain size of approx. 100 μm, Fig. 1(b).

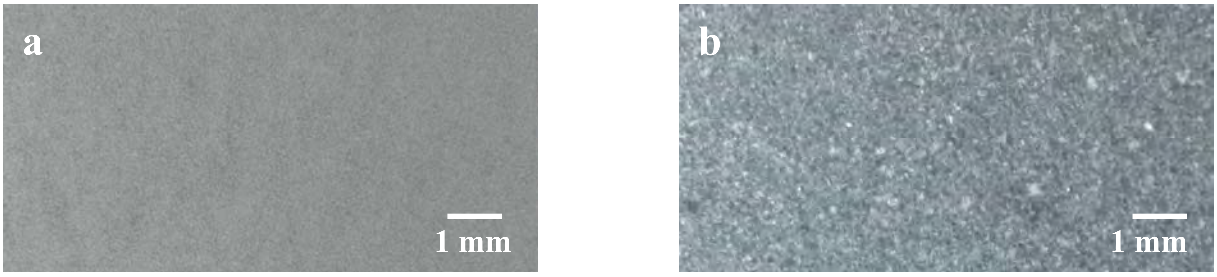

Figure. 1. Macrographs of (a) the AR steel and (b) the 1100-QTQE steel.

3.2 Tensile, fracture toughness and blunt notch four-point bend tests

Tensile test results obtained at -150°C and -196°C for the AR and 1100-QTQE steels are summarised in Tab. 2. For a given testing temperature, compared to the AR steel, the YS, UTS and the YS / UTS ratio increased for the 1100-QTQE steel, whereas the n value decreased. The RA values were similar. On decreasing the testing temperature from -150°C to -196°C, for a given steel condition (AR or 1100-QTQE), the YS, UTS and the YS / UTS ratio increased, whereas both the n and the RA values decreased. The El values remained practically unchanged. Fig. 2(a) shows the values of sharp crack fracture toughness determined at -150°C, for the AR and the 1100-QTQE steels plotted as normal cumulative distribution functions (cdf). The mean fracture toughness decreased from 94.3 ± 14.3 MPa $m^{1/2}$ for the 1100-QTQE steel to 58.4 ± 6.85 MPa $m^{1/2}$ for the AR steel. This decrease is significant at the 5% level of significance, assuming two normal populations having equal variance at the 1% level of significance. The 1100-QTQE steel exhibited, in general, improved combinations of YS and fracture toughness compared to the AR steel. The local fracture stress, σ_f, values for blunt notch SE(B)-0.4T specimens are represented in Fig. 2(b). The AR steel had lower σ_f values (1948-2041 MPa, at -150°C and 2017-2192 MPa, at -196°C), compared to the 1100-QTQE steel (2591-2641 MPa, at -150°C and 2364-3014 MPa, at -196°C).

Table 2. Tensile properties

Specimen	T (^{o}C)	YS (MPa)	UTS (MPa)	YS / UTS	El (%)	RA (%)	n
AR							
SX25.3-3.2+1.3	-150	779 (830)	866	0.90	18.4	54	0.136
SX25.3-3.2+1.1	-196	917 (978)	978	0.94	18.0	29	0.121
SX25.3-3.2+1.2	-196	917 (988)	988	0.93	18.7	15	0.134
mean	-196	917 (983)	983	0.94	18.4	22	0.128
1100-QTQE							
SX25.3-2.2+1.1	-150	978	1070	0.91	16.6	49	0.071
SX25.3-2.2+1.9	-150	1013	1100	0.92	15.0	45	0.072
SX25.3-2.2+1.3	-150	1044	1108	0.94	16.0	46	0.053
mean	-150	1012	1093	0.92	15.9	47	0.065
SX25.2-1.2'+1'.7	-196	1182 (1192)	1227	0.96	17.1	29	0.064

(upper) and lower yield points values;

T—Testing temperature; YS—0.2% yield strength; UTS—ultimate tensile strength;

El—elongation to failure; RA—reduction of area; n—strain hardening exponent

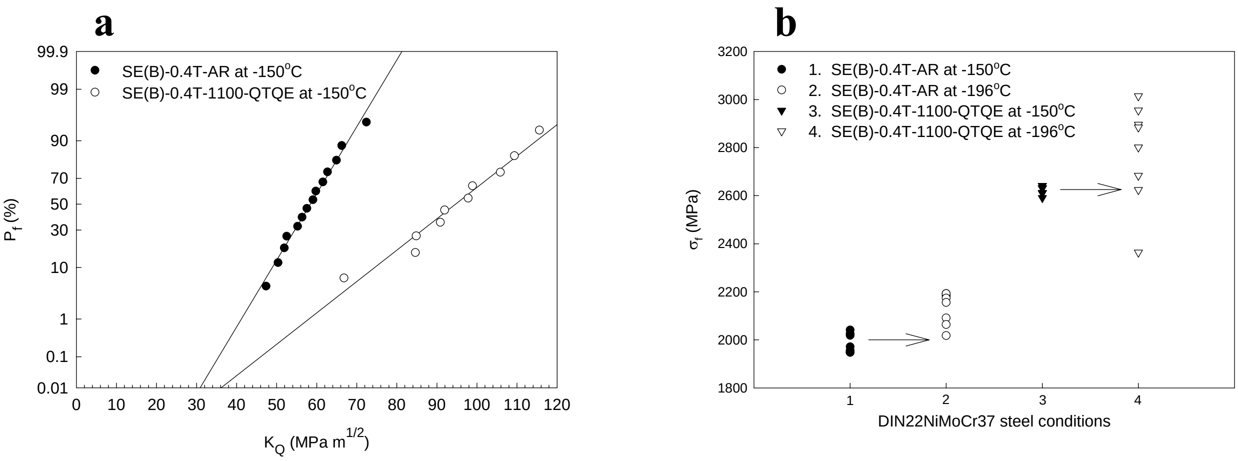

Figure 2. (a) Normal cdf of fracture toughness values for precracked SE(B)-0.4T specimens, and (b) local fracture stress, σ_f, values for blunt notch SE(B)-0.4T specimens.

4. References

[1] Standard specification for general requirements for steel plates for pressure vessels, American Society for Testing and Materials, Philadelphia, ASTM A20/A20M-05, Vol. 01.04; 2004.

[2] Standard specification for quenched and tempered vacuum-treated carbon and alloy steel forgings for pressure vessels, ASTM A508/A508M-04b, Vol. 01.05; 2005.

[3] P. Bowen, S.G. Druce, J.F. Knott, Effects of microstructure on cleavage fracture in pressure vessel steel, Acta Mater. 34(6) (1986) 1121-1131.

[4] S. Raoul, B. Marini, A. Pineau, Effects of microstructure on the susceptibility of a 533 steel to temper embrittlement, J. Nucl. Mater. 257 (1998) 199-205.

[5] S.G. Druce, Effects of austenitisation heat treatment on the fracture resistance and temper embrittlement of MnMoNi steels, Acta Mater. 34(2) (1986) 219-232.

[6] M.J. Balart, J.F. Knott, Simulated coarse-grained heat-affected-zone microstructures in DIN22NiMoCr37 steel, submitted for publication (2006).

[7] J. Heerens, D. Hellmann, Development of the Euro fracture toughness data set, Eng. Fract. Mech. 69(4) (2002) 421-449.

[8] M.J. Balart, J.F. Knott, Low temperature fracture properties of DIN 22NiMoCr37 steel in fine grained bainite, and coarse grained tempered embrittled martensite, in preparation (2006).

Effective domain wall obstacle interactions for micro-mechanical modeling of ferroelectric ceramics

A.Yu. Belov[1,2], **W.S. Kreher**[1]

[1]**Institut für Werkstoffwissenschaft, Hallwachsstrasse 3, Technische Universität Dresden, 01062 Dresden, Germany, belov@tmfs.mpgfk.tu-dresden.de;** [2]**Institute of Crystallography RAS, Moscow, Russia.**

ABSTRACT

The temperature dependent ferroelectric hysteresis is used to probe the pinning potential for the domain wall motion. It is shown that microscopic parameters (the obstacle strength and zero field activation energy) characterizing the effective interactions between domain walls and obstacles in ferroelectric ceramics can be directly assessed from the experimental data on the temperature dependence of the coercive field. The approach is based on an expression for the thermal-activation-based mobility of domain walls implemented within the framework of a time-dependent constitutive model, which describes microstructural evolution of ferroelectric ceramics in terms of rate equations for a suitable set of internal variables. Thus explicit links between the features of the microscopic interactions and the electro-mechanical behaviour of ferroelectric ceramics at meso- and macroscopic scale can be made.

1. Introduction

Polarization reversal in ferroelectric ceramics occurs either by growth of the existing domains favourably oriented relatively to the applied electric field (or stress) and by nucleation of new domains. The domain growth proceeds by the domain wall (DW) motion and its kinetics is controlled by different mechanisms characterized by different time scales. The DW mobility can be limited either by the formation time of a critical size nucleus on the domain wall or by the time of its depinning from various obstacles such as vacancies, interstitials, as well as pairs or even more complex aggregates of positively and negatively charged defects. Limited information on the atomic-scale processes of unpinning of domain walls from obstacles is one of the main issues in linking between the dynamics of individual DWs and the microstructure evolution in polycrystalline ferroelectrics. In lead zirconate titanate (PZT) piezoceramics the internal friction measurements indicate that the DW behaviour is influenced by a complex interplay between dopants (‘soft’ and ‘hard’) and oxygen vacancies. However, the atomic structure of the pinning defects and the mechanism of unpinning itself are still a matter of debates. In the statistical theories of the DW motion in fluctuating force fields, caused by randomly distributed obstacles, the dispersion of the random force (assumed normal) is the main parameter controlling the irreversible domain wall displacement and hysteresis [1-2]. Thus, the behaviour of the DW ensembles is determined by the probability for a DW to encounter an obstacle sufficiently strong to pin it. The statistical models describe the wall displacements under weak fields, where the polarization dependence on the electric field has the form of the Rayleigh loop, and also yield the coercive field in terms of the random pinning force dispersion. Fig. 1 illustrates an important limitation of the model of random athermal obstacles [1-2]: as the temperature decreases, the hysteresis curve of a soft PZT piezoceramic transforms into the Rayleigh loop, even if the electric field is as twice as higher than the RT coercive field. Therefore, the temperature dependent ferroelectric hysteresis can be used as a tool to probe the pinning potential. In this approach, the dispersion of the activation energy required for a DW to surmount the obstacles becomes the main characteristic of the pinning field (a similar problem in theory of dislocations was considered in [3]). Analysing experimental data for doped PZT ceramics, it was suggested [4] that the interaction between DWs and obstacles can be described by a single 'effective' activation energy in a wide temperature range. Here, we give some extensions of the method.

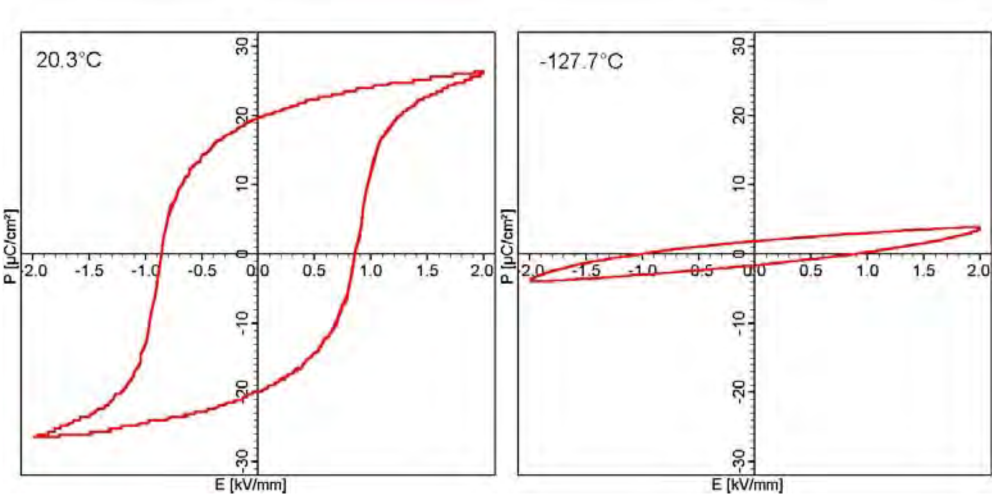

Figure 1. Experimental hysteresis (left) and Rayleigh (right) loops in a commercial piezoelectric ceramic Sonox P53 at the frequency of 50 Hz. Data are from the web site http://www.piezolab.de.

2. Constitutive model for ferroelectric ceramics

A ferroelectric ceramic is assumed to have M distinct domain orientations in a grain, with each variant I being characterized by its volume fraction ξ_I as well as its spontaneous strain $\boldsymbol{\varepsilon}^{s(I)}$ and polarization $\boldsymbol{P}^{s(I)}$. Here, simulations were performed for tetragonal ceramics ($M = 6$). The average values of the spontaneous strain and polarization in a grain with a polydomain structure are represented as

$$\begin{bmatrix}\boldsymbol{\varepsilon}^{s}\\ \boldsymbol{P}^{s}\end{bmatrix}=\sum_{I=1}^{M}\begin{bmatrix}\boldsymbol{\varepsilon}^{s(I)}\\ \boldsymbol{P}^{s(I)}\end{bmatrix}\xi_I \ . \tag{1}$$

The constitutive relations for the crystal (grain) are derived under an assumption (known as the Reuss method) that the electric field $\boldsymbol{E}$ and stress $\boldsymbol{\sigma}$ are identical in all variants

$$\begin{bmatrix}\boldsymbol{\varepsilon}\\ \boldsymbol{D}\end{bmatrix}=\left(\sum_{I=1}^{M}\begin{bmatrix}\boldsymbol{S}^{(I)} & \boldsymbol{d}^{(I)T}\\ \boldsymbol{d}^{(I)} & \boldsymbol{\kappa}^{(I)}\end{bmatrix}\xi_I\right)\begin{bmatrix}\boldsymbol{\sigma}\\ \boldsymbol{E}\end{bmatrix}+\begin{bmatrix}\boldsymbol{\varepsilon}^{s}\\ \boldsymbol{P}^{s}\end{bmatrix} . \tag{2}$$

Here, $\boldsymbol{S}^{(I)}$, $\boldsymbol{d}^{(I)}$, and $\boldsymbol{\kappa}^{(I)}$ are the tensors of elastic, piezoelectric, and dielectric constants of the I variant. In ceramics Eq. (1) and (2) must be further averaged over grain orientations, for example, using a discrete set of representative grain orientations instead of a continuous distribution function [5]. Each orientation in the set possesses a system of M variants, with the total number of variants used for averaging being $N = MK$, where K is the number of the systems. Correspondingly, summation in Eq. (1) and (2) is expanded over all N variants. However, the switching is possible only between M variants, which belong to one system.

According to [4], the constitutive model of a ferroelectric ceramic can be formulated as a set of rate equations for the domain volume fractions $\{\xi_I\}$, with the transformation rate for each variant *I* being represented as

$$\dot{\xi}_I = \sum_{J=1, J\neq I}^{N} \{-w_{IJ} + w_{JI}\} \quad , \quad w_{IJ} = w_0 \exp\left\{-\frac{\Delta H(f_{IJ})}{kT}\right\}\xi_I^{\alpha}, \tag{3}$$

and the switching fraction ξ_I^{α}, where the exponent α is a model parameter, is introduced to account for the DW annihilation as the volume occupied by the variant *I* vanishes. For the enthalpy of activation we adopt an expression [6]

$$\Delta H(f_{IJ}) = \Delta H_0 \left\{1 - \frac{f_{IJ}}{f_*}\right\}. \tag{4}$$

The defect strength f_* and the activation barrier height ΔH_0 characterize the atomic-scale interactions between the domain walls and obstacles. The most significant part of the driving force for the transformation $I \to J$ is $f_{IJ} = -E_i \Delta P_i^s - \sigma_{ij}\Delta\varepsilon_{ij}^s$, where $\Delta P_i^s = P^{s(I)} - P^{s(J)}$ and $\Delta\varepsilon_{ij}^s = \varepsilon_{ij}^{s(I)} - \varepsilon_{ij}^{s(J)}$ are the jumps of the spontaneous polarization and strain across DW. The constitutive model outlined above provides a method for a direct assessment of the parameters f_* and ΔH_0. As is shown in [4], for a model ferroelectric with only two variants *I* and *J*, corresponding to 180° domain switching with the driving force $f = 2P^0E$, the system of Eqs. (3) and (4) admits an analytical solution yielding the following estimate for the coercive field

$$\frac{E_c(T)}{E_*} = 1 - \frac{kT}{\Delta H_0} \ln\left(\frac{w_0}{4\nu}\frac{E_*}{E_0}\frac{1}{g(\alpha)}\frac{kT}{\Delta H_0}\right). \tag{5}$$

Here, the function $g(\alpha)$ is about unity, E_0 and ν are amplitude and frequency of a triangular electric field, and the normalized defect strength is introduced via $f_* = 2P^0E_*$. In agreement with experimental data for a number of piezoceramics [7-8], the coercive field (5) depends on *T* nearly linearly and therefore can be represented as

$$\frac{E_c(T)}{E_*} = 1 - \frac{T}{T_*}, \tag{6}$$

where the weak logarithmic dependence of T_* on *T* is neglected. Now the parameters E_* and T_* can be extracted from the slop of the experimental plot presented in Fig. 2, whereas the barrier height ΔH_0 is calculated from Eq. (5). An example of such calculations is given in Tab. 1. Fig. 2 also shows the dependence $E_c(T)$ simulated for 90° domain switching with a nearly isotropic distribution of grain orientations. The defect strength in this case is related to the parameter E_* from Tab. 1 as $f_* = \sqrt{2}P^0E_*$.

Table 1 Parameters for obstacles in a piezoceramic PZT-4 extracted from Fig. 2 and conditions of the measurements [8]. The results of calculations are given for $w_0 = 10^{11}$ and 10^{10} Hz (in parentheses).

E_0 (MV/m)	ν (Hz)	$2P^0$(C/m^2)	T_* (K)	E_* (MV/m)	ΔH_0 (eV)
2.5	1.0	0.60	575	3.1	0.85 (0.74)

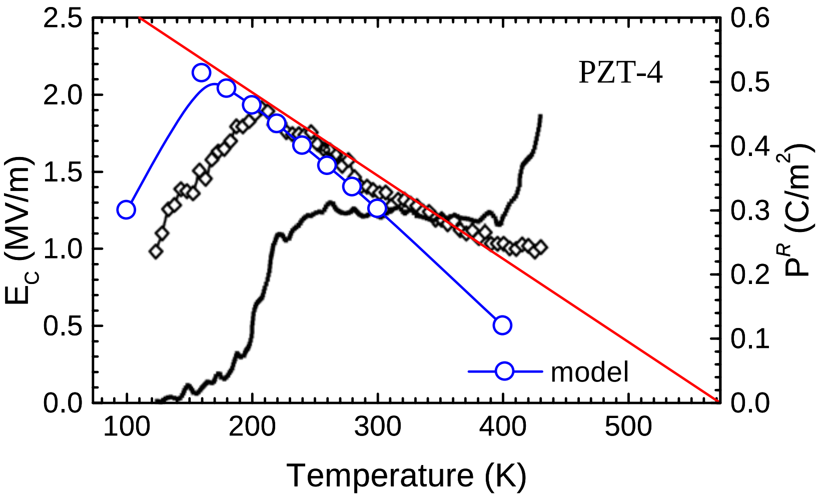

Figure 2. Computed and experimental [8] coercive field vs. temperature in a piezoceramic PZT-4. Computations were performed for a tetragonal ceramic and ten nonequivalent grain orientations in a plane containing the electric field ***E***.

3. Conclusions

Using a rather simple constitutive model, we showed that the temperature behaviour of the coercive field in ferroelectric ceramics is consistent with the assumption that the interaction between domain walls and obstacles is described by a single ‘effective’ activation energy. This hypothesis gives rise to good agreement between the model and experiment in a wide temperature range, including room temperature. A noticeable discrepancy occurs only at low temperatures. The simple structure of the constitutive equations makes the model very suitable for micro-mechanical applications, primarily to multi-axial problems.

Acknowledgements

Support from Deutsche Forschungsgemeinschaft is gratefully acknowledged.

References

[1] H. Kronmüller, “Statistical theory of Rayleighs law”, Z. Angew. Phys. **30**, 9 (1970),
[2] O. Boser, “Statistical theory of hysteresis in ferroelectric materials”, J. Appl. Phys. **62**, 1344 (1987).
[3] R. E. Forman, “Dislocation dynamics with random barrier height and spacing”, Phil. Mag. **26**, 553 (1972).
[4] A. Yu. Belov and W.S. Kreher, “Simulation of microstructure evolution in polycrystalline ferroelectrics-ferroelastics”, Acta Mater. **54**, 3463 (2006).
[5] A.Yu. Belov and W.S. Kreher, “Viscoplastic behavior of perovskite type ferroelectrics”, Mater. Sci. Eng. B **118**, 7 (2005).
[6] U. F. Kocks, A. S. Argon, and M. Ashby, “Thermodynamics and kinetics of slip”, Progr. Mater. Sci. **19**, 1 (1975).
[7] I. W. Chen and Y. Wang, “A domain wall model for relaxor ferrolectrics”, Ferroelectrics **206**, 245 (1998).
[8] M. W. Hooker, “Properties of PZT-based piezoelectric ceramics between -150 and 250°C”, NASA Report No. CR-1998-20878, 1998.

Stress Induced Grain Boundary Migration in Polycrystalline Cu Lines

D.N. Bentz, M.O. Bloomfield, J.-Q Lu, R. J. Gutmann, and T.S. Cale

Focus Center- New York, Rensselaer: Interconnections for Hyperintegration
Rensselaer Polytechnic Institute, Troy, NY, USA 12180-3590
email: calet@rpi.edu

ABSTRACT

We discuss our ‘grain-continuum’ approach to model stress-driven grain boundary migration of polycrystalline Cu lines. We combine a multiple-material level-set representation of the grain structure, in a code named PLENTE, and finite-element calculations performed by Comsol Multiphysics 3.2. The anisotropic elastic constants of single crystal Cu are used for each grain in the structure (film/line). A temperature change is imposed and grain boundary velocities are calculated from the differences in the computed strain energies across grain boundaries. We apply this approach to idealized polycrystalline films and to polycrystalline Cu lines embedded in silicon dioxide. For polycrystalline films under tension, we show that <100> fiber texture grains grow at the expense of <111> grains since they are weaker in the plane.

1. Introduction

Models and software that predict the properties, performance and reliability (PPR) of materials, structures, and systems are key elements of a ‘virtual wafer fab’; *i.e.*, *in silico* design, fabrication, and testing of integrated circuits (ICs). The PPR of materials have foundations at the atomic scale; however, their impact on manufactured items, such as on ICs, depends significantly upon structural and microstructural details. As such, there is considerable interest in understanding how grain structure affects PPR as well as the fundamental processes behind grain structure evolution [1]. Several approaches have been used to predict PPR of materials, structures, and systems that can be roughly labelled atomistic, ‘modified-continuum’, and ‘grain-continuum’ approaches. Atomistic models can account for fine details, but these methods are not yet feasible for simulating many IC structures and processes, *e.g.*, on the spatial and temporal scales needed to interpret reliability studies on commonly used test structures. Modified-continuum models, which include such things as Hall-Petch correlations, do not account for microstructural details well.

Our grain-continuum (GC) approach is designed to deal with microstructure on engineering spatial and temporal scales. GC models treat grains as a collection of distinct, interacting continua. Each grain in a GC simulation is represented by its boundaries and any internal field variables, such as composition, stress, or temperature. PLENTE [2,3] is a GC software that can represent and evolve grain structures. In this paper we discuss stress-induced grain boundary migration [4], using a combination of PLENTE and Comsol Multiphysics 3.2 (CM), a commercial finite element code. We simulate the effects of grain orientations on the elastic response of an idealized polycrystalline thin film and simple grain evolution due to strain energy release. We then demonstrate our approach on a more IC-relevant structure, a polycrystalline Cu line segment encased in silicon dioxide.

2. Effects of Elastic Anisotropy

Single grains of Cu have anisotropic elastic characteristics which impact the stresses in polycrystalline structures. The elastic modulus for single crystal Cu is 2.9 times as large in the

<111> direction than it is in the <100> direction [5], as shown in Fig. 1. When a mechanical load is placed on a polycrystalline structure in which grains of different orientations are present, stresses are distributed throughout the grain structure in a complex manner.

In the finite element model, the elastic constants are assigned to each grain in the system through the elasticity matrix C_{grain}, which is defined as

$$\sigma = C_{grain}\varepsilon_{el} \tag{1}$$

Here, the elasticity matrix relates the six components of the stress vector (σ), including normal and shear components, to the strain in vector form (ε_{el}). The values in C_{grain} depend on the crystallographic orientation chosen for the particular grain. For a crystal of Cu with the <100> directions aligned with the lab frame, the elasticity matrix has three unique non-zero components; C_{11} = 168.4 GPa, C_{12} = 121.4 GPa, and C_{44} = 75.4 GPa [5]. Once the desired orientation of a grain is chosen, the elasticity matrix is rotated.

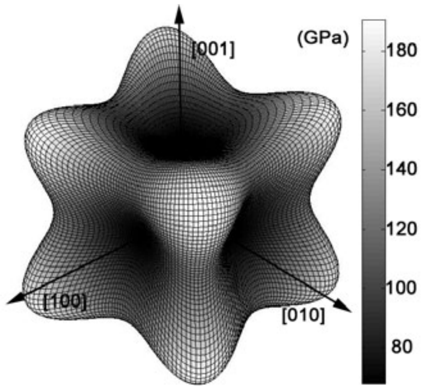

Figure 1. Spherical plot of the directional dependence of Young's modulus for single crystal Cu.

In these elasticity models, grains are treated as individual elastic materials that undergo no topological changes during the stress-strain calculation. We also assume no slipping occurs at grain boundaries or material interfaces. As an example, we examine an idealized thin film composed of hexagonally shaped Cu grains. Fig. 2 shows a 6 μm by 5.2 μm rectangular film containing 17 grains (or parts of grains). The 1 μm thick film has been deposited on an oxidized 1 mm thick silicon wafer where the oxide layer is 1 μm thick. The geometry is periodic in the plane, and is not capped. The system is cooled from an assumed stress-free state at 525 K to 425 K and the stresses from the CTE mismatch between the various materials are computed. When the Cu film is treated as homogeneous and isotropic using the properties of bulk Cu (that is, when the effects of the grains are ignored), the film exhibits a uniform strain energy throughout the Cu of ~0.4 J/cm^3. When the film consists of grains with their <111> axes perpendicular to the film surface, the strain energy resulting from the temperature change is ~0.6 J/cm^3. It is 50% higher than the isotropic case due to the larger in-plane Young's modulus.

Fig. 3a shows the strain energy distribution computed for a film in which one of the grains has been rotated such that a <100> axis is aligned with the surface normal. Inside and around the <100> grain the strain energy density range from ~0.9 J/cm^3 to ~0.4 J/cm^3. The effective Young's modulus of the center grain in the plane of the film is significantly lower than the moduli of the grains around it. This effect illustrates how grain structure can provide a driving force for migration of atoms.

3. Stress Induced Atomic Migration

Models that include strain energy as a driving force for grain boundary motion have been used, together with curvature driven grain boundary migration [6] to explain strain-induced abnormal grain growth in Cu films [7]. We write the grain boundary velocity as proportional to the strain energy difference across a grain boundary, Δ*u*, and the grain boundary mobility M_{GB} as

$$\boldsymbol{v}_{\varepsilon} = \Delta \boldsymbol{u}\ \boldsymbol{M}_{GB}\ \hat{\boldsymbol{n}}_{GB} \tag{2}$$

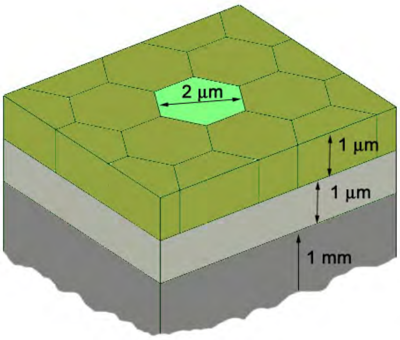

Figure 2. Schematic of the thin polycrystalline Cu film discussed in the text.

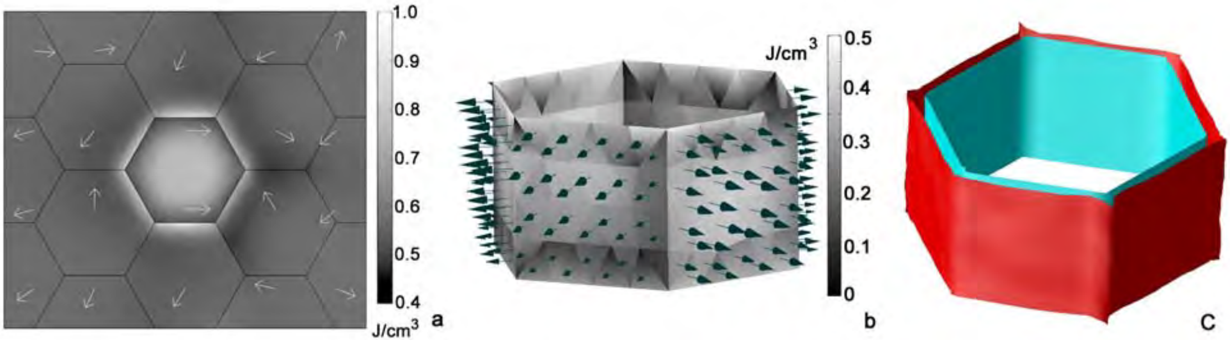

Figure 3. (a) Strain energy density at the horizontal plane in the middle of the film discussed in the text. Grains are oriented with their <111> axis normal to the plane of the film and a uniform, random distribution of in-plane rotations, except for the center grain which is rotated such that the <100> axis is aligned with the normal to the plane of the film. White arrows indicate in-plane <010> directions. (b) Arrows show the magnitude and direction of the grain boundary velocities, as computed using the differences in strain energies between the <100> and <111> grains. (c) Perspective image of the grain boundary of the center grain before and after being moved by PLENTE, after 12.5 hours at 425 K.

Here $\hat{\boldsymbol{n}}_{GB}$ is a unit vector normal to the grain boundary pointing towards areas of higher strain energy. As atoms leave a grain of high strain energy and move across a grain boundary to a grain with lower strain energy, the grain boundary moves in the opposite direction. Strain energy is computed in terms of the components of stress σ_i and strain ε_i as

$$\boldsymbol{u} = \frac{1}{2}\sum_{i} \boldsymbol{\varepsilon}_i \boldsymbol{\sigma}_i \qquad (3)$$

The mobility may be expressed as

$$\boldsymbol{M}_{GB} = \frac{\boldsymbol{b}\,\boldsymbol{\upsilon}\,\Omega}{\boldsymbol{kT}} \exp\left(-\frac{\Delta \boldsymbol{G}}{\boldsymbol{kT}}\right) \qquad (4)$$

Here *b* is the distance the grain boundary is displaced by the addition of an atom, υ is the Debye frequency, Ω is the atomic volume, *k* is the Boltzmann constant, *T* is absolute temperature and ΔG is the free energy associated with atomic exchange across the grain boundary [3].

To illustrate, we examine the grain boundary motion for the computed strain energies of the Cu film shown in Fig. 3a. Using the same stress conditions as described above we examine the strain energy distribution of the film composed of a <100> textured grain surrounded by grains of <111> texture. This structure exhibits strain energy differences between the <100> and <111> grains of 0.1 to 0.45 J/cm^3. Using literature values for the terms of M_{GB} [3] and approximating ΔG as 1 eV [3], we see that stresses in the film promote the growth of the <100> grain. While the center of the <100> grain has higher strain energies than the surrounding <111> grains, at the grain boundary the <100> strain energies are lower. This is attributed to the <100> grain being softer in the plane of the film and strain in the plane of the grain boundary being continuous due to the no-slip condition.

4. Evolution of a Polycrystalline Cu Line

We demonstrate the interaction of PLENTE and CM in a polycrystalline Cu line encapsulated in an oxide film on a silicon wafer. Fig. 4a shows the initial structure developed in PLENTE, using an isotropic deposition model. The structure is a 1.0 μm segment of a long Cu line, with a 0.4 μm by 0.4 μm cross section, surrounded by oxide on both sides, sitting on 0.3 μm of oxide, and capped with 0.3 μm of oxide. The oxide sits on a thick piece of silicon. A grain boundary fitted finite element mesh was developed by PLENTE, as an extension of the method detailed in [8], and exported to CM. In CM, all grains in the line, except for one, have a <111> orientation with respect to the surface of the line. The front/center grain in Fig. 4 has a <100> orientation. We use these particular grain orientations only to illustrate the model. Stresses are generated in the line structure by cooling it from a stress free-state at 525 K down to 425 K. For this temperature change, strain energies in the line are between 0.1 and 0.4 J/cm^3. Strain energy differences between the <100> and <111> grains are between 0.0 and 0.2 J/cm^3. Grain-boundary velocities are computed as discussed above. The velocities are then exported back into PLENTE where the level-set representation is updated. Fig. 4b shows one view of the line segment after evolving the structure for 30 hours. Interpreting the motions of the grain boundaries is more complex than in the thin simple film studied above. The <100> grain is surrounded on three sides by grains of <111> texture as well as the oxide.

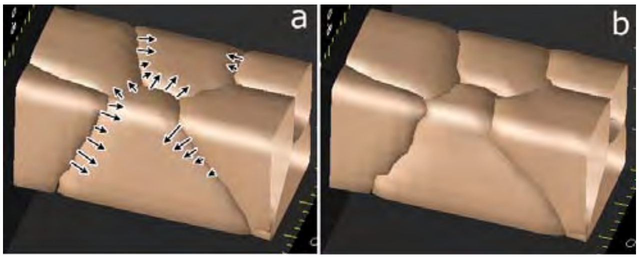

Figure 4. (a) Initial grain structure in an oxide-encapsulated Cu line as described in the text. Arrows help guide the eye regarding grain boundary motion. (b) Grain structure after 30 hours of evolution with the strain energy driven model, as described in text. For demonstration purposes, time evolution is carried beyond the likely range of validity.

5. Conclusions

We present an approach to using GC models to examine the effects of thermally induced stresses on Cu grain evolution. The thermal expansion mismatch between the polycrystalline Cu and the surrounding materials creates stresses. Finite element calculations indicate that jumps in strain energy can exist across grain boundaries in these Cu films due to orientation effects. The model we present uses the local strain energy difference between grains as the driving force for grain boundary evolution. These differences are converted to grain boundary velocities using estimates of grain boundary mobilities. PLENTE uses these velocities to evolve the representation of the grain structure. The cycle can be repeated to simulate large changes in grain structure. CM and PLENTE interact by exchanging grain boundary fitted meshes.

Acknowledgments

This work was supported by MARCO, DARPA and NYSTAR through the Interconnect Focus Center.

References

[1] International Technology Roadmap for Semiconductors, <http://www.itrs.net/>.
[2] M. O. Bloomfield, D. F. Richards, and T. S. Cale, *Phil. Mag.* **83**(31-34), 3549-68 (2003).
[3] M. O. Bloomfield and T. S. Cale, *Microelec. Eng.* **76**, 195-204 (2004).
[4] D.N. Bentz, M.O. Bloomfield, H. Huang, J.-Q Lu, R. J. Gutmann, and T.S. Cale, in *Proc. 2006 Inter. Conf. on Sim. of Semi. Proc. and Dev.*, 2006 (IEEE), in press.
[5] G. Simmons and H. Wang, *Single crystal elastic constants and calculated aggregate properties: a handbook* (M.I.T. Press, Cambridge, MA, 1971).
[6] R. Carel, C. V. Thompson, and H. J. Frost, *Acta Mat*. **44**(6), 2479-94 (1996).
[7] C. V. Thompson, *Ann. Rev. Mat. Sci.* **30,** 159-190 (2000).
[8] M.O. Bloomfield, D.F. Richards, and T.S. Cale, *Lecture Notes in Comp. Sci.* **3516**, 49-56 (2005).

A new micromechanical approach to account for internal lengths within plastically deforming polycrystals

Stéphane Berbenni, Nicolas Nicaise, Marcel Berveiller

Laboratoire de Physique et Mécanique des Matériaux, CNRS,
ENSAM, 57078 Metz Cedex 03, France
Stephane.Berbenni@metz.ensam.fr;
Nicolas.Nicaise@metz.ensam.fr;Marcel.Berveiller@metz.ensam.fr

ABSTRACT

This paper introduces a new micromechanical approach based on the description of the granular microstructure and the formation of discrete (spatial-temporal) intragranular plastic slip heterogeneities by at least 2 characteristic internal lengths: the first one is the individual grain size and the second one is the spatial length between active slip bands corresponding to inhomogeneous plastic strain in the interior of grains. These two characteristic internal lengths are observable and can be measured using microscopy. The micromechanical model considers grains as spherical inclusions (with a given diameter) embedded in a homogeneous (infinite) medium, and, *non uniform* plastic strain field within the individual grain characterized by the internal lengths. We find that in contrast with the mean field approaches based on the classic Eshelby formalism where the effect of grain diameter on internal stresses vanishes, the average of internal stresses over the grain as well as the internal energy depend on both introduced characteristic internal lengths.

1. Introduction

In a recent contribution [1], we investigated the role of grain size distribution on the yield stress of heterogeneous materials using an elastic-viscoplastic self-consistent model based on Translated Fields. We assumed a grain size dependent plastic strain rate in a classic mean-field approach assuming homogeneous plastic strain within grains. Significant grain size dispersion effects were found on the overall behaviour and on local fields.

Here, we are seeking to determine the role of slip heterogeneities in plastically deforming polycrystals on the intracrystalline mechanical fields. Experimental investigations [2] showed that plastic flow of crystalline solids at the grain scale is strongly heterogeneous due to the formation of slip lines and slip bands. In this paper, we use micromechanical tools to describe slip bands as the carriers of ‘discrete particles’ of plastic slip. The plastic strain field is described by specific spatial functions representing the occurrence of slip bands. This implies that plastic strain within grain is no more homogeneous as classic mean field approaches such as self-consistent models. We will focus numerical results on the influence of grain size on mean fields over a spherical grain and on internal elastic energy.

2. Micromechanical Theory

2.1. Field equations

We consider a spherical grain of volume Vg with radius R (Fig. 1) embedded in an infinite matrix V (undeformed at infinity). In the present theory, elastic properties are supposed homogeneous and isotropic. Field equations at any point $\underline{r}$ inside Vg are:

$$\sigma_{ij,j}(\underline{r}) = 0 \text{ (stress equilibrium without body forces)} \tag{1}$$

$$\begin{cases} \varepsilon^{T}_{ij}(\underline{r}) = \frac{1}{2}\left(u_{i,j}(\underline{r}) + u_{i,j}(\underline{r})\right) \text{ (total strain)} \\ \beta^{T}_{ji}(\underline{r}) = u_{i,j}(\underline{r}) \text{ (total distortion)} \end{cases} \tag{2}$$

In Eq.(2), $\underline{u}$ is the total displacement field. We consider an elastic body with a given “eigenstrain” (denoted $\underline{\underline{\varepsilon}}^{*}$) representing the fluctuating inelastic field due to slip heterogeneities within Vg:

$$\varepsilon^{T}_{ij}(\underline{r}) = \varepsilon^{e}_{ij}(\underline{r}) + \varepsilon^{*}_{ij}(\underline{r}). \tag{3}$$

In the present theory, elastic properties are supposed homogeneous and isotropic:

$$\sigma_{ij}(\underline{r}) = C_{ijkl}\left(\varepsilon^{T}_{ij}(\underline{r}) - \varepsilon^{*}_{ij}(\underline{r})\right) \text{ with } C_{ijkl} = \mu\left(\delta_{ik}\delta_{jl} + \delta_{il}\delta_{jk}\right) + \lambda\delta_{ij}\delta_{kl}, \tag{4}$$

where (μ , λ) are Lamé moduli.

2.2. Plastic strain source model

We assume that $\underline{\underline{\varepsilon}}^{*}$ is incompressible ($\varepsilon^{*}_{kk} = 0$) and is, in a first attempt, a simple periodic field containing internal characteristic lengths associated with heterogeneous plastic strain within the grain which embodies periodic slip bands (in one direction denoted *k*):

$$e^{*}_{ij}(\underline{r}) = e^{0*}_{ij}\left[1 + \exp(i2\pi p x_k n_k)\right] \text{ if } \underline{r} \in \text{Vg}, \quad e^{*}_{ij}(\underline{r}) = 0 \text{ if } \underline{r} \notin \text{Vg}, \tag{5}$$

where the *microstructural parameter* p=R/h (p is an integer) contains both characteristic lengths (R and h being respectively the grain radius and the spatial period of the plastic strain). The source can be seen as a unidirectional traveling wave function (Fig. 1) carrying plastic slip along the unit vector $\underline{n}$ (unit normal to slip planes). If one considers the asymptotic case where p → 0, we find $\underline{\underline{\varepsilon}}^{*}(\underline{r}) = 2\underline{\underline{e}}^{0*}$, which becomes a classic problem [3].

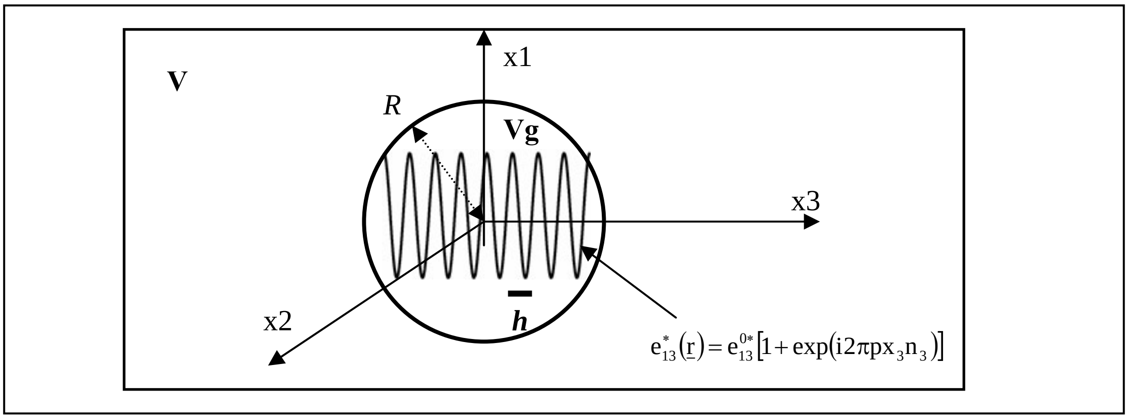

Figure 1. Spherical grain Vg of radius R embedded in an infinite matrix V

2.3. Fourier transform method

We solve the problem using the Fourier transform technique (see e.g. Mura [4]), given periodicity of plastic strain source to determine (i) the mean total distortion over the grain, namely $\overline{\underline{\underline{\beta}}^{T}}^{Vg}$, (ii) the mean internal stresses over the grain, namely $\overline{\underline{\underline{\sigma}}}^{Vg}$, and, (iii) internal elastic energy, namely ϕ_e. Using the Fourier transform of $\underline{\underline{\beta}}^{T}(\underline{r})$, the *mean distortion* yields:

$$\overline{\beta^{T}_{lk}}^{Vg} = \frac{1}{Vg}\frac{1}{8\pi^3}\int_{V_\xi}\tilde{\beta}^{T}_{lk}(\underline{\xi})\int_{Vg}\exp(i\underline{\xi}\cdot\underline{r})dV_r dV_\xi \text{, with } \tilde{\beta}^{T}_{lk}(\underline{\xi}) = 2\mu\xi_l\xi_j\tilde{e}^{*}_{ij}(\underline{\xi})\tilde{G}_{ik}(\underline{\xi}). \tag{6}$$

where $\tilde{\beta}^{T}_{lk}(\underline{\xi})$ is obtained after solving the set of field equations in the Fourier space V_ξ (for any vector $\underline{\xi}$). In Eq.(6), $\tilde{G}_{ik}(\underline{\xi})$ is the elastic Green function (see Mura [4]). The Fourier transform of the plastic source (Eq. 5) is:

$$\tilde{e}^{*}_{ij}(\underline{\xi}) = e^{0*}_{ij}\left(\tilde{\Theta}(\underline{\xi}) + \tilde{\Theta}(\underline{\xi} - 2\pi p\underline{n})\right), \tag{7}$$

where the first term is $\tilde{\Theta}(\underline{\xi}) = \int_{Vg}\exp(i\underline{\xi}\cdot\underline{r})dV_r = \frac{4\pi}{\xi^3}(\sin[R\xi] - R\xi\cos[R\xi])$ and the second one $\tilde{\Theta}(\underline{\xi} - 2\pi p\underline{n})$ results from the Fourier convolution theorem. We deduce the *mean internal stress* over Vg from Eqs.(4) and (6).

The *internal elastic energy* is computed started from its definition $\phi_e = -\frac{1}{2}\int_{Vg}\sigma_{ij}(\underline{r})e^{*}_{ij}(\underline{r})dV_r$ and using the power theorem to get its expression in the Fourier space:

$$\phi_e = -\frac{1}{8\pi^3}\frac{1}{2}\int_{V\xi}\tilde{\sigma}_{ij}(\underline{\xi})\tilde{e}^{*}_{ij}(\underline{\xi})dV_\xi, \tag{8}$$

where $\tilde{e}^{*}_{ij}(\underline{\xi})$ and $\tilde{\sigma}_{ij}(\underline{\xi})$ are computed previously.

3. Application and Numerical results

Mean internal stress over the grain and internal elastic energy are computed in the specific case of Fig. 1 for which the plastic source spreads along the (x3) axis:

$$\frac{\overline{\sigma_{13}}^{Vg}}{e^{0*}_{13}} = -2\mu\left(\frac{1}{3} + \frac{4}{15}\frac{\lambda+\mu}{\lambda+2\mu}\right) + \mu\frac{3}{\pi}\left(I^{(p)}_1 - I^{(p)}_2 - 4\frac{\lambda+\mu}{\lambda+2\mu}\left[I^{(p)}_1 - I^{(p)}_3\right]\right), \tag{9}$$

$$\begin{aligned}\frac{\phi^{e}}{8\mu\pi R^3\left(e^{0*}_{13}\right)^2} = &\left(\frac{1}{9} + \frac{4}{45}\frac{\lambda+\mu}{\lambda+2\mu}\right) + \\ &\frac{1}{\pi}\left(-I^{(p)}_1 + I^{(p)}_2 - \frac{1}{2}I^{(p)}_4 + \frac{1}{2}I^{(p)}_5 + 2\frac{\lambda+\mu}{\lambda+2\mu}\left[I^{(p)}_4 - I^{(p)}_6 + 2I^{(p)}_1 - 2I^{(p)}_3\right]\right)\end{aligned}. \tag{10}$$

Each previous quantity is composed of a constant Eshelby type term (for given μ and λ) and a second p-dependent one (p=R/h) containing the double integrals $I_1^{(p)}, I_2^{(p)}, I_3^{(p)}, I_4^{(p)}, I_5^{(p)}$ and $I_6^{(p)}$ solved numerically. The evolution of the mean internal stress (Eq.(9)) and the internal elastic energy (Eq.(10)) are reported on Fig. 2 as a function of p. The values for elastic isotropic constants are μ=80000 MPa and λ=120000 MPa.

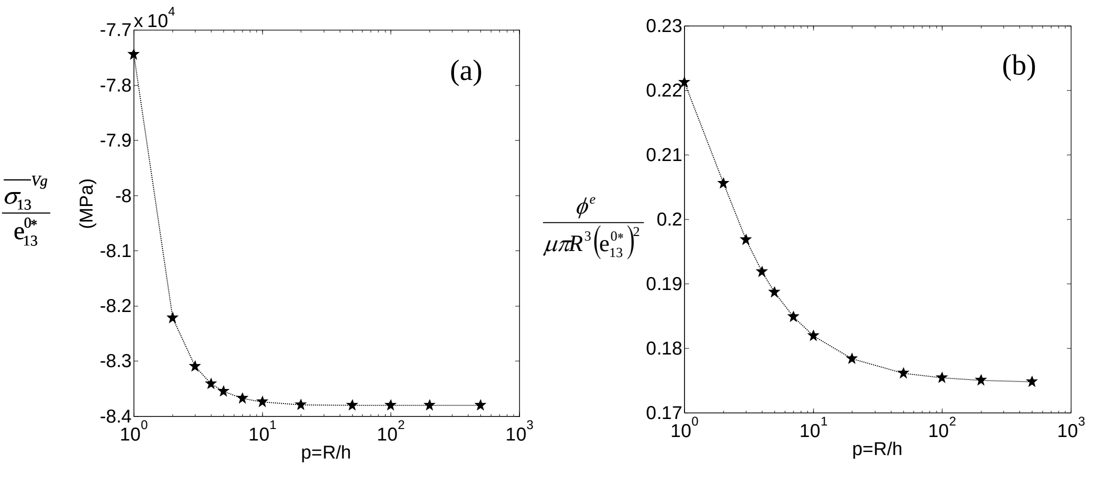

Figure 2. Evolution as a function of p: (a) Internal stress, (b) Internal elastic energy.

Fig. 2 proves both quantities depend significantly on p=R/h which should give new prospects regarding the grain size effect in polycrystals. When p is low, e.g. p=1, grain size effects occur on internal stress (~7% of relative contribution) and on internal elastic energy (~25% of relative contribution). Conversely, when p increases, both quantities tend to the Eshelby solutions of the problem.

4. Conclusions and perspectives

We have identified periodic slip bands within a spherical grain as a periodic unidirectional plastic strain traveling the whole grain. The spacing between bands is modeled by the period of the considered non uniform plastic strain within the grain. Assuming a constant spacing between bands at any grain size, we found that the mean internal stress over the grain as well as the internal energy are grain size dependent until very large values of frequencies for which the classic Eshelby solutions are recovered. From this work, the driving forces associated with the process of slip bands generation in grains of different sizes will be studied in details and other periodic plastic strain fields will be also considered.

Acknowledgements

The authors thank the “Agence Nationale de Recherche” (ANR) for financial support.

References

[1] S. Berbenni, V. Favier, M. Berveiller, Int. J. Plast., In Press (2006).
[2] H. Neuhäuser. In: Dislocations in Solids (vol. 4), F.R.N. Nabarro (Ed.), North-Holland, Amsterdam, pp. 319-440, 1984.
[3] J.D. Eshelby, Proc. Roy. Soc A 241, 376 (1957).
[4] T. Mura, Micromechanics of Defects in Solids (2nd ed.), Kluwer, Dordrecht, 1987.

ParaDiS: crystal strength by direct simulation

Vasily Bulatov [1], *V.V. Bulatov* [1], *R. Cook* [1], *T. Diaz de la Rubia* [1], *J.N. Florando* [1], *M. hiratani* [1], *G. Hommes* [1], *L.L. Hsiung* [1], *T.G. Pierce* [1], *M.. Rhee* [1], *M. Tang* [1], *Wei Cai* [2]

[1] *Lawrence Livermore National Laboratory, University of California, L-367, P. O. Box 808, 94551 Livermore, United States of America*

[2] *Durand building, Room 259, 496 Lomita Mall, Department of Mechanical Engineering, Stanford University, 94305-4040 Stanford, United States of America*

The beauty of dislocation theory is its economy of means: it distills the whole complexity of crystal plasticity to the motion and interaction of dislocations lines that occupy a tiny fraction of the material volume while the rest of the material remains essentially perfect and featureless. Thus, if one were to simulate, on a computer, dislocation motion in physically realistic ways, the overall response to external loads and, thus, material strength could be directly computed.

Such a direct calculation is a daunting task given that dislocation motion takes place on the length and time scales of nanometers and picoseconds whereas the strength response is defined by the collective motion of huge numbers of dislocation lines on the scales of tens of microns and seconds. Even though material scientists have known for over 70 years that crystal strength is defined by dislocation behaviors, it has been impossible so far to put this knowledge to practical use and to compute crystal strength. Massively parallel computing appears to be the only viable approach to closing the wide gap between the levels of computational performance afforded by the existing Dislocation Dynamics codes and that required to compute crystal strength for practical engineering applications.

Development of an efficient new approach for DD simulations on massively–parallel computing platforms has been the objective of the ParaDiS project at LLNL since its inception in 2001. This project spawned new developments in dislocation theory [1], materials physics [2], and mathematical algorithms and computer science [3,4] that combine into a powerful new computational approach. ParaDiS is not only a versatile virtual material-testing machine but simultaneously an amazing computational in situ microscope and a proving ground for the statistical theory of dislocations. Here we report on our recent direct calculations of plastic strength and hardening in BCC metals producing new insights on the origin of dislocation patterns.

[1] W. Cai et al. A non-singular continuum theory of dislocations. J. Mech. Phys. Solids 54, 561-587 (2005).

[2] V. V. Bulatov et al. Dislocation multi-junctions and strain hardening. Nature

440, 1148-1153 (2006).

[3] V. V. Bulatov et al. Supercomputing 2004,

http://www.sc-conference.org/sc2004/schedule/pdfs/pap206.pdf

[4] G. Hommes et al. Supercomputing 2006, submitted.

Influence of Superimposed Normal Loading on the Shear Strength in bcc Metals

Miroslav Černý, Jaroslav Pokluda

Institute of Engineering Physics, Faculty of Mechanical Engineering, Brno University of Technology, Technická 2, CZ--616 69 Brno, Czech Republic.

ABSTRACT

The influence of stress applied perpendicularly to a slip plane during shear deformation of a crystal on the shear strength is important in many deformation processes. As an example, one can consider a nanoindentation process as a combination of shear and compressive deformations in the vicinity of an indentor. Previous studies, based on the empirical Lennard-Jones potential, suggested nearly linear dependence of the theoretical shear strength on the normal tensile and compressive loading. The aim of this study is to verify those results using an ab initio approach for bcc Nb, Mo and W. The three bcc crystals were subjected to shear deformations in ⟨111⟩{112} slip system. Linear dependence was confirmed.

1. Introduction

The influence of a stress applied perpendicularly to slip planes during shear deformation on strength is important in many real deformation processes. In general, the combination of shear and compressive (or even tensile) stress can appear in specific parts of various machine components or in materials that support geotechnical constructions. However, this problem can be studied also at atomistic level. For example, one can analyze a process of dislocation nucleation in the vicinity of nanoindentors induced by shear and compressive deformations. Coupling of shear and normal stress components also determines a critical stress for glide of screw dislocations in bcc crystals [1].

Previous calculations concerning the coupling of normal and shear stresses [2], based on the empirical Lennard-Jones potential, suggested nearly linear dependence of the theoretical shear strength (TSS) on the normal tensile and compressive loading. However, in this study, the slip planes remained undistorted (atomic positions within the planes were fixed) along the entire shear deformation path. The aim of this study is to verify those results using an ab initio approach for three particular bcc metals (Nb, Mo and W).

In the last decade, the theoretical strength was extensively studied from first principles. The papers [3-4] were focused on crystals subjected to pure shear loading. In those studies, two common slip systems: ⟨111⟩{110} and ⟨111⟩{112} were investigated in bcc crystals. TSS values computed for the two slip systems were very similar, particularly for the elements that were selected also for our study. Very recently, molecular dynamics simulations of Mo crystal sheared under superposed hydrostatic loading [5] revealed that the influence of combined loading can lead to qualitatively different failure mechanisms.

2. Computational details

The selected bcc crystals were subjected to homogeneous shear deformations in $\langle 111\rangle\{112\}$ slip system. Along the deformation path, the system was fully relaxed in order to minimize all stress tensor components with the exceptions of superimposed normal stress σ_n (controlled by our computational procedure) and the resolved shear stress τ. The maximal value of shear stress τ_{max} obtained along the deformation path was considered to be the TSS.

For the electronic structure calculations, we utilized the Vienna Ab initio Simulation Package (VASP). This code uses plane wave basis set and projector augmented- wave potential [6]. The exchange-correlation energy was evaluated using the generalized-gradient approximation (GGA) of Perdew and Wang (1992). The 17×15×11 *k*-points mesh was used in all our calculations. The solution was considered to be self-consistent when the energy difference of two consequent iterations was smaller than 10 eV. The stress relaxation was performed using Hellman-Feynman forces.

3. Computed results and discussions

Tab. 1 contains computed values of the equilibrium lattice parameter a_0 (1Å=10^{-10} m), the bulk modulus B and the shear modulus G along with experimental data [7]. Computed G values for shear in {112} plane are compared with values obtained from experimental elastic constants [8] using relation

$$G = \left(C_{11} - C_{12} + C_{44}\right)/2\,. \tag{1}$$

Table 1 Computed values of the equilibrium lattice parameter a_0 and both the bulk B and the shear G moduli along with experimental values.

Element		a_0 (Å)	B (GPa)	G (GPa)
Nb	comp.	3.30	177	35
	expt.	3.30	170	40
Mo	comp.	3.15	268	132
	expt.	3.15	272	128
W	comp.	3.18	318	156
	expt.	3.16	323	163

As can be seen from Tab. 1, the a_0 values well agree with experimental data (within 1%). Also the calculated elastic moduli values mostly coincide within 4% with the exception of G modulus of Nb, where the computed value underestimates the experimental one by 12%.

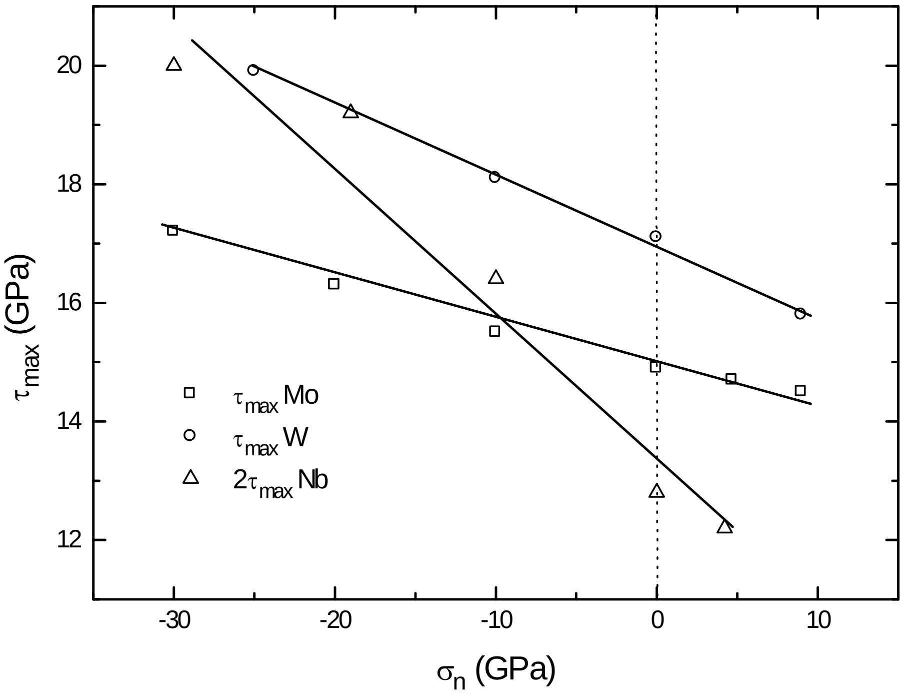

Figure 1. Theoretical shear strengths as functions of superimposed normal stresses for 111{112} slip system in Nb, Mo and W.

The shear in {112} planes follows strictly the ⟨111⟩ direction with minor distortions of the slip planes. The computed dependencies of τ_{max} on normal stress σ_n for the general ⟨111⟩{112} slip system are plotted in Fig. 1. In case of Nb, $2\tau_{max}$ values are plotted in order to fit conveniently all values into one diagram. The dependences are nearly linear as follows from the linear regression lines of the displayed data points. Each line in Fig. 1 can be simply parameterized as

$$\tau_{\max} = \tau_r - k\sigma_n \,, \tag{1}$$

where τ_r correspond to theoretical shear strengths without superimposed normal stress and the k parameters describe slopes of the linear regression lines.

Table 2 Computed values of TSS at zero normal stress τ_r and slopes of linear regression lines k along with available literature data.

Element	TSS$_L$ (GPa)	TSS$_O$ (GPa)	τ_r (GPa)	k (GPa)
Nb	6.4	-	6.6	0.13
Mo	15.8	14.8	15.0	0.07
W	-	17.4	17.0	0.12

Parameters of all displayed linear dependences were collected in Tab. 2. For comparison, the TSS values computed by Luo et al. [3] (TSS$_L$) and by Ogata et al. [4] (TSS$_O$) are also included in Tab. 2. It should be noted that their relaxation procedures correspond to our calculations with controlled zero normal stress. As can be seen, our results are in a reasonable agreement with the reported values.

4. Conclusions

Atomistic modelling of shear in ⟨111⟩{112} slip system in three bcc metals under superimposed normal tensile and compressive stress was performed using ab initio calculations. The theoretical shear strength was computed for several values of the normal stress. It was found that the ideal shear strength increases (decreases) almost linearly with increasing compressive (tensile) stress.

Acknowledgements

This research was supported by European agency COST (Action P19) and the Ministry of Education and Youth of the Czech Republic under the grant No. OC 148.

References

[1] K. Ito, V. Vitek, Phil. Mag. A 81 (2001) 1387.
[2] A. Kelly, W. R. Tyson, A. H. Cottrell, Phil. Mag. 15 (1967) 567.
[3] W. Luo, D. Roundy, M. L. Cohen, J. W. Morris, Jr., Phys. Rev. B 66 (2002) 094110.
[4] S. Ogata, J. Li, N. Hirosaki, Y. Shibutani, S. Yip, Phys. Rev. B 70 (2004) 104104.
[5] D. Xu, R. Yang, J. Li, J. Chang, H. Wang, D. Li, S. Yip, Comp. Mater. Sci. 36 (2006) 60.
[6] G. Kresse, J. Hafner, Phys. Rev. B 48 (1993) 13115; P. E. Blöchl, Phys. Rev. B 50 (1994) 17953.
[7] C. Kittel, Introduction to Solid State Physics, 8th Edition, John Wiley & Sons, 2005.
[8] G. Simmons, H. Wang, Single Crystal Elastic Constants and Calculated Aggregate Properties: A Handbook, MIT Press, Cambridge, MA, 1971.

Fe- BCC Plasticity At Low Temperatures, From Molecular Dynamics To Discrete Dislocation Dynamics

Julien Chaussidon, Marc Fivel, David Rodney

GPM2, ENSPG, 101 rue de la physique, BP 46,
38402 Saint Martin d'Hères cedex, France

ABSTRACT

In order to get a better understanding of cleavage in nuclear reactor pressure vessels made of bainitic steels, we use a multi-scale approach involving molecular dynamics (MD), discrete dislocation dynamics (DD) and finite elements. We present here the first step: the MD to DD transition. We use a potential that reproduces the twinning/antitwinning asymmetry and stabilizes the glide of screw dislocations on (110) plane. We performed a set of MD simulations at low temperatures (50K to 150K) in a BCC structure to determine the velocity law of screw dislocations and local rules for dislocation motion. We distinguished three regimes of propagation depending on the stress and temperature. Then we introduced these local rules into a DD code taking into account the twinnning/antitwinning asymmetry. We finally used a ferritic lath geometry including initial source configurations and stresses determined by post-mortem TEM.

1. Introduction :

Nuclear reactor pressure vessels are made of bainitic steels, with α-Fe laths. In case of accident, cold water is injected which can lead to ductile to brittle transition and a brittle fracture by cleavage. At low temperatures, plasticity in BCC metals is controlled by the motion of screw dislocations which is not well understood. This study aims at a better understanding of this low temperature plasticity in BCC Fe through a multi-scale approach involving MD, DD and finite elements. In the present paper, we will focus on the first scale-transition: from MD to DD.

2. MD simulations :

2.2 Static Simulations:

Firstly we performed static (temperature = 0K) simulations in order to understand screw dislocation slip geometry at low temperature [1]. It exists several EAM potentials of BCC iron leading to different core structures and slip geometries. We have chosen to test two different potentials: Simonelli potential [2] which predicts a degenerate core structure for screw dislocations and Mendelev potential [3] which predicts a non degenerate core structure. From the simulations, we computed the Peierls stress as a function of the orientation of the Maximum Resolved Shear Stress Plane (MRSSP). The two potentials show an asymmetry of the Peierls stress between the twinning and antitwinning region,in agreement with observations made on tension/compression tests. The Mendelev potential is selected because of its ability to stabilize (110) glide over most of the orientation range, as observed experimentally (fig. 1.).

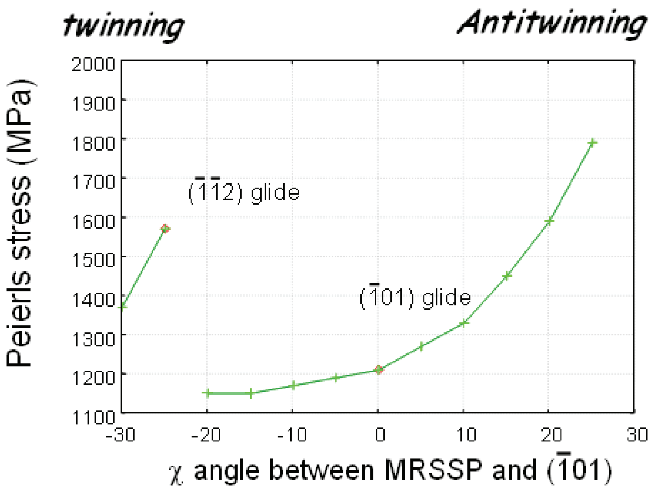

Figure 1. Peierls stress vs χ angle with Mendelev potential

2.3 Dynamic simulations:

2.3.1 Procedure:

We used Mendelev potential to perform dynamic simulations. We investigated a range of temperatures between 50K and 150K and a range of stresses between 200 MPa and 700 MPa with a 64 nm long screw dislocation in order to observe thermally activated phenomena such as double kink nucleation. We used free boundaries conditions as in static simulations. We applied a shear stress resolved on a (110) plane. The simulation duration is 100 ps corresponding to a typical DD simulation timestep.

2.3.2 Results:

We distinguished 3 regimes of propagation depending on stress and temperature.
For each case, the velocity of the edge parts is constant and about 4.5 nm.ps^{-1}.
At low stresses and low temperatures, we observed a single kink-pair regime, with average glide on (110) by double kink nucleation in the horizontal (110) plane. The two edge parts glide rapidly along the screw dislocation and annihilate with themselves thanks to the periodic boundary conditions applied along the dislocation. The screw line is restored between two double kinks. The length of a double kink is d, the size of a Peierls valley. But we noticed that the double kinks pass through an instable position at d/2.
At higher stresses and temperatures, there is a transcient avalanche regime: one double kink initiates several others. Between two avalanches, there is significant waiting times (several ps).
For higher stresses and temperatures we reach a rough regime characterized by cross-kink formation and debris left behind the dislocation line.
These results are summarized in fig.2. Each point represents one simulation, with the screw velocity in nm.ps^{-1} and the average glide plane orientation from the (110) MRSSP. We can notice that for a reason that is not clear the velocity of screw dislocation is unrealistically high, which is why we only consider the geometric results as reliable enough to be introduice in the DDD code.

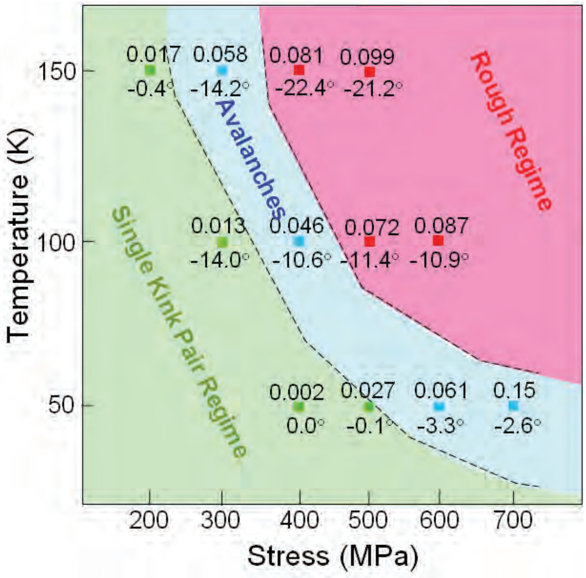

Figure 2. Regimes of propagation depending on stress and temperature.

3. DDD Simulations:

Information from the atomic scale are introduced in a DD code [4] as local rules. In particular, we accounted for the glide asymmetry. We also adopted a screw dislocation velocity law based on strain rate jump experiments. With this new DD code we can describe the thermally activated motion of dislocations in α-Fe.

We used TEM observations to reproduce ferritic lath configurations, especially activated glide system, initial configuration and applied stress field. Dislocation sources are localized in the grain boundaries. Furthermore, some tilt boundaries have been observed, which is why we applied bending stresses to the simulation cell.

In the future we will use this kind of simulations to predict where and how cleavage is initiated inside a ferritic lath.

Aknowledgements:

The authors thank C. Robertson for his helpful work on TEM and F. Louchet for fruitfull discussions.

References:

[1] J. Chaussidon, M. Fivel, D. Rodney *Acta Mat.* (in press).
[2] G. Simonelli, R. Pasianot, E. Savino, *Mater. Res. Soc. Symp. Proc.*, **291**, p.567, (1993).
[3] M. Mendelev, S. Han, D. Srolovitz, G. Ackland, D. Sun, M. Asta, *Philos. Mag.*, **83,** p.3977, (2003).
[4] M. Verdier, M. Fivel et I. Groma, *Mod. Sim. Mater. Sci. Eng.*, **6** (6), pp 755-770, (1998).

Elasto - Plasticity as a Limit of Cosserat Plasticity

Krzysztof Chełmiński[1], **Patrizio Neff**[2]

[1]**Faculty of Mathematics and Information Science, Warsaw University of Technology, Pl. Politechniki 1, 00-661 Warsaw, Poland, kchelmin@mini.pw.edu.pl,** [2]**Fachbereich Mathematik, Darmstadt University of Technology, Schlossgartenstrasse 7, 64289 Darmstadt, Germany, neff@mathematik.tu-darmstadt.de**

ABSTRACT

In this article we investigate the regularizing properties of Cosserat elasto-plastic models in a geometrically linear setting. Extending previous work we show that for the class of all quasistatic models of monotone type, solutions to the problem with microrotations are well-posed. For vanishing Cosserat effects we show also that the model with microrotations approximates the classical Prandtl-Reuss solution in an appropriate measure valued sense.

1. Formulation of the problem and the main result

Let us denote by $\Omega \subset \mathbb{R}^3$ a bounded domain with smooth boundary $\partial\Omega$. To determine a quasistatic deformation process of an inelastic body with microrotations in the infinitesimal setting we have to find the displacement vector $u : \Omega \times \mathbb{R} \to \mathbb{R}^3$, the microrotation matrix $A : \Omega \times \mathbb{R} \to \mathfrak{so}(3)$ (the last symbol denotes the Lie-algebra of skew-symmetric 3×3 matrices) and the vector of internal variables $z : \Omega \times \mathbb{R} \to \mathbb{R}^N$ such that

$$\begin{aligned}
\mathrm{Div}\sigma &= -f\,,\\
\sigma &= 2\mu\,(\varepsilon - \varepsilon_p) + 2\,\mu_c\,(\mathrm{skew}(\nabla u) - A) + \lambda\,\mathrm{tr}[\varepsilon]\cdot I\,,\\
-l_c\,\Delta\mathrm{axl}(A) &= \mu_c\,\mathrm{axl}(\mathrm{skew}(\nabla u) - A)\,, \qquad\qquad (1)\\
\dot{z} &\in g(-\rho\nabla_z\psi(\varepsilon, z, A))\,,\\
\rho\psi(\varepsilon, z, A) &= \mu\|\varepsilon - \varepsilon_p\|^2 + \frac{\lambda}{2}(\mathrm{tr}[\varepsilon])^2 + \mu_c\|\mathrm{skew}(\nabla u) - A\|^2\\
&\quad + 2l_c\|\nabla\mathrm{axl}(A)\|^2 + Lz\cdot z\,,\\
u_{|\partial\Omega} &= u_d\,, \quad A_{|\partial\Omega} = A_d\,, \quad z(0) = z^0\,.
\end{aligned}$$

Here, $\varepsilon = \mathrm{sym}(\nabla u)$ denotes the classical infinitesimal elastic strain tensor and ε_p denotes the inelastic strain tensor which belongs to the set of internal variables. The vector z consists of ε_p and other components needed to describe the deformation process. Let us denote by B the projector $Bz = \varepsilon_p$. μ, λ are positive Lame constants, $\mu_c > 0$ is the Cosserat couple modulus and $l_c := \mu\, L_c^2 > 0$ is a material parameter where L_c with units of length defines an internal length scale. The operator skew denotes the skew-symmetric part of a 3×3 tensor and axl is the standard isomorphism between the set $\mathfrak{so}(3)$ and $\mathbb{R}^3$. g is the inelastic constitutive multifunction, which we assume to be maximal monotone, to satisfy $0 \in g(0)$ and $\mathrm{tr}[g] = 0$. Inelastic flows with these properties are called of monotone type (see [1]). ψ is the free energy function, $L \in \mathbb{R}^{N\times N}_{\text{sym}}$ is a positive semi-definite operator such that the operator $Mz = 2\mu B^T Bz + Lz$ is positive definite. u_d, A_d are given Dirichlet boundary data, z^0 are given initial data and f describes external body forces acting on the material.

Main Theorem *Suppose that the constitutive multifunction g is a maximal monotone mapping with $0 \in g(0)$, $\mathrm{tr}[g] = 0$ and the given data f, u_d, A_d satisfy: for all times $T > 0$*

$$\begin{aligned}
&f \in C^1([0,T], L^2(\Omega,\mathbb{R}^3))\,, && \ddot{f} \in L^2((0,T)\times\Omega,\mathbb{R}^3)\,,\\
&u_d \in C^2([0,T], \mathbb{H}^{\frac{1}{2}}(\partial\Omega,\mathbb{R}^3))\,, && \dddot{u}_d \in L^2((0,T), \mathbb{H}^{\frac{1}{2}}(\partial\Omega,\mathbb{R}^3))\,,\\
&A_d \in C^2([0,T], \mathbb{H}^{\frac{3}{2}}(\partial\Omega,\mathfrak{so}(3)))\,, && \dddot{A}_d \in L^2((0,T), \mathbb{H}^{\frac{1}{2}}(\partial\Omega,\mathfrak{so}(3)))\,.
\end{aligned} \tag{2}$$

Moreover, assume that the initial data $z^0 \in L^2(\Omega,\mathbb{R}^N)$ are chosen such that the initial value of $\nabla_z\psi$ belongs to the domain of the maximal monotone operator g. Then the system (1) possesses a global in time, unique solution (u, z, A) with the regularity: for all $T > 0$

$$\begin{aligned}
&u \in \mathbb{W}^{1,\infty}((0,T), \mathbb{H}^1(\Omega,\mathbb{R}^3))\,, \qquad z \in \mathbb{W}^{1,\infty}((0,T), L^2(\Omega,\mathbb{R}^N))\,,\\
&A \in \mathbb{W}^{1,\infty}((0,T), \mathbb{H}^2(\Omega,\mathfrak{so}(3)))\,.
\end{aligned}$$

Our Main Theorem implies that for all monotone models in the inelastic deformation theory the independent microrotations have a regularizing effect: the strains remain in L^2 and the solution is found in $\mathbb{H}^1$. This is at variance with the case without Cosserat effects where we observe a lack of regularity of the strain and the inelastic strain tensors (see for example [2]).

2. Yosida approximation and energy estimates

In this section we present an approximation process for system (1). We rewrite system (1) with the Yosida approximation g_η instead of g and try to pass to the limit $\eta \to 0^+$. Thus, for $\eta > 0$ we study the following system of equations

$$\begin{aligned}
\mathrm{Div}\sigma^\eta &= -f\,, \\
\sigma^\eta &= 2\mu\,(\varepsilon^\eta - \varepsilon_p^\eta) + 2\,\mu_c\,(\mathrm{skew}(\nabla u^\eta) - A) + \lambda\,\mathrm{tr}[\varepsilon^\eta]\cdot I\,, \\
-l_c\,\Delta \mathrm{axl}(A^\eta) &= \mu_c\,\mathrm{axl}(\mathrm{skew}(\nabla u^\eta) - A^\eta)\,, \qquad (3) \\
\dot{z^\eta} &= g_\eta(-\rho\nabla_z\psi(\varepsilon^\eta, z^\eta, A^\eta))\,, \\
\rho\psi(\varepsilon^\eta, z^\eta, A^\eta) &= \mu\|\varepsilon^\eta - \varepsilon_p^\eta\|^2 + \frac{\lambda}{2}(\mathrm{tr}[\varepsilon^\eta]\,I)^2 + \mu_c\|\mathrm{skew}(\nabla u^\eta) - A^\eta\|^2, \\
&\quad +2l_c\|\nabla \mathrm{axl}(A^\eta)\|^2 + Lz\cdot z^\eta\,, \\
u^\eta_{|\partial\Omega} &= u_d\,, \quad A^\eta_{|\partial\Omega} = A_d\,, \quad z^\eta(0) = z^0
\end{aligned}$$

with the same data f, u_d, A_d, z^0 as for the system (1). Existence and uniqueness results for system (3) follow by standard methods. The main idea in the limit procedure $\eta \to 0^+$ is based on the coerciveness of the energy associated with the problem. A proof of this statement can be found in [3].

3. Approximation of perfect elasto-plasticity

In this section we study the limit process $\mu_c \to 0^+$ of vanishing Cosserat effects in the Cosserat-Prandtl-Reuss model, this means in (1) with the Prandtl-Reuss flow rule. Let us denote by $\mathcal{M}^{3\times3}_{\mathrm{sym}}(\Omega)$ the Banach space containing all bounded Radon measures in Ω with values in $\mathrm{Sym}(3) = \mathbb{R}^{3\times3}_{\mathrm{sym}}$, by $\mathrm{dev}\,\mathcal{M}^{3\times3}_{\mathrm{sym}}(\Omega)$ the subspace of $\mathcal{M}^{3\times3}_{\mathrm{sym}}(\Omega)$ consisting of measures with vanishing trace and by $\mathcal{BD}(\Omega)$ the space of bounded deformations $\{u \in L^1(\Omega, \mathbb{R}^3) : 1/2(\nabla u + \nabla^T u) \in \mathcal{M}^{3\times3}_{\mathrm{sym}}(\Omega)\}$ (for more details see [5]). Moreover, let us denote with $L^\infty_w((0,T), X)$ the space of bounded and weakly measurable functions defined on the interval $(0,T)$ with values in the Banach space X. Finally, denote by K the set of admissible stresses in the Prandtl-Reuss flow rule, which we assume to be of the form $K^d \times \mathbb{R}$ and $K^d \subset \mathrm{dev}\,\mathrm{Sym}(3)$ is closed, convex, bounded set with $0 \in \mathrm{int}(K^d)$.

Definition 1 [measure-valued solutions] Let f be a given external force and u_d be a given Dirichlet boundary data. We say that a pair (u, ε_p) satisfies the equations of the Prandtl-Reuss model in the sense of measures if $u \in \mathbb{W}^{1,\infty}_w((0,T), \mathcal{BD}(\Omega))$, $\varepsilon_p \in \mathbb{W}^{1,\infty}_w((0,T), \mathrm{dev}\,\mathcal{M}^{3\times3}_{\mathrm{sym}}(\Omega))$, $\varepsilon(u) - \varepsilon_p = \frac{1}{2}(\nabla u + \nabla^T u) - \varepsilon_p \in \mathbb{W}^{1,\infty}((0,T), L^2(\Omega, \mathrm{Sym}(3)))$, the balance of linear momentum $-\mathrm{Div}\sigma = -\mathrm{Div}(2\mu(\varepsilon - \varepsilon_p) + \lambda\mathrm{tr}[\varepsilon]\cdot I) = f$ is satisfied in the L^2-sense and the inelastic constitutive equation is satisfied in the measure sense. This means that for all $\tau \in L^2(\Omega, \mathrm{Sym}(3))$, such that $\mathrm{Div}\tau \in L^2(\Omega, \mathbb{R})$ and $\tau(x) \in K$ for a.e. $x \in \Omega$ the expression $\langle \dot{\varepsilon}_p, (\sigma - \tau)\rangle$ is a nonnegative measure. Moreover, the Dirichlet boundary condition is satisfied in the normal direction $u_{|\partial\Omega}\cdot n = u_d \cdot n$, where n is the normal unit vector to the boundary $\partial\Omega$.

Definition 2 [safe-load condition] We say that the given force f satisfies the safe-load condition if there exists a function $u_d^* \in \mathbb{W}^{1,\infty}((0,T),\mathbb{H}^1(\Omega,\mathbb{R}^3))$ such that the following linear elastic problem

$$\begin{aligned} -\mathrm{Div}\sigma^*(x,t) &= f(x,t)\,, \\ \sigma^*(x,t) &= 2\mu\,\varepsilon(u^*(x,t)) + \lambda\mathrm{tr}[\varepsilon(u^*(x,t))]\cdot I\,, \\ u^*(x,t)_{|\partial\Omega} &= u_d^*(x,t)_{|\partial\Omega} \end{aligned}$$

possesses a solution $u^* \in \mathbb{W}^{1,\infty}((0,T),\mathbb{H}^1(\Omega,\mathbb{R}^3))$ such that $\sigma^*(x,t) \in K$ for a.e. $(x,t) \in \Omega\times(0,T)$ and

$$\exists\, c^* > 0 \quad dist(\sigma^*(x,t),\partial K) \geq c^* \quad \text{for a.e.}(x,t) \in \Omega\times(0,T)\,.$$

Theorem *Let us assume that f, u_d, A_d satisfy (2) and f satisfies the safe load condition. Moreover, suppose that the initial data $\varepsilon_p^0 \in L^2(\Omega, \mathrm{dev\,Sym}(3))$ are chosen such that the initial value of ε^{μ_c} belongs to $L^2(\Omega,\mathrm{Sym}(3))$ and $2\mu\,(\varepsilon^{\mu_c}(x,0) - \varepsilon_p^0(x)) \in K$ for a.e $(x,t) \in \Omega\times(0,T)$.*
Then for $\mu_c \to 0^+$ the sequence $\{(u^{\mu_c}, \varepsilon_p^{\mu_c})\}$ of solutions to the Cosserat-Prandtl-Reuss problem possesses a subsequence which converges weakly to a solution in the measure sense of the perfect elasto-plasticity and the sequence $\{A^{\mu_c}\}$ converges strongly in the space $C([0,T],\mathbb{H}^1(\Omega,\mathfrak{so}(3)))$ to a harmonic function, which satisfies the Dirichlet boundary condition $A_{|\partial\Omega} = A_d$.

For all proofs of results presented in this summary we refer to [4].

Acknowledgements

The research of the first author was supported by polish government grant no. 1-P03A-031-27.

References

[1] H.D. Alber. *Materials with Memory. Initial-Boundary Value Problems for Constitutive Equations with Internal Variables.*, volume 1682 of *Lecture Notes in Mathematics*. Springer, Berlin, 1998.
[2] K. Chełmiński. Coercive approximation of viscoplasticity and plasticity. *Asymptotic Analysis*, 26:105–133, 2001.
[3] P. Neff and K. Chełmiński. Infinitesimal elastic-plastic Cosserat micropolar theory. Modelling and global existence in the rate independent case. *Proc. Roy. Soc. Edinb. A*, 135:1017–1039, 2005.
[4] P. Neff and K. Chełmiński. Approximation of Prandtl-Reuss plasticity through Cosserat-plasticity. *submitted to Quart. Appl. Math.*
[5] R. Temam. *Problemes mathématiques en plasticité.* Gauthier-Villars, Paris, 1983.

Effective mechanical behavior of isotropic multi-micro-cracked materials

Luciano Colombo

Department of Physics - University of Cagliari, Cittadella universitaria, I-09042 Monserrato (Ca), Italy

The macroscopic mechanical behavior of a degraded material depends upon the positional and orientational internal distribution of cracks, as well as upon the interactions among them. In many fields - ranging from structural engineering, to materials science, to geophysics - a key issue is to evaluating the effective elastic properties (stiffness tensor) governing the behavior of a multi-micro-cracked material on the macroscopic scale.

The present work is addressed at investigating the elastic properties of micro-cracked solids, by considering dispersions of cracks with arbitrary orientational distributions. Our model is developed through homogenisation techniques in order to predict the effective macroscopic elastic and mechanical behaviour.

We develop a formal unified theory covering all of the orientational distributions of cracks, including the totally random distribition and the ordered one (corresponding to parallel crack axis). The micro-mechanical averaging allows us to obtain closed-form expressions for the macroscopic or equivalent elastic moduli of the overall material under the hypothesis of low cracks density. They are found to depend upon the density of cracks and upon their orientational distribution, which is completely defined by suitable order parameters.

The analysis has been performed in two-dimensional (2D) elasticity (plane stress and plane strain) with slit like cracks and in three-dimensional (3D) elasticity with planar circular cracks. In particular, we prove that the 2D elastic behaviour of such a micro-cracked material is completely defined by one order parameter, which depends on the given angular distribution. On the other hand, the elastic characterisation in three dimensions depends on two order parameters. The particular cases of isotropic orientations of cracks (both in 2D and in 3D) have been generalised to higher values of the cracks density by means of the method of the iterated homogenisation, which leads to some differential equations. Their solutions show that the equivalent elastic moduli depend exponentially on the cracks density.

This work has been funded by MIUR under project PON-CyberSar.

Constructing and characterising tailor-made grain boundary dominated structures for atomistic simulations

P. M. Derlet, C. Brandl, H. Van Swygenhoven

Paul Scherrer Insitute, ASQ/NUM – Materials Science & Simulation, PSI-Villigen, CH-5232, Switzerland

ABSTRACT

Experiments have consistently revealed that the plastic deformation properties of bulk metallic nanocrystalline materials depend sensitively on grain boundary structure and the missorientation topology of the grains. We present a number of methodologies in which we can construct atomic configurations that contain particular levels of missorientation connectivity, CSL and Sigma boundary content, extrinsic grain boundary dislocation content and the presence of twin lamella within the grain interiors.

1. Introduction

The search for understanding of deformation mechanisms in nanocrystalline (nc) metals has widely profited from the use of molecular dynamics, revealing as possible plastic deformation mechanisms, grain boundary (GB) accommodation processes such as GB sliding and intra-granular slip that involves dislocation emission and absorption at GBs [1]. Thus the details of the GB structure and network structure are expected to play a central role in determining the plastic deformation properties of nc materials. Past simulations have been predominatly concerned with computer generated nc samples containing random missorientations, and thus predominantly a general high angle GB content. On the other hand, careful analysis of experimental samples in the TEM evidences the presence of many special GBs including coincidence site lattice (CSL) boundaries, perfect and general sigma boundaries and low-angle pure tilt boundaries [2]. In other words, there might be a discrepancy between the type of GB structures incorporated in the simulations and those present in experimental samples.

In the present work we introduce a method of computer sample construction in which we include clusters of grains containing special boundaries with in the nc network, with the goal of studying the influence of the presence of special boundaries in MD deformation simulations [3]. We also show an example of how such special GBs can exhibit unique dislocation source properties for the case of a vicinial twin boundary (VTB) [4].

2. Grain boundary network construction and deformation properties

For molecular dynamics simulations of fully three dimensional nanocrystalline metals, it has been common practice to use the Voronoi method [5]. In the present work, the sample geometry is constructed using the Voronoi method in combination with a Delaunay triangulation, using the ‘‘Qhull’’ set of algorithms [6]. The Delaunay triangulation is the geometrical triangulation between the Voronoi centers equivalent to the ‘‘nerve’’ of the Voronoi cells. Applied to the construction of the nc sample it can thus be used to map out the interconnectivity of the GB network, which is essential for a GB characterization of the sample. In this way the Voronoi cell structure and the facets corresponding to each individual GB are found geometrically, allowing for the characterization of the sample prior to the atomistic simulation. For the present study we have constructed three types of nc samples in which clusters of three grains are connected via CSL and low angle grain boundaries.

Fig. 1a displays such a CSL connected cluster containing a symmetric sigma=3 twin, a non-symmetric sigma=3 twin and a non-symmetric sigma=9 boundary. When such clusters are inserted into a general high angle GB network containing grain with a mean grain diameter of 5 nm, the resulting plasticity due to GB sliding regime is reduced when compared to a similar nc sample containing only general high angle GBs [3]. Fig 1b, now shows a cluster of three grains connected via low angle twist free grain boundaries – the 100 dislocations that accommodate the miss-orientation are arrowe. Upon loading, such lattice dislocation structures propagate with a change in resulting GB structure that can lead to grain coalescence [7].

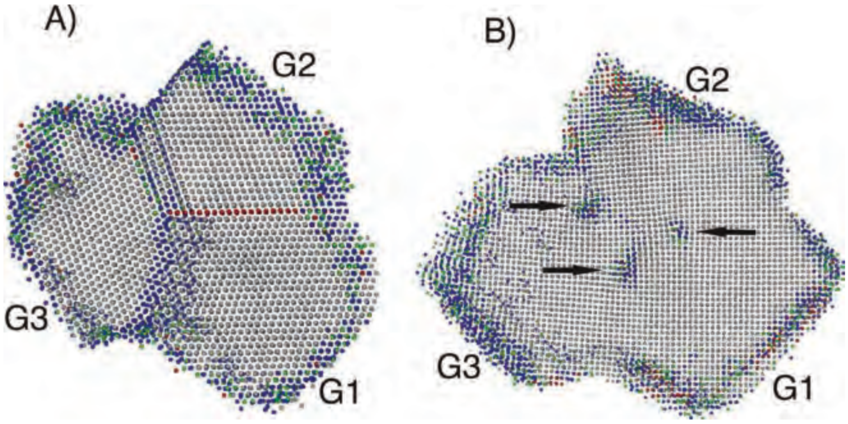

Figure 1: Sections of clusters from a) a CSL sample viewed along a (110) direction, b) a low angle (100) tilt sample viewed along a (100) direction. The black arrows indicate (100) lattice dislocations.

4. Dislocation nucleation at a vicinial twin boundary.

Understanding the role played by twin boundaries in the deformation mechanisms of nc metals is becoming of increasing importance, not only because many of the common synthesis methods produce a non-negligible amount of grown-in twins, but also because some techniques, such as pulsed electrodeposition, allow the optimisation of twin boundary content within GBs. It is well established that misfit due to any small deviation in lattice misorientation across the boundary will be accommodated by step structures made of an alternation between coherent and incoherent twin boundaries. Such a twin dominated GB structure can be defined as a vicinal twin boundary.

Here we study the behaviour of a VTB in an nc structure, and demonstrate that the presence of step structures as small as one atomic plane can trigger dislocation sources emitting dislocations on glide planes non-parallel to the TB planes. The sources are situated at the intersection of the step structure with a general grain boundary. These glide planes intersect but do not contain the entire step structure, resulting in migration of the neighbouring perfect twin segment. The simulations are performed on nc-Al, since this is the only material producing full dislocations in MD of nc systems [8]. Fig. 2 displays such a GB prior to deformation a) and during two stages of deformation b) and c). The view is nearly perpendicular to the VTB where atoms are coloured according to the local crystalline order. For ease of interpretation, the fcc atoms are left out, and only the red (hexagonal close-packed coordinated), green (other 12 coordinated) and blue (non-12 coordinated) atoms of the grain are shown. The surrounding GBs are pictured by grey planes.

Upon loading, three full dislocations are emitted on the plane with the highest Schmid factor for this grain. At larger deformations these dislocations begin propagating into the grain interior (fig. 2b), whilst a fourth dislocation is emitted from a triple junction on a slip plane that is parallel with the perfect twin segments. This plane has the second highest Schmid factor for the grain. Despite the relatively large number of dislocations nucleating and propagating on different slip planes within this grain, it is remarkable that all dislocations are finally absorbed in opposite neighbouring GBs leaving behind no footprint of a dislocation network (Fig. 2c). Comparing the structure of the VTB between Fig. 2a and 2c, it is clear that the observed dislocation activity has changed the structure of the VTB. This changes result in a migration of the entire VTB whilst at the same time changing the structural details of the twin-step structure. Indeed during deformation the length of some step structures increase while others decrease.

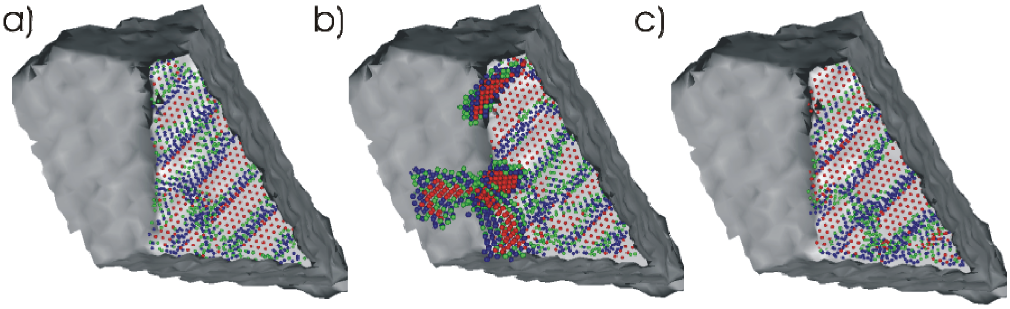

Figure 2: View of grain interior containing a vicinial twin boundary structure as a function of time during uniaxial loading, where (a) is the configuration prior to loading and (b)–(c) during plastic loading.

5. Discussion

The above MD simulations underline the importance of both the type of grain boundaries and the connectivity of the grain boundaries through the nanocrystalline network. By introducing only a small degree of connectivity via particular classes of special grain boundaries as clusters of three grains, the resulting deformation properties can be altered. Since x-ray diffraction techniques constitute a primary method of microstructural characterisation, a recent numerical algorithm [9] that allows for the efficient calculation of entire x-ray powder diffraction spectrum for a multi-million atom configurations can be used to investigate the shape and form of X-ray spectra as function of such tailor-made structures allowing for the validation of the traditional peak analyses procedures used to extract microstructural information from experimental X-ray diffraction spectra. Future work will be concerned with increasing the spatial extent of the aforementioned missorientation connectivity, with the hope of developing more realistic nanocrystalline networks. The X-ray diffraction spectrum of such tailor made structures can then be calculated for a direct comparison to experiment.

Acknowledgements

The authors acknowledge the financial support of the Swiss-FN (Grant No. 2000-056-835).

References

[1] H. Van Swygenhoven, Science 66, 296 (2002).
[2] K. S. Kumar, H. Van Swygenhoven, S. Suresh, Acta Mater 51, 5743 (2003).
[3] A.G. Frøseth, H. Van Swygenhoven, P.M. Derlet, Acta Mater. 53, 4847 (2005).
[4] A.G. Frøseth, P.M. Derlet, H. Van Swygenhoven, Scripta Mater. 54, 477 (2006).
[5] G. Z. Voronoi, Reine Angew Math 134, 199 (1908).
[6] C. B. Barber, D. P. Dobkin, H. T. Huhdanpaa, ACM Trans Math Soft 22, 469 (1996).
[7] H. Van Swygenhoven, P. M. Derlet, A. Hasnaoui, Phys Rev B 66 ,024101 (2004).
[8] H. Van Swygenhoven, P. M. Derlet, A. G. Frøseth, Nat Mater 3, 399 (2004).
[9] P.M. Derlet, S. Van Petegem, H. Van Swygenhoven, Phys Rev B 71, 024114 (2004).

Size Effects on the Strength of Micro-crystals

Jaafar El-Awady [1], *N.M. Ghoniem* [1]

[1] *University of California, Los Angeles (UCLA), 48-121 Engineering IV, 420 Westwood Plaza, 90034 Los Angeles, United States of America*

We present a study of the plastic deformation of micron-size single crystals using 3D parametric dislocation dynamics. An assessment of the crystal-size dependence of the stress versus strain response will be analyzed for cylindrical microcristals oriented for single slip having sample diameters in the range 0.25 to 10 5m. A finite deformation formulation of dislocation dynamics is developed to study the effect of loading axis rotation on the activation of slip event avalanches. Statistical aspects of dislocation production from crystal surfaces, activation of internal dislocation sources, and the cross-slip process are included in the analysis. The boundary element method (BEM) is used to calculate the image field due to the finite dimensions of the crystal, and the solution is superimposed on the elastic field resulting from dislocation ensembles in an infinite medium. The results of computer simulations are compared to the experimental measurements of Uchic et. al. on single crystal nickel micro-compression samples (Science, Vol. 305. no. 5686, pp. 986 - 989).

Multi-Time Scale Analysis of Cyclic Deformation in Polycrystalline Metals

Sivom Manchiraju, [1] Somnath Ghosh [3]

Abstract

A dual-time scale finite element model is developed in this paper for simulating cyclic deformation in polycrystalline alloys. The material is characterized by crystal plasticity constitutive relations. The finite element formulation of the initial-boundary value problems with cyclic loading involves decoupling the governing equations into two sets of problems corresponding to two different time scales. One is a long time scale (low frequency) problem characterizing a cycle-averaged solution, while the other is a short time scale (high frequency) problem for a remaining oscillatory portion. Cyclic averaging together with asymptotic expansion of the variables in the time domain forms the basis of the multi-time scaling. The crystal plasticity equations at the two scales are used to study cyclic deformation of a titanium alloy Ti-6Al. This model is intended to study the fatigue response of a material by simulating a large number of cycles to initiation.

1 Introduction

Many metals and alloys find widespread utilization in various high performance applications such as automotive and aerospace components. During service, many of these components are exposed to cyclic loading conditions resulting in their fatigue. Fatigue failure in the microstructure evolves in three stages [1], viz. (i) crack nucleation due to inhomogeneous plastic flow or grain boundary failure, (ii) subsequent crack growth by cyclic stresses, and (iii) coalescence of cracks to cause fast crack propagation. Traditionally Fatigue design uses the stress-life or S-N approach and the strain-life approach e.g. the Coffin-Manson rule or uses linear elastic fracture mechanics based approach like the Paris law [3]. Although these models have worked well for alloys under specific test conditions, a lack of underlying physics and microstructure based considerations impede their portability to generic materials and load conditions.

Microstructural features that include morphological and crystallographic characteristics, e.g. crystal orientations and misorientations, grain boundary geometry etc, govern the mechanical behavior and fatigue failure response. Crystal plasticity theories with explicit grain structures are effective in predicting localized cyclic plastic strains [4, 5]. The recent years have seen significant efforts in modeling cyclic plasticity and fatigue with considerations of microstructural stress-strain evolution[6, 7, 8, 4, 8, 9]. Most simulations performed with 3D crystal plasticity are in the range of 100 cycles [4, 8, 9] and the results are subsequently extrapolated for fatigue predictions as solution by conventional methods of time integration is prohibitively expensive. Yu and Fish [10] have proposed a temporal homogenization method in which they assumed all the variables to be locally periodic in temporal domain. But for a deformation with evolving plastic variables, periodicity in temporal domain cannot be assumed.

---

[1] Graduate Research Associate

[3] Corresponding Author, Nordholt Professor, Department of Mechanical Engineering, The Ohio State University, Columbus, OH, USA, E-mail: ghosh.5@osu.edu

A method of solution of crystal plasticity equations is developed in this paper using two time scales involving compression and rarefaction. From the set of crystal plasticity based governing equations, it develops a decoupled set of equations characterized by the two time scales. One is a long time scale (low frequency) problem characterizing a cycle-averaged solution, while the other is a short time scale (high frequency) problem for a remaining oscillatory portion. The multi-time scaling results in an enormous gain (about 50 times) in computational efficiency over single time integration with almost no loss of accuracy.

2 Crystal Plasticity Constitutive Relations

The material studied in this work is a crystal with a hexagonal close packed or *hcp* structure, e.g. titanium alloys, consisting of 5 different families of slip systems to a total of 30 slip systems [6]. The deformation behavior of the hcp material in this paper is modeled using a rate dependent, isothermal, elastic-viscoplastic, finite strain, crystal plasticity formulation following the work [6, 7] which is summarized below.

$$\boldsymbol{S} = \boldsymbol{C} : \boldsymbol{E}^e, \qquad \boldsymbol{F} = \boldsymbol{F}^e \boldsymbol{F}^p, \qquad \det\left(\boldsymbol{F}^e\right) > 0 \quad \text{where } \boldsymbol{E}^e = \frac{1}{2}\left(\boldsymbol{F}^{e\mathrm{T}}\boldsymbol{F}^e - \boldsymbol{I}\right)$$

$$\boldsymbol{L} = \dot{\boldsymbol{F}}^p \boldsymbol{F}^{p-1} = \sum_{\alpha}^{nslip} \dot{\gamma}^\alpha \boldsymbol{s}^\alpha, \quad \dot{\gamma}^\alpha = \dot{\gamma}_0 \left|\frac{\tau^\alpha}{g^\alpha}\right|^{\frac{1}{m}} \mathrm{sign}(\tau^\alpha), \quad \tau^\alpha = (\boldsymbol{F}^{e\mathrm{T}}\boldsymbol{F}^e\boldsymbol{S}) : \boldsymbol{s}^\alpha$$

$$\dot{g}^\alpha = \sum_{\beta}^{nslip} h^{\alpha\beta}\left|\dot{\gamma}^\beta\right|, \quad h^\beta = h_0\left|1 - \frac{g^\beta}{g_s^\beta}\right|^r \mathrm{sign}\left(1 - \frac{g^\beta}{g_s^\beta}\right), \qquad g_s^\beta = g_{s0}\left(\frac{\dot{\gamma}^\beta}{\dot{\gamma}_0}\right)^c$$

$$\tau_{\mathrm{eff}}^\alpha = |\tau^\alpha - \tau_{\mathrm{kin}}^\alpha|, \qquad \text{and } \tau_{\mathrm{kin}}^\alpha = (\boldsymbol{\sigma}_{\mathrm{kin}} \cdot \boldsymbol{n}^\alpha)\cdot \boldsymbol{m}^\alpha$$

$$\boldsymbol{\sigma}_{\mathrm{kin}} = \sum_\alpha \Omega^\alpha(\boldsymbol{m}^\alpha \otimes \boldsymbol{n}^\alpha + \boldsymbol{n}^\alpha \otimes \boldsymbol{m}^\alpha), \quad \dot{\Omega}^\alpha = c\,\dot{\gamma}^\alpha - d\,\Omega^\alpha\left|\dot{\gamma}^\alpha\right| \tag{1}$$

3 Decomposition of Constitutive Variables into Averaged and Oscillator Parts

When subjected to an oscillating load, the deformation behavior exhibits an oscillatory behavior about an averaged or ’macroscopic’ evolution of state variables. The frequency or rate of change of averaged variables is generally quite slow in comparison with the frequency of the applied cyclic loads. Consequently, it is conceivable to introduce two different time scales in the solution. A coarse time scale t, for the average variables which can be solved by time increments that are significantly longer than the period of a single cycle and a fine time scale τ, that is necessary for providing adequate resolution to the rapidly varying behavior due to the oscillating load. The relation between the two time scales t and τ may be defined as $t = \epsilon\tau$, where $\epsilon << 1$ is a small positive scaling parameter. A superscript ϵ associated with a variable denotes its association with both the time scales. Consequently, all the response fields in the body $\phi^{(\epsilon)}(\boldsymbol{x}, t)$ at a given spatial location **x** are assumed to exhibit dependence on the coarse time scale t and the fine time scale τ and is expressed as: $\phi^{(\epsilon)}\,(\boldsymbol{x}, t) = \phi(\boldsymbol{x}, t, \tau)$

Using chain rule and the relation between the time scales, the time derivatives in the two time scales is given as:

$$\dot{\phi}^{(\epsilon)} = \frac{\partial \phi^{(\epsilon)}}{\partial t} = \frac{\partial \phi}{\partial t} + \frac{1}{\epsilon}\frac{\partial \phi}{\partial \tau} \tag{2}$$

The cycle-averaged field variable over a period T in the fine time-scale $\tau = \frac{t}{\epsilon}$, at time t is defined as

$$\bar{\phi}(t) = \langle \phi(t, \tau) \rangle = \frac{1}{T}\int_{\frac{t}{\epsilon}}^{\frac{t}{\epsilon}+T} \phi(t, \tau)\ d\tau \tag{3}$$

The symbol $< \cdot >$ corresponds to the averaging operator. A general decomposition of all variables in the constitutive equation is therefore proposed in the following form:$\phi(t, \tau) = \bar{\phi}(t) + \tilde{\phi}(t, \tau)$. The bar in the expression corresponds to the solution of a set of 'macroscopic' or averaged equations. The tilde, on the other hand, refers to the remainder of the solution (oscillatory portion). Typically the amplitude of the oscillations is a monotonic function of time, and the oscillations vary in both the t and the τ scales. Thus it is prudent to assume that the non-periodic oscillatory part may be obtained by the superposition of monotonically varying amplitude on a periodic cyclic response. Thus the oscillatory portion is decomposed multiplicatively and additively as:

$$\tilde{\phi}(t, \tau) = \tilde{\phi}^{nos}(t, \tau)\tilde{\phi}^{per}(\tau) = \tilde{\phi}^{osc}(t, \tau) + \tilde{\phi}^{c}(t) \tag{4}$$

Because of multiplicative decomposition,the oscillator is zero at the exact same cycle-reference time $\hat{\tau}$ ($\in [0, T]$) in each cycle.This serve as the initial conditions for the oscillatory solution in each cycle. The additive decomposition in equation (4) is needed to annual the additional term in the average solution due to the non-periodicity of the oscillatory part such that cyclic average of oscillator is zero. Four independent variables are identified in the crystal plasticity based finite element equations. They are: (i) the displacement field vector **u**, (ii) the plastic deformation gradient tensor $\boldsymbol{F}^p$, (iii) the slip system resistance parameter g^{α} and (iv) scalar kinematic variable Ω^{α}. These four independent variables can be decomposed into average and the oscillator and the oscillator is decomposed further following (4).

From the characteristics exhibited by typical oscillatory solution the oscillator $\tilde{\phi}(t, \tau)$ can be expanded in an asymptotic series. Thus any field variable $\phi(t, \tau)$ can be expanded as:

$$\phi^{(\epsilon)}(t, \tau) = \underbrace{\bar{\phi}(t) + \left[\tilde{\phi}^{osc(0)}(t, \tau) + \tilde{\phi}^{c(0)}(t)\right]}_{\phi^{(0)}} + \epsilon \underbrace{\left[\tilde{\phi}^{osc(1)}(t, \tau) + \tilde{\phi}^{c(1)}(t)\right]}_{\phi^{(1)}} + \epsilon^2 \underbrace{\left[\tilde{\phi}^{osc(2)}(t, \tau) + \tilde{\phi}^{c(2)}(t)\right]}_{\phi^{(2)}} + o(\epsilon^3) \tag{5}$$

The time derivative of these independent variables $\phi^{(\epsilon)}(t)$, are expressed by substituting equation (5) in (2) as

$$\begin{aligned}\dot{\phi}^{(\epsilon)}(t) = \frac{1}{\epsilon}\left(\frac{\partial \tilde{\phi}^{nos(0)}(t, \tau)}{\partial \tau}\right) + \left(\frac{\partial \bar{\phi}(t)}{\partial t} + \frac{\partial \tilde{\phi}^{osc(0)}(t, \tau)}{\partial t} + \frac{\partial \tilde{\phi}^{c(0)}(t)}{\partial t} + \frac{\partial \tilde{\phi}^{osc(0)}(t, \tau)}{\partial \tau}\right) \\ + \sum_{n=1,2,\cdots} \epsilon^n \left(\frac{\partial \tilde{\phi}^{osc(n)}(t, \tau)}{\partial t} + \frac{\partial \tilde{\phi}^{c(n)}(t)}{\partial t} + \frac{\partial \tilde{\phi}^{nos(n+1)}(t, \tau)}{\partial \tau}\right)\end{aligned} \tag{6}$$

3

With the expansions of the primary variables and their time derivative,(5,6), all derived variables in the constitutive equations are derived and consequently the original initial-boundary value problem is decomposed into an average IBVP and different orders of oscillatory IBVP.

3.1 The Averaged Problem

The average initial-boundary value problem can be summarized as:

$$\text{Equilibrium:}\quad \bar{\sigma}_{ij,j} + \bar{b}_i = 0;\quad \text{B.Cs:}\quad \bar{\sigma}_{ij} n_j =< t_i^* > \quad on \quad \Gamma_t \quad \bar{u}_i =< u_i^* > \quad on \quad \Gamma_u$$

$$\text{Constitutive Relations:}\quad \bar{F}_{ij} = \bar{F}^e_{ik} \bar{F}^{p-1}_{kj};\quad \bar{E}^e_{ij} = \frac{1}{2}(\bar{F}^e_{ki} \bar{F}^e_{kj} - \delta_{ij})$$

$$\bar{S}_{ij} = C_{ijkl} \bar{E}^e_{kl};\quad \dot{\bar{F}}^p_{ik} \bar{F}^{p-1}_{kj} = \sum_{\alpha}^{nslip} \dot{\bar{\gamma}}^{\alpha} \boldsymbol{s}^{\alpha}_{ij}$$

together with the evolution of plastic variables $\bar{\gamma}^{\alpha}$,$\bar{g}^{\alpha}$ and $\bar{\Omega}^{\alpha}$ which are summarized below.

$$\begin{aligned}
\text{Shear strain rate (S):}\quad & \dot{\gamma}^{\alpha(0)} = \dot{\bar{\gamma}}^{\alpha(0)} + \dot{\tilde{\gamma}}^{\alpha(0)} = \dot{\gamma}_0 \left| \frac{\bar{\tau}^{\alpha}_{\text{eff}} + \tilde{\tau}^{\alpha(0)}_{\text{eff}}}{\bar{g}^{\alpha}} \right|^{\frac{1}{m}-1} \left(\frac{\bar{\tau}^{\alpha}_{\text{eff}} + \tilde{\tau}^{\alpha(0)}_{\text{eff}}}{\bar{g}^{\alpha}} \right) \\
\text{Flow rule (F):}\quad & \frac{\partial(\bar{F}^p)_{ij}}{\partial t} + \frac{\partial(\tilde{F}^p)^{osc(1)}}{\partial \tau} = \sum_{\alpha=1}^{nslip} \dot{\gamma}^{\alpha(0)} s^{\alpha}_{ik} \bar{F}^p_{kj}, \\
\text{Hardening evolution (H):}\quad & \frac{\partial \bar{g}^{\alpha}}{\partial t} + \frac{\partial(\tilde{g}^{\alpha})^{osc(1)}}{\partial \tau} = \sum_{\beta=1}^{nslip} (\bar{h}^{\alpha\beta} + \tilde{h}^{\alpha\beta(0)}) \left| \dot{\bar{\gamma}} + \dot{\tilde{\gamma}}^{(0)} \right|^{\beta} \\
\text{Backstress evolution (B):}\quad & \frac{\partial \bar{\Omega}^{\alpha}}{\partial t} + \frac{\partial(\tilde{\Omega}^{\alpha})^{osc(1)}}{\partial \tau} = c(\dot{\bar{\gamma}} + \dot{\tilde{\gamma}}^{(0)})^{\alpha} - d\bar{\Omega}^{\alpha} \left| \dot{\bar{\gamma}} + \dot{\tilde{\gamma}}^{(0)} \right|^{\alpha}
\end{aligned} \tag{7}$$

3.2 The Oscillatory Equations: Zero-th Order

Isolating the coefficients of ϵ^{-1} in the evolution equations results in the zero-th order equations for plastic variables in the oscillatory problem. They are:

$$\text{Flow rule (F):}\quad \frac{\partial(\tilde{F}^p)^{osc(0)}_{ij}}{\partial \tau} = \sum_{\alpha}^{nslip} \dot{\gamma}^{\alpha(-1)} s^{\alpha}_{ik} F^{p(0)}_{kj} = 0$$

$$\text{Hardening evolution (H):}\quad \frac{\partial(\tilde{g}^{\alpha})^{osc(0)}}{\partial \tau} = 0;\quad \text{Backstress evolution (B):}\quad \frac{\partial(\tilde{\Omega}^{\alpha})^{osc(0)}}{\partial \tau} = 0 \tag{8}$$

Thus,the Zero-th order terms of the oscillatory plastic variables may be assumed to be zero.

3.3 The Oscillatory Equations: First Order

The first order oscillators can be solved using the averaged and the zero-th order oscillators from the following equations:

$$\begin{aligned}
\text{Shear strain rate (S):}\quad & \dot{\tilde{\gamma}}^{\alpha(0)} = \dot{\gamma}_0 \left| \frac{\bar{\tau}^{\alpha}_{\text{eff}} + \tilde{\tau}^{\alpha(0)}_{\text{eff}}}{\bar{g}^{\alpha} + \tilde{g}^{\alpha(0)}} \right|^{\frac{1}{m}-1} \left(\frac{\bar{\tau}^{\alpha}_{\text{eff}} + \tilde{\tau}^{\alpha(0)}_{\text{eff}}}{\bar{g}^{\alpha} + \tilde{g}^{\alpha(0)}} \right) - \bar{\dot{\gamma}}^{\alpha} \\
\text{Flow rule (F):}\quad & \frac{\partial(\tilde{F}^{p})^{osc(1)}}{\partial\tau} = \sum_{\alpha=1}^{nslip} \dot{\gamma}^{\alpha(0)} s^{\alpha}_{ik} (\bar{F}^{p}_{kj} + \tilde{F}^{p\ (0)}_{kj}) - \frac{\partial(\bar{F}^{p})_{ij}}{\partial t} \\
\text{Hardening evolution (H):}\quad & \frac{\partial(\tilde{g}^{\alpha})^{osc(1)}}{\partial\tau} = \sum_{\beta=1}^{nslip} (\bar{h}^{\alpha\beta} + \tilde{h}^{\alpha\beta(0)}) \left|\bar{\dot{\gamma}} + \dot{\tilde{\gamma}}^{(0)}\right|^{\beta} - \frac{\partial\bar{g}^{\alpha}}{\partial t} \\
\text{Backstress evolution (B):}\quad & \frac{\partial(\tilde{\Omega}^{\alpha})^{nos(1)}}{\partial\tau} = c(\bar{\dot{\gamma}} + \dot{\tilde{\gamma}}^{(0)})^{\alpha} - d(\bar{\Omega}^{\alpha} + \tilde{\Omega}^{\alpha(0)}) \left|\bar{\dot{\gamma}} + \dot{\tilde{\gamma}}^{(0)}\right|^{\alpha} - \frac{\partial\bar{\Omega}^{\alpha}}{\partial t}
\end{aligned} \tag{9}$$

4 Cycle Averaged Effective Constitutive Equations

The coupled evolution equations (7) cause the coupling between the averaged and the oscillatory problems. If all the response fields are assumed to be locally periodic in τ, the averaged and the oscillatory problems can be decoupled by applying averaging operator $< \cdot >$ to the coupled evolution equations. The periodic assumption, made in [10], is however not valid in case of evolving plastic variables. In the present work, a decoupling scheme that does not depend on periodicity assumptions is proposed.Sets of time scale or cycle-averaged constitutive equations are developed for this purpose. An averaged function $\bar{\phi}\,(t)$ can be interpreted as a function that is the result of continuous representation of a set of data points $\bar{\phi}(n)$, obtained from detailed single scale simulation. The cycle averaged equations are defined for the evolution of any averaged variable $\frac{\partial(\bar{\phi})}{\partial t}$, subjected to cycle averaged applied load. For example, the evolution equation for the averaged shear strain rate is expressed as:

$$\frac{\partial\bar{\gamma}^{\alpha}}{\partial t} = \dot{\gamma}^{*\alpha}_0 \left| \frac{\bar{\tau}^{\alpha} - \bar{\tau}_{\text{kin}}}{\bar{g}^{\alpha}} \right|^{\frac{1}{m}} \text{sign}(\bar{\tau}^{\alpha} - \bar{\tau}_{\text{kin}}) \tag{10}$$

where $\dot{\gamma}^{*\alpha}_0$ is a yet to be determined coefficient that is expected to be a function of time or other evolving variables. This coefficient is developed from considerations of the link between the averaged and the oscillatory solutions. The averaged rate $\frac{\partial(\bar{\phi})}{\partial t}$ is not dependent on the assumption of periodicity. As a one dimensional illustration, consider a non-periodic function: $\frac{\partial\phi}{\partial t} = tsin(\omega t)$ with initial conditions: $\phi(0) = 0$ The solution to this problem is $\phi(t) = \frac{-tcos(\omega t)}{\omega} + \frac{sin(\omega t)}{\omega^2}$ The cyclic average of the solution is $\bar{\phi}(t) = 0$ and therefore $\frac{\partial\bar{\phi}}{\partial t} = 0$. But, the application of the averaging operator $< \cdot >$ on both sides of the differential equation yields: $\left\langle \frac{\partial\phi}{\partial t} \right\rangle = -\frac{1}{\omega} \quad \Rightarrow \quad \bar{\phi}(t) = -\frac{t}{\omega} \neq 0$. Thus average effective rate is able to capture the average while the conventional homogenization fails for the case of non-periodic functions. Because $\tilde{g}^{\alpha} \ll \bar{g}^{\alpha}$ (7) and for most cases $\bar{g}^{\alpha}$ is almost constant within each cycle.Thus $\dot{\gamma}^{*}_0$ is only a function of resolved shear stress. To quantify this dependence, the oscillations in the resolved shear stress $\tilde{\tau}^{\alpha}$, are represented by characteristic parameters for example, amplitude. While in the present study, only one parameter is used to characterize the oscillator, use of more parameters is being considered in future studies to improve accuracy. The function f is determined by crystal plasticity FEM simulations for a single crystal by a single time scale integration process for different values of $\overline{\tau}^{\alpha}$ and $\tilde{\tau}^{\alpha}$. With knowledge of the average and the amplitude of the oscillation of τ^{α}, the parameter $\dot{\gamma}_0^{*\alpha}$ can be obtained by interpolating from these results.However, the amplitude of the oscillatory part is unknown apriori during the solution stage of the averaged problem.The asymptotic expansions of equations (8) show that the zero-th order oscillations in plastic variables are zero. As long as $\epsilon \tilde{F}_{ij}^{p(1)} \rightarrow 0$, the response in the resolved shear stress oscillator $\tilde{\tau}^{\alpha}$ is close to elastic response,or the oscillator amplitude is constant with time. For $\epsilon \tilde{F}_{ij}^{p(1)}$ to be large, large oscillations in shear strain rate are needed, for which $\frac{\tau^{min}}{\tau^{max}} \rightarrow -1$.Such a case is not investigated here. Similarly the averaged evolution equations for hardness evolution and the back-stress are also defined. In conclusion, once the averaged solution for all the evolving variables are obtained in the CPFEM model, the dual time scale total solution is obtained by superposing different orders of the oscillatory solution for convergence to the true solution.

5 A Numerical Example

This dual-time scale algorithm is used to study the deformation response of polycrystalline titanium alloy Ti-6Al subjected to cyclic loading using experimentally validated CPFEM ([6]). The cyclic response is simulated using both the single time scale and the multiple time scale algorithm.The constitutive laws are implemented in the commercial finite element code MSC MARC ([11]). A unit cube of polycrystalline aggregate is modeled by descretizing the cube by 2744 cubic elements with eight integration points. Each element in the FE model represents one grain and is assigned a specific orientation. Statistical equivalence in Orientation, misorientation and microtexture between the simulated and experimental microstructures is achieved by using a method developed and described in ([7]). The pressure profile applied is sinusoidal with frequency of 1 Hz, mean of 500 MPa and amplitude of 250 MPa and the deformation response for hundred cycles is simulated. Because the applied loading is of high frequency, the single time integration simulation requires around 50 time increments for the solution for each cycle. In the multi-time scale algorithm, the average problem is solved using the effective constitutive equations outlined in section 4.Since the loading is not oscillatory, the time increments required for the solution of the average problem is limited only by the accuracy of the implicit time integration ([5]) for the effective constitutive equation. The average simulation took around 30 minutes to solve for 100 cycles resulting in approximately a sixty times computational gain. Upon obtaining the solution of the average problem, the oscillatory problems are solved for the last five cycles and superposed on the average solution to recover the total solution. Figure (1) shows the volume averaged total strain in the loading direction in the polycrystalline aggregate obtained from the single time-scale and multiple time-scale solutions. The volume averaged plastic strain in the loading direction with these two approaches is compared in figure (2a). Excellent agreement is found in the macroscopic or averaged solutions. For comparison at the microscopic level, the shear slip in an active slip system at an integration point in an element by the two methods is plotted in figure (2b). The dual-time scale algorithm solution agrees very well with the single time scale solution at both macroscopic scale and grain level. The proposed two-time scale algorithm can achieve very high computational gain with almost no loss of accuracy for problems with cyclic loading and deformation.

6 Conclusions

A novel two-scale algorithm in the temporal domain is developed in this paper to study anisotropic-plastic material response under cyclic loading. The initial boundary value problem is decomposed into an uncoupled set of averaged problem and oscillatory problems. Effective constitutive equations are developed for the averaged problem in order to decouple the average and the oscillations. The resulting averaged constitutive equations do not rely on any assumptions of periodicity. The averaged problem being devoid of any oscillations, can be solved with time increments that are of the order of multiple time periods of the cyclic loading. The algorithm is validated by analyzing the deformation response of polycrystalline Ti-6Al under high frequency sinusoidal pressure. The results from multi-time scale solutions match very well with the results obtained from single time integration, both macroscopic scale and at grain level. On the other hand, the computational efficiency is enhanced almost sixty times.This multi-scale analysis in time makes it possible to study the fatigue response of materials in an explicit manner for considerations of evolution of critical microstructural variables. It opens a possibility of solving these problems for the entire fatigue life in contrast to the extrapolation and empirical studies that are used presently [8].

References

[1] S. Suresh, Fatigue of Materials, Cambridge University Press, Cambridge, 1996.

[2] L.F. Coffin, Fatigue, Ann. Rev. Matls. Sci. 2 (1973) 313-348.

[3] P.C. Paris, The fracture mechanics approach to fatigue, Fatigue-An Interdisciplinary Approach, Syracuse University Press, 1964.

[4] V.P. Bennett, D.L. McDowell, Polycrystal orientation distribution effects on microslip in high cycle fatigue,Int. J. Fatigue, 25 (2003) 27-9.

[5] S.R. Kalidindi, C.A. Bronkhorst, L. Anand, Crystallographic texture evolution in bulk deformation processing of fcc metals, J. Mech. Phys. Solids 40 (1992) 537-569.

[6] V. Hasija, S. Ghosh, M.J. Mills, D.S. Joseph, Modeling Deformation and Creep in Ti-6Al alloys with Experimental Validation, Acta Mater. 51 (2003) 4533-4549.

[7] D. Deka,D. Joseph, S. Ghosh, M.J. Mills, Crystal plasticity modeling of deformation and creep in Polycrystalline Ti-6242, Metall. Trans. A, (in press), 2006.

[8] S. Sinha and S. Ghosh, Modeling cyclic ratcheting based fatigue life of HSLA steels using crystal plasticity FEM simulations and experiments”, International Journal of Fatigue (in press).

[9] H.S. Turkmen, R.E. Loge, P.R. Dawson, M. Miller, On the mechanical behavior of AA 7075-T6 during cyclic loading, Int. J. Fatigue 25 (2003) 267-281.

[10] Q. Yu, J. Fish, Temporal homogenization of viscoelastic and viscoplastic solids subjected to locally periodic loading, Comput. Mech. 29 (2002) 199-211.

[11] MSC-MARC Reference Manuals, 2005, MSC. Software Corporation.

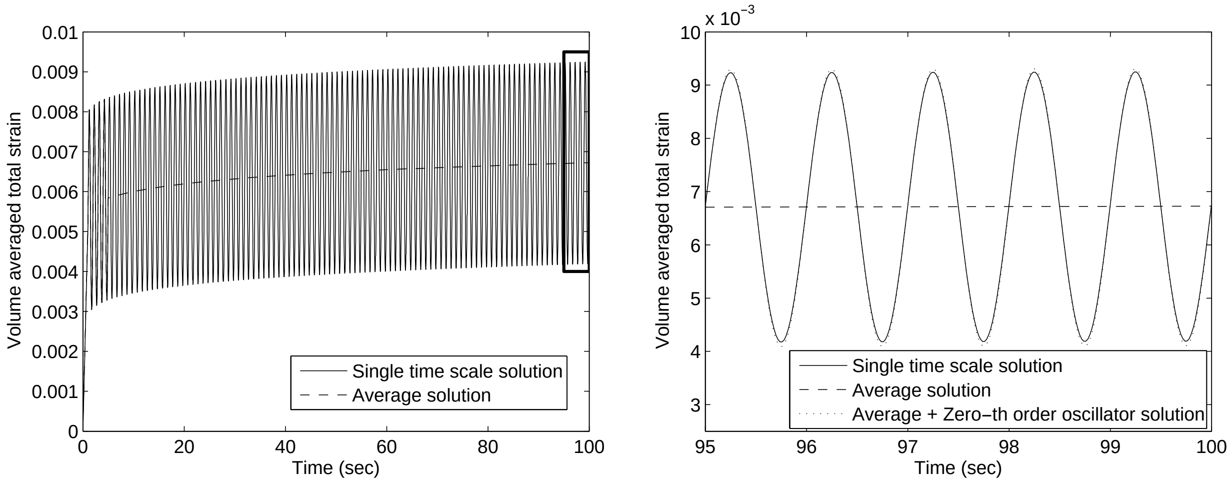

Figure 1: Volume averaged total strain in the loading direction

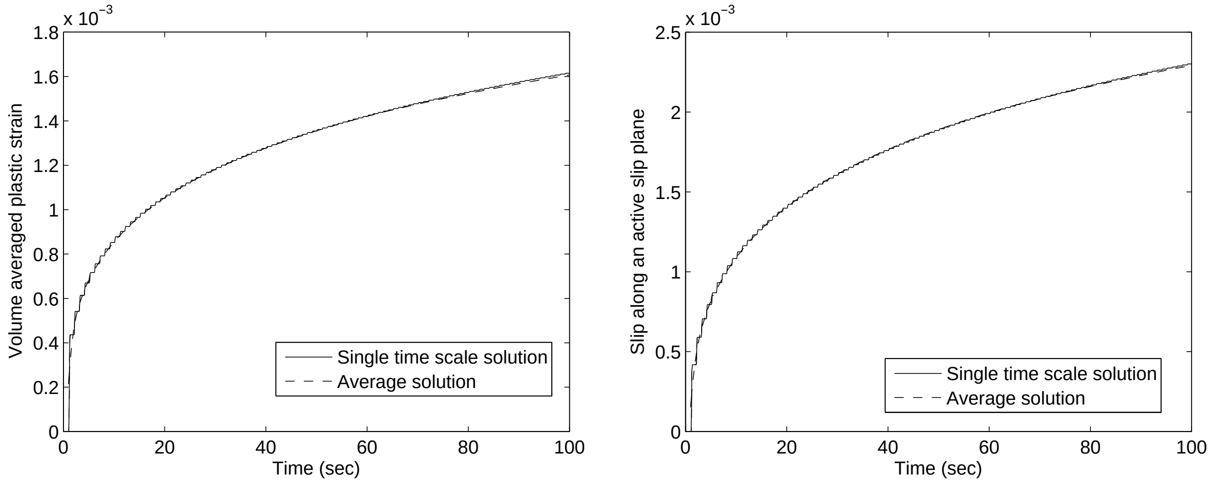

Figure 2: (a) Volume averaged plastic strain in loading direction, (b) Slip along an active slip system at an integration point of an element

A Framework for Automated 3D Microstructural Analysis & Representation

Michael Groeber[1], Michael D. Uchic[2], Dennis M. Dimiduk[2], Yash Bhandari[3], and Somnath Ghosh[3]

[1] The Ohio State University, Department of Materials Science and Engineering, 477 College Rd., Columbus, OH 43210 USA, groeber.9@osu.edu
[2] Air Force Research Laboratory, Materials & Manufacturing Directorate, AFRL/MLLMD, 2230 Tenth St., Wright-Patterson AFB, OH 45433 USA, Michael.Uchic@wpafb.af.mil, Dennis.Dimiduk@wpafb.af.mil
[3] The Ohio State University, Department of Mechanical Engineering, 650 Ackerman Rd., Columbus, OH 43210 USA, bhandari.11@osu.edu, ghosh.5@osu.edu

ABSTRACT

Over the past five years there have been significant advances in developing serial-sectioning methods that provide quantitative data describing the structure and crystallography of grain-level microstructures in three dimensions (3D). The subsequent analysis and representation of this information can provide modeling and simulation efforts with a highly-refined and unbiased characterization of specific microstructural features. For example, the grain structure and crystallography of an engineering alloy could be characterized and then translated directly into a 3D volume mesh for subsequent Finite Element Analysis. However, this approach requires a multitude of data sets in order to appropriately sample the intrinsic heterogeneity observed in typical microstructures. One way to circumvent this issue is to develop computation tools that create synthetic microstructures that are statistically-equivalent to the measured structure. This study will discuss the development of software programs that take as input a series of Electron Backscatter Diffraction Patterns from a serial sectioning experiment, and output a robust statistical analysis of the 3D data, as well as generate a host of synthetic structures which are analogous to the real microstructure. Importantly, the objective of this study is to provide a framework towards complete microstructure representation that is consistent with quantifiable experimental data.

1. Introduction

The ability to characterize microstructure is an important tool for materials scientists, because it allows one to quantify microstructure-property relations and anticipate the capability of a material to perform in a given application as a function of process history. For example, it is known that the grain size distribution of a material has a strong effect on mechanical properties; therefore, an accurate measure of the grain size distribution is desirable to predict material performance.

Classic methods for characterizing microstructure usually involve analyzing 2D images from a sectioned surface. Grain boundaries and second-phase particles can be delineated, and stereological methods can subsequently be used to infer three-dimensional (3D) statistical attributes from the 2D microstructural images. However, there are a number of microstructural parameters such as feature connectivity, true feature shape, and the number of features per unit volume that cannot be inferred [1]. For the previous example of grain size measurements, a common stereological measurement—mean linear intercept—can be used to determine average grain size, but only for certain assumptions of grain morphology. In addition, many stereological parameters yield only average scalar quantities to describe microstructural features. Recognizing that many properties (notably those linked with failure) are governed by the extreme values of the microstructure, it is evident that characterizing the full distribution of these features may be more appropriate for some models. The need to more completely characterize microstructures has led to the development of methods that allow one to directly obtain 3D microstructural data.

A framework for 3D morphological representation, from data collection and processing, to microstructure characterization, and ultimately representation, is discussed in this paper. For data collection, a Dual Beam Focused Ion Beam-Scanning Electron Microscope (DB FIB-SEM) is used to acquire a 3D data set comprised of Electron Back-Scatter Diffraction (EBSD) maps via serial-sectioning. Processing and analysis of the data is performed using two programs, “Micro-Imager” and “Micro-Imager3D”, which have been developed for this work. Micro-Imager automatically defines grains and grain boundary segments in each 2D EBSD map and calculates various statistical features of the microstructure, allowing some 3D characteristics of the polycrystalline microstructure to be predicted. Meanwhile, Micro-Imager3D automatically reconstructs the series of 2D maps into a 3D volume and defines grains and grain boundaries in 3D. Lastly, the generation of statistically equivalent synthetic structures by “SIRI-3D”, another program developed in this work, will be discussed. The collection of programs and experimental characterization processes define a new and automated methodology for providing a more complete description of grain-level microstructures.

2. Material Details

For this study a fine-grained nickel-base superalloy (IN100) was selected. The microstructure of IN100 is shown in a number of data forms in Fig. 1. The microstructure of IN100 presents advantages and complications to this experimental technique. A main advantage is the fine grain size (~3 μm average diameter) allows for many grains to be contained in the meso-scale volume that can be interrogated by the Dual Beam FIB-SEM. Another advantage is that Ni forms high “quality” EBSD patterns, which enables high-speed data acquisition. A complication that arises is the γ and γ' phases cannot be distinguished by EBSD pattern analysis for the experimental data collection conditions. Therefore, when performing the statistical analysis, phase-type is not considered. This does not present difficulties during analysis, but should be addressed if constituent properties are assigned to the grain model.

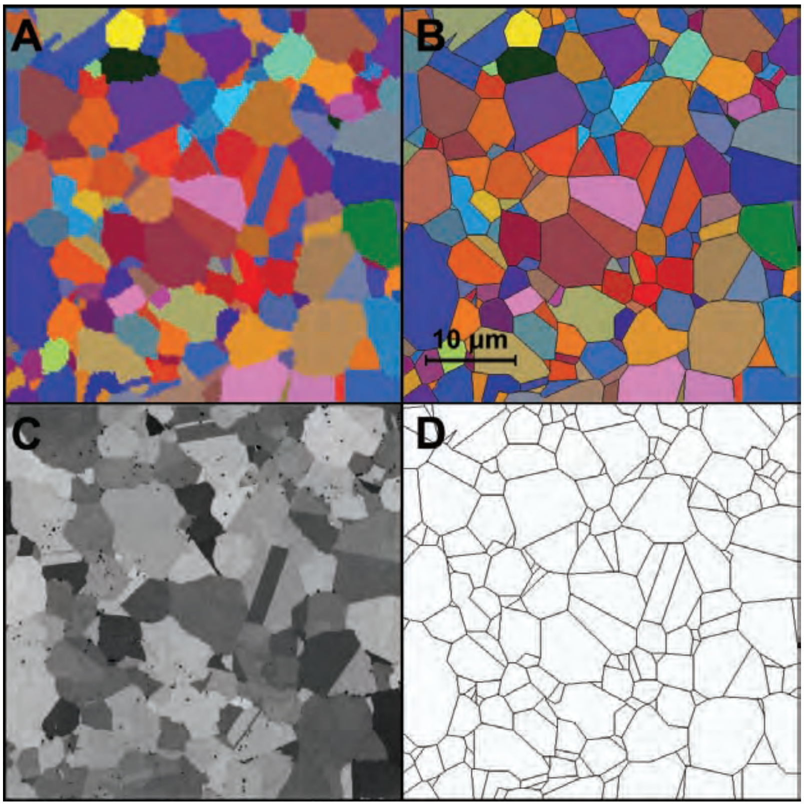

Figure 1: Microstructure of IN100 Ni-Based Superalloy, (a) grain map from an EBSD scan, with pixel size approximately 250 nm, (b) grain map after grain approximation by Micro-Imager, (c) scanning ion microscope image, and (d) binary image of the grain boundaries as created by Micro-Imager for improved stereology measurements (Compare with ion image seen in (c)).

3. FIB-EBSD Serial Sectioning Data Collection and Reconstruction

The full details of the serial-sectioning experiment can be found in [2] and thus will only be discussed briefly here. The serial-sectioning experiment in the DB FIB-SEM is comprised of moving the sample repeatedly between two microscope stage positions. These positions are the "sectioning" position and the "EBSD analysis" position. Image recognition is used for precise and automated alignment of the sample. When the sample is in the sectioning position, the FIB is used to mill a cross-section surface. After sectioning, the sample stage is rotated and translated to bring this cross-section face into the EBSD analysis position. An EBSD map is collected for each section before returning to the sectioning position. One key advantage of acquiring EBSD maps is that this information allows for unsupervised segmentation of grains and grain boundaries, which can be difficult to perform using image data.

Reconstruction of the entire stack of EBSD maps provides a 3D data set that can be analyzed and compared to individual 2D sections. The pixels in each orientation map will from this point be treated as voxels in 3D space. Following the reconstruction it is necessary to identify each grain for subsequent measurements, and the orientation data provides a clear path to automated segmentation. The misorientation of neighboring voxels can be determined and used to group voxels together as grains. If the misorientation is below a critical value, 4° in this work, then the voxels belong to the same grain. Once all sets of contiguous points with similar orientation are identified, data cleaning routines are run to refine the quality of the data set. Cleanup routines consist of filters for minimum grain size to remove individual erroneous data points, as well as alignment procedures to ensure the 3D volume is reconstructed properly.

4. Statistical Analysis

The initial analysis of the experimental data consisted of a classical 2D characterization. Micro-Imager was used to segment grains and measure a suite of parameters from each 2D orientation map. Micro-Imager measures the full distribution of each parameter rather than only the average like many stereological calculations. The probability density functions (PDFs) of each parameter were calculated and compared across each section. This level of analysis can be used to quantify variability through the sectioning depth as shown in Fig. 2, but is not a true 3D analysis and is very limited in its quantitative application. Additionally, there are other complications with stereological analysis regarding the assumption of feature morphology and distribution through the sectioning plane when performing the extrapolation from 2D to 3D. A number of stereological correction factors for determining grain volume are shown in Fig. 2, relative to the average grain volume as determined by the 3D analysis. The sensitivity of the extrapolation to the assumed feature morphology is a concern, and highlights the need for true 3D analysis.

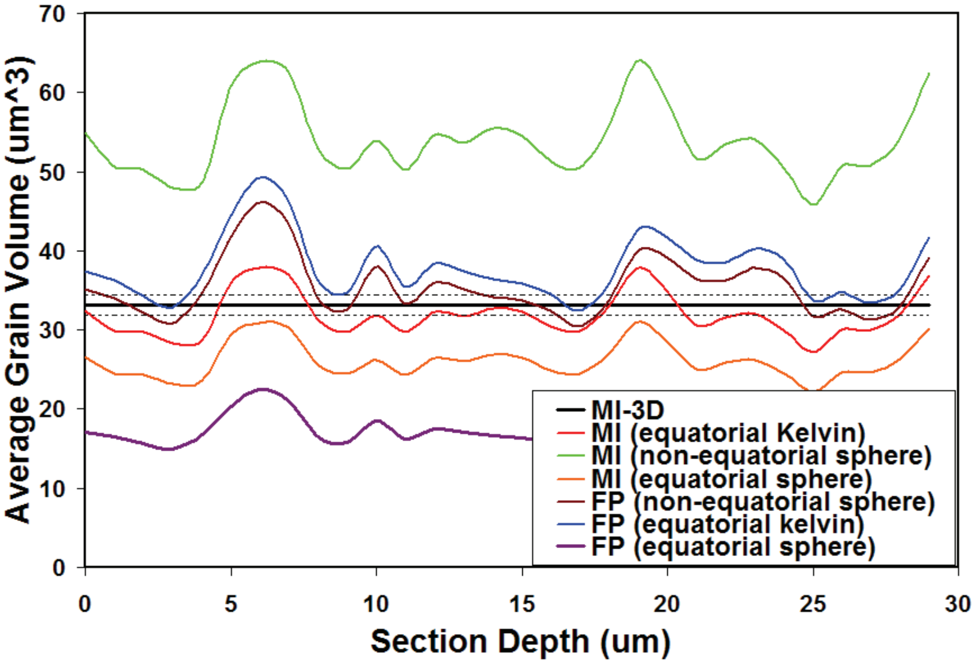

Figure 2. Comparison of various stereological assumptions applied to the series of 2D EBSD maps that comprise a 3D data set. The initials MI and FP refer to analysis performed by the software programs Micro-Imager and Fovea Pro. Thickness refers to the position of the 2D slice

in the 3D serial sectioning data. The solid black line is the average volume as calculated by Micro-Imager3D from the 3D reconstructed volume.

In conjunction with the 2D analysis, a suite of morphological parameters were measured in 3D for each grain. The 3D measurements clearly show that certain stereological assumptions are inaccurate for this particular microstructure while others may generally provide a reasonable description of the average value (see Fig. 2). In addition, the measurements performed by MicroImager in both 2D and 3D allow for more sophisticated statistics to be calculated. Classical characterizations rarely contain information about the relationships between various microstructural constituents. An example of one such relationship is the shape of a grain (the principal moments) as a function of the grain volume. This relationship can be directly calculated using MicroImager3D, and the application of this data is discussed further in section 5. Other relationships take into account the local environment of each grain, such as the number of neighboring grains. Figure 3 shows the probability distribution of the number of neighbors for each grain as a function of the grain size (volume). In this figure, one can observe that the average number of neighbors steadily increases with grain volume.

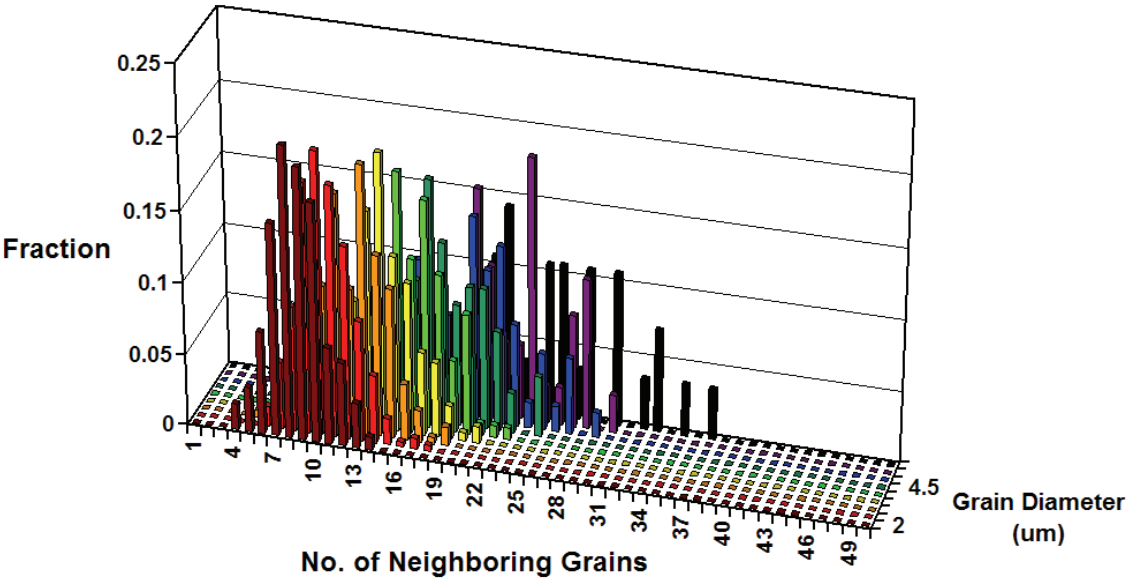

Figure 3. Plot displays changes in the distribution of number of neighbor grains as a function of grain size. The distributions broaden and shift to larger values as grain size increases.

The culmination of the statistical analysis is the creation of a relationship grid, which links the probability distributions for a suite of microstructural parameters, and allows for complex constraints to be enforced during the generation of synthetic structures. As an example, for this work grain volume was chosen as a free parameter and all other parameters were considered as functions of volume. First, the volume distribution was partitioned into bins and each grain was placed in a bin correlating with its volume. Then, the distribution of every other morphological parameter was calculated with respect to each volume bin. For example, the number of neighbors of each grain in a particular volume bin is obtained and the probability distribution for every bin can be calculated (Fig. 3). These relationship grids serve as the reference for the synthetic microstructure generator, which is discussed in the next section.

5. Synthetic Microstructures for Computational Modeling

Beyond statistical characterization of 3D microstructures, there is an additional need to supply modeling and simulation efforts with realistic grain-level microstructures. For example, experimentally-collected 3D voxel data could be directly meshed for FE analysis, or the voxelized data could be smoothed to help remove aliasing and then meshed for FE analysis. While direct conversion of the experimental data into a form suitable for modeling and simulation provides an extremely realistic input, one limitation with this approach is that a new data set needs to be collected each time one requires a different microstructural arrangement. The data collection process is somewhat time consuming and thus, limited in scale. Therefore, in addition to developing direct conversion processes, here we discuss a new methodology for creating synthetic microstructures that are statistically-equivalent to the experimental microstructure. These synthetic forms can supply modeling and simulation efforts with an endless supply of statistically equivalent microstructure representations and, can have various levels of complexity depending on the requirements of the model input. Tessellation and growth models have been used by a number of researchers to create synthetic microstructures [3,4]. However, the statistical inputs used in these efforts have often been generated from a 2D analysis. The 3D characterization methodology discussed previously allows for more accurate and potentially more sophisticated descriptors to constrain the synthetic microstructures.

SIRI-3D is a custom suite of programs that has been developed in this work to generate statistically equivalent synthetic microstructures. SIRI-3D (Statistically Induced Realistic Inputs) is made up of three principal codes. The first code, Constrained Grain Packer (CGP), focuses on the creation of voxel-based, grain-level microstructures that are statistically equivalent to the input 3D data set. The second code, Seed Point Generator (SPG), focuses on generating and tessellating seed points for a biased Voronoi tessellation that smoothes the voxelized volume generated by CPG. The final code, Orientation Arrangement Routine (OAR), assigns crystallographic orientations to the grains resulting in orientation- and misorientation-distribution functions which are equivalent to the original data set. Next, we briefly describe the functionality of each code.

First, CGP uses the size and shape information calculated by MicroImager3D to generate grains to populate the volume. In this process the PDF of grain volume is sampled until the volume of the grains is equal to the volume to be filled. After collecting the volume of each grain, the shape of each grain is determined. For the microstructure in this study, each grain is represented by an ellipsoid with principal axes (a,b,c). From the experimental data MicroImager3D calculates the principal moments of each grain and converts these into aspect ratio relationships (b/a and c/a) that define the grain shape. As mentioned previously the experimental grain volumes have been binned and each bin has its own unique PDFs for grain shape. CGP uses this series of PDFs to randomly sample the shape for each grain, so that each grain is assigned a volume and two aspect ratios.

Next, CGP determines the arrangement of the grains inside the volume. The statistical relationships used in this process are the following: the number of first-nearest-neighbor grains as a function of grain volume, and the distribution of first-nearest-neighbor grain sizes as a function of grain volume. Grains are sequentially placed within the volume at random, not allowing for overlap of more than 5%. When a potential position is selected for a new grain, the grains that have already been successfully placed in the structure and directly neighbor the new grain are checked against the following criteria to determine the suitability of this arrangement. The first criterion is an "ideal" number of first-nearest neighbors, the value of which is determined from the mean value of the PDF of the number of first-nearest neighbors for the pre-existing grain's volume bin. If the addition of the new grain moves the number of neighbors closer to the mean, a positive value is returned, otherwise a negative value is returned. The magnitude of the returned value is scaled by the distance from the mean (i.e., in units of standard deviation). This process is repeated for each grain that borders the new grain. At the end of this process, if the total sum is positive then the program examines the second criterion, otherwise a new position is selected. The second criterion considers the relative size of each neighboring grain. Here, the series of PDFs for the distribution of first-nearest-neighbor grains sizes as function of grain volume are used. The probability of occurrence for each grain pair based on size-differences is determined, and the value for the lowest probability out of all of the pairs is selected. A random number between 0 and 1 is generated, and if that number is less than the lowest probability the potential position is accepted, otherwise a new position is selected. This process is carried out until every grain is successfully placed.

Upon placement of all the grains, CGP fills the gaps that are left between ellipsoids. This is accomplished by a pseudo-grain growth process. Unassigned voxels are assigned to the grain with which they share the most surface area. If a voxel shares equal surface area with two grains, the larger grain accepts the unassigned voxel. This helps to ensure that small grains are not greatly increased during gap filling. Last, CGP calculates all the same statistics generated in the characterization of the experimental volume for verification of equivalence.

SPG uses the voxelized volume generated by CGP and generates seed points for a Voronoi tessellation. Initially SPG takes the centroids of the grains as the only seed points, and additional seed points are added inside of the larger grains to "push out" their boundaries. These additional seed points are needed because Voronoi tessellations create boundaries equidistant between seed points. If only the centroids of the grains are used as seed points, the distribution of grains moves from log-normal towards Gaussian by truncating the volume of larger grains and transferring this volume to small grains. The use of additional points inside of large grains alleviates this problem.

The frequency and location of additional seed points is determined as follows. For each neighboring pair of grains, the ratio of their volumes is calculated, and an additional seed point is added to larger grain. The placement of this new seed point is such that the ratio of the distance from centroid to grain boundary will be equal to the ratio of their volumes. Once the additional seed points have been added, SPG tessellates the structure and identifies the Voronoi cells belonging to each grain. Note that after tessellation, every grain is comprised of a number of Voronoi cells, and the larger grains can have many more cells. Visually the resulting structure appears to be similar to the experimental volume, as shown in Fig. 4. In this figure, the volume on the left is the experimentally-determined voxel data, the volume in the middle is the statistically equivalent voxel volume from CGP, and the volume on the right is the smoothed volume after Voronoi tessellation by SPG.

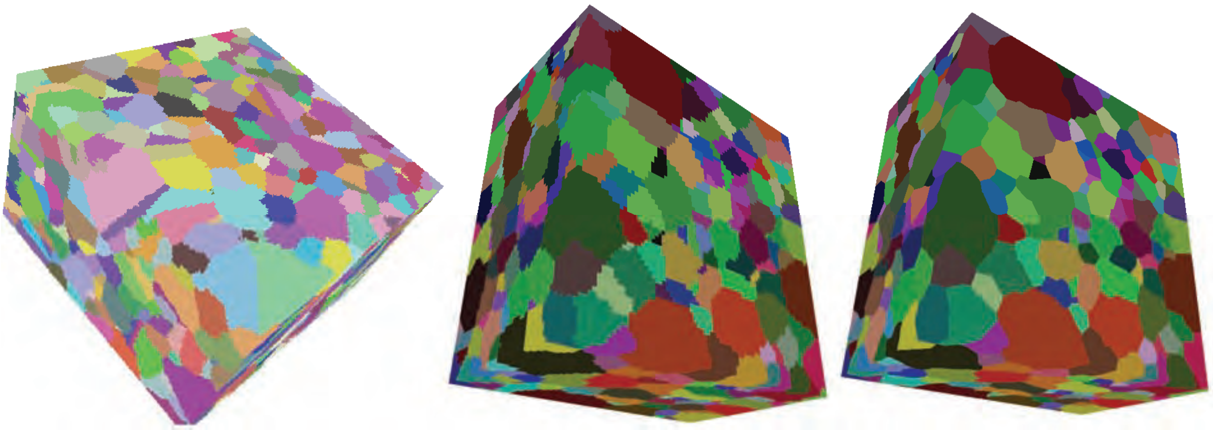

Figure 4. Grain structure: (left) of the reconstructed volume; (middle) generated by CGP; and (right) smoothed by SPG for comparison. Note that the volumes generated by CGP and SPG are the same structure (only one has been smoothed) and thus appear visually identical. However, while they are both statistically equivalent to the reconstructed volume, they are not the same structure and thus appear only visually similar. (The volume shown is 40µm x 40µm x 25µm)

The last step in creating the synthetic microstructure is the assignment of grain orientation. OAR uses the orientation distribution function (ODF) and misorientation distribution function (MODF) from the experimental data to assign orientations to the smoothed grains. The orientations are generated by sampling the ODF and are initially assigned randomly. The MODF of the synthetic structure is then calculated and compared to the experimental MODF. The bins of the synthetic structure MODF that deviate most significantly from the experimental MODF are identified, and grains in those bins are iteratively shuffled until the MODF matches the experimental maps (this process can be thought of as a biased Monte Carlo method).

6. Conclusions

This study has introduced both experimental and computational procedures that enable a new methodology for microstructural analysis and representation. A true 3D characterization and analysis has been performed, and this information can be used to assess 2D stereological extrapolations. Additionally, 3D synthetic structures have been created and meshed for subsequent Finite Element Analysis. As a whole, this study is a first attempt to create a fully-automated process that will collect 3D microstructural information via serial sectioning, provide quantitative measurements of property-controlling microstructural features, and generate realistic statistically equivalent structures for modeling.

References

[1] DeHoff RT. *J. Microscopy* 1983; 131: 259-263.

[2] Groeber MA et al. *Materials Characterization,* In Press.
[3] Rollett AD et al. *Scripta Materialia,* Vol. 55, 2006, pp 75-80.
[4] Coster M et al. *Image Anal. Stereol.,* Vol. 24, 2005, pp. 105-116.

A Micro-Macro Approach For Frost Heave Of Hardened Cement Paste And Mortar

M. Hain, P. Wriggers

Institute of Mechanics and Computational Mechanics
Department of Civil Engineering
Leibniz University of Hannover
Appelstr. 9a, D-30167 Hannover, Germany
e-mail: {hain, wriggers}@ibnm.uni-hannover.de

ABSTRACT

Based on a three dimensional computer-tomography of hardened cement paste (hcp) at the micrometer length scale, a finite element model is introduced with different constitutive equations for each phase. In order to identify the inelastic constitutive parameters of the phases, one has to solve an inverse problem. If the constitutive parameters are identified, homogenization techniques are performed to derive the effective properties. Damage due to frost can be simulated at the microstructural level through thermo-mechanical coupling and a material model for ice. The abovementioned approach for hcp is used for a meso-scale model of mortar.

1. Hardened cement paste

The three dimensional geometry of hcp is based on a computer-tomography at the micrometer length scale. A finite element model of this micro-structure is developed with different constitutive equations for the three parts unhydrated residual clinker, pores and hydration products. The hydrated part of hcp is described by a visco-plastic constitutive equation of Perzyna-type

$$\mathcal{P} = \boldsymbol{\sigma} : \dot{\boldsymbol{\epsilon}}^{\mathrm{pl}} + \tfrac{1}{\eta}\phi(f) \quad , \quad \phi(f) = \begin{cases} 0 & ; f \leq 0 \\ \frac{1}{m+1} f^{m+1} & ; f > 0 \end{cases} \quad , \quad f := \alpha \mathrm{tr}\, \boldsymbol{\sigma} + \|\mathrm{dev}\, \boldsymbol{\sigma}\| - \sqrt{\tfrac{2}{3}} k_f \tag{1}$$

and includes isotropic damage. The other parts are assumed to remain elastic. For details of the microstructural model please refer to [1].

1.1 Parameter identification

The elastic properties of the phases are taken directly from the literature [2], but the constitutive equation of the hydrated part contains inelastic parameters, which neither can be obtained through experimental testings nor can be taken from the literature. Therefore one has to solve an inverse problem which yields the identification of these properties. The identification is carried out by minimizing an objective function. For computational efficiency and robustness a combination of the stochastic genetic algorithm and the deterministic Levenberg-Marquardt method is used [3].

1.2 Homogenization

Once the constitutive parameters have been identified, homogenization is performed [4]. Based on the finite element solution the volume averages of the stress and the strain can be evaluated via

$$\langle \boldsymbol{\sigma} \rangle = \frac{1}{|\Omega|} \int\limits_{\Omega} \boldsymbol{\sigma} \mathrm{d}\Omega \quad , \quad \langle \boldsymbol{\epsilon} \rangle = \frac{1}{|\Omega|} \int\limits_{\Omega} \boldsymbol{\epsilon} \mathrm{d}\Omega. \tag{2}$$

Subsequently, the effective material properties are calculated using a least-squares approach. For the numerical analysis the whole representative volume element (RVE) is embedded within a matrix of average stiffness, this is sometimes referred to as window-method. Additionally, statistical tests for parameters of the homogenization, e.g. the size of the window or RVE have been performed. For comparison two-dimensional calculations under plain stress and plain strain conditions have also been carried out.

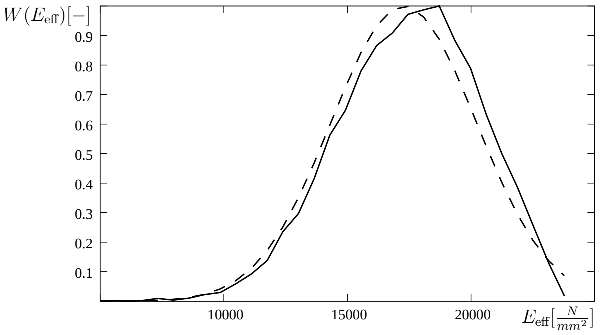

Figure 1. Probability density of E_{eff}.

Table 1. Experimental versus numerical results.

	$E_{\text{eff}}^{\text{med}}$ $\frac{N}{mm^2}$	$\nu_{\text{eff}}^{\text{med}}$ –
exp. series 1	17 460	0.210
exp. series 2	17 730	0.210
num. 3D	17 280	0.203
num. plain stress	10 450	0.234
num. plain strain	10 480	0.205

The homogenization yields probability densities for the effective elastic properties which are close to a GAUSSian distribution (dashed lines). Furthermore, the numerical results correspond very well to accompanying experimental results of hcp. As expected, only three-dimensional calculations provide reliable results.

1.3 Thermo-mechanical coupling

In order to analyze frost heave inside the micro-structure, a constitutive model for ice is applied to the water filled parts of the micro-structure. Here, a visco-plastic model of PERZYNA-type is chosen [5]. YOUNG's modulus of ice is expected to depend on the temperature

$$E(\Theta) := E_0 + \frac{E_\infty - E_0}{\mathrm{e}} \exp\left[1 - \exp\left(\frac{\Theta + 5}{2.5}\right)\right] \tag{3}$$

and the other constitutive parameters are assumed to remain constant. Transient thermal conduction is introduced and the mechanical and thermal constitutive equations are coupled. The weak form of the mechanical equilibrium reads

$$G_{int}^{\boldsymbol{u}} = \int\limits_{\Omega} \mathrm{grad} \boldsymbol{\eta}_{\boldsymbol{u}} : \mathbb{C} : \big(\boldsymbol{\epsilon} - \alpha_t(\Theta - \Theta_0)\mathbf{1}\big) \mathrm{d}\Omega. \tag{4}$$

Within this approach, cooling down of hcp leads to strain, but strain due to mechanical loadings doesn‘t change the temperature.

Depending on the degree of humidity the increase of volume during the freezing process leads to damage which yields an inelastic material behavior, e.g. the damage $\langle D \rangle$ within the micro-structure grows.

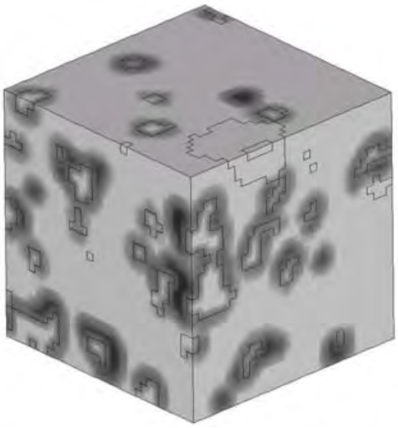

Figure 2. Damage (black) due to frost.

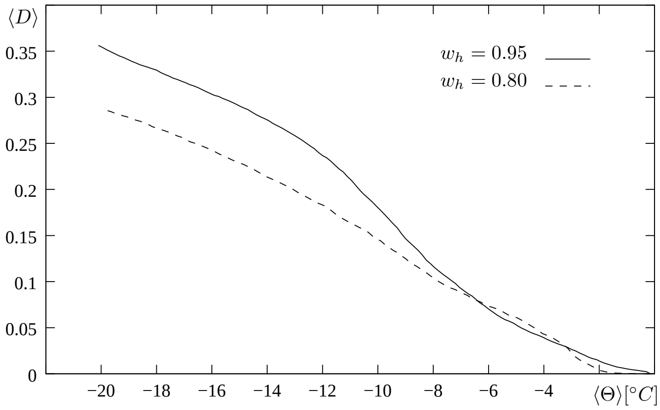

Figure 3. Dependency of damage on humidity.

2. Mortar

On the next length scale a model for mortar is introduced. It consists of an effective material of hcp, pores, particles and a cohesive zone between particles and matrix. The three dimensional geometry of mortar is generated by an algorithm, which shuffles spherical particles and pores in order to get close to a given size distribution. One obtains a particle/pore distribution and furthermore an artificial mortar. A corresponding finite-element mesh is generated using the technique of hanging nodes [6]. Numerical simulations of mortar shows damage zones near stress concentrations such as in-between particles.

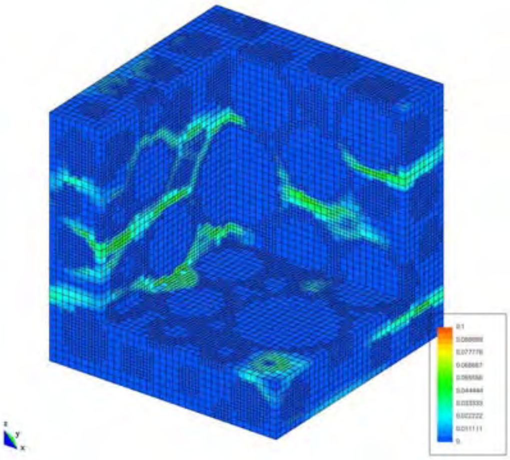

Figure 4. Damage in mortar.

Acknowledgment

Financial support from the German Research Foundation (*Deutsche Forschungsgemeinschaft*) is gratefully acknowledged. All experimental results have been performed by the *Institut für Bauforschung* at Aachen, Germany. The *Bundesanstalt für Materialforschung und -prüfung* in Berlin, Germany provided the CT-scans of hcp.

References

[1] Hain and Wriggers. A micro-macro approach for hardened cement paste including damage due to frost. *Computational Modelling of Concrete Structures*, pages 109–118, 2006.

[2] Bernard, Ulm, and Lemarchand. A multiscale micromechanics-hydration model for the early-age elastic properties of cement-based materials. *Cement and Concrete Research*, 33:1293–1309, 2003.

[3] Geiger and Kanzow. *Numerische Verfahren zur Lösung unrestringierter Optimierungsaufgaben.* Springer Verlag, 1999.

[4] Zohdi and Wriggers. *An Introduction to Computational Micromechanics.* Springer Verlag, 2004.

[5] Kolari, Kouhia, and Kärnä. Ice failure simulation–softening material model. *Proceedings of the 16th IAHR International Symposium on Ice, Dunedin, New Zealand*, pages 154–159, 2002.

[6] Löhnert. *Computational homogenization of microheterogeneous materials at finite strains including damage.* PhD thesis, Universität Hannover, 2004.

On the Multipolar Character of Dislocation Distributions

Craig S. Hartley[1]

[1]**El Arroyo Enterprises, 231 Arroyo Sienna Drive, Sedona, AZ 86336**
ElArroyo_Enterprises@msn.com

ABSTRACT

Quantitative characterization of dislocation distributions in deformed materials forms the basis for a class of field variables that serve as source functions in field theoretic treatments of the properties of a dislocated continuum. Applications to real structures assign the source strength to an appropriate summation of the contributions of sources within a volume element, δV, with centroid at $\mathbf{r}'$. The response field of the medium at a field point, $\mathbf{r}$, due to the sources follows from the definition of an appropriate Green's function, which is then integrated over the total volume subject to applicable boundary conditions. This work derives an expression for the dipole moment of a dislocation distribution that depends on both the relative spacing and the net orientation of dislocations in the array. The development employs a modification of the Dislocation Density Vector in which positive and negative dislocations (defined in terms of the angle between the tangent vector and the Burgers vector) contribute separately to the count of dislocations intersecting a plane of measurement. The dipole tensor contains information on the Burgers vector of the dislocations and the mean spacing of unlike pairs, which provides the source strength necessary to calculate the distortion field of the distribution. This development provides a basis for the description of the source strength of dislocation arrays produced by dislocation dynamics calculations and of dislocation arrays observed in transmission electron micrographs, providing a mechanism for expressing experimental observations of dislocation structures of deformed materials in terms of a continuum quantity.

1. Introduction

Field theories of plastic deformation based on dislocation concepts require descriptions of dislocation content and behavior that not only capture the distribution and behavior of dislocations in crystals but also present information on these properties in a manner compatible with the formalism of continuum mechanics. The necessary descriptions take the form of material properties that act as source tensors for internal stresses. The Nye tensor, which describes the net flux of Burgers vectors due to dislocations crossing an oriented surface, is a familiar example [1]. While this tensor describes an aspect of the net dislocation content within a suitably chosen representative volume element (RVE), it does not address the multipolar character of the dislocation distribution within the RVE [2]. Information on the lattice distortion field arising from this feature of the dislocation distribution is lost if the source considers only the volume average of properties of the distribution contained in the RVE.

2. Dipole Moment of a Dislocation Distribution

To develop a description incorporating the dipolar character of a dislocation distribution, we begin with the process introduced by Nye to determine the net Burgers vector of dislocations crossing an arbitrarily oriented element of area, δA, having unit outward normal, **n,** and bounded by a closed curve, δC. Positive and negative intersections of dislocations with δA are defined according to the procedure described by Hartley [3]. Initially consider only dislocations lying on the same slip plane with the same Burgers vector, **b**. In general the **t** vectors of the dislocations intersecting δA are arbitrarily oriented with respect to **n**.

The lengths, projected parallel to **n**, per unit volume of positive and negative dislocations crossing δA are numerically equal to the number of intersections per unit area of the corresponding dislocations with δA. The magnitudes of the dislocation density vectors $\boldsymbol{\rho}^+$ and $\boldsymbol{\rho}^-$ are equal to the total lengths per unit volume of dislocations having the same sign. The orientation of $\boldsymbol{\rho}$ depends on the edge-screw character of the array and the scalar products of $\boldsymbol{\rho}^\pm$ with **n** are the number of signed intersections of dislocations per unit area normal to **n**, regardless of the orientations of individual dislocations in the array. It is important to recognize that this definition carries no information about the orientation of individual dislocations in the array, but only depends on the length per unit volume projected along **n**.

Corresponding definitions of positive and negative components of the Nye tensor, $\boldsymbol{\alpha}^\pm$, follow from these definitions of signed dislocation densities [3,4]. This definition applies to each active slip system and the total Nye tensor is the sum of the contributions from each such system in the RVE. Clearly if $\boldsymbol{\rho}^+$ and $\boldsymbol{\rho}^-$ are equal for a particular slip system, the net dislocation density, the system's contribution to the Nye tensor associated with the RVE and any resulting long-range lattice distortion all vanish. Nevertheless, there exists a shorter range lattice distortion field due to the multipolar character of the distribution, which is not accounted for by the Nye tensor.

Define a coordinate system based on $\boldsymbol{\rho}^\pm$ as shown in Fig. 1. The ξ axis is parallel to $\boldsymbol{\rho}$, the υ axis is normal to the common slip plane of the dislocations such that the positive direction points towards the region of lattice dilatation associated with edge and mixed dislocations, and η forms a right-handed set. The angle ψ is the acute angle between $\boldsymbol{\rho}^+$ and **b**. The vectors $\boldsymbol{\rho}^\pm$ are separated from one another by the vector **d**, whose magnitude is the perpendicular distance between $\boldsymbol{\rho}^\pm$ and whose positive direction points from $\boldsymbol{\rho}^+$ to $\boldsymbol{\rho}^-$. We now define the dipole strength per unit area of the array as the dyadic product $|\boldsymbol{\rho}^+|\mathbf{b}\otimes\mathbf{d}$.

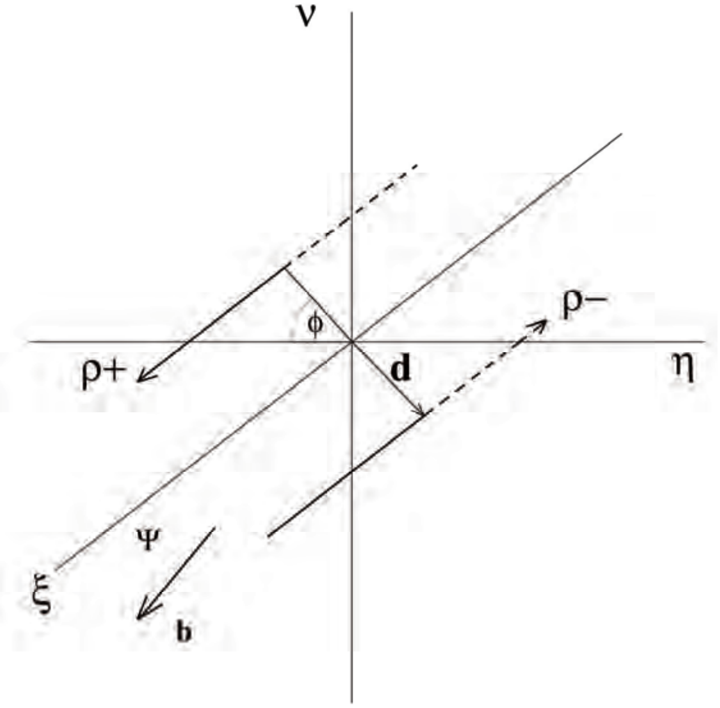

Figure 1. Coordinate System for Dislocation Distribution

Consider an array of dislocations on the same slip system such that $\boldsymbol{\rho}^+ = -\boldsymbol{\rho}^-$, which results in $\boldsymbol{\alpha} = \mathbf{0}$. Construct an array of parallel mixed dislocations of alternating signs and arrange them on a square Taylor lattice normal to $\boldsymbol{\rho}^{\pm}$ as shown in Fig. 2. Since the mean area per dislocation of the same sign is $1/|\boldsymbol{\rho}^{\pm}|$, the mean spacing between dislocations of like sign is $(\boldsymbol{\rho}^{\pm})^{-1/2}$. To a first approximation we assume that dislocations of both signs are arranged on interpenetrating square lattices, so that $|\mathbf{d}| = \tfrac{1}{2}\sqrt{(2/|\boldsymbol{\rho}^{\pm}|)}$. In the $(\eta\upsilon\xi)$ coordinate system $\mathbf{b} = |\mathbf{b}|(\sin\psi, 0, \cos\psi)$ and $\mathbf{d} = |\mathbf{d}|(\sqrt{1/2}, \sqrt{1/2}, 0)$. The dipole tensor per unit area of the array then becomes

$$P = \left(\frac{|\mathbf{b}|\sqrt{|\boldsymbol{\rho}|}}{2}\right)\begin{bmatrix} \sin\psi & \sin\psi & 0 \\ 0 & 0 & 0 \\ \cos\psi & \cos\psi & 0 \end{bmatrix} \qquad [1]$$

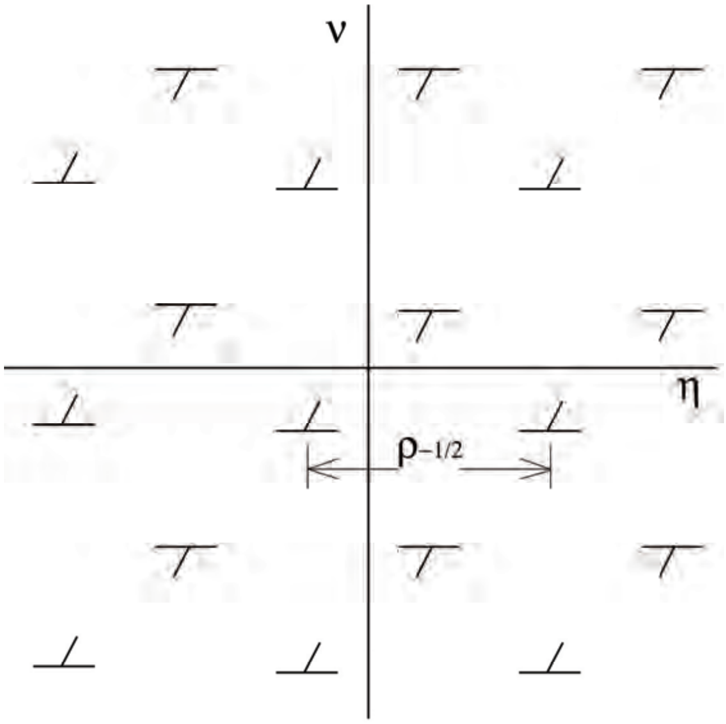

Figure 2. Equivalent Multipolar Array of Dislocations

3. Discussion

The method presented in this paper for assigning a value to the dipole moment of a dislocation array differs from that presented by Kröner [4] and LeSar and Richman [5] in that we first describe the entire dislocation array by a single vector, then develop a dipole moment based on that vector. This technique is valid for determination of far-field effects of the array, but not for calculations of effects at distances of the order of a few times the mean spacing of dislocations in the array. Nevertheless, the compact method of representing an array of dislocations having a distribution of orientations should provide a useful basis for the description of the dislocated state in deformed materials.

Acknowledgements

The author gratefully acknowledges the support of the U.S. Air Force Office of Scientific Research.

References

[1] JF Nye, Acta Met., **1**, 153 (1953).
[2] E Kröner, Inelastic Behavior of Solids, edited by MF Kanninen, RI Jaffee and AR Rosenfield, McGraw-Hill, New York, NY, 137 (1970).
[3] CS Hartley, Proc. Second Int. Conf. on Multiscale Modeling of Materials, edited by N. Ghoniem, Mechanical Engineering Department, UCLA, Los Angeles, CA, 59, (2004).
[4] E Kröner, Appl. Mech. Rev., 15, 599 (1962).
[5] R LeSar and JM Richman, Phys. Rev. B 65, 144110, (2002).

A Yield Stress Model For Both Metals And Polymers: Effects For Strain Rate And Temperature

Ch. Husson[1,2], J. Richeton[2], S. Ahzi[2]

[1] GIP-Institut Supérieur d'Ingénierie de la Conception, Equipe ERMeP
27 rue d'Hellieule, 88100 Saint-Dié des Vosges, France
e-mail : christophe.husson@insic.fr
[2] Institut de Mécanique des Fluides et des Solides, UMR 7507 ULP/CNRS
4 rue Boussingault, 67000 Strasbourg, France
e-mail: ahzi@imfs.u-strasbg.fr

ABSTRACT

The stress-strain response of metallic materials and alloys is influenced by the temperature at which deformation occurs and by the loading rate. To model this behavior over a wide range of temperatures and strain rates we propose to use the strain rate / temperature superposition principle. An increase in temperature will have a similar effect on the yield stress as a decrease in strain rate. Although the use of the superposition principle has been recently proposed to model the yield behavior of solid amorphous polymers, we will show that this type of approach can be extended for metals. In the case of HEL (high elasticity limit) steel on a wide range of temperatures and strain rates, we obtained a good agreement with experimental data from the literature.

1. Introduction

At low homologous temperatures, the physical processes involved in plastic deformation of metals are dislocation motions and theirs corresponding interactions with obstacles. Generally, the descriptions of flow are governed by kinetic flow theory which refers to the dislocation glide at a fixed obstacle structure. At higher strain rates (and lower temperatures) a more marked dependence on both temperature and strain rate becomes apparent. This dependence is usually associated with thermally-activated processes for which temperature and strain rate are related through Arrhenius-type laws.

Concerning polymeric materials, the deformation process is typically described by two kinds of approach, namely continuum rheological models and molecular-based theories of yield [1]. Yield and flow stress can also be regarded as thermodynamically activated processes with associated activation energy and volume. Temperature and stress both increase the molecular mobility (rate of conformational changes) and accelerate the time scale at which the material deforms.

In this paper, we propose to apply a polymer theory to metallic materials. As for polymers, the plastic strain rate of metals could also be expressed as a function of the hyperbolic sine of the flow stress. In particular, we will show that the cooperative model and the associated superposition principle between temperature and strain rate can be used to describe the flow stress of the HEL steel. For a wide range of temperatures and strain rates, the model was in good agreement with experimental data found in the literature.

2. The cooperative model

2.1. Brief summary

For the description of the yield behavior, σ_y, of amorphous polymers on a wide range of temperatures and strain rates, Richeton et al. [2] proposed to make use of the cooperative model. This model is originally based on the work of Fotheringham and Cherry [3] where the following modifications were granted to the original Eyring equation [4]:

- it is assumed that the effective stress, σ^*, is written according to an internal stress, σ_{int}:

$$\sigma^* = \sigma_y - \sigma_{int} \text{ where } \sigma_{int} = \sigma_{int}(0) - mT \tag{1}$$

where $\sigma_{int}(0)$ is the internal stress at 0K and m is a constant material parameter [2].

- it is postulated that the yield process involves a cooperative motion of polymer chain segments. The strain rate, $\dot{\varepsilon}$, is given by:

$$\dot{\varepsilon} = \dot{\varepsilon}^* \sinh^n\left(\frac{\sigma^* V}{2k_B T}\right) \tag{2}$$

where $\dot{\varepsilon}^*$ is a characteristic strain rate, n is a constant material parameter describing the cooperative character of the yield process, V is an arbitrary activation volume, k_B is the Boltzmann's constant and T is the absolute temperature.

Combining Eqn. 1 and 2, the form of the cooperative model is given by:

$$\sigma_y = \sigma_{int} + \frac{2k_B T}{V} \sinh^{-1}\left(\dot{\varepsilon}/\dot{\varepsilon}^*\right)^{1/n} \tag{3}$$

It was also shown that the characteristic strain rate, $\dot{\varepsilon}^*$, derives from an Arrhenius expression relating strain rate, activation energy, ΔG, and temperature.

2.2. Strain rate / temperature superposition principle

It is widely known that temperature and strain rate significantly influence the mechanical behavior of polymeric materials. In particular, a decrease in strain rate will have a similar effect on the yield stress as an increase in temperature [4]. For amorphous polymers, the curves representing the reduced yield stress, versus the natural logarithm of strain rate, for various temperature can be shifted horizontally and vertically to create a master curve at a reference temperature, T_{ref} [5].

3. Experimental results

Originally the cooperative model was applied for the mechanical response of amorphous polymers. Here we propose to use this formalism to describe the yield stress of metals on HEL steel [6]. To illustrate the predictive capability of ours proposed model, we select the yield at an arbitrary strain of 10% and compared our predicted results to the experimental ones of Awade [6].

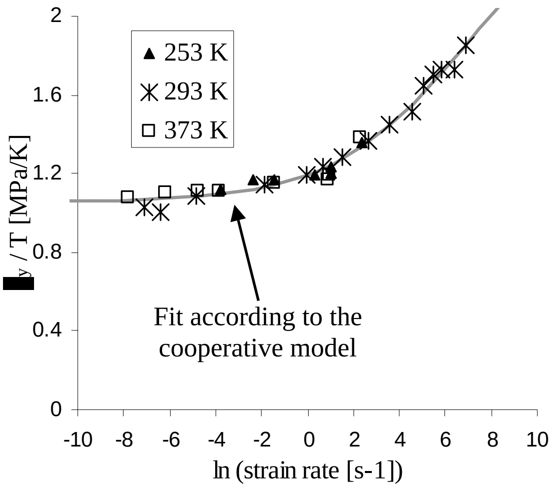

Figure 2. Master curve built at 298°K for HEL steel.

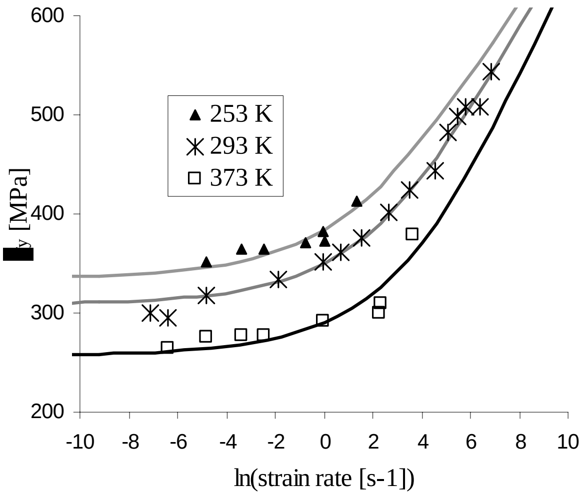

Figure 3. Validation of the cooperative model for the yield stress of HEL steel.

As it is shown in Fig. 2, it was possible to build a master curve from the experimental data at a chosen reference temperature (T_{ref} = 298 K). The horizontal and vertical shifts were determined to obtain a good superposition of the experimental data for a wide range of temperatures (253K, 293K and 373 K) and strain rates (from the quasi-static to the dynamic regime). In addition, this master curve can be described by the cooperative model according to Eqn. 3.

Fig. 3 shows the influence of strain rate on the flow stress of HEL steel for three different temperatures. The cooperative model provides a good agreement of the experimental data over a wide range of strain rates and temperatures.

6. Conclusions

As it was the case for polymeric materials, the use of the superposition principle relating temperature and strain rate can describe the yield behavior of metals as well. Through the use of the cooperative model, we have shown that this type of approach yields results in good agreement with experimental data for HEL steel.

References

[1] Richeton, J., S. Ahzi, L. Daridon and Y. Rémond, J. Phys. IV, **110**, 39-44 (2003).
[2] Richeton, J., S. Ahzi, L. Daridon and Y. Rémond, Polym., **46**, 6035-6043 (2005).
[3] Fotheringhan, D., and B.W. Cherry, J. Mat. Sci. **11**, 1368-1371 (1976).
[4] Eyring, H., J., Chim. Phys., **4**, 283-291 (1936).
[5] Bauwens-Crowet, C., J.C. Bauwens and G. Homès, J. Polym. Sci. A, **7**, 735-742 (1969).
[6] Awade, A., 2005, *Crash automobile - Importance de la température et de l'anisotropie dans les essais dynamique in Colloque national MECAMAT sur les Mécanismes et Mécanique du Comportement, de la Dégradation et de la Rupture des Matériaux sous Sollicitations Dynamiques,* Aussois 2005, France, Electronic Proceedings CD edited by C. Genin, F. Hild et L. Rota.

Fracture Prediction In Sheet Metal Forming Process: Application To The Deep-Drawing Of OFHC Copper

Ch. Husson[1,2], F. Bilteryst[1], M. Oudjene[1], S. Ahzi[2]

[1] GIP-Institut Supérieur d'Ingénierie de la Conception, Equipe ERMeP
27 rue d'Hellieule, 88100 Saint-Dié des Vosges, France
e-mail : francois.bilteryst@insic.fr; mourad.oudjene@insic.fr
[2] Institut de Mécanique des Fluides et des Solides, UMR 7507 ULP/CNRS
4 rue Boussingault, 67000 Strasbourg, France
e-mail: ahzi@imfs.u-strasbg.fr; christophe.husson@insic.fr

ABSTRACT

To correctly model the behavior of OFHC copper during the deep drawing, it is necessary to develop robust tools to simulate the hardening and the damage evolution during deformation. For this, we used a semi-empirical description of stress-strain response based on mechanical threshold stress approach. The effect of strain hardening, strain-rate hardening, pressure and thermal softening have been incorporated for a wide range of loading rates. The physical aspects of the deformation response are taken into account via the mechanical threshold stress model. This approach uses the flow stress at 0K temperature such that deformation can be quantified in the absence of thermally activated processes and an Arrhenius type expression relating strain rate to activation energy and temperature. The proposed plasticity model is combined with a non-linear isotropic damage evolution law based on the theory of continuum damage mechanics. The model has been implemented in the form of a User Material Subroutine in the FE code ABAQUS. We simulated the stamping process and the Nakazima test. The fracture phenomenon is also addressed in this study. At the same time we focus on the integrating role played by Virtual Reality in the post-processing of such simulations

1. Introduction

The stamping of thin metallic sheets is a widely used industrial forming process. It allows producing thin walled parts of complicated shape. The process consists in the plastic deformation of an initial flat blank subjected to the action of rigid tools (punch, die) while constrained on the periphery by a blank holder. In this contribution, we focus on the modelling of the plasticity and damage behaviours of thin OFHC copper sheet (thickness below 1 mm) during a cylindrical cup deep drawing (benchmark test of *Numisheet'2002*) with the help of a physically-based model, for the description of plasticity as well as damage.

2. Modeling

2.1. Isotropic plasticity model

For metals at low homologous temperatures, the physical processes involved in plastic deformation are dislocation motions and their interactions with obstacles. To describe the flow stress evolution we used the kinetic flow theory. This approach refers to the dislocation glide at a fixed obstacle structure where dislocation junctions are regularly distributed on the slip plane. In general principles of thermally activated processes, the plastic shear strain rate could be expressed as function of the free energy of activation which depends on the strength, shape and distribution of obstacles, as well as the applied stress. The equivalent flow stress is written as the sum of three contributions: an athermal contribution σ_{ath} (i.e. the dislocation interaction with long-range barriers), an “intrinsic strength” σ_i, which models yield (“intrinsic” barrier to thermally activated dislocation motion and dislocation-dislocation interactions: this part is not considered for a pure copper), and a state variable σ_e, which evolves with deformation to model hardening [1]. The terms σ_i and σ_e are further decomposed as a product of their respective values $\hat{\sigma}_i$ and $\hat{\sigma}_e$, in a reference state at 0K (Mechanical Threshold Stress [1]) and reference strain rate $\dot{p}_0$, with scaled temperature-strain rate functions $S_i(\dot{p},T)$ and $S_e(\dot{p},T)$. In equation form, we have

$$\sigma_{eq} = \sigma_{ath} + \sigma_{th} = \sigma_{ath} + \hat{\sigma}_i S_i(\dot{p},T) + \hat{\sigma}_e S_e(\dot{p},T) \tag{1}$$

where $\dot{p}$ is the equivalent strain rate, T is the temperature and the functions S are an Arrhenius description of thermally activated deformation [2] ($0 \le S \le 1$). The term $\hat{\sigma}_e$ is described empirically using the Kovàcs-Vörös quasi-static stress [3] take account the change in dislocation density from the onset of straining and the macroscopic strain-hardening rate due to dislocation accumulation according to the strain rate and the temperature [2].

2.2. Thermodynamic damage model

Plastic deformation in metals induces damage which can be described by nucleation, growth and coalescence of micro-voids and/or micro-defects. In the case of isotropic damage, a scalar variable D is used to indicate the degree of deterioration of the material when it is subjected to loading. This variable can be interpreted as a surface density of discontinuities (micro-cracks or cavities). The present damage model is based on thermodynamics of irreversible processes using a new form of the ductile damage dissipation potential [4] and is valid for a wide range of strain rates (10^{-4} to 10^{+4} s^{-1}) and at low homologous temperatures ($T<0.5T_{melt}$):

$$\begin{array}{lll} D = D_i & \text{if} & p < p_{th} \\ D - D_i = \left(D_{cr} - D_i\right)\left[\displaystyle\int_{p_{th}}^{p}\left[\sigma_{eq}\right]^2 dp \Bigg/ \int_{p_{th}}^{p_{cr}}\left[\sigma_{eq}\right]^2 dp\right]^K & \text{if} & p_{th} \le p < p_{cr} \\ D = D_{cr} & \text{if} & p \ge p_{cr} \end{array} \tag{3}$$

where D_{cr} is the critical damage at failure, D_i is the initial damage, K is a non-linear damage exponent. p_{th} and p_{cr} are the threshold and failure equivalent strain are proposed according to the strain rate, the temperature and the tri-axiality factor [2]:

$$p_{cr} = \varepsilon_{th}(\dot{p},T)\left[\frac{\varepsilon_{cr}^{qs}}{\varepsilon_{th}^{qs}}\right]^{1/f\left(\sigma_H/\sigma_{eq}\right)} \quad \text{and} \quad p_{th} = \varepsilon_{th}(\dot{p},T)\left[\frac{\varepsilon_{cr}^{qs}}{\varepsilon_{th}^{qs}}\right]^{1/f\left(\sigma_H/\sigma_{eq}\right)-1} \tag{4}$$

Here $f(\sigma_H/\sigma_{eq})$ is the tri-axiality factor where σ_H is the hydrostatic stress, ε_{cr}^{qs} and ε_{th}^{qs} are respectively the quasi-static uni-axial critical strain and the quasi-static uni-axial threshold strain.

3. Three dimensional Finite Element simulations

3.1. Numerical consideration

The models discussed in the previous section is implemented in a User Material Subroutine of the commercial Finite Element code ABAQUS, which enables “explicit” analysis of boundary value problems and is particularly suitable for the problems involving surface contacts as is the study cases.

In this section, we present the FE simulations of a thin OFHC copper sheet with the proposed hardening and damage models. The sheet thickness is 1 mm. The elements are eight-node linear brick with reduced integration and hourglass control. The die, blank-holder and punch are all treated as rigid bodies meshed with 4-node 3-D bilinear rigid quadrilateral elements. The friction coefficient (Coulomb law) for the contacting surface between the tools and the sheet is set to a typical value of 0.01 which is representative of a good lubrication.

Two Finite Element simulations were realised:

- First, the simulation of the 3D deep-drawing process (Fig. 1). The punch radius and the die radius are respectively equal to 9.5 mm and 7 mm (punch radius: 50 mm). For symmetry reason, just one quarter of the problem is simulated. The numerical simulations were carried out with a constant blank holder force of 17.50 kN (for the ¼ of the blank), a punch stroke of 40 mm and a punch speed of 10 m/s.
- Second, the simulation of the Nakazima test (Fig. 2). This one is a thin sheet forming test using a hemispherical punch, a circular die and a circular blank-holder to determinate the forming limit curve (denoted FLC). FLC are usually used to predict the possible failure in a sheet metal forming process.

3.2. FE simulations of the deep-drawing process

Fig. 1 and 2 shows the results of the numerical simulations. The failure of a cylindrical cup drawing can be analyzed in a manner similar to a Nakazima test.

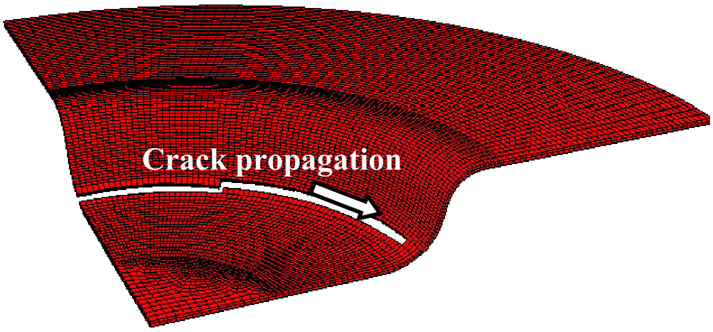

Figure 1. FE results: deformed mesh obtained during the deep-drawing.

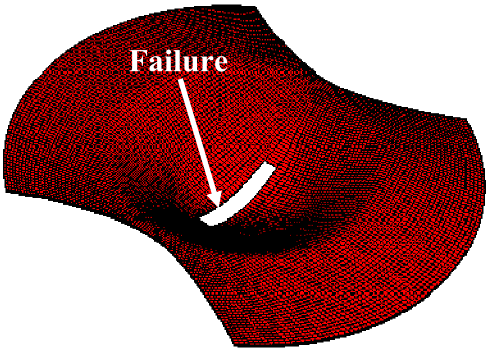

Figure 2. FE results: deformed mesh obtained during Nakazima test.

During sheet metal stamping operation, the thin sheet is subjected to more complex solicitations as damage, hardening and initiation and propagation of cracks leading to rupture. We can observe that the fracture appears above the punch. The physical interpretation begins with the investigation of the highest maximum stress factor intensity. In particularly, a uniform deformation is observed prior to the onset of necking.

4. The application of the Virtual Reality in the study of microstructure

At the same time we focus on the integrating role played by Virtual Reality (denoted VR) in the post-processing of such simulations. VR technology has the potential to provide an integrated environment for the analysis and optimization of such processes. VR techniques have already been applied in combination with finite element analysis or computational fluid dynamics, sensitivity analysis, design optimization for different practical industrial applications. We can refer to [5] for some various examples without summarising the state-of-art of such researches. Different leads can be explored. The main one deals with the benefits when using a 3D visualization system in order to analyze the microstructure evolution (as the hardening, the micro-voids, the texture) in the thickness during the processes (Fig. 3). Moreover such 3D systems and dedicated software permit to compare different models (which may be computed from different FE softwares) in the same working environment.

Figure 3. Application of the VR in the study of the Nakazima FE simulations: study of the localized necking and the failure.

5. Conclusions

Based on the results obtained in the present work the following conclusions can be made:

- Numerical simulations of the deep-drawing process and the Nakazima test of a copper sheet have been developed using an elastic-viscoplastic material model combined with a non-linear isotropic damage evolution law based on the CDM theory,
- Some significant aspects of simulations, obtained with ABAQUS/Explicit, are discussed,
- The integrating role played by VR in the post-processing of FE simulations is presented.

References

[1] Follanbee, P.S., and U.F. Kocks, Acta Metall., **36**, 81-93 (1988).
[2] Husson, Ch.,2004, *Simulation numérique de la mise en forme des matériaux métalliques appliqués à la connectique:étude de la découpe*, PhD thesis, ULP, Strasbourg, Fr.
[3] Kovacs, I., and G. Vörös, Int. J. Plast., **12**, 35-43 (1996).
[4] Husson, Ch., S. Ahzi, L. Daridon and T. courting, J. Phys. IV, **110**, 63-68 (2003).
[5] Wasfy, T. and A. Noor, Adv. Eng. Soft., **32**, 717-730 (2001).

Precipitate shape and coherency loss mechanisms in Au-Rh alloys

Brian D. Wirth[1], *Peihua Jing*[1], *Hyon-Jee Lee*[1], *Jae-Hyok Shim*[1]

[1]*Nuclear Engineering Department, University of California, Berkeley, 4151 Etcheverry Hall, Dept of Nuclear Engineering, UC Berkeley, 94706 Berkeley, United States of America*

In precipitate hardened materials, the strength and creep properties are controlled by dislocation interaction and detachment mechanisms with the precipitate obstacles, which depend on the precipitate interfacial structure. We present the results of atomistic simulations to investigate the precipitate shape and coherency loss in Au-Rh with a large (6%) lattice misfit and the dislocation – precipitate interaction and bypass mechanisms. N-body, Sutton-Chen type method interatomic potentials have been derived to accurately describe the elastic properties of Au and Rh, the Au-Rh interfacial energy and mixing enthalpy. The results provide insight into the precipitate coherency loss mechanisms and the effect of precipitate coherency on dislocation interaction and bypass.

Molecular dynamics of a 2D Lennard-Jones body with shape memory

Oliver Kastner

Ruhr-Universität Bochum, Lehrstuhl Werkstoffwissenschaft, Institut für Werkstoffe, Universitätsstr. 150, 44801 Bochum, Germany

We investigate the thermodynamic properties of a qualitative molecular dynamic model of austenite-martensite transitions as they occur in shape memory alloys. The model, still in 2D, uses Lennard-Jones pair potentials for the calculation of the atomic interactions. Recently it was shown that it is possible to identify different lattice structures by use of two atom species, interpreted as austenite and two variants of martensite [1, 2]. A small test assembly of 41 particles ("crystallite") transforms uniformly between these configurations. It exhibits temperature-dependent and non-monotone (load, strain)-curves and thus temperature-dependent free energies which are non-convex.

The model may be used for qualitative description of quasi-plasticity, pseudoelasticity and the shape memory effect as they appear in larger bodies that allow for the formation of micro structure. Here we represent a particular simple approach: A larger body is modeled as a weekly interacting "chain" of 41-atom crystallites. The chain is exerted to uniaxial loads in numerical (hard, soft)-device tests at

different temperature. The load-strain characteristic of the chain is strongly influenced by the phase selection of the individual chain links according to temperature and load applied. Quasi-plasticity appears as the result of martensitic de-twinning of chain links upon loading at low temperature and pseudo-elasticity as load-induced austenite-martensite transitions at high temperature. The shape memory effect is represented by temperature induced martensite-austenite transitions of the unloaded chain.

Our chain-model is motivated by discrete models for elasto-plasticity that make use of snap springs [3, 4]. While snap springs are bi-stable and cold elements, the 41-atom crystallites are tri-stable and thermalized. The chain of crystallites represents qualitatively a thermo-mechanical material that may undergo phase transitions.

References

[1] O. Kastner, Molecular Dynamics of a 2D model of the Shape Memory Effect. Part I: Model and Simulations, Continuum Mech. and Thermodyn. 2003, 15(5)

[2] O. Kastner, Molecular Dynamics of a 2D model of the Shape Memory Effect. Part II: Thermodynamics of a small system, Continuum Mech. and Thermodyn. (in print)

[3] I. Müller, P. Villagio, A model for an elastic-plastic body, Archive for Rational Mechanics and Analysis 1978, 65(1), 25-46

[4] G. Puglisi, T. Truskinovsky, Mechanics of a discrete chain with bi-stable elements, J. Mechanics and Physics of Solids 2000, 48(1), 1-27

Modelling Investigation of Interfacial Disconnection Mechanisms

H. A. Khater[1], **A. Serra**[2], **D. J. Bacon**[1] **and R. C. Pond**[1]

[1]**Department of Engineering, The University of Liverpool, Brownlow Hill, Liverpool L69 3GH, United Kingdom, h.khater@liv.ac.uk;** [2]**Department de Matematica Aplicada III, Universitat Politecnica de Catalunya, ETSE Camins, Jordi Girona 1-3, 08034 Barcelona, Spain.**

ABSTRACT

Twinning and sessile disconnections, TDs and SDs, are investigated in $\{10\bar{1}2\}$ twin boundaries in zirconium (Zr) using atomic-scale computer modelling. TDs were found to glide along the interface in response to an applied shear stress of 1.7 MPa at 0K. SDs cannot move along the interface without concomitant long-range diffusion. These defects act as modest barriers to TDs; the applied stress must exceed 27 MPa to enable TDs to surmount such obstacles in a process which is conservative overall. With an applied stress of 100 MPa, SDs act as stress concentrators and TD dipoles were observed to nucleate there and expand outwards; these sources of TDs also operate in a conservative manner.

1. Introduction

The mechanism of $\{10\bar{1}2\}$ twinning, which is an important mode of deformation in HCP metals, involves the motion of twinning disconnections (TDs) along the matrix-twin interface. A disconnection is an interfacial discontinuity characterised by its Burgers vector and step height (**b**, h) as explained by Hirth and Pond [1], and their presence in HCP metals has been supported by many TEM observations [2]. The kinetics of the twinning processes are not determined solely by the mobility of TDs however; further considerations include the nature of sources of TDs, and possible obstruction to their passage along the interface by encountering obstacles such as other interfacial defects. An example of the latter would be a sessile disconnection (SD) created by decomposition of a crystal dislocation that impinges on the interface [3]. Serra and Bacon [4] demonstrated that sessile disconnections can also act as sources of TD dipoles when an applied stress becomes concentrated at the defect. The object of the present work is to study further the mechanisms of (i) TD sources and (ii) motion of a TD through a SD, as depicted schematically in Fig. 1, by simulation of a model of Zr.

Mobile disconnections have small $|b|$ parallel to the boundary and small h [5]; for the TD in $(10\bar{1}2)$ twins in Zr, $|b| = 0.19\,a_0$, where a_0 is the hexagonal lattice parameter, and h $=1.17a_0$, corresponding to two $(10\bar{1}2)$ inter-planar spacings, $2d_{(10\bar{1}2)}$. On the other hand, SDs exhibit **b**s inclined to the interface, so motion along the interface would require long-range diffusion of material to or from the defect. TDs and SDs cannot move into either of the crystals without creating an extended fault, and the latter can act as concentrators of an applied stress, thereby generating dipoles of glissile TDs at a critical stress [4].

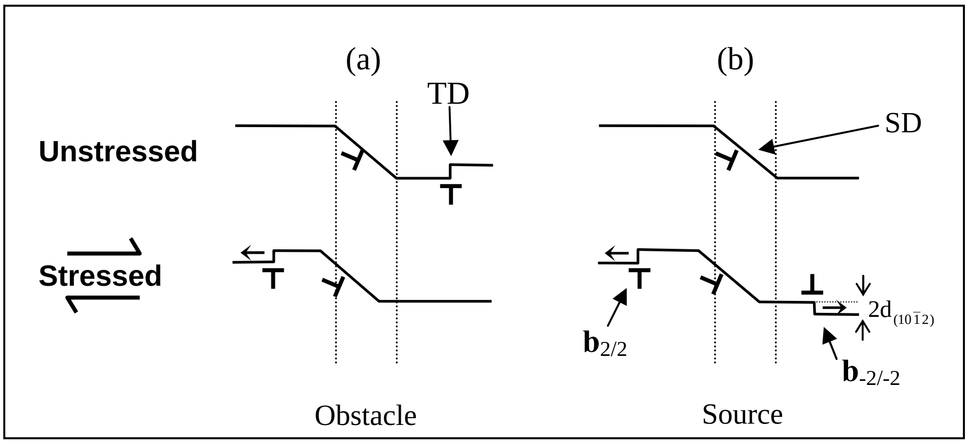

Figure 1: Schematic illustrations of (a) a TD passing through a SD obstacle, and (b) a SD acting as a source of TD dipoles. The sense of the applied stress and direction of the TD motion are indicated by arrows.

2. Atomic Scale Computer Simulations

Twin crystals studied in this paper were created with periodic boundary conditions in the plane of the boundary and fixed boundary conditions normal to it according to the procedure developed by Serra and Bacon [6] for bi-crystals. Crystals were strained incrementally by shifting the upper block of atoms by small steps, each being followed by full relaxation to minimize the potential energy. The atomic interactions were computed using a central force many-body potential of the Finnis-Sinclair type for HCP Zr ($c/a_0=1.5952$) derived by Ackland et al [7]. The $(10\bar{1}2)$ twin was created by welding two crystals, designated λ and μ for upper and lower crystals respectively, along the composition plane; each crystal contained a surface step of appropriate height for creation of the relevant disconnection. The surface step risers on both crystals were translation vectors, $\mathbf{t}(\lambda)$ and $\mathbf{t}(\mu)$, and the difference between these vectors expressed in the same frame equals $\mathbf{b}$ of the disconnection [8]. If the step heights on the λ and μ crystals are $pd_{(10\bar{1}2)}$ and $qd_{(10\bar{1}2)}$, respectively, the Burgers vector is denoted by $\mathbf{b}_{p/q}$; for example the TD for this twin is either $\mathbf{b}_{2/2}$ or $\mathbf{b}_{-2/-2}$ depending on the sign of $\mathbf{b}$ and h, as depicted in Fig. 1. The threshold shear stress at 0K for this defect to glide along the interface is 1.7 MPa. Glide of the $\mathbf{b}_{2/2}$ TD leftwards along the twin boundary results in migration of the boundary upwards by $2d_{(10\bar{1}2)}$; one complete sweep across the model causes the plastic displacement of the upper surface by $\mathbf{b}_{2/2}$.

To create a SD with $\mathbf{b}$ inclined to the twin boundary, the surface steps on the two crystals must have different heights. Fig. 2 shows the atomic configuration of a relaxed twinned crystal with a $\mathbf{b}_{-7/-8}$ disconnection, i.e. the boundary steps down by $7d_{(10\bar{1}2)}$ in the λ crystal and $8d_{(10\bar{1}2)}$ in the μ crystal, and the components of $\mathbf{b}_{-7/-8}$ are $0.14a_0$, $0.50a_0$ and $0.59a_0$ along $[10\bar{1}1]$, $[1\bar{2}10]$ and the boundary normal respectively. To study the TD source, shear stresses were applied to an isolated $\mathbf{b}_{-7/-8}$ SD as in Fig. 2. TDs with opposite signs, i.e. $\mathbf{b}_{2/2}$ and $\mathbf{b}_{-2/-2}$, were emitted and expanded outwards allowing the boundary to migrate upwards by $2d_{(10\bar{1}2)}$ for each pair created. Three images of the SD source at different strain stages are shown in Fig. 4, indicating the migration of the boundary and the associated lateral motion of the $\mathbf{b}_{-7/-8}$; only miscoordinated atoms are depicted in this figure. The threshold stress for this process at 0K is 100 MPa.

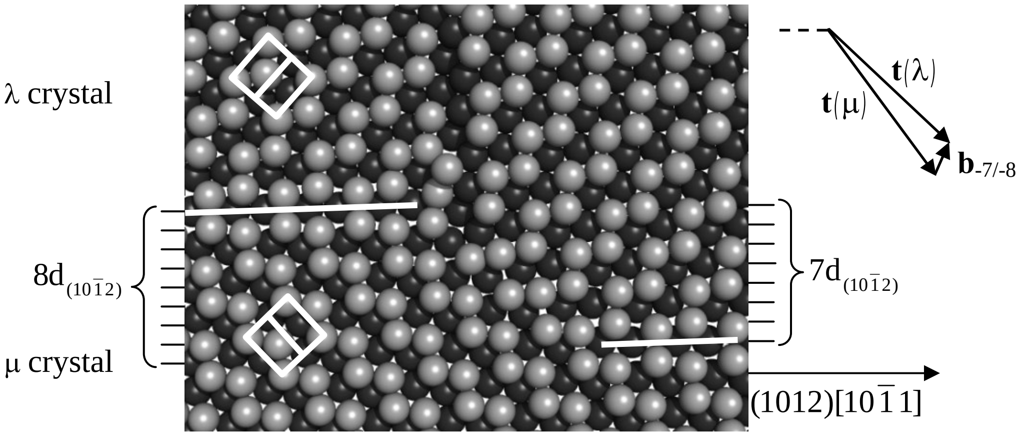

Figure 2: $[1\bar{2}10]$ projection of the $(10\bar{1}2)$ twin boundary with a sessile disconnection $\mathbf{b}_{-7/-8}$ superimposed; the boundary location and crystal unit cells are indicated in white.

To investigate the effectiveness of the $\mathbf{b}_{-7/-8}$ SD as an obstacle to the motion of a $\mathbf{b}_{2/2}$, Fig. 1(a), it was necessary to create such a pair in the absence of an applied stress. This was achieved by creating a meta-stable $\mathbf{b}_{-5/-6}$ SD which spontaneously decomposed into a $b_{-7/-8}$ + $b_{2/2}$ pair as shown in Fig. 3. Under an applied stress the TD started to move, passing through the SD and sweeping along the boundary; the threshold stress for this process at 0K is 27 MPa.

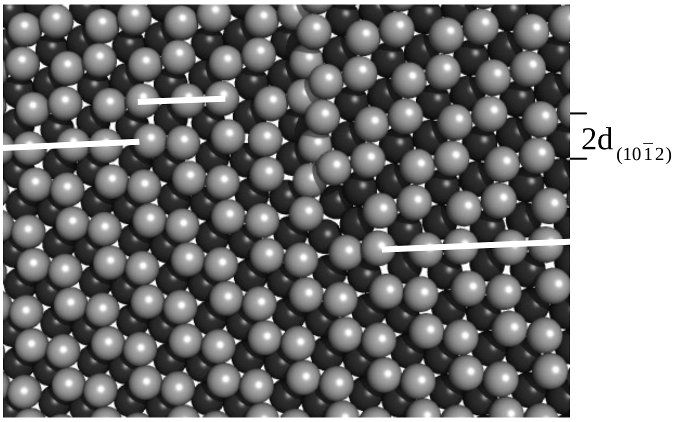

Figure 3: $[1\bar{2}10]$ projection of the $(10\bar{1}2)$ twin boundary showing a $\mathbf{b}_{-7/-8}$ SD with nearby $b_{2/2}$ TD.

3. Discussion and Conclusions

Atomic scale computer simulation is valuable for investigating the interfacial mechanisms of SDs acting as sources of TD dipoles and as obstacles to the motion of individual TDs. At 0K and using a strain increment of the order 10^{-5}, the threshold stress for source operation is 100 MPa, an applied shear stress of 27 MPa is necessary for a TD to traverse $b_{-7/-8}$ SDs, and the threshold stress required for glide of a TD along an obstacle-free twin boundary is 1.7 MPa, showing that SDs act as modest impediments to the glide of TDs and that considerably higher stresses are needed for nucleation of TD dipoles. It has been shown elsewhere [5] that both mechanisms in Fig. 1 are conservative. Consider the mechanism in Fig. 1(a); at first sight it might seem that the TD must climb up the riser of the SD, but, in fact, the diffusional flux needed for this is compensated by the lateral motion of the SD, as depicted schematically in Fig. 1(a) and seen dynamically in Fig. 4.

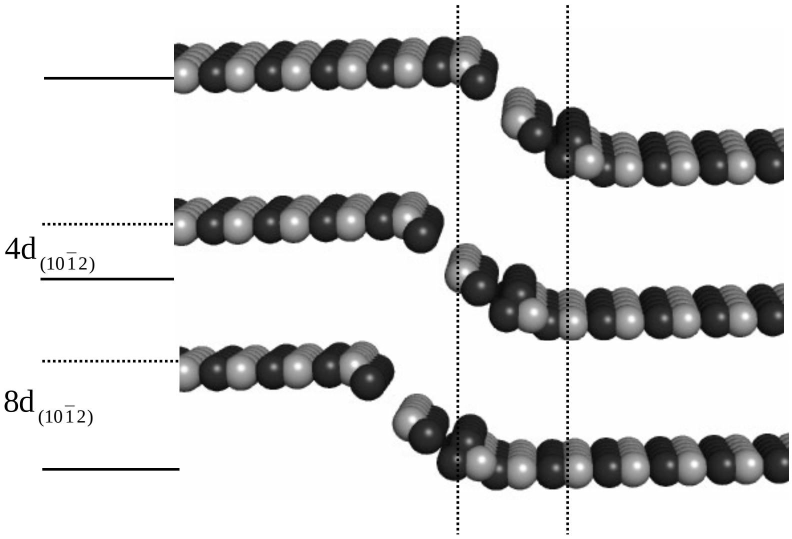

Figure 4: $[1\bar{2}10]$ projection of the $(10\bar{1}2)$ twin boundary showing sequential images of the interface region during operation of the $\mathbf{b}_{-7/-8}$ SD as a TD source; solid line at the left of the figure indicates the original position of the interface.

Further work is in progress using molecular dynamics to find the temperature dependence, asymmetry and strain-increment sensitivity of the threshold stresses. The motion of atoms at defect cores is also being tracked to gain insight into the fundamental aspects that determine these stresses.

Acknowledgements

H. A. Khater is grateful to the Egyptian Ministry of Higher Education for financial support.

References

[1] J. P. Hirth and R. C. Pond, Acta. Mater. **44**, 4749 (1996).
[2] G. C. Wealtherly, A. Perovic and V. Perovic, Phil. Mag. A **79,** 2071 (1999).
[3] A. Serra, D. J. Bacon and R. C. Pond, Metal. Mater. Trans. **33A**, 809 (2002).
[4] A. Serra and D. J. Bacon, Phil. Mag. A **73**, 333 (1996).
[5] R. C. Pond, A. Serra and D. J. Bacon, Acta. Mater. **47**, 1441 (1999).
[6] A. Serra and D. J. Bacon, Z. Metallkd. **95**, 242 (2004).
[7] G. J. Ackland, S. J. Wooding and D. J. Bacon, Phil. Mag. A **71,** 553 (1995).
[8] R. C. Pond, Dislocations in Solids, (ed. F. R. N. Nabarro) **8**, 1 (1989), Amsterdam, North-Holland.

Mesomechanical Simulation of Elastic Wave Propagation in Al_2O_3 Ceramics

Sascha Knell, **Martin Sauer**, **Klaus Thoma**

Fraunhofer Institute for High-Speed Dynamics, Ernst-Mach-Institute
Eckerstrasse 4, 79104 Freiburg, Germany
sascha.knell@emi.fraunhofer.de

ABSTRACT

In this work the influence of grain anisotropy of densely sintered alumina on the evolution of an elastic pressure wave is investigated. The analysis is conducted via a transient FEM simulation of an Al_2O_3 polycrystal which is generated using power diagram tessellation. Each grain is treated as an anisotropic single crystal exhibiting an arbitrary crystal orientation. The attained results show that grain anisotropy has a significant impact on shape and amplitude of a propagating plane wave. Depending on the grain orientation, pressure peaks occur which are usually located at the grain boundaries. Their magnitudes surpass the homogeneous pressure level of an isotropic comparison simulation by 10 %.

1. Introduction

A number of constitutive models exists which describe the material response, including failure, of ceramics under impulsive loads at the macro scale. These models are either phenomenologically or micromechanically motivated. They represent ceramics as homogeneous continua. In order to better motivate macroscopic models and at the same time get a deeper understanding of the physical mechanisms which govern the material response, ceramics have to be studied at the grain level. On this mesoscopic scale, the influence of grain structure inherent factors such as grain orientations, grain size distribution and grain or grain boundary strength can be studied. For example, Zavattieri et al. [1] presented transient, two dimensional simulations of an inclined flyer plate impact accounting for grain visco-plasticity and grain boundary failure. Zhang et al. [2] studied the influence of plasticity at the shocked equilibrium state of an artificially generated three-dimensional polycrystal.

The objective of this work, motivated by the references mentioned above, is the numerical investigation of the influence of arbitrarily orientated, anisotropic grains on the dynamic evolution of an elastic wave travelling through a three dimensional, artificially generated Al_2O_3 polycrystal. We were particularly interested in the stress distribution at the grain boundaries. Al_2O_3 was chosen as material due to its widespread applications and the existing firm database. The grain structure was created via power diagrams. The underlying method is described in detail by Kühn [3]. It provides the basis for a tetrahedral mesh that permits the usage of an explicit FEM code.

2. Methods

The material parameters used for the constitutive elasticity model employed for the Al_2O_3 grains, which exhibit a trigonal symmetry, are taken from the work of Duan et al. [4]. The moduli were calculated via first principle molecular dynamics by imposing small deformations on a virtual sample at different pressure levels. The corresponding values including the averaged bulk and shear modulus are given in Tab 1. In consequence of the method by which the data was derived, it was interpreted as tangent moduli in a pressure dependent hypoelastic rate formulation, Eqn 1, where $\boldsymbol{\sigma}^{\nabla J}$ is the Jaumann rate of stress, **C** the tensor of elastic tangent moduli, p the pressure and **D** the rate of deformation tensor.

$$\boldsymbol{\sigma}^{\nabla J} = \mathbf{C}(p) : \mathbf{D},\ \mathbf{C}(p) = \mathbf{C}_0 + p\,\mathbf{C}_1 \qquad (1)$$

Table 1 Pressure dependent elastic moduli of Al_2O_3 taken from [4].

	C_{11}	C_{33}	C_{44}	C_{12}	C_{13}	C_{14}	K	G
M [MPa]	501	502	157	161	125	-19	258	168
dM/dp	5.52	5.1	2.03	3.09	3.57	0.19	4.06	1.44

In accordance with the transient nature of the problem and the kind of constitutive relation an in-house FEM code following the updated Lagrange formulation with explicit time integration was chosen for the simulation. The polycrystal is discretized with 500000 isoparametric, first order tetrahedrons. A typical element side length is in the order of 80 nm.

3. Simulation Procedure

We present two simulations, one with arbitrarily orientated anisotropic-elastic grains and a second one with isotropic grains. By comparing the two simulations, the influence of the anisotropy can be quantified. The artificial grain structure used for the simulations exhibits a mean grain size of 1 µm, Fig 1. This value is typical for densely sintered alumina. The necessity to avoid the occurrence of very small elements currently results in non-smooth boundaries of the meshed structure. This issue will be addressed in future work. An elastic wave is imposed on the square base of the structure via a velocity boundary condition. The pulse has an effective period of 0.096 ns which is divided into three intervals of equal duration, a sine-shaped rise, a plateau with a magnitude of 200 m/s and a sine-shaped fall. Lateral movement of the sides of the volume is prevented in order to ensure the propagation of a plane wave.

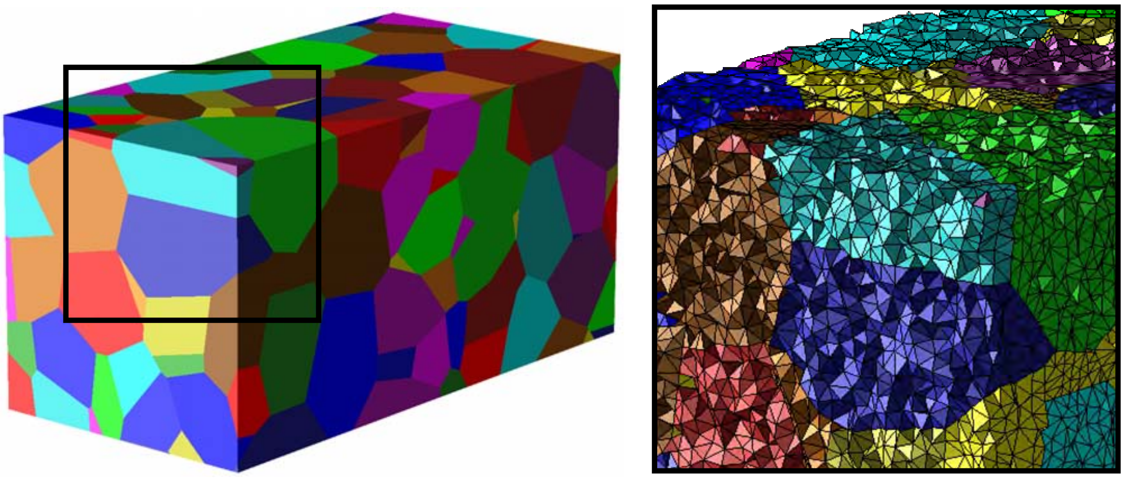

Figure 1 Left: Artificial grain structure generated via power diagram tessellation.
Right: Detail of the tetrahedral meshed structure.

4. Results and discussion

Fig 2 shows the pressure wave profiles at three different times for the isotropic and the anisotropic case. The section displayed is located half way between the top and bottom surface of the sample shown in Fig 1. The peak pressures which occurred during the passage of the wave in each element are displayed in Fig 3. Single grains and grain boundaries are clearly identifiable in the anisotropic case due to pressure jumps at the grain boundaries. In addition, both shape and magnitude of the wave signal change significantly in the anisotropic case. The peak pressures of the anisotropic case surpass the one of the isotropic variant at several points by at least 10 %.

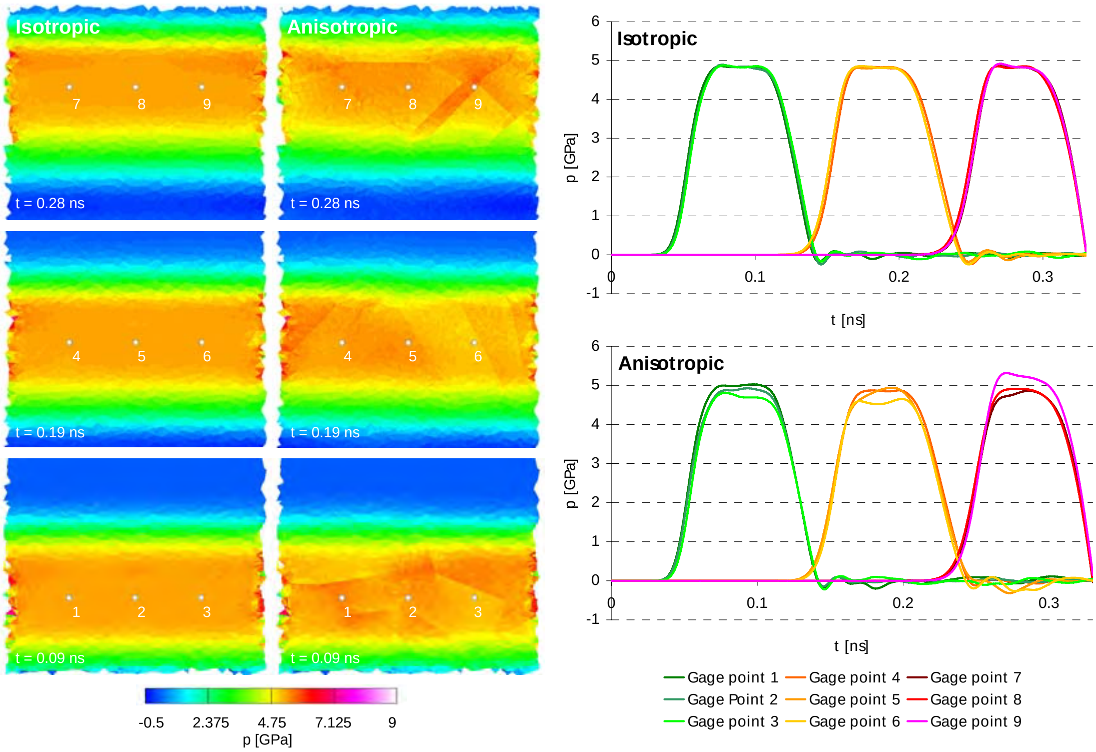

Figure 2 Left: Pressure contour plot sections for the isotropic and anisotropic case (section taken when the pressure wave passes the gage points).
Right: Pressure time signals taken at the gage points.

The phenomena responsible for wave profile alterations and pressure deviations are easily identified. Restraints build up due to the different directional compressibility of the grains. The alterations of wave shape and magnitude are only caused by direction dependant impedance differences of the grains. Taking into account the minor distinct anisotropy of the Al_2O_3 single crystal, the impact of the above mentioned mechanisms on the attained results is remarkable.

5. Conclusion

We conducted simulations of elastic wave propagation through an artificial, three dimensional Al_2O_3 polycrystal. The results show that even minor distinct grain anisotropy has a significant influence on the wave profile and the maximum pressure. This proves that for the investigation of the failure of ceramics on the grain scale, grain anisotropy has to be taken into account. Such investigations are within the scope of future work.

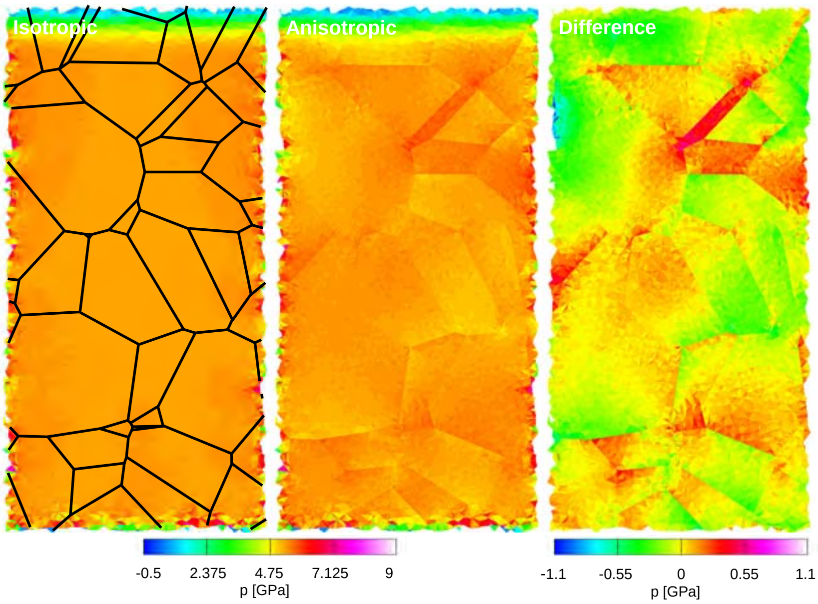

Figure 3 Peak pressure contour plots, from left to right: isotropic with overlaid grain boundaries, anisotropic and the difference between the two.

Acknowledgements

We thank Martin Kühn from EMI for the generation of the polycrystal meshes.

References

[1] P. D. Zavattieri, P. V. Raghuram, H. D. Espinosa. A computational model of ceramic microsrtructures subjected to multi-axial dynamic loading. Journal of the Mechanics and Physics of Solids 49, 2001, pp. 27-68.

[2] K. S. Zhang, M. S. Wu, R. Feng. Simulation of microplasticity-induced deformation in uniaxially straind ceramics by 3-D Voronoy polycrystal modeling. International Journal of Plasticity 21 (2005) 801-834.

[3] Martin Kühn. Optimierung von Power-Diagrammen zur Modellierung keramischer Mikrostructuren. Diplomarbeit, EMI-Bericht 15/05, Fraunhofer Institut für Kurzzeitdynamik & FU Hagen, 2005.

[4] Wenhui Duan, Bijaya B. Karki, and Renata M. Wentzcovitch. High-pressure elasticity of alumina studied by first principles. American Mineralogist, Volume 84, pages 1961-1966, 1999.

Irreversible Strain and Dammage in the Brittle Fracture Materials

N. Konchakova
Voronezh State University, University Sq. 1, 394006 Voronezh, Russia
e-mail kontchakova@yandex.ru

ABSTRACT

The present research is based on the notion of irreversible strain of solids due to shear localization and formation of real sliding surfaces. It is well established that compound composite materials, such as soils, rocks and brittle fracture materials, while under strain, form a quasi material, where plastic deformation is realized due to fragmentation of a solid into separate parts, their displacement along the sliding surfaces and rotation so as to originate a quasi-continuum. This concept is the key idea for the synthetic theory of strength and is developed in the present work.

1. **Introduction**

Mathematical simulating of rock and brittle fracture materials deformation results in the necessity to consider models with non-symmetric tensors, which, in its turn, gives a possibility to assess material internal mechanical relations and analytically describe peculiarities of the dynamic behaviour of compound media, observed in experiments [1].

The following researches [2 –3] analyze several well-known continuum models with regard for tensor non-symmetry, and obtained a general energy equation of a strained continuum with non-symmetric stress tensors. In the case of plane deformation, the energy equation takes the form:

$$\int_L \overline{\sigma}_n \cdot \overline{u}\, ds + \int_V \rho \overline{F} \cdot \overline{u}\, d\tau = \int_V \left\{ (\sigma_{ii}\varepsilon_{ii}) + (\tau_{xy} + \tau_{yx})\gamma_{xy} + \omega_z(\tau_{xy} - \tau_{yx}) \right\} d\tau \quad , \qquad (1)$$

where n is the external normal to Surface S (L is the track of this surface, while $z=const$); $\overline{\sigma}_n$ is the stress vector; $\overline{u}$ is the displacement; $\overline{F}$ corresponds to body forces; ρ is the density of the body forces; the point indicates the scalar product of the vectors;

$$\gamma_{xy} = \frac{1}{2}\varepsilon_{xy} = \frac{1}{2}\left(\frac{\partial v}{\partial x} + \frac{\partial u}{\partial y}\right), \quad \varepsilon_{xy} = \left(\frac{\partial v}{\partial x} + \frac{\partial u}{\partial y}\right); \qquad \omega_z = \frac{1}{2}\left(\frac{\partial v}{\partial x} - \frac{\partial u}{\partial y}\right).$$

The right part of the equality (1) represents potential energy of deformations. The possibility for such form of the energy equation is justified by the experimental data on non-symmetry of deformations [3-4], which is physically more natural and is more often observed in experiments than the effect of the stresses' non-symmetry. The introduced function ω_z is rotation of the continuum elements, while γ_{xy} describes the shear on the areas in question. It is well established [5] that under the same τ_{xy} and τ_{yx}, the values γ_{xy} and γ_{yx} may differ. This leads to the necessity to consider non-symmetry of the stress tensor in a mathematical model.

2. **Procedure and Numerical Metods**

In the case of an elastic-plastic problem for a continuum, having brittle fracture properties (in the study of rock behaviour near an excavation, in particular or the brittle fracture materials deformation), the stress field does not have singularities, while the strain field does. That is why in order to find a complete solution, it is appropriate to introduce the prefracture zone, adjoining on the inside to the elastic-plastic boundary and filling the plastic region. The stress distribution within this zone is the same as in the plastic region, and the strain distribution is derived from the compatibility condition and the fracture condition or the strength criterion. The mathematic simulator, allowing for analysis of material behaviour in such setting, is known as the Synthetic Theory of Strength. It was firstly introduced by E. Shemyakin, Academician of Russian Academy of Sciences (RAS), in his works [5-6].

The strength criterion under shear strains for continuums with non-symmetric tensors is defined by the second invariant of the strain tensor is constant [1]. In the case of problems with the symmetry in the direction of one of the axes, let us consider a plane deformation. The constancy of I_2 within the area in question (the prefracture zone) takes the form:

$$\left(\varepsilon_x - \varepsilon_y\right)^2 + 4\gamma_{xy}\gamma_{yx} = \text{const} \; .$$

Let us take the principal shear value $\Gamma = \Gamma_e$, corresponding to fragmentation of a solid into elementary parts by the sliding surfaces under strain, as the constant placed in the right part of the criterion. In the case of a brittle fracture, the fracture is connected with the appearance of shear strains. The diagram, determining the material behaviour is the diagram “maximum tangential stress – principal shear”, which has a so-called “descending leg” [5]. This diagram is derived from experiments on loading under conditions of a homogeneous simple shear and on compound loading (this situation, in particular, happens in a rock element), accomplished by a group of Russian scientists of the Siberian branch of RAS [5]. Γ is an independent criterion, describing irreversible strains. Therefore, the requirement for finite strains, after the stresses have achieved their critical values and the principal shear’s further growth in the region of irreversible strains (in the prefracture zone) is the constancy condition for Γ, which is the strength criterion under shear strains:

$$\left(\varepsilon_x - \varepsilon_y\right)^2 + \varepsilon_{xy}^2 = \Gamma_e^2 \; . \qquad (2)$$

In the case of plane deformation for a brittle fracture model, this criterion is introduced in [1]. It is necessary to note that in the case of a plane deformation, the second invariant of the strain tensor coincides with the second invariant of the tensor (deviator) in a tree-dimensional case.

While considering the possibilities for the apparatus of the 4-dimensional formalism, as an integrating approach of continuum mechanics, this statement, in particular, is the key idea to apply the 4-tensors to the model of the synthetic theory of strength and to generalize models in the case of an originally isotropic homogeneous material.

Let us consider a problem on rock deformation near an excavation of a circular cross-section. The stress field in the prefracture zone for the model calculated. The stress field outside the zone of irreversible strains is calculated with the apparatus of functions of a complex variable The prefracture zone, itself, covers the excavation contour completely and is restricted by the elastic-plastic boundary, which is an ellipse. We obtain the system of the first-order equations for the definition of the deformation in the prefracture zone [1, 3]:

$$\frac{\partial \tilde{\omega}}{\partial x} - \cos 2\psi \cdot \frac{\partial \psi}{\partial x} + \sin 2\psi \cdot \frac{\partial \psi}{\partial y} = 0 \; , \qquad \frac{\partial \tilde{\omega}}{\partial y} + \sin 2\psi \cdot \frac{\partial \psi}{\partial x} + \cos 2\psi \cdot \frac{\partial \psi}{\partial y} = 0 \qquad (3)$$

Computation of the displacements in the sliding lines nodes gives an opportunity to specify a real position of the continuum elements as a result of strain. Numeric solution of the problem on diaxonic non-symmetric extension of a solid near the excavation with a circular cross-section, is found for the case $\sigma_x^{\infty} = A = 3.0$, $\sigma_y^{\infty} = B = 2.5$., *p=0.1.* Here A and B are mutually perpendicular efforts, acting at infinity in the direction of the axes *Ox* and *Oy* accordingly, p is the pressure along the opening’s contour. Numeric modelling is accomplished by the method of characteristics. The lines of the strain field peculiarities in question reveal places of most slippage of structure elements along the real sliding lines and indicate the zones of the earliest fracture near the excavation.

Within the model in question, the problem on rock behaviour in a ring domain surrounding the excavation is additionally considered. In this case, special attention is drawn to the behaviour of the hoop stresses [6].

3. Results

The strain field can be computed with the help of either the theory of plastic flow, or with a model of the synthetic theory of strength. In the problem on stress and strain distribution in an eccentric pipe, it is extremely difficult to determine the displacement field for a model of the plastic flow theory. Knowledge of the prefracture zone geometry and introduction of the criterion (2) enable to calculate the displacement field and restore the evolution scheme of irreversible strain in the zone of irreversible strains, while the external actions are given.

Thus, the solution of the elastic-plastic problem with the help of the criterion (2), and, therefore, the system (3), enables to observe the evolution of material strain (rock) in terms of real sliding surfaces in the whole zone of irreversible strains, from its origin till the excavation contour, and to calculate the displacement field in the prefracture zone. The model of the synthetic theory of strength allows to compute the displacement field in the plastic region, reveal the displacement field singularities, observed in experiments on fracture of solids, rocks and brittle fracture materials. The concept of real sliding lines and their role in mechanics fully corresponds to experimental study of the material behaviour in mezomechanics, in particular, with appearance of fracture characteristic lines and formation of regular block structures in a homogeneous isotropic material

Acknowledgements

The author is sincerely grateful to Pr. P. Steinmann and Pr. Kienzler for fruitful discussion of the work results at a seminar of the Chair of Applied Mechanics of Keizerslautern Technical University and at the seminar on continuum mechanics at Bremen University.

The research is accomplished in the framework of the INTAS programme (Grant No. 05-109-4767).

References

1. E. Shemyakin, An brittle fracture of solid (a plate strain), News of Russian Academy of Science, Mechanics of Solid, N 2, pp. 145-150, 1997
2. N. Konchakova About the Construction of Models of Continuum with Non-Symmetrical Tensors, Moscow University Mechanics Bulletin, N 4, pp. 42-48, 2002.
3. N. Konchakova Some Mathematical Models of Deformation of Continuums with Non-Symmetrical Tensors, Modern Problems of Mechanics and Applied Mathematics (in Russian) – Voronezh, V. I, pp. 218-225, 2000.
4. P. Steinmann Application of Material Forces to Hyperelastostatic fracture mechanics. I. Continuum mechanical setting, Int.J. Solid& Structures 37, pp. 7371-7391, 2000.
5. E Shemyakin. Synthetic Theory of Strength. Part. I, Physical Mezomechanics. V 2, N 6. pp. 63-69, 1999.
6. E. Shemyakin An Brittle Fracture of Solid, Part II (about the shear strength of rock parts), Moscow University Mechanics Bulletin, N 3, pp. 76-81, 2003.
7. N. Konchakova The Analisis of Stress and Displacement near the Elastic-Plastic Boundary in Galin’s Problem, Moscow University Mechanics Bulletin, Vol. 59, N 2, pp. 44-51, 2004.

MULTISCALE MODELING OF FRACTURE IN FIBER-REINFORCED COMPOSITES

Javier LLorca[1], *Carlos González*[1], *Javier Segurado*[1]

[1]*Polytechnic University of Madrid, E. T. S. de Ingenieros de Caminos, Ciudad Universitaria, 28040 Madrid, Spain*

The fracture behavior of a SiC fiber-reinforced Ti matrix composite beam in presence of a notch perpendicular to the fibers is simulated by means of a multiscale model based on an embedded cell approach in three dimensions. Experimental observations demonstrate that damaged was localized in a very narrow zoned close to the notch root where severe plastic deformation of the Ti matrix occurred and was accompanied by fiber fracture and pull-out from the matrix. Following these observations, the representation of the material in front of the notch tip - where damage was going to be concentrated - included the actual fiber-matrix topology in the composite, while the remainder of the beam was represented by a linear thermo-elastic, transversally-isotropic homogeneous solid. The damage and fracture micromechanisms which controlled the onset of fracture (namely, plastic deformation of the matrix, brittle fiber fracture and fiber/matrix frictional sliding) were included in the behavior of the different phases and interfaces: fiber fracture was simulated through random fracture planes and special cohesive elements that allow to reproduce brittle fiber failure according to a Weibull statistics, while interface failure was also introduced using cohesive elements and standard contact algorithms. In addition, the corresponding micromechanical parameters (fiber strength and Weibull modulus, interfacial strength and fracture resistance, matrix flow stress within the composite) were independently measured.

The mechanical response of the beams in three-point bending was computed using the finite element method, and a new control technique was presented to obtain the whole load-displacement curve at a reasonable computational cost when progressive damage throughout the model (due to the simultaneous development of multiple cracks and frictional sliding) led to severe numerical instabilities. The simulation results were in good agreement with the experimental data at both the microscopic and the macroscopic level, demonstrating the potential of this approach to simulate the fracture behavior of complex, heterogeneous materials. Finally, further applications of these multiscale applications are briefly noted.

A formulation based on Fast Fourier Transforms for the calculation of the micromechanical behavior of plastically deformed 3-D polycrystals

Ricardo Lebensohn

Los Alamos National Laboratory, MST8 - MS G755, 87544, Los Alamos, United States of America

We present a numerical formulation based on Fast Fourier Transforms (FFT) to obtain the micromechanical fields in plastically deformed 3-D polycrystals. This formulation, originally developed as a fast algorithm to compute the linear and nonlinear response of composites using as input a digital image of their microstructures, has been adapted to deal with 3-D polycrystals deforming by dislocation glide. The FFT-based model provides an exact solution of the governing equations, has better performance than a Finite Element calculation for the same purpose and resolution, and can use voxel microstructure data as direct input. To illustrate the capabilities of this formulation we will show its predictions, together with comparisons with statistical models and experimental results, of effective properties, local fields, global and local texture development, and microstructure evolution in fcc and hcp materials.

Dislocation dynamics simulations in bcc metals

Ronan MADEC

CEA DPTA, BP12, 91680 Bruyeres-le-Chatel, France

Dislocation dynamics simulations have now reached a stage where they are able to tackle such problems as the formation of dislocation microstructures and forest hardening in single cristals deformed in the bulk. In principle, the effective connection between the mesoscopic and continuum approaches of plasticity is based on the knowledge of the interaction matrix between slip systems and of the dislocation mean free paths, from which a hardening matrix can be derived. The purpose of the present work is to establish this connection in the case of BCC metals, using a dislocation dynamics simulation that will be briefly described. Emphasis will be put on the determination of the interaction matrix in the high temperature regime, above the so-called „athermal temperature“ at which lattice friction vanishes. Results on dislocation mean free paths as a function of the type of obstacles to dislocation motion will also be discussed.

Selected Examples of Cellular Automata - Finite Element Modelling in Material Processing

Jerzy Gawąd[1], Piotr Macioł[1], Łukasz Madej[1], Maciej Pietrzyk[1]

Affiliations: [1]Interdisciplinary Centre for Materials Modelling, AGH University of Science and Technology, Faculty of Metals Engineering and Industrial Computer Science, al. Mickiewicza 30, 30-059 Krakow, jgawad@metal.agh.edu.pl, pmaciol@metal.agh.edu.pl, lmadej@metal.agh.edu.pl, pietrzyk@metal.agh.edu.pl

ABSTRACT

Finite Elements (FE) method is the commonly used method for macro scale modelling of material behaviour in metal processing. Application of the FEM to the microscale phenomena leads to numerous difficulties due to discontinuous nature of these processes. On the other hand, the Cellular Automata (CA) method is widely applied to simulate the behaviour of discontinuous materials at the microscale level. This work is a study of possibilities given by coupling FE with CA. A brief description of the coupled Cellular Automata – Finite Element (CAFE) multiscale models and selected examples of application are presented in the paper. The difficulties arising in practical CAFE application are discussed. The models developed for prediction of microstructure evolution in metal possessing (i.e. metal forming, thixoforming, heat treatment, etc.) and strain localization phenomena during deformation are shown. The capabilities of accounting for stochastic phenomena occurring in the discontinuous materials in microscale and its influence on macroscale behaviour are presented, as well.

1. Introduction

Multiscale behaviour can be found in almost every aspect of material processing. Combination of macroscale (e.g. shape), mesoscale (e.g. phase distribution) and microscale (e.g. grain distribution) phenomena results in final product properties. Suitable solutions for these problems can be obtained from multiscale modelling, dealing with interactions between phenomena appearing in different scales in the material subjected to the deformation.

Numerical methods based on assumptions of domain continuity and deterministic character of phenomena occurring in materials is commonly used in modelling of thermo-mechanical processes. The finite elements method is the basis of these solutions [1,2]. Over the years of intensive development, numerous improvements have been proposed to include into numerical simulations for example microstructure evolution model based on differential equations [3]. In consequence, a conventional multi scale model has been created. However this approach has several limitations, i.e. only continuous domains can be taken into account during simulation.

That is the reason why an alternative computational method, capable of overcoming those limiting factors, has been sought after for several years. The coupled Cellular Automata– Finite Element multi scale model is one of the possible solutions. The main advantage of the CAFE approach is a complete separation of the material behaviour from the structural response. Such an approach creates new possibilities for more accurate description of material behaviour subjected to the deformation.

The objective of this work is to show immense capabilities of the developed CAFE approach to model thermo-mechanical operations. Particular attention is put on solving various difficulties arising during creation of the CAFE models.

2. Selected problems of coupling CA and FE methods

The CAFE methodology has been extensively studied over last several years. The main assumptions and results obtained from the developed models are described in [4]. More detailed discussion of the most significant features related with combining two different computational methods are described below. CAFE theory is based on automata spaces, bound with the finite element integration points. Creation of the relatively simple CAFE model is not an issue, because it is easy to fulfil all the assumptions of the method. However, in more complicated simulations of metal processing operations, the model has to face difficulties mainly associated with information exchange between scales. For example, major obstacles have already become visible, when remeshing appears in the FE mesh during simulation of the strain localization in material. As a consequence, there is a change in the number of the mesh nodes, as well as in the number of Gauss integration points. Therefore, a problem with attaching the CA spaces to the FE nodes appear (Fig.1). To solve this problem an alternative set of points is introduced in the sample area [5]. In this case number of CA spaces is constant during the deformation process. This approach enables remeshing process and a change in the nodes number in the FE mesh. Information exchange between FE and CA points in the macro scale is performed using interpolation technique from the Smoothed Particle Hydrodynamic (SPH) method.

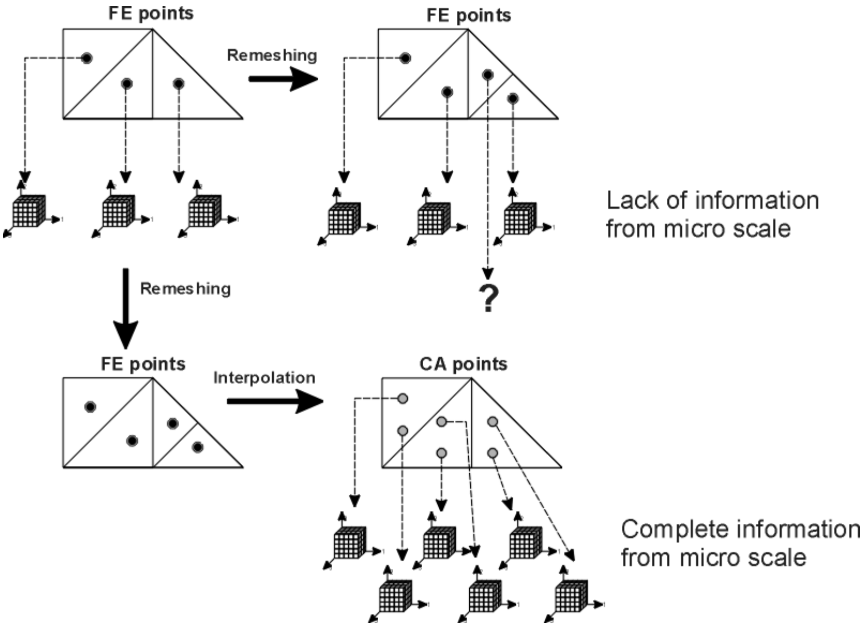

Figure 1 Illustration of the remeshing problem in the multi scale CAFE approach.

Another issue is connected with diverse material properties among the FE mesh. The problem occurs for example in hot axisymmetrical compression tests when the dynamic recrystallization (DRX) is accounted for. The CA simulation of microstructure evolution implements the constitutive model of the flow stress σ_f, which is crucial for the FE solution and depends mainly on temperature and strain rate fields. Every finite element in the mesh is exclusively connected with separate CA space, which acts as a model of the microstructure evolution. Therefore, different microstructure images can be attached to different regions of the material (Fig.2). In consequence, the material description, such as distribution of grain size or grain orientation, can vary among the simulated sample. While the CA model of DRX is sensitive to the initial microstructure characteristic [6], the response of the model for similar inputs (i.e. temperature and strain rate) can be dissimilar, because of differences in the state of microstructure.

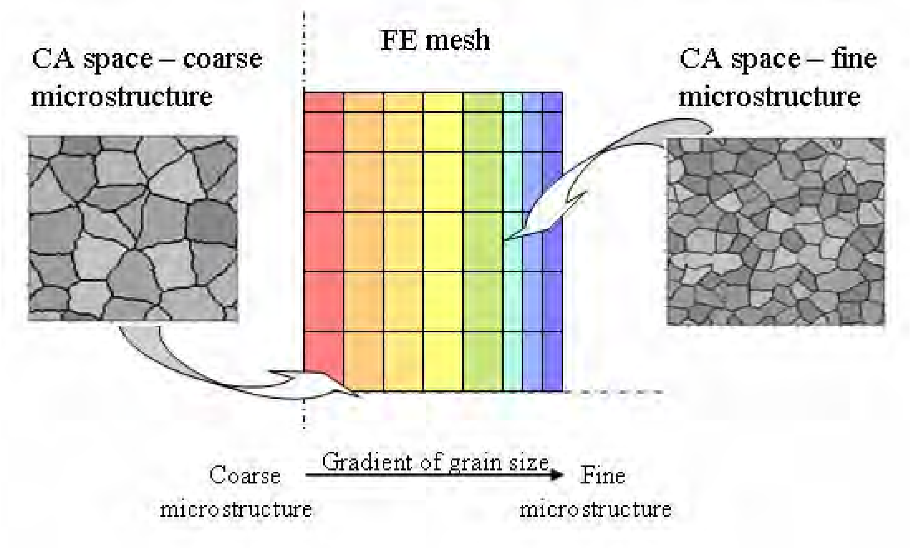

Figure 2. Gradient of the microstructure CA images along the FE mesh.

Due to nonlinearity of mechanical equations system, the FE solver makes use of the Newton-Raphson (N-R) procedure, which requires several trial steps in each time increment and calculations of flow stress, which are based on the CA simulation (Fig.3). Since the temperature and the strain rate are given as constants in the N-R search, recalculation of CA in trial steps can be replaced with the interpolation between the two most recent results of the CA method.

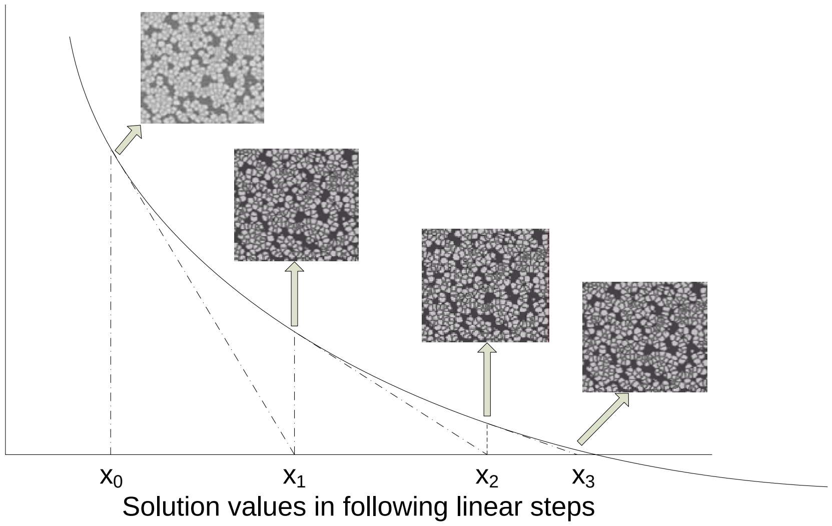

Figure 3 Different solutions in each ”trial“ step of Newton-Raphson solution

An interesting case of CA and FE combination appears also in numerical analysis of thixoforming. CFD simulations are usually based on Eulerian or Arbitrary Lagrangian-Eulerian (ALE) material representation and nonlinear solution [7]. Problem with attaching nodes and integration points to a proper CA space is similar to previously described problem with remeshing operation and in same cases it can be solved with similar methods. The other way is to find a mesh, where one FE node in the following time steps represents not “the idem” CA space, but “the same” CA space.

As it had been mentioned, nonlinearity of the solution constrains “trial” steps. Material data have to be provided for each solution. When material parameters are strongly dependent on material state, it is necessary to compute these data for each linear system independently. In the CAFE methodology, material state is computed basing on the CA simulation, complying material history. Combination of multiply linear solution and history dependent CA simulations extorts “reversibility” of the CA simulations, with one “trial” solution for each linear system solution.

3. Summary

Presented CAFE method is a promising solution for modelling of different multiscale phenomena, in both solids and fluids. In the cases, when nonlinearity and mesh deformation are negligible, employing of the CAFE method is rather simple. However, as it was presented, there are some significant obstacles that have to be overcome for more sophisticated examples. To solve these problems the trial CA solutions, or the mapping between CA and FE spaces, are introduced. However, it leads to increase of computing time and further efforts have to be made to reduce the computational complexity. Some FE simulations of industrial problems are still extremely difficult to be combined with the CA method, especially when full Eulerian or ALE solutions are used. The further works will focus mainly on up- and downlinking between CA and FE level methods, including mapping of the results between incompatible CA and FE spaces, as well as Eulerian FE meshes integration with CA spaces.

Acknowledgements

This work is supported by the MNiSW, project no. 11.11.110.643.

References

[1] Zienkiewicz, O.C. and Taylor, R.L., 1989: *The Finite Element Method*, McGraw Hill.

[2] Pietrzyk, M., 2000: Finite Element Simulation of Large Plastic Deformation, *J. Mat. Proc. Techn.*, **106**, 223-229.

[3] Pietrzyk, M., 1990: Finite Element Based Model of Structure Development in the Hot Rolling Process, *Steel Res.*, **61**, 603-607.

[4] Madej L., Hodgson P.D., Pietrzyk M., 2006 (in press): Multi scale rheological model for discontinuous phenomena in materials under deformation conditions, *Comp. Mat. Sci.*.

[5] Madej, L., Hodgson, P.D., Pietrzyk, M., 2005: The Remeshing Problem in the Multi Scale Strain Localization CAFE Approach, *Lecture Series on Computer and Computational Sciences*, **4**, 365-368.

[6] Gawąd, J., Madej, L., Szeliga, D., Pietrzyk, M., 2005: Cellular Automaton Technique as a Tool for a Complex Analysis of the Microstructure Evolution and Rheological Behaviour, *Acta Met. Slov.*, **11**, 45-53.

[7] Gawąd, J., Macioł, P., Pietrzyk, M., 2005: Multiscale Modeling of Microstructure and Macroscopic Properties in Thixoforming Process Using Cellular Automation Technique, *Arch. Metal. Mater.*, **50**, 549-562.

Atomistic Study of Moving Dislocations in Disordered Alloys

Jaime Marian

Lawrence Livermore National Laboratory, 7000 East Avenue, L-367, 94551 Livermore, United States of America

Using atomistic simulations of dislocation motion in Ni and Ni-Au alloys we report a detailed study of the mobility function as a function of stress, temperature and alloy composition. We analyze the results in terms of analytic models of phonon radiation and their selection rules for phonon excitation. We find a remarkable agreement between the location of the cusps in the $sigma$-v relation and the velocity of waves propagating in the direction of dislocation motion. We identify

and characterize three regimes of dissipation whose boundaries are essentially determined by the direction of motion of the dislocation, rather than by its screw or edge character.

Multiscale analysis of gas transport properties in fruits by means of microscale material models

**H.K. Mebatsion[1*], P. Verboven[1], Q.T. Ho[1], B.E. Verlinden[2], F. Mendoza[1], T.A. Nguyen[1],
B.M. Nicolaï[1,2]**

**[1]BIOSYST-MeBioS, Katholieke Universiteit Leuven, W. De Croylaan 42, B-3001
Leuven, Belgium, *E-mail: Hibru.Mebatsion@biw.kuleuven.be**
**[2] Flanders Centre of Postharvest Technology, W. De Croylaan 42, B-3001 Leuven,
Belgium**

ABSTRACT

Mass transfer of oxygen, carbon dioxide and water in apple and pear fruit is vital for fruit quality during and after storage. Apparent material parameters (e.g., gas and moisture diffusivity) that are measured incorporate both actual physical properties and the effect of the microscale geometry of the tissue. However, this relationship is not understood well to date. A multiscale paradigm is required to bridge the knowledge gap. Quantitative characterization of the structure at the cellular and the sub cellular scale is an essential part to develop models at the microscale that can be used to predict apparent material properties. This paper presents an ellipse tessellation algorithm to generate a 2D geometrical model of the microstructure of pear tissue. The model tissue geometry was generated from the fitted-ellipses, which were truncated when neighbouring areas overlap. As a result, a virtual microstructure consisting of truncated ellipses fills up the entire space with the same number of cells as that of microscopic images and with similar area, orientation and aspect ratio distributions. Statistical analysis showed that the virtual geometry generated with this approach yields spatially equivalent geometries to that of real fruit microstructures. Compared to the more common algorithm of Voronoi tessellation, ellipse tesselation was superior for generating the microstructure of fruit tissues. The paper further demonstrates that the generated tissue models can be readily exported into a finite element environment via interfacing codes to perform *in silico* experiments for estimating apparent gas diffusivities in comparison with measured values, and investigating their relation with fruit microstructure.

Keyword : ellipse tesselation, microstructure, finite element analysis, diffusion, food quality

1. Introduction

Materials are dual in nature; they are continuous when viewed at large scales and discrete when viewed at atomic scale. In understanding the interdependence between these scales, multiscale material modelling approach is crucial. Microstructures are transitional scales from atomic to macroscale. As a result, modelling microstructure becomes a prerequisite for understanding the transitional theoretical frameworks and modelling techniques to bridge the knowledge gap between length scale extremes [5]. During the past decades, several types of Voronoi based models have been used to represent microstructures of different materials such as aggregates of grains in polycrystals [10], composite materials [6], ceramic microstructures [3] and fruit microstructure [8]. The Poisson Voronoi diagrams (PVDs) have been extensively used and studied by different authors [7, 8]. [8] generated Poisson Voronoi diagrams having similar statistical properties (area, orientation and aspect ratio) as that of apple parenchyma microstructures. However, the spatial statistics of the real cells and the representative PVDs were proved different [9]. As a result, generation of statistically and spatially equivalent geometric models remained unsolved.

2. Materials and methods

The study was based on images of fruit cellular structures obtained from light microscopy. Sample preparation and image acquisition procedures outlined by [8] were followed. Samples from Conference pear parenchyma tissues were used. The geometrical characteristics of cells were estimated using moment calculations and moment based ellipse-fitting algorithms outlined by [8].

Microscopic fruit cell sections are elliptical (aspect ratio greater than one) [8, 12]. The conic sections fitting to scattered data procedure [5] generates the best-fit ellipse for the given set of points on the natural boundary of microscopic images. The model tissue geometry was generated from the ellipses, which were truncated when neighbouring areas overlap. By doing so, as many truncated ellipses as there are cellular images were generated filling the entire cellular space (for details refer to [9]).

The spatial analysis of the microscopic and the virtual tissues were performed by expressing spatial arrangements in terms of their location with respect to one another by means of a "*weighting function*" [1,11]. In this study, the weighting function was defined as the inverse of the distance between the geometric centres (centroids) of two cellular regions. *Moran's I*, local indicators of spatial association (LISA) and *Geary's C* tests were used to test the spatial variability of the microscopic image and its virtual counterparts. For details of the spatial tests of the microscopic and the virtual tissues, refer to [9]. From the individual *Moran's I* values and that of the white random field a hypothesis of spatial significance can also be tested [9].

3. Results and discussion

Fig. 1 shows Conference pear microscopic image and its equivalent ellipse tessellation virtual tissue respectively. The statistical comparison between area distribution of microscopic images and virtual tissues are presented in Fig. 2. There was a good agreement the microscopic image and the virtual tissue for the statistical distribution of the geometrical parameters (Fig. 2a) as well as for their spatial relationship (Fig. 2.b, c &d). The statistical *Kolmogorov-Smirnov* test proved that area, orientation and aspect ratio distributions of the micrograph and the virtual tissue were equal at 5% level of significance.

The spatial comparison using *Moran's I* tests also showed that the virtual tissue was a good approximation of the real microscopic image. *The Moran's I* values of the microscopic image and the ellipse tessellated virtual tissue were 0.0150 and 0.0136, respectively. The Moran's I values show the presence of positive spatial association (compared to -0.0156 for random white field). Concerning the *Z* scale of the microscopic image and the ellipse tesselation, there was no enough evidence to reject the null hypothesis of no spatial correlation (with Z=1.2930 and 1.2367 which are less than $Z_{\alpha/2}$ (1.96) or with p-values of 0.1986 and 0.2140 which are greater than 0.05). The LISA test clearly shows the presence of comparable trend in local spatial associations between microscopic images and ellipse tessellated counterparts

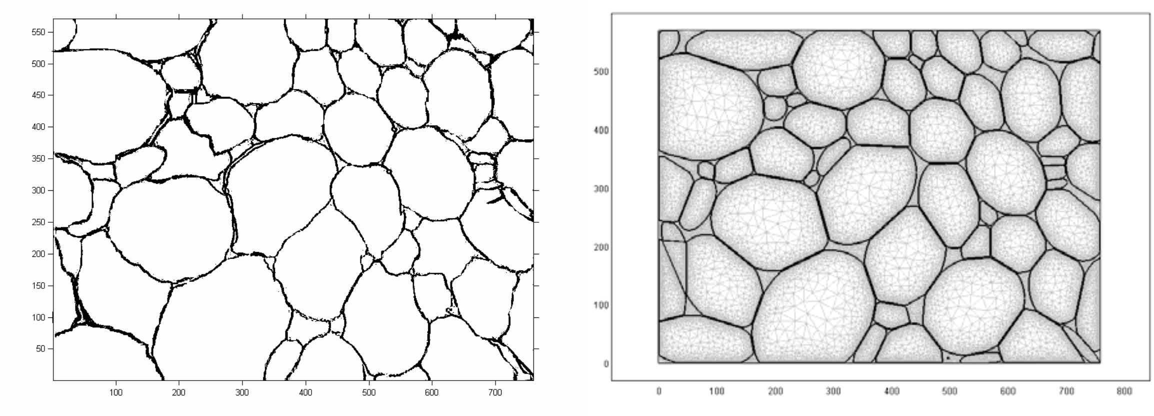

(a) (b)

Figure 1: Micrograph and ellipse tessellated virtual Conference pear parenchyma tissue. (a) micrograph; (b) meshed virtual tissue in Femlab environment.

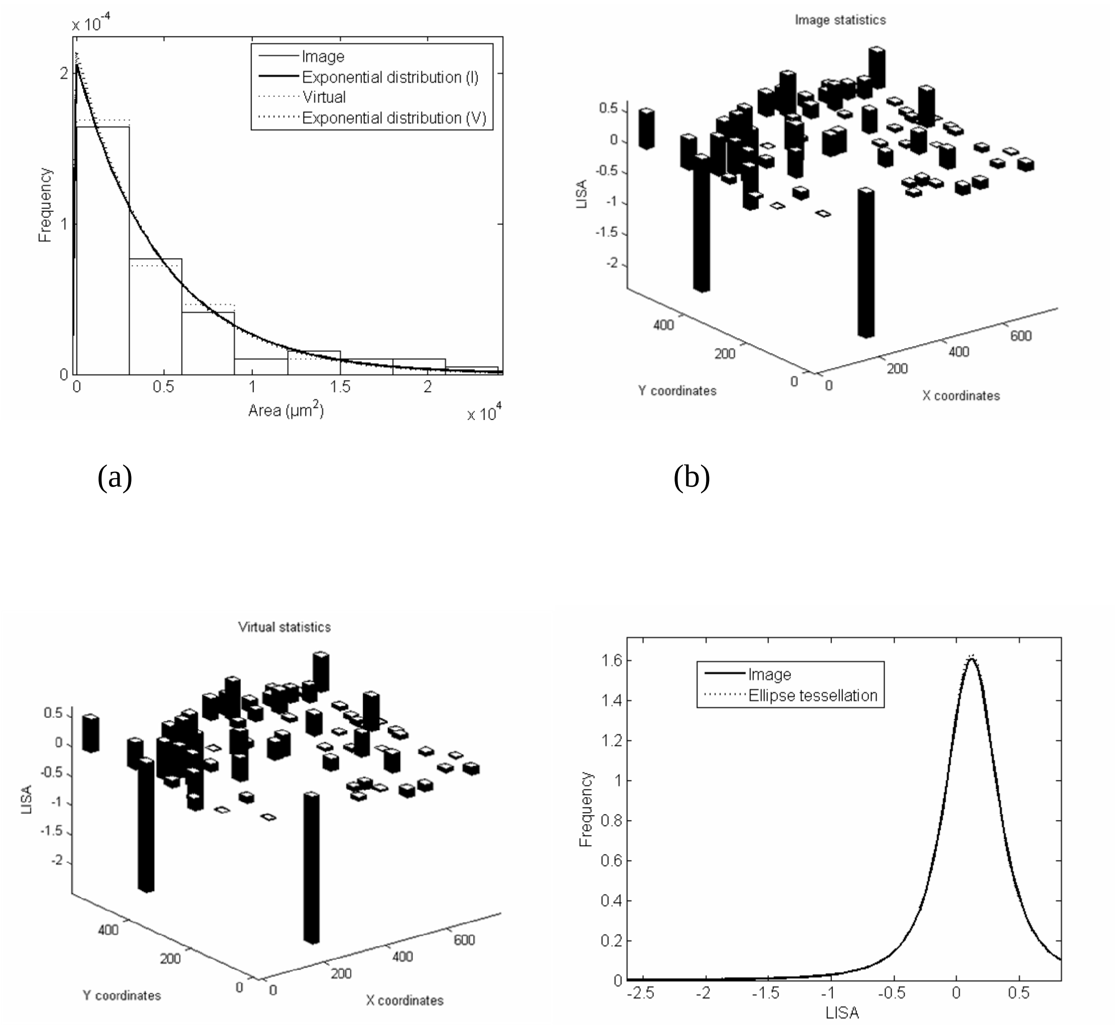

(a) (b)

(c) (d)

Figure 2. Area and LISA distributions of the micrograph and its equivalent virtual tissue. (a) area distribution; (b) LISA of the microscopic image; (c) LISA of the virtual tissue; (d) LISA frequency distributions

4. Conclusion

A novel ellipse tesselation algorithm for generating geometrically and spatially equivalent virtual tissues microscopic fruit tissues was developed. These virtual tissues could be exported in a finite element environment (such as Femlab) via interfacing Matlab code to be used in multiscale modelling of gas and moisture transport in fruits. Compared to the more common algorithm of Voronoi diagrams, both the centroid based Voronoi diagrams (CVDs) and the Poisson Voronoi diagrams (PVDs), ellipse tesselation was superior for generating the microstructure of tissue. The difficulty of generating virtual tissues for regular microscopic fruit tissues (such as onion) and tissues with large cells surrounded by smaller ones or vice versa was overcome by our new tessellation algorithm.

Such microstructural model avoids a tiresome classical continuum modelling approach where transfer properties that appear in the macroscopic transport equation are determined experimentally. As such, the heterogeneous properties of tissue and complex microstructural structures are rather recognized and separate model parameters and boundary conditions are defined to perform *in silico* experiments. This leads to a better understanding of the physics of the process.

Acknowledgement

Financial support by the Flanders Fund for Scientific Research (FWO-Vlaanderen) (project G.0200.02) and the K.U.Leuven (project IDO/00/008 and OT 04/31, IRO PhD scholarship for Q.T. Ho and T.A. Nguyen) are gratefully acknowledged. Pieter Verboven is a postdoctoral researcher of the Flemish Fund for Scientific Research (FWO-Vlaanderen).

References

[1] Brown, M. A., Economic Geography. 58(3), 247-261 (1982).
[2] Cliff, A.D.; Ord, J.K., Spatial processes: Models & applications. (London, UK, 1981).
[3] Espinosa, H.D.; Zavattieri, P., Amer. Inst. Physics. pp 333-338 (2000).
[4] Fitzgibbon, A.; Pilu, M.; Fisher, R. B., IEEE Trans. Pattern Anal. Mach. Intel. 21(5), 476-480 (1999).
[5] Ghoniem, N.M., Busso, E.P., Kioussis, N., Haung, H., Philosophical magazine, 83(31-34), 3475-3528 (2003).
[6] Ingraffea, A.R.; Iesulauro, E.; Dodhia, K.; Wawrzynek, P.A., Fifth World Congress on Computational Mechanics, Vienna, Austria (2002).
[7] Mattea, M.; Urbicain, M.J.; Rotstein, E., Chem. Eng. Sci. 44, 2853-2859 (1989).
[8] Mebatsion, H. K.; Verboven, P.; Verlinden, B. E.; Ho, Q.T.; Nguyen, T.A.; Nicolaï, B. M., Comput. Electron. Agric. 52, 36-48 (2006).
[9] Mebatsion, H.K., Verboven, P., Ho, Q.T., Mendoza, F., Verlinden, B., Nguyen, T.A., Nicolaï, B.M., CMES-Comp. Model. Eng. Sci. (in press).
[10] Nygards, M.; Gudmundson, P., Material Science and Eng. 325, 435-443 (2002).
[11] Odland, J. Spatial Autocorrelation. Scientific geography series (Sage publication, USA, 1988).
[12] Schotsmans, W., PhD thesis (Katholieke Universiteit Leuven, Leuven, Belgium, 186 p., 2003)

The effect of Titanium content on the Microstructure and Wear Properties of Fe-TiC Composite

Kambiz Mehrabi[1], *E. Tohidloo,*[2]*, M.R. Rahimipour*[3]

[1]*University of Leoben, Physical Metallurgy & Materials Testing, Salzlände 14/8/4, Franz Josef Straße 18, A-8700 Leoben, Austria*

[2]*Materials Science and Engineering Group, University of Sistan & Baloochestan, Zahedan,, Iran*

[3]*Department of Ceramic, Materials and Energy Research Center, Tehran, Iran*

In this work ferrotic composites were synthesized by the method of In-situ. The effect of Titanium content on microstructure and wear properties of this composites were investigated. The In-situ melting of cast iron, ferrotitanium and commercial pure iron in high frequency induction furnace caused reaction between carbon and titanium which produced titanium carbide particles within the melt. Four specimens with 2.5 wt.% carbon and containing 4,6,8 and 10 wt.% titanium were synthesized. The specimens were studied by using x-ray diffraction (XRD) , scanning electron microscope (SEM) equipped with EDX, image analyzer , optical microscope (OM), wear resistance , macro and micro- hardness testers.

As a result, the matrix microstructure and the amount, shape, size and distribution of TiC particles can be modified by controlling the chemical composition. It is found that an increase in the amount of TiC particle will result in an increase of hardness and the wear resistance.

Metallurgical Characteristics of ESR Processing in Recovery of C300 Maraging Steel Scraps

Kambiz Mehrabi[1], *M.R. Rahimipour*[2]

[1]*University of Leoben, Physical Metallurgy & Materials Testing, Salzlände 14/8/4, Franz Josef Straße 18, A-8700, Leoben, Austria*

[2]*Department of Ceramic, Materials and Energy Research Center, Tehran, Iran*

Maraging steels categorize as a group of martensitic steels possessing ultra high strength along with good fracture toughness. They are highly alloyed, generally contain Co, Mo, Ti and have very low levels of carbon and other impurities. Maraging steels are highly expensive because of costly alloying element contents such as Ni and Co. Reduction of alloy cost has been the subject of many researches.

In this research, C300 maraging steel scraps were recovered to C350 maraging steel by Electroslag Remelting (ESR) method. Less sensibility to primary ingot, desirable specified reactions and economical aspects are some of the benefits of this process.

For the Present investigation some specimens were prepared with various slag compositions. Volume fraction, density and size distribution of inclusions in the ingots and the electrode were determined in a quantimet image analyzer. These results were supplemented by spectrophotometer and SEM equipped with EDX. Mechanical properties of specimens in the heat-treated and aged conditions were assessed and compared with standard Properties of C350 maraging steel.

The present results confirm that recovery of maraging steels by ESR method is successful and mechanical Properties are according to standard.

Relating Ab Initio Mechanical Behavior of Intergranular Glassy Films in β-Si3N4 to Continuum Scales

Anil Misra[1], *Jun Cheng*[2], *Wai-Yim Ching*[2], *Lizhi Ouyang*[3]

[1]*Department of Civil and Mechanical Engineering, University of Missouri-Kansas City, 13857 Pembroke Drive, KS 66224 Leawood, USA*

[2]*Department of Physics, University of Missouri- Kansas City, 350H Flarsheim Hall, 5100 Rockhill Road, 64110 Kansas City, USA*

[3]*Department of Physics and Mathematics, Tennessee State University, 3500 John A. Merritt Blvd., 37221 Nashville, USA*

Nanometer thin intergranular glassy films (IGFs) form in polycrystalline ceramics during sintering at high temperatures. The structure and properties of these IGFs are significantly changed by doping with rare earth elements. We have performed highly accurate large-scale ab initio calculations of the mechanical properties of both undoped and Yittria doped (Y-IGF) model, shown in Fig. 1, by theoretical uniaxial tensile experiments [1]. For example, uniaxial strain was applied in the x-direction in small increments, while the y- and z-dimensions of the model were kept constant such that the strain components were $\varepsilon 11 \neq 0$, while $\varepsilon 22 = \varepsilon 33 = 0$. Similar theoretical experiments have been performed by loading in the other two directions. At each strain, all atoms in the model were fully relaxed using Vienna Ab initio Simulation Package VASP [2] until the residual force on each atom was reduced to less than 0.01 eV/Å. The relaxed model at a given strain serves as the starting position for the next increment of strain before the model is fully relaxed again. This process is carried on until the total energy (TE) and stress data show that the "sample" is fully fractured. Fig. 2 shows the stress components σ11, σ22, and σ33 and the increase in TE as a function of applied strain ε11. Interesting differences are seen between the stress-strain response of undoped and Y-doped models. For the undoped model, the lateral stresses σ22 and σ33 show very little increase in the first few load steps which correspond to the initial linear portion of the σ11-ε11 curve. This stress-strain behavior indicates that the initial atomic structure of the IGF is such that there is negligible coupling between the x- and the y-z directions. However, once the σ11-ε11 behavior becomes non-linear the lateral stresses increase, indicating that the atomic structure evolves with loading [1].

To relate the ab initio calculations to the continuum scales we analyze the atomic-scale deformation field under this uniaxial loading [1]. Fig. 3 shows the local strain field ε11, calculated for a 4.0 Å radius and the superimposed deformed ball and stick model. The local strain field is plotted using a color scheme with the saturation limit set at ±4% strain which is the value for complete fracture (see Fig. 2). We note that the applied strain in the x-direction is mostly accommodated by the IGF part of the model and the crystalline part experiences almost negligible strain. As the overall strain on the sample is incrementally increased, the local strain field evolves such that locations proximal to the softer spots, like that circled in red, attract higher strains. As the load progresses, the strain concentration spots tend to coalesce and eventually form a persistent strain localization zone across the IGF as seen in Figure 4(d) at the strain of 2.7% corresponding to the peak stress. The deformation pattern obtained through ab initio calculations indicates that it is possible to construct discrete grain-scale models that may be used to bridge these calculations to the continuum scale as depicted in Fig. 4.

References:

1. J. Chen, L. Ouyang, P. Rulis, A. Misra, W. Y. Ching, Phys. Rev. Lett. (in print).
2. G. Kresse, J. Hafner, Phys. Rev. B, 47, 558 (1993); G. Kresse, J. Furthmuller, Comput. Mat. Sci., 6, 15 (1996).

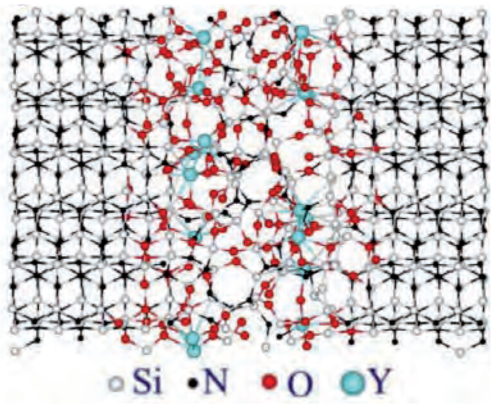

Fig. 1. The ball and stick model of the relaxed Y-IGF between β-Si_3N_4 crystal layers with Y ions near the interfacial region.

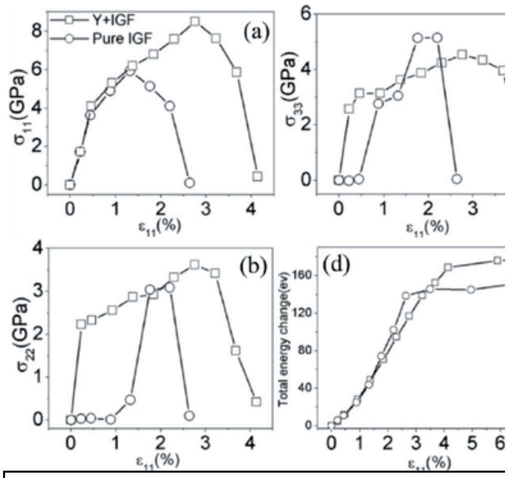

Fig. 2. Stress-strain relationship of the pure an
Y-doped IGF models.

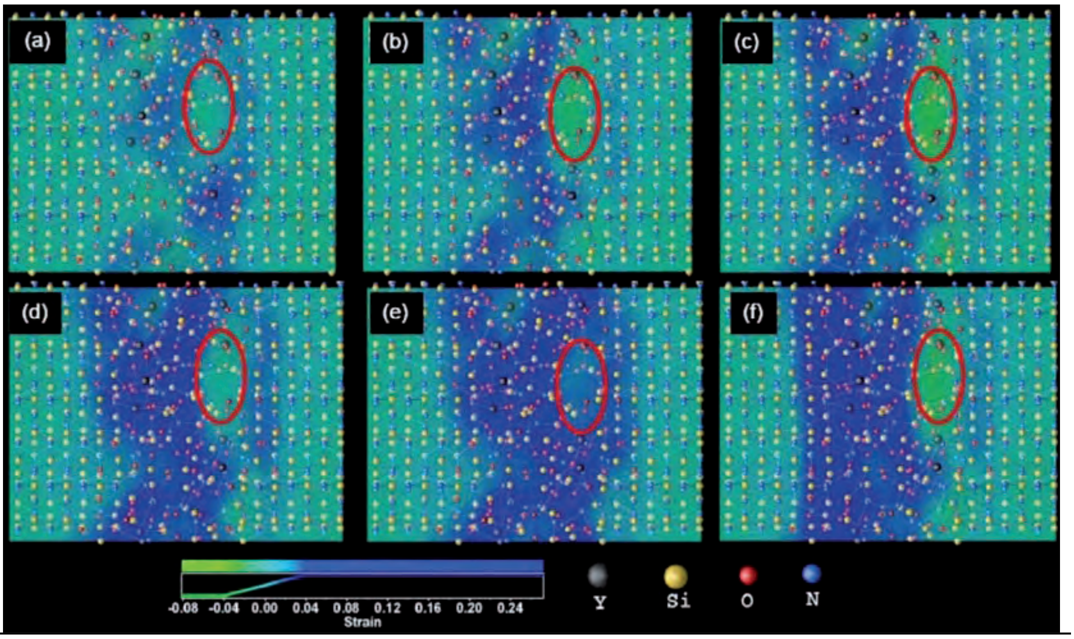

Fig. 3. Local strain field of the Y-IGF as a function of deformation under increasing strain: (a) 0.5%; (b) 0.9
2.3%; (d) 2.7 %; (e) 3.1 % and (f) 3.7%.

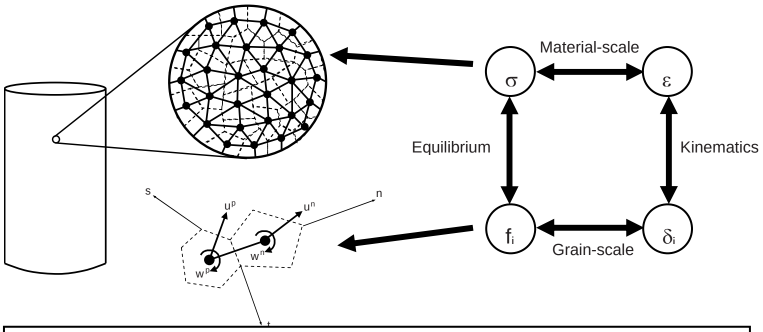

Fig. 4. Grain-scale models that may bridge *ab initio* calculations to the continuum scale.

Grain size dispersion effects on local and overall behaviours of heterogeneous materials

Nicolas Nicaise, Stéphane Berbenni and Marcel Berveiller

Laboratoire de Physique et Mécanique des Matériaux, UMR-CNRS 7554
ENSAM CER de Metz, 4 rue Augustin Fresnel, 57 078 Metz Cedex
Téléphone : 03.87.34.54.30
nicolas.nicaise@metz.ensam.fr, stephane.berbenni@metz.ensam.fr,
marcel.berveiller@metz.ensam.fr

ABSTRACT

The overall behaviour and the evolution of the internal structure of metals composed of grains with different sizes are simulated using an elastic-viscoplastic self-consistent approach. The Representative Volume Element is composed of randomly distributed spherical grains with a grain size distribution following a log-normal statistical function. Numerical results obtained for IF steels display that the overall yield stress depends not only on the mean grain size but also on the grain diameter dispersion. The study of the evolution of the internal structure indicates an increase of second order internal stresses with grain size dispersion. This effect is more pronounced for fine-grained metals.

1. Introduction

The micro-macro transition theories were developed to model the inelastic behavior of heterogeneous materials starting from the local (heterogeneous) behavior of their constituents. The interaction between grains is described by Eshelby's inclusion approaches, which is considered as accurate when grain size distribution is assumed uniform. Nevertheless, grain size effect is lacking in the aforementioned framework despite the well recognized Hall-Petch effect. In this approach, the only source of heterogeneity arises from grain size dispersion. The aggregate is composed of randomly distributed isotropic spherical grains with a grain size distribution following a log-normal statistical function. The local behavior is supposed to be elastic-viscoplastic with a reference stress depending in the individual grain size. The overall behavior is calculated and a deviation from the classical Hall-Petch relation is observed. The fluctuations of mechanical fields related to grain size dispersion is on the same order than the ones arising from crystallographic heterogeneities.

2. Modeling

2.1. Grain size distributions

The Representative Volume Element (RVE) is composed of N spherical grains with non-spatially correlated sizes. Commonly, grain size distributions follow statistical log-normal density probability functions [1]. A log-normal distribution function Lgn(M,S) of the grain diameter D is defined as the variable x follows a normal distribution, with x=Ln(D). M and S are respectively the mean and the standard deviation of the variable x. Thus, the probability density function of the log-normal distribution is:

$$P(D|M,S)=\frac{1}{S\sqrt{2\pi}D}\exp\left(-\frac{(Ln(D)-M)^2}{2S^2}\right). \tag{1}$$

A discretisation by 0.1 µm step gives a good approximation of the continuous statistic. Numerical values of M and S are determined to cover mean grain diameters from 2 to 100µm with same relative dispersions ΔD/D (where D means D_{mean} in this notation). The case of nanostructured materials is not considered (D_{min}=0.1µm).

2.2. Behavior of the grains

The behaviour of the grains is supposed elastic-viscoplastic. The linear elastic properties are supposed homogeneous and isotropic. The viscoplastic strain rate $\dot{\boldsymbol{\varepsilon}}^{vp\,I}$ of each grain "I" follows the so called Odqvist law:

$$\dot{\varepsilon}_{ij}^{vp\,I} = \frac{3}{2}\left(\frac{\sigma_{eq}^{I}}{\sigma_{ref}^{I}}\right)^{n} \frac{\sigma'^{I}_{ij}}{\sigma_{eq}^{I}}. \tag{2}$$

where σ_{eq}^{I} is the Von Mises equivalent stress defined in terms of the deviatoric stress tensor $\boldsymbol{\sigma'}^{I}$. n is set to characterize low strain rate sensitivity (1/n).

The reference stress σ_{ref}^{I} combines a grain size dependence (Hall-Petch type behavior) and a plastic strain one (isotropic Ludwik-Hollomon's type strain hardening) as follows:

$$\sigma_{ref}^{I} = \sigma_0 + k\left(D^I\right)^{-m} + h\left(\varepsilon_{eq}^{p\ I}\right)^{q}. \tag{3}$$

In Eqn. (3), D^I is the grain size of the grain, σ_0 is the friction stress, and k, m, h, and q are materials parameters (identical for the whole grains) and were identified for typical IF steels [3-4].

2.3. Self-consistent approximation

A self-consistent procedure using the "translated fields" technique was developed [4-5]. For an elastic-viscoplastic medium with homogeneous elastic moduli $\mathbf{C}$ and heterogeneous viscoplastic compliances, the interaction law between local stress rates $\dot{\boldsymbol{\sigma}}$ and overall one $\dot{\boldsymbol{\Sigma}}$ reads:

$$\dot{\boldsymbol{\sigma}} = \dot{\boldsymbol{\Sigma}} + \mathbf{C} : \left(\mathbf{I} - \mathbf{S}^{E}\right) : \left(\mathbf{A}^{B^e} : \dot{\mathbf{E}}^{vp} - \dot{\boldsymbol{\varepsilon}}^{vp}\right). \tag{4}$$

where $\mathbf{S}^{E}$ is the elastic Eshelby tensor, $\dot{\mathbf{E}}^{vp} = \overline{\dot{\boldsymbol{\varepsilon}}^{vp}}$, and, $\mathbf{A}^{B^e}$ is the viscoplastic strain rate concentration tensor related to the homogenous viscoplastic moduli $\mathbf{B}^{e}$ of the effective medium:

$$\mathbf{A}^{B^e} = \left(\mathbf{I} + \boldsymbol{\Gamma}_{l}^{B^e} : \boldsymbol{\delta}\mathbf{b}^{e}\right)^{-1},\ \boldsymbol{\delta}\mathbf{b}^{e} = \mathbf{b} - \mathbf{B}^{e}. \tag{5}$$

In Eqn.(5), $\boldsymbol{\Gamma}_{l}^{B^e}$ represents the local part of the modified Green tensor associated with $\mathbf{B}^{e}$. In the particular case describe before, Eqn.(4) writes simply:

$$\dot{\boldsymbol{\sigma}}^{I} = \dot{\boldsymbol{\Sigma}} + 2\mu(1-\beta)\left(\frac{5\eta}{3\eta + 2\eta^{I}}\dot{\mathbf{E}}^{vp} - \dot{\boldsymbol{\varepsilon}}^{vp\,I}\right),\ \beta = \frac{2(4-5\nu)}{15(1-\nu)}. \tag{6}$$

where η^I et η are respectively the viscoplastic moduli of the grains "I" and of the aggregate.

3. Results

Tensile tests at a prescribed strain rate of $|\dot{E}| = 8\times10^{-3}\ s^{-1}$ are simulated until a macroscopic strain of 10%. Macroscopic and microscopic results are presented.

3.1. Overall tensile stress/strain responses and yield stresses

Tensile stress/strain responses are reported on Fig. 1 for two mean grain sizes and several relative dispersion ΔD/D. In the case of D_{mean}=4µm, a softening due to grain size dispersion is observed (Fig. 1(a)). This effect decreases with increasing mean grain size (Fig. 1(b)). The global effect of dispersion is reported on Fig. 1(c), where the yield stress (conventional yield stress at 0.2%) is plotted for different mean grain sizes and relative dispersions ranging from 0 to 5. The Hall-Petch effect is more affected for small grain size.

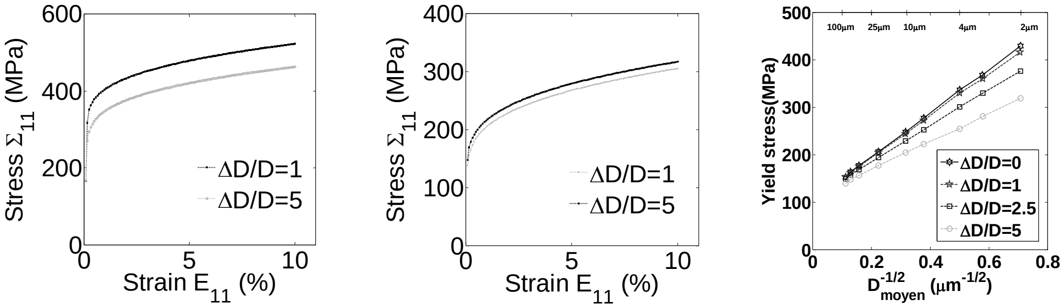

(a) D_{mean}=4μm (b) D_{mean}=80μm (c) Yield stress

Figure 1 Overall stress/strain tensile responses and yield stress

3.2. Local fields

Local plastic strains and local stress components (in tensile direction) evolutions are reported on Fig. 2 for ΔD/D=5 and D_{mean}=4μm. This figure shows important heterogeneity for the local fields. Concerning the plastic strain (Fig. 2(a)), as expected, coarsest grains contributed more to the deformation than the smallest one. Important fluctuations of internal stresses are observed (Fig. 2(b)) and three regimes occur. First, the finest grains are a little bit subjected to 2nd order internal stresses. Then, a transient regime occurs, and finally, a third one, deals with a decrease of internal stresses as grain size increases. Hence, it is worth noticing that local stress fluctuations are on the same order than the ones related to heterogeneities associated with plastic anisotropy found for polycrystalline IF steels [6].

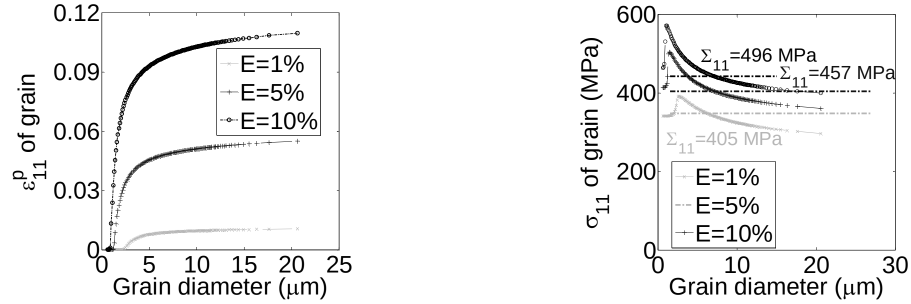

(a). Evolution of the plastic strains (b) Evolution of the local stresses

Figure 2 Local fields for D_{mean}=4μm and ΔD/D=5

4. Conclusion

Assuming a single mechanism responsible for the grain size dependence, it is found that not only the mean grain size plays a role but also grain size dispersion has an impact on overall behavior and on the evolution of the internal structure. This one is more important for fine-grained metals than for coarse-grained ones. Predicted local fields fluctuations are significant for fine-grained metals with relatively broad dispersions.

Acknowledgements

The authors thank the “Agence Nationale de Recherche” (ANR) for financial support

References

[1] F. J. Humphreys and M. Hatherly, Recrystallization and related annealing phenomena, Elsevier Science, Oxford (1995)
[2] B.L. Li, W.Q. Cao, Q. Liu, W. Liu, Flow, Mater. Sci. Engng. A356 (2003)
[3] R. Narayanasamy, C.S. Narayanan, Mater. Sci. Engng. A399 (2005)
[4] H. Sabar, M. Berveiller, V. Favier, S. Berbenni, Int. J. Solids Structures 39 (2002)
[5] S. Berbenni, V. Favier, M. Berveiller, Int. J. Plast., In Press (2006)
[6] P. Lipinski, M. Berveiller, E. Reubrez, J. Morreale, Arch. Appl. Mech. 65 (1995)

MICROMECHANICAL MODELLING OF SHARP INDENTATION EXPERIMENTS IN SINGLE CRYSTALS AND POLYCRYSTALS

Jan Ocenasek[1], *Ovidi Casals*[2], *Jorge Alcalá*[2]

[1]*Christian Doppler Laboratory for High Performance Alloys, Lehrstuhl für Werkstoffkunde und Werkstoffmechanik, TU München, Boltzmannstrasse 15, 85747 Garching, Germany*

[2]*Universitat Politécnica de Catalunya, ETSEIB, Avda Diagonal 647, Barcelona, Spain*

This work involves continuum finite element modelling of sharp indentation experiments performed in fcc metallic single crystals and polycrystalline aggregates. The aim of the investigation is to establish the micromechanics of plastic deformation within a single grain and its evolution as the plastic zone underneath the indenter spreads through neighbouring grains. The simulations are performed for single crystals as well as in a polycrystalline aggregate, where each of the grains is assumed to deform through a crystal plasticity model. In single crystal indentation, full three-dimensional simulations are conducted to capture the true features of pyramidal (Vickers and Berkovich) indentations. In the polycrystalline aggregate, the constitutive model gives the description of dislocation slip, whereas the finite element mesh sets the kinematic constraints between neighbouring microstructural units. In the latter simulations, the finite element mesh is subjected to wedge indentation under plain strain conditions. The mesh is composed of different regions, resembling a characteristic microstructure of "in-plane" equiaxial grains, whose governing parameters for the crystal plasticity model and individual orientations can be set a priori. With this investigation, we seek to evaluate the degree of isotropy in the contact response attained for grains with arbitrary orientation and the role of grain boundary strengthening. It is found that hardness and the amount of material pileup and sinking-in developing at the contact boundary are rather insensitive to crystalline orientation irrespectively of the governing constitutive parameters. The simulations thus show that there exists a direct similarity between crystal plasticity analyses of indentation experiments and those made by recourse to the J2 associated flow theory, which describe the macroscopic behaviour of a perfectly isotropic metallic polycrystalline aggregate.

New Estimates Of Effective Elastic Properties Of Semi-Crystalline Polymers

O. Gueguen(1), **S. Ahzi**(1), **A. Makradi**(1), **S. Belouettar**(2)

(1) Université Louis Pasteur, IMFS-UMR7507, 2 Rue Boussingault Strasbourg, France, gueguen@imfs.u-strasbg.fr,ahzi@imfs.u-strasbg.fr, makradi@imfs.u-strasbg.fr.
(2) LTI, Research Center Henry Tudor, 70 Rue de Luxembourg, L-4221 Esch-sur-Alzette, Luxembourg, salim.belouettar@tudor.lu

ABSTRACT

In this paper effective elastic constants of semi-crystalline polymers are computed through homogenisation methods. The polymer is considered as a two-phase composite made up of an amorphous and a crystalline phase. To improve the prediction of the polymer mechanical properties, we develop new estimates which take into account not only the relative volume of each phase but also the polymer morphology. We applied these estimates to isotropic polyethylene (PE), isotactic polypropylene (iPP) and poly(ethylene terephthalate) (PET). We obtain a good agreement in comparison with experimental results, for different rate of crystallinities.

1. Introduction

Based on well-known averaging methods (**1**, **2**), we propose new estimates for isotropic PE, iPP and PET. We compare the different average bounds and discuss their effective elastic estimates with morphological considerations for different crystallinities. To illustrate our results, we compare them to experimental ones from the literature (**3**-**4**).

2. Composite models

The general formulation of the effective elastic stiffness for composites is based on the work of Eshelby (**5**) and is expressed for N inclusions by:

$$\underline{C}^{eff} = \underline{C}^{M} + \sum_{I=1}^{N} f_I \left(\underline{C}^{I} - \underline{C}^{M} \right) : \underline{A}^{I} \qquad (1)$$

Where $\underline{C}^{eff}$ is the effective elastic stiffness; $\underline{C}^{M}$, $\underline{C}^{I}$ are the elastic stiffness for the matrix and the inclusion, respectively. f_I is the volume fraction of the inclusion embedded in the matrix (Fig 1). $\underline{A}^{I}$ is the localisation tensor we estimate in our models.

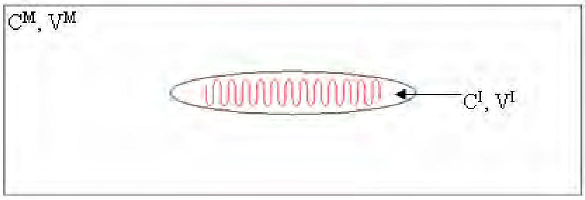

Figure 1: Inclusion embedded in a uniform infinite domain.

The definitions of the localisation tensor are defined for each model as follows:

Table 1 Definition of the concentration tensors for different models

Mori-Tanaka model	$\underline{A}^I = \left(f_I : \left[\underline{I} + \underline{S} : \underline{C}^{M^{-1}} : (\underline{C}^I - \underline{C}^M) \right]^{-1} + (1 - f_I)\underline{I} \right)^{-1}$ (2)
Composite-Inclusion	Four concentration tensors are defined ($\underline{Q}^c, \underline{Q}^a, \underline{R}^c, \underline{R}^a$): $\begin{cases} \underline{\varepsilon}^c = \underline{Q}^c \underline{\varepsilon}^I ; \underline{\varepsilon}^a = \underline{Q}^a : \underline{\varepsilon}^I \\ \underline{\sigma}^c = \underline{R}^c : \underline{\sigma}^I ; \underline{\sigma}^a = \underline{R}^a : \underline{\sigma}^I \end{cases}$ (3a, b) To derive $\underline{C}^I = f_a \underline{C}^a \underline{Q}^a + (I - f_a)\underline{C}^c \underline{Q}^c$ (4) Then $\underline{A}^I = \left(f_I : \left[\underline{I} + \underline{S} : C^{eff^{-1}} : (\underline{C}^I - \underline{C}^M) \right]^{-1} + (1 - f_I)\underline{I} \right)^{-1}$ (5)

Where $\underline{S}$ is the Eshelby tensor; $\underline{\varepsilon}^i, \underline{\sigma}^i$ are the strain and stress of each phase. $\underline{I}$ is the identity tensor of ourth order.

3. Results

We apply the above discussed homogenisation methods. Results are shown in Fig 2, 3.

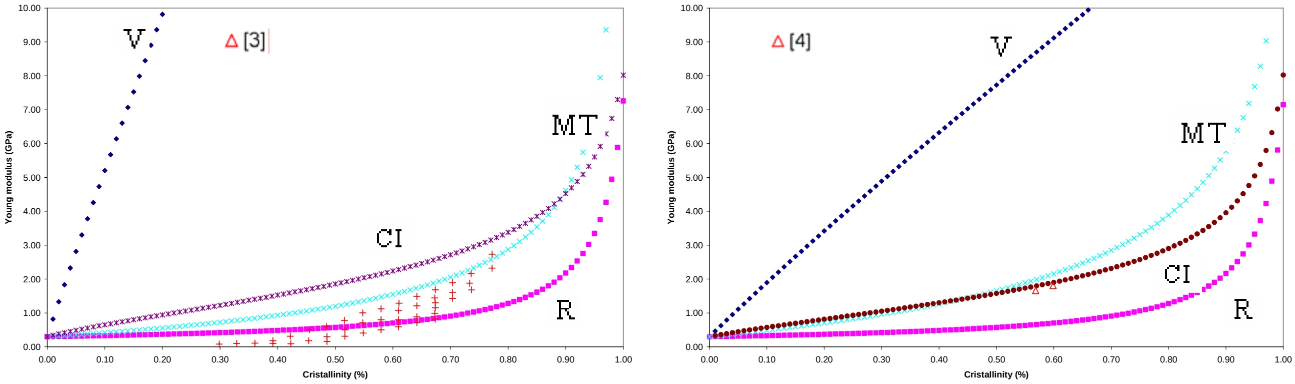

(a) (b)

Figure 2: Prediction of the Young modulus of PE (a) and iPP (b).
Comparison with experimental results.

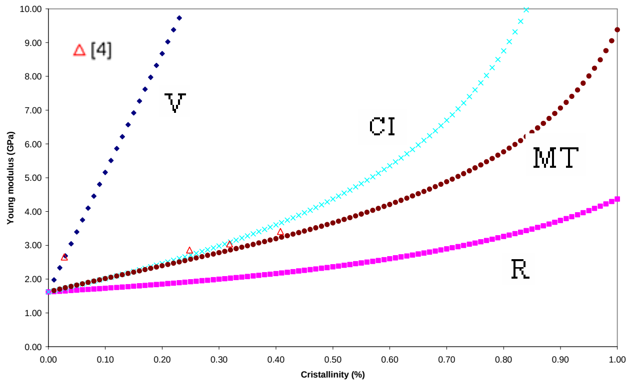

Figure 3: Prediction of the Young modulus of PET.
Comparison with experimental results.

4. Conclusion

The use of the classical bounds (Voigt and Reuss) leads to far-apart estimates of the effective elastic properties, especially for high rate of cristallinities. Our new estimates reduced considerably the gap relative to the classical bounds, except for high concentration of the crystalline phase. They are in good agreement with experimental results.

Acknowledgement

We would like to express our gratitude to the Education and Culture Ministry of the *Grand Duché of Luxembourg* and to *the Centre Henri-Tudor* for supporting our research.

References

[1] S. Ahzi, DM. Parks and AS. Argon, *Estimates of the overall Elastic properties in semi-crystalline polymers*, Current Research in the thermo-mechanics of polymers in the Rubbery-Classy Range **203**, 31 (1995).

[2] T. Mori, K. Tanaka, *Average stress and average elastic energy of materials with misfitting inclusions*, Acta Metallurgica **21**, 571 (1973).

[3] J. Janzen. *Elastic moduli of semi-crystalline Polyethylene compared with theoretical micromechanical models for composites,* Polymer Engineering and Science **32**, 1242 (1992).

[4] F. Bedoui, J. Diani, G. Regnier, *Micromechanical modeling of elastic porperties in polyolefins*, Polymer **45**, 2433 (2004).

[5] J.D. Eshelby, *The determination of the elastic field of an ellipsoidal inclusion and related problems*, Proc. R. Soc. Lond. **241**, 376 (1957).

Strain rate and temperature effects in atomic-scale dislocation-obstacle interactions

Yury Osetskiy[1], *D.J. Bacon*[2]

[1] *ORNL, One Bethel Valley Road, Oak Ridge, TN 37831-6138 USA*
[2] *Materials Science and Engineering, Department of Engineering, The University of Liverpool, Liverpool L69 3 GH, UK*

We present results of large-scale atomic-level study of a gliding edge dislocation encountering different obstacles in pure Fe and Cu and in Fe-Cu alloys. We have studied dislocations moving under different applied strain rates ($2x10^5$-10^8s^{-1}) and temperatures (0-600K). The critical resolved shear stress (CRSS) was determined and modifications to the atomic structure of dislocation and obstacle were studied for each case. It is found that the dependence of the CRSS on strain rate and temperature is different for different obstacles in different metals. It also varies with obstacle size. The possible reasons for such dependence are discussed.

Atomic-scale effects in dislocation-obstacles interactions

Yury Osetskiy[1], *D.J. Bacon*[2]

[1]*ORNL, One Bethel Valley Road, P.O.Box 2008, MS-6138, 37831, Oak Ridge, United States of America*
[2]*Department of Engineering, The University of Liverpool, L69 3GH, Liverpool, United Kingdom*

Strengthening due to voids and secondary phase precipitates can be a significant radiation effect in metals. Treatment of this by elasticity theory of dislocations is difficult when specific details atomic structure of the obstacle and dislocation are influential. In this paper we report results of large-scale atomic-level modelling of a gliding edge dislocation overcoming spherical voids in fcc copper and bcc iron and also Cu-precipitates in iron. Obstacles of up to 6nm diameter were studied. We demonstrate that atomistic modelling is able to reveal important effects which are beyond the continuum approach. Some arise from features of the dislocation core and crystal structure, others involve dislocation climb and phase transformation effects. Large obstacles of ≥5nm obey the equation for strengthening by the Orowan mechanism and can be estimated within the continuum approach with a high accuracy.

Potential Range Effects and the Properties of Materials

A.A. Ostapovets and V. Paidar

Institute of Physics, ASCR, Na Slovance 2, 182 21 Praha 8, Czech Republic
paidar@fzu.cz

ABSTRACT

Applicability of the models used for simulation of crystal defects was tested. Three transformation paths were considered to study the behaviour far from the equilibrium: Bain and Zener deformations for bcc-fcc transition and shuffling of atomic planes for bcc-hcp. The lattice stability depends strongly on the range of acting interatomic forces. This result is even more important for the investigation of complex structures where displacive phase transformations are observed.

1. Introduction

Modelling of shape memory materials may be sensitive to the description of interatomic forces as it requires the investigation of material properties far from the equilibrium. Various approaches to this issue can be encountered in the literature. The pair-wise Morse potentials were used in the study of shear-modulus instabilities in press-induced bcc-hcp phase transitions in [1]. The pseudopotentials were employed for alkali metals in the investigation of the Bain transformation where different paths including constant volume, uniaxial straining and loading were considered [2].

The n-body potentials have been extensively applied in the examination of crystal defects. For example, the martensitic transformations in NiAl were studied by molecular dynamics simulations using embedded atom method in [3]. A potential of the same category for zirconium was utilized in the study of twinned microstructures [4].

To a limited extent, the displacive phase transformation can be treated within *ab initio* models as well. Using a high-precision band structure method – full potential linearized augmented plane waves – the total energy was calculated along the tetragonal distortion path for bcc alkali metals and vanadium, fcc calcium, and hexagonal scandium and titanium [5].

In the present paper, the exponential n-body potentials [6] will be tested in order to evaluate applicability of models differing in the range of acting interatomic forces. The elastic behaviour of such potentials was systematically studied in [7] and these potentials were used in the investigation of segregation phenomena in binary alloys of transition and noble metals.

2. Interatomic potentials

The total cohesive energy is expressed as a sum over all atoms in the system

$$E = -\sum_i (E_b^i + E_r^i) \ , \qquad (1)$$

and it is composed of the bonding contributions based on the d-band density of electron states

$$E_b^i = -\left\{\sum_j \xi^2 \exp\left[-2q\left(\frac{r_{ij}}{r_0}-1\right)\right]\right\}^{1/2} \tag{2}$$

and contributions of repulsive forces represented by the pair-wise potential of Born-Mayer type

$$E_r^i = \sum_j A \exp\left[-p\left(\frac{r_{ij}}{r_0}-1\right)\right]. \tag{3}$$

The energy is then given by four adjustable parameters ξ, A, p and q. r_{ij} is an interatomic distance between the atoms i and j, and r_0 is the equilibrium first neighbour separation. Two parameters, p and q, are dimensionless and two, A and ξ, are in units of energy.

The truncation of the potential is done by the fifth order polynomials

$$U(r) = \alpha(r-r_{\mathrm{u}})^5 + \beta(r-r_{\mathrm{u}})^4 + \gamma(r-r_{\mathrm{u}})^3\,, \tag{4}$$

where the coefficients α, β, γ are determined from the conditions of continuity of the potential functions and derivatives at r_{l} and r_{u}. The potential functions given by (2) and (3) are applied only for the interatomic separations smaller than r_{l} and the potentials are approaching zero at r_{u}. Three types of potentials have been tested: the potential approximated by the polynomials (4)

i) between the first and second
ii) between the second and third
iii) between the third and fourth neighbours in the fcc lattice

The potentials were fitted to the cohesive energy of 2.954 eV per atom and to the fcc lattice parameter of 0.409 nm corresponding to silver. The p/q ratio of 3 and the pq product of 27 giving a sound behaviour close to equilibrium were chosen [7].

3. Transformation paths

In order to examine the behaviour of our models far from the equilibrium, three transformation paths have been considered:

I) Bain transition preserving the atomic volume along a tetragonal deformation path, i.e., the crystal is extended in the c-direction while it is contracted in the perpendicular a- and b-directions. If the c/a ratio is equal to 1 for the bcc lattice, the fcc lattice is obtained for c/a=√2, hence, the parameter describing the transformation trajectory is *s=c/a*.

II) Zener transition is another transformation between the bcc and fcc lattices. The shear of bcc lattice on the (101) plane in the $[\bar{1}01]$ direction that induces the fcc topology has to be accompanied by additional deformations to convert isosceles triangles (two first and one second bcc neighbours) into equilateral triangles (all three first fcc neighbours) on the close-packed planes, i.e., on (101) in bcc and (111) in fcc, respectively.

III) Atomic shuffling of every second atomic plane that transforms bcc lattice into hexagonal close packed one. The atoms of the upper neighbouring plane situated in between the second bcc neighbours in the underlying plane are shifted to the centres of the triangles in hcp lattice. Again additional deformation has to convert isosceles bcc triangles into equilateral hcp ones.

4. Comparison of the models with different potential ranges

It is shown in Fig. 1 that the energy of the system along the transformation trajectories is very sensitive to the potential range. For the short-range potentials truncated at the distance of the second neighbours, the minima corresponding to the fcc/hcp and bcc structures have comparable energies. The bcc lattice is unstable along the Zener and shuffling paths for the potentials truncated at the third and fourth neighbours, there is only a shallow minimum or inflexion point for the tetragonal Bain path. Since the hcp energy is lower than the fcc energy for the potential truncated at the third neighbours while it is higher for the truncation at the fourth neighbours, it can be anticipated that the fcc stacking fault energy is negative for the third-neighbour truncation indicating instability of the fcc lattice. The fcc and hcp energies for the second-neighbour truncation must be identical.

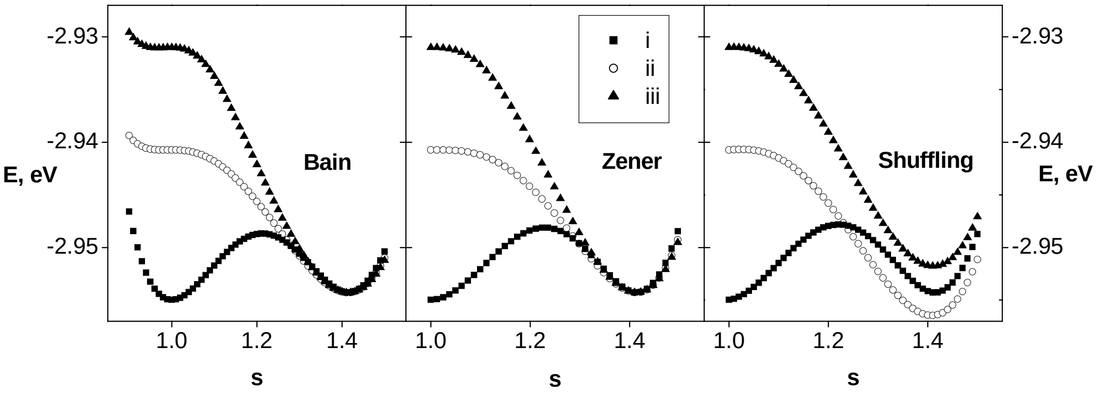

Fig. 1. Crystal energy along the transformation paths for three potential truncations. *s* is the parameter describing transformation paths, it is equal to 1 for bcc and √2 for fcc/hcp.

5. Conclusions

A pronounced influence of the potential range on the transformation behaviour along three paths important for displacive phase transformations has been demonstrated.

Acknowledgements

Support by the Institute Research Project AV0Z10100520 and COST program P19 OC149 is gratefully appreciated.

References

[1] J. Zhao, D. Maroudas, F. Milstein, Phys. Rev. B 62 (2000) 13799.
[2] F. Milstein, H.E. Fang, Phil. Mag. A 70 (1994) 621.
[3] Z. Shao, P.C. Clapp, J.A. Rifkin, Metall. Trans. A 27 (1996) 1477.
[4] U. Pinsook, G.J. Ackland, Phys. rev. B 62 (2000) 5427.
[5] V.L. Sliwko, P. Mohn, K. Schwarz, P. Blaha, J. Phys. Cond. Matter 8 (1996) 799.
[6] V. Rosato, M. Guillopé, B. Legrand, Phil. Mag. A 59 (1989) 321.
[7] V. Paidar, A. Larere, L. Priester, Modelling Simul. Mater. Sci. Eng. 5 (1997) 381.

Two-Scale Modelling of Sintering Deformation

Jingzhe Pan

Department of Engineering, University of Leicester
Leicester, LE1 7RH, UK; e-mail: jp165@le.ac.uk

ABSTRACT

The paper presents a general framework of two-scale modelling for computer simulation of the sintering process of powder compacts. The macroscopic finite element analysis for the sintering deformation of a powder compact is connected with a microscopic analysis of matter redistribution at the particle scale. At the continuum scale, the sintering body is treated as a porous viscous sold with changing density and grain-size. At the particle scale, all the major matter redistribution mechanisms, including diffusion in the solid state or through a liquid phase, vapour evaporation and condensation, and grain-boundary migration, are considered. The classical virtual power principle in solid mechanics is extended to the matter transportation problem at the microscopic scale and applied to formulating the multiscale modelling strategy.

1. Introduction

Almost all ceramic products and an increasing number of metal, polymer and glass products are made by the compaction and subsequently sintering of powder compacts. During the sintering process, the powder compacts are fired to consolidate sometimes in a controlled atmosphere. For ceramics this is perhaps the only viable manufacturing technology at a large scale. For other materials, the technology is often used to produce components of unusual chemical compositions or microstructures. During the sintering process the relative density of the powder compact increases typically from 60% to almost 100%; the average grain-size increases typically by an order or magnitude; and the component size shrinks typically by 20-30%. The sintering deformation at the macroscopic scale is strongly coupled with the microstructural evolution. Sintering is therefore an ideal platform to study multi-scale modelling [1]. In this paper a general framework is presented for a two-scale model of the sintering deformation. A statistically averaged velocity of atomic migration is used to describe matter redistribution at the microscopic (particle) scale. Using a virtual power principle, the macroscopic stresses are related to the macroscopic strain rates through the microscopic velocity field.

2. Virtual power principle for microscopic matter transportation and constitutive law

Figure 1 shows schematically the two-scale sintering model considered in this paper. Figure 1 (a) shows a finite element model of a component which experiences viscous deformation during sintering. Figure 1(b) shows some of the microscopic processes responsible for the macroscopic deformation. For the sintering problem, it can be assumed that the particles (or grains) are rigid and that the macroscopic deformation is a manifestation of matter redistribution at the microscopic scale. At elevated temperatures, atoms can migrate away from the grain-boundaries through various diffusion routes and deposit onto the pore surface. This matter redistribution can either occur entirely in the solid state or, if a liquid phase exists, the solid phase can dissolve into a thin liquid film within the grain-boundaries and diffuse into the pores through the liquid phase.

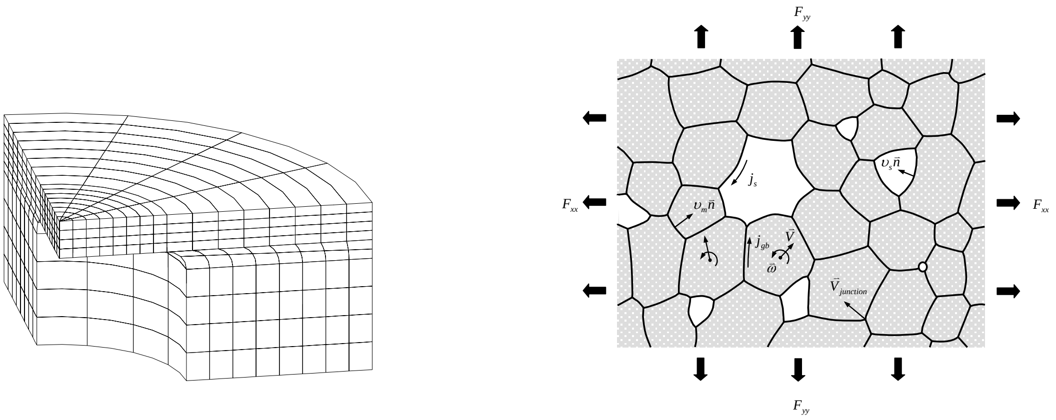

a). A finite element model at the macroscopic scale.

b. A representative unit of the porous material showing the microstructure.

Figure 1. A two-scale model for sintering deformation

As matter is removed from the grain-boundaries and fill up the pores, the grains approach each other leading to a macroscopic deformation (shrinking) of the solid. At the same time atomic rearrangement normal to the grain-boundaries makes the grain-boundaries migrate towards smaller grains, leading to grain-growth. Atoms can also evaporate from one part of the surface of a pore and deposit onto another part of the surface, leading to neck growth between the particles without densification. All these matter redistribution mechanisms can be summarised by a "statistically averaged atomic migration velocity" $\vec{\upsilon}$. Inside a solid grain, $\vec{\upsilon}$ is simply the lattice diffusion flux. Within a thin layer of the interface (grain-boundary or pore surface), $\vec{\upsilon}$ can be decomposed into $\vec{\upsilon}_{//}$, which is parallel to the interface and corresponds to diffusion (through grain-boundary, free surface or a liquid film), and $\vec{\upsilon}_{\perp}$, which is normal to the interface and corresponds atomic dissolution or precipitation, vapour evaporation and condensation, or grain-boundary migration.

The driving force for the matter redistribution is the reduction of the total free energy E of the powder compact given by

$$E = \int_{grain-boundaries} \gamma_{SS}\, dA + \int_{pore-surface} \gamma_{SV}\, dA \ . \tag{1}$$

in which γ_{SS} and γ_{SV} represent the specific interfacial energies for the grain-boundary and the free-surface respectively. Lets $\vec{F}$ represent a thermodynamic driving force corresponding to $\vec{\upsilon}$, $\vec{P}$ the distributed mechanical force on the boundary Γ of the representative unit and $\vec{u}$ the velocity of boundary Γ. The virtual power principle in solid mechanics can be extended to the microscopic matter transportation problem in the following format:

$$\sum_{all\_atoms} \vec{F} \cdot \delta\vec{\upsilon} + \delta\left(\frac{dE}{dt}\right) - \int_{\Gamma} \vec{P} \cdot \delta\vec{u}\, d\Gamma = 0 \tag{2}$$

in which δ represents a virtual variation of the following variable. Assuming a linear kinetic law for simplicity (although the approach developed here is not limited to the linear law):

$$\vec{\upsilon} = M\vec{F} \tag{3}$$

in which M represents the mobility of the atoms which strongly depends on the temperature and local environment, equation (2) can be rewritten as:

$$\int_V \left(\frac{C}{M\Omega} \vec{\upsilon} \cdot \delta \vec{\upsilon} \right) dV + \delta \left(\frac{dE}{dt} \right) - \int_\Gamma \vec{P} \cdot \delta \dot{\vec{u}} d\Gamma = 0 \,, \tag{4}$$

in which C represents the concentration of the migrating species and Ω the atomic volume. Let σ_{ij} and $\dot{\varepsilon}_{ij}$ represent the macroscopic stress and strain-rate tensors respectively. We have a well-known relationship due to Hill:

$$\int_\Gamma \vec{P} \cdot \delta \dot{\vec{u}} d\Gamma = \left(\sigma_{ij} \delta \dot{\varepsilon}_{ij} \right) V, \tag{5}$$

in which V is the total volume of the representative unit. Substituting (5) into (4) provides the following constitutive law:

$$\sigma_{ij} = \frac{\partial \Psi}{\partial \dot{\varepsilon}_{ij}} \tag{6}$$

in which Ψ is known as the strain-rate potential which is given by

$$\Psi = \frac{1}{V} \left\{ \frac{1}{2} \int_V \left(\frac{C}{M\Omega} \vec{\upsilon} \cdot \vec{\upsilon} \right) dV + \frac{dE}{dt} \right\} . \tag{7}$$

Expressions (6) and (7) connect the macroscopic stresses with the macroscopic strain rates through the microscopic velocity field. Cocks[2] derived these expressions for the case of solid state diffusion using bonding theorems following previous works by Needleman and Rice, McMeeking and Suo. For details of these references see the review article [1]. Here these previous works are extended to include all the possible matter distribution mechanisms in the very concise format by formulating a virtual power principle in terms of the atomic migration velocity.

For sintering controlled by solid state diffusion, expression (7) can be reduced to the format used by Cocks[2]. Considering grain-boundary diffusion, surface diffusion and grain-boundary migration, the interface diffusional flux $\vec{j}$ is defined as the volume of matter passing through a unit slab of the diffusion layer per unit time. Let h represent the thickness of the diffusion layer, then $\vec{j} = \vec{\upsilon}_{//} h$. Noticing that $dV = hdA$ in Eq. (7), Ψ can be rewritten into the format used by Cocks[2]:

$$\Psi = \int_{\text{interface}} \left(\frac{1}{2M_{diff}} \vec{j} \cdot \vec{j} \right) dA + \int_{\text{grain-boundary}} \left(\frac{1}{2M_m} \vec{\upsilon}_\perp \cdot \vec{\upsilon}_\perp \right) dA + \frac{dE}{dt} \tag{8}$$

in which two effective kinetic mobilities have been introduced: $M_{diff} = hM\Omega$ and $M_m = M\Omega / h$. This immediately leads to an advantage of the approach taken in this paper. In numerical simulations a non-dimensional group is often used:

$$\overline{M}_m = \frac{M_m d^2}{M_{gb}}, \tag{9}$$

in which d is the average grain-size and M_{gb} is the effective mobility for grain-boundary diffusion. It is reasonable to assume that the atomic mobility M is the same for $\vec{\upsilon}_{//}$ and $\vec{\upsilon}_{\perp}$. Therefore we have

$$\overline{M}_m = \frac{M_m d^2}{M_{gb}} = \left(\frac{d}{h}\right)^2. \tag{10}$$

Equation (10) is a significant expression because it dictates that $\overline{M}_m$ depends only on the ratio between the particle size and the thickness of the diffusion layer. The size effect of the grains (or particles) on the sintering kinetics is therefore controlled by $\overline{M}_m$.

The constitutive relationship given by Eqs. (6) and (7) have been used in two different ways:

a) An "on-line" constitutive law was developed which interacts with the finite element analysis for macroscopic deformation of sintering[4]. This approach was used to model damage evolution in the sintering of powder compact containing hard inclusions in which powder particles may either separate or approach each other depending on the macroscopic strain state. The constitutive law is analytical but "derived on line" depending on the macroscopic strain state of the powder compact[4].

b) The relationship is being used to numerically compute the constitutive law for a representative unit which contains a large enough microstructure. For a given set of macroscopic strain rates, the microscopic velocity field is solved numerically using a finite element scheme for the microscopic problem. The corresponding macroscopic stresses are then determined numerically using Eqs (6) and (7).

Acknowledgements

This work is supported by an EPSRC research grant S57996.

References

1. J. Pan (2003), Modelling sintering at different length scales, *International Materials Reviews*, Vol. 48, pp. 69-85.
2. A.C.F. Cocks (1994), The structure of constitutive laws for the sintering of fine grained materials, *Acta Metall.* 1994, **42**, 2191-2210.
3. H.N. Ch'ng and J. Pan (2006), Sintering of particles of different sizes, *accepted by Acta Materialia.*
4. R. Huang and J. Pan (2006), Multi-scale modelling of damage evolution during the sintering of powder compacts containing hard inclusions, *to appear in Mechanics of Materials.*

The Effect of Porosity on the Elastoplastic Behavior of High Performance-Cast Alloys

M. Ries[1], *B. Hadler*[1], *C. Krempaszky*[2], *E. Werner*[1]

[1]*Technical University Munich, Institute for Materials Science and Mechanics of Materials, Garching, Germany*
[2]*Christian Doppler Laboratory for Material Mechanics of High Performance Alloys*

In the design of cast high performance components, the knowledge of the effect of porosity on strength and durability is of high significance. In this contribution, a model on the mesoscopic scale is proposed to investigate the impact of the topological aspects of the defects on the macroscopic mechanical properties of the material. In a first step only the geometrical properties of the porosity are embedded, micromechanical properties, e.g. anisotropy of the grains and influence of grain boundaries, are neglected. The constitutive behavior of the matrix is assumed to be that of the nonporous material. As a result the homogenized macroscopic behavior of the porous material is obtained. The impact of porosity is quantified by the reduction of Young‘s modulus and yield limit. For the experimental validation of the simulations uniaxial tensile tests were conducted in a deformation dilatometer, concerning the elastic and elastoplastic properties of porous and non-porous specimens. The damage-mechanisms are investigated on broken specimens by micrographs and SEM-analysis near the fracture surface to implement them in the model in a later step. The tensile tests are conducted at room temperature and 900 °C. The volume-fraction of the porosity of the specimen is obtained previously by computer tomography. The aim is to identify adequate parameters for the description of the mechanical behavior of the porous area in a suffcient accuracy, that can be obtained by non-destructive analysis in a way as simple as possible.

Preliminary developments of 3D dislocation dynamics modelling adapted to 16MND5 ferritic steel in connection with TEM observations

Christian Robertson[1], *J. Chaussidon*[2], *K. Obrtlik*[3], *M. Fivel*[2], *D. Rodney*[2]

[1]*CEA-Saclay, SRMA, Building-455, 91191 Gif-sur-Yvette, France*

[2]*GPM2, CNRS/INPG, BP 46, 101 Rue de la Physique, 38 402 St Martin d'Hères, France*

[3]*IPM, Academy of Sciences, Zizkova 22, 616 62 Brno, Czech Republic*

This work is a part of a broader, multi-scale modeling project, dealing with the prediction of 16MND5 ferritic steel toughness. The results presented hereafter are regarded as a first step towards the development of 3D dislocation dynamics models (DD), used to provide a detailed description of the sub-grain plasticity in 16MND5 grains. Generally, brittle fracture in ferritic (bcc) metals has a cleavage character and all the established cleavage mechanisms involve dislocation-based, crystal plasticity. Therefore, it is believed that comprehensive toughness prediction models could be established, provided they account for the scale of dislocation dynamics modelling. In the past, dislocation structures developing in uni-axial tension were examined extensively, both in single and poly-crystals. In 16MND5 steel however, the corresponding experimental data is missing. Since this material is made of very thin laths (typically, 1 µm); a significant effect of the internal interfaces on the dislocation arrangements is to be expected.

Here, TEM observations in 16MND5 tensile specimens after deformation at 4 different temperatures and 2 plastic strain levels are described in details. The presented data includes all the information needed to run three dimensional DD simulations adapted to this material, i.e. the lath boundary orientations, the dislocation sources (types, position, length, density), the lath deformation mechanism, etc. In the future, the typical TEM observed deformation structures would also be compared to the numerically generated structures, for final model validation. One important prior step is the determination of the individual screw dislocation mobility and cross-slip characteristics, for different applied stress and temperature. This information is obtained using molecular dynamic simulations (MD), at the atomic scale. The MD results are consistent with a thermal activation scheme, accounting for the twinning/anti-twinning dislocation core symmetries effect on the cross-slip plane selection.

Nonlinear Dynamic FE Analysis of an Artificial Bird Striking an Aero-engine Fan Blade

R. H. Mao*, S. A. Meguid and T. Y. Ng
School of Mechanical and Aerospace Engineering, Nanyang Technological University, Singapore 639798. Tel (+65) 67904072; E-mail: rhmao@ntu.edu.sg

ABSTRACT

In the present investigation, explicit 3-D finite element analysis is carried out using the commercial code LS-DYNA to study the nonlinear transient response of a 4-lb artificial bird striking an engine fan blade. Both the bird and the blade are simulated using Lagrangian formulations. The homogenized fluidic constitutive formulation of the bird followed the Brockman hydrodynamic model, which was found to be the most appropriate through the validation test. The blade, on the other hand, was modeled as a viscoplastic material of the Perzyna type. In addition, an 8-lb bird strike case was examined to address the lack of heavy bird strike data.

Nomenclature (in SI units)

D = Diameter of Bird (m);
F = Impact Force (N);
L = Length of Bird, $L=2D$, (m);
m = Total Mass of Bird, $m = \frac{5}{12}\pi D^3 \cdot \rho_0$, (kg);
P = Pressure, $P = \frac{F}{\frac{\pi}{4}D^2}$ (Pa);
P_{ad} = Normalized Pressure, $P_{ad} = \frac{P}{\frac{1}{2}\rho_0 \cdot U_0^2}$;
t = Time (s);
T = Normalized Time, $T = t \cdot U_0 / L$;
U_0 = Initial Velocity of Bird, U_0=225m/s;
ρ ; ρ_0 = Mass Density of Bird; Initial Mass Density of Bird, ρ_0=943kg/m^3;
μ = Mass Density Changing Ratio of Bird, $\mu = \frac{\rho}{\rho_0} - 1$.

1. Introduction

Aircrafts of all types have been subject to bird strike ever since they began to co-sharing the skies at the beginning of the last century. Worldwide, it is conservatively estimated that collisions between aircraft and birds cost the aviation industry over US$1.2 billion each year[1]. With the advent of explicit finite element codes in the late 1980’s, numerical simulations have since been widely used to evaluate the impact capability of different aircraft components, among which the most vulnerable is the engine fan system. At present, however, the prevailing ingestion standard is limited to 4-lb birds, and this unfortunately excludes many species of large flocking birds, such as Canadian geese and white pelicans. By using explicit 3-D finite element analysis, the present study firstly investigates the problem of a pre-calibrated 4-lb artificial bird impacting a typical flexible aero-engine fan blade. Following this, a heavier 8-lb bird impacting the same blade model will be examined.

2. Finite Element Modeling

At high speeds (>200m/s), the nonuniformity and inhomogeneity of the bird tissue becomes negligible. The bird can be considered as a homogeneous jet of fluid impinging on the structure[2], with a polynomial fitted pressure

$$P = C_0 + C_1\mu + C_2\mu^2 + C_3\mu^3 . \qquad (1)$$

The Brockman hydrodynamic model is used here, and the modules are taken as C_0=0, C_1=2323MPa, C_2=5026MPa and C_3=15180MPa[3]. In addition, eight-node solid elements (solid 164) are employed for the bird model. The bird is modeled as a hemispherical-ended cylinder with an aspect ratio of 2:1 and mass density of 943kg/m^3. The diameters (D) for the 4-lb and 8-lb birds are respectively 0.1138m and 0.1434m. Details of the calibration for the bird modeling can be found in Meguid et al.[4]. Due to the high strain rates associated with this problem, the selected constitutive law for the Titanium alloy Ti-6Al-4V is of the visco-plastic type

$$\sigma_y(\varepsilon^P_{eff}, \dot{\varepsilon}^P_{eff}) = \sigma_y(\varepsilon^P_{eff}) \ \ (1 + (\frac{\dot{\varepsilon}^P_{eff}}{C})^{\frac{1}{P}}) \qquad (2)$$

where $\dot{\varepsilon}^P_{eff}$ is the effective plastic strain rate, C and P are strain rate parameters which are experimentally determined, and $\sigma_y(\varepsilon^P_{eff})$ is the initial quasi-static yield stress. Shell-163 element in LS-DYNA was used to simulate the blade with 31 nodes in the axial direction and 61 nodes in the radial direction.

3. Results and Discussion

The time-histories of the 4-lb and 8-lb artificial birds striking a typical aero-engine fan blade are shown in Figs. 1(a)~(d) and 2(a)~(d), respectively. The fluid-like behavior of the bird is clearly observed. Figures 1(e) and 2(e) are the deformed blade at their respective normalized time when following the impact event, i.e., the impact force drops to zero. As expected, the blade deformation for the case of 8-lb bird is significantly higher compared to the case of the 4-lb bird, with respective maximum plastic strains of 0.055 and 0.090.

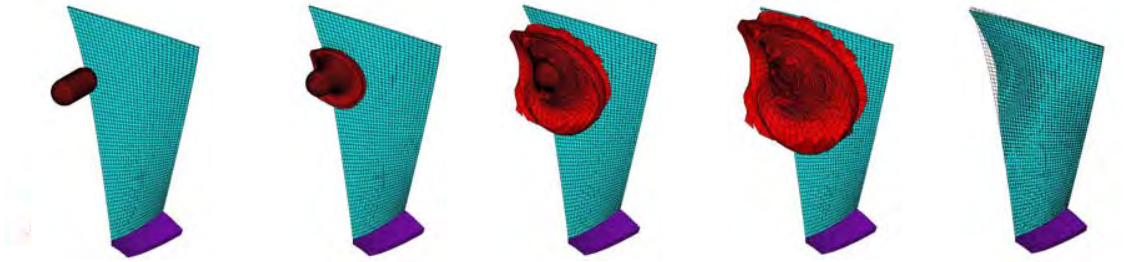

(a) $T = 0$ (b) $T = 0.50$ (c) $T = 1$ (d) $T = 1.34$ (e) $T = 1.34$

Figure 1. 4-lb bird striking a flexible fan blade.

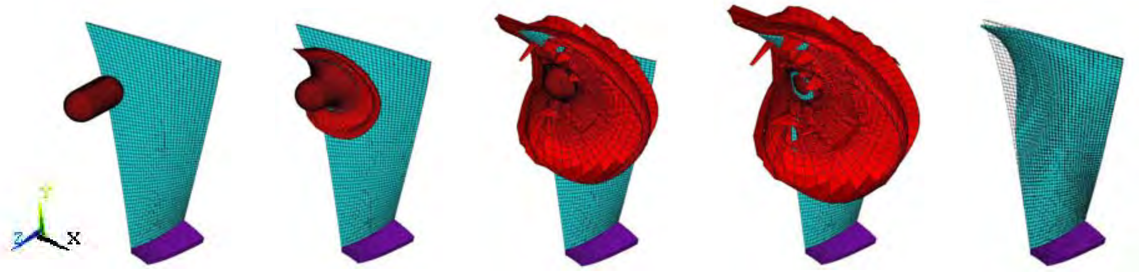

(a) $T = 0$ (b) $T = 0.50$ (c) $T = 1$ (d) $T = 1.33$ (e) $T = 1.33$

Figure 2. 8-lb bird striking a flexible fan blade.

The normalized impact forces in the X, Y and Z directions for a 4-lb bird are shown in Fig. 3 in the left. It is clear that the impact forces in the X and Y directions are much lower than the impact force in the Z direction, as the bird's initial velocity is in the Z direction. The impact forces in the Z direction for both 4-lb and 8-lb birds are shown in the right of Fig. 3. The maximum impact force is found to be about 360kN for the case of the 4-lb bird; and it is increased to about 520kN for the 8-lb bird.

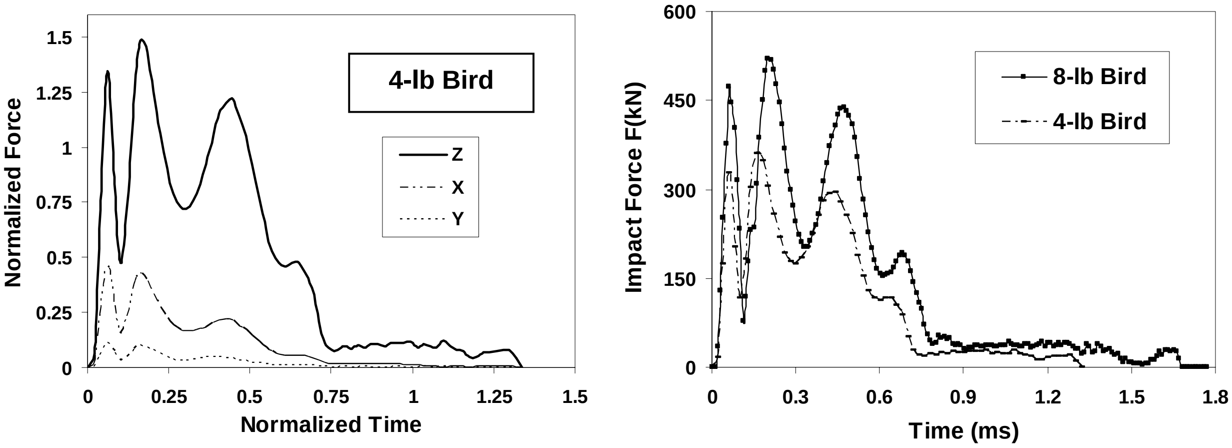

Figure 3. Impact Force Variations for the Bird-Blade Strike.

4. Conclusion

The engine fan blades are expected to withstand powerful impact from birds, and whose fracture may lead to catastrophic outcomes due to containment failure or loss of thrust and power supply to the aircraft. While aircraft manufacturers undertake ample in-house testing prior to certification, it can be a very costly affair, and it is thus highly desirable to have predictive numerical models to assess the bird impact resistance of various aircraft components. The Lagrangian bird-blade formulation, if accurately modeled, is appropriate for the simulation of bird strike on a fan blade. In this work, 4-lb and 8-lb birds were considered, and it was found that the 8-lb bird exerts a maximum force which is 1.44 times that of the 4-lb bird. In addition, the maximum plastic strain of the blade was found to be 64% higher for the larger bird impact case.

References

[1] Allan J. R., The costs of birdstrikes and birdstrike prevention, Human Conflicts with Wildlife: Economic Considerations, US Department of Agriculture, Fort Collins, pp. 147-153, 2002.

[2] Wilbeck, J. S., Impact behavior of low strength projectiles, Report No. AFML-TR-77-134, Air Force Materials Lab., Air Force Wright Aeronautical Lab's, Wright-Patterson Air Force base, OH, 1977.

[3] Brockman R. A. & Held T. W., Explicit finite element method for transparency impact analysis, WL-TR-91-3006, University of Dayton Research Institute, Dayton (OH-USA), 1991.

[4] Meguid S. A., Ng T. Y. & Mao R. H., Numerical bird strike simulation using explicit finite element analysis, Report AS-0001-2006, School of Mechanical & Aerospace Engineering, Nanyang Technological University, 2006.

Constitutive Modelling Based on Physical Mechanisms

Franz Roters

Max-Planck-Institut für Eisenforschung, Max-Planck-Str. 1, 40237 Düsseldorf, Germany

The constitutive equations describe the development of the material behaviour during a deformation process. If complex boundary conditions have to be considered the Finite Element Method (FEM) has become the standard method for the simulation of forming processes. However, the constitutive models used within the FEM framework are usually rather simple empirical ones. In recent years the Crystal Plasticity FEM (CPFEM) was developed to better account for the anisotropic forming behaviour of crystalline materials. The CPFEM introduces the crystallographic slip systems into the simulation framework by reducing the degrees of freedom for the plastic deformation to shear on those slip systems. This implies that the constitutive equations now apply to the individual slip systems, but again rather simple power law formulations are used in the classic CPFEM. By comparison with experiments it is shown that these simple constitutive descriptions are not sufficient to correctly describe the local deformation behaviour for strongly inhomogeneous deformation conditions, e.g. nanoindentation of single crystals or simple shear of bicrystals. In these cases more sophisticated constitutive models are needed. Such models should be built on the physical mechanisms connected with dislocation dynamics and take into account additional microstructural features such as strain gradients and grain boundaries. One such model is introduced and it is demonstrated how the prediction of the local deformation behaviour is improved for the experiments mentioned before.

Modelling Of Texture Evolution For HCP Materials Using Different Approaches (Sachs, Constrained-Hybrid, Self-Consistent, Taylor)

S. M'Guil[1a], S. Ahzi[1b] , H. Garmestani[2]
[1]ULP - IMFS - UMR 7507 CNRS, 2 rue Boussingault, 67000 Strasbourg, FRANCE
[2]Materials Science and Engineering, Georgia Institute of Technology, Atlanta, GA, USA
[1a]mguil@imfs.u-strasbg.fr,[1b]ahzi@imfs.u-strasbg.fr,[2]hamid.garmestani@mse.gatech.edu

ABSTRACT

Low symmetry crystalline structures usually lack the required five independent slip systems for the accommodation of an arbitrary plastic deformation and thus, the classical Taylor models are not applicable. Here, we consider hexagonal materials, such as Ti and Mg, for which the pyramidal slip has a much higher critical resolved shear stress that the basal and prismatic slip. Since the hard systems will not be activated, the c-direction will not be able to plastically deform. In order to describe this behaviour, we use the modified Viscoplastic Taylor model of Parks and Ahzi, the viscoplastic Sachs model and the viscoplastic self-consistent model. In this paper, we compare texture predictions from these different models. We also compare to the results from the viscoplastic Taylor model (when pyramidal slip is included).

1. Different models available for HCP materials

Modeling of polycrystal plasticity is rooted in the work of Sachs and Taylor. Sachs suggested that shear stresses on the principal slip systems are the same for all slip systems. The original Taylor model assumes that the plastic deformation of a polycrystalline material is uniform and the crystals must possess at least five independent slip systems to accommodate an arbitrary plastic deformation. In the present work, we consider hexagonal polycrystals with very hard <c+a> pyramidal systems. This implies that the single crystals are inextensible along their c-axis. To explicitly account for this kinematic deficiency, Parks and Ahzi [1] and Shoenfeld et al. [2] formulated the constraints due to kinematic deficiencies. The constrained directions of the single crystals are defined as the crystallographic directions that cannot deform plastically. They proposed a modified rigid-viscoplastic [1] and an elastic-viscoplastic [2] Taylor models (known as the Constrained-Hybrid or Projection models) for crystals possessing only four or fewer independent slip systems. Other models, such as the viscoplastic self-consistent model were also recently proposed for constrained crystals [3-4]. In the work of Ahzi et al. [3], the Sachs, the self-consistent and the Constrained-Hybrid models were utilized to predict texture evolution in a class of low symmetry crystals comprising less than five independent slip systems. We note that the viscoplastic Sachs and the self-consistent models allow for the hard systems not be activated as long as their critical resolved shear stress is higher enough. In this study, we use the viscoplastic self-consistent (VPSC) code of Lebensohn and Tomé [5].

2. Results: uniaxial compression for Titanium (c/a=1.587) and Magnesium (c/a=1.624)

HCP materials, such as Ti and Mg, deform primarily by basal and prismatic slip. The basal and prismatic planes are mutually orthogonal. However, because the slip directions are all confined to the basal plane, there are only two independent systems of each type. Thus, basal and prismatic slips together possess only four independent slip systems. The <c+a> pyramidal slip is much harder to activate. Based on data given in literature, the critical resolved shear stresses for the used slip system for Titanium and Magnesium are given in Tab. 1.

Table 1. Deformation modes and relative CRSS for Ti and Mg

Name	Plane	Direction	Relative CRSS: Ti	Relative CRSS: Mg
Basal <a>	(0002)	$<11\bar{2}0>$	6	1
Prismatic <a>	$(1\bar{1}00)$	$<11\bar{2}0>$	1	38
Pyramidal <c+a>	$(11\bar{2}\bar{2})$	$<11\bar{2}3>$	10	50

In Fig. 1, we plot the stress-strain response, under axisymmetric compression, obtained with different approaches for Titanium and Magnesium. These simulations were conducted without any hardening (critical resolved shear stresses are kept constants). In Fig. 2, we plot the slip activity for both materials. Texture developments, at 60% true strain, are shown by the pole figures in Fig. 3 for Titanium and in Fig. 4 for Magnesium. For the stress-strain response, we see that all models fall between the Taylor and the Sachs models in the first stage of deformation. However, at large strains, the Constrained-Hybrid (CH) model predict higher stresses which are due to orientational (textural) hardening. We note that the CH model does not include the pyramidal systems. The response of VPSC is different for the two materials. For Magnesium, the stresses overshoot at high strains when the pyramidal systems start to be activated. This is not the case for Titanium since the prismatic systems are soft which sustains plasticity to a much larger level without **a** need for the pyramidal systems. For texture results, basal slip rotates the c-axis towards the compression axis. This is observed in the results of all models but with some differences mainly in the texture sharpness.

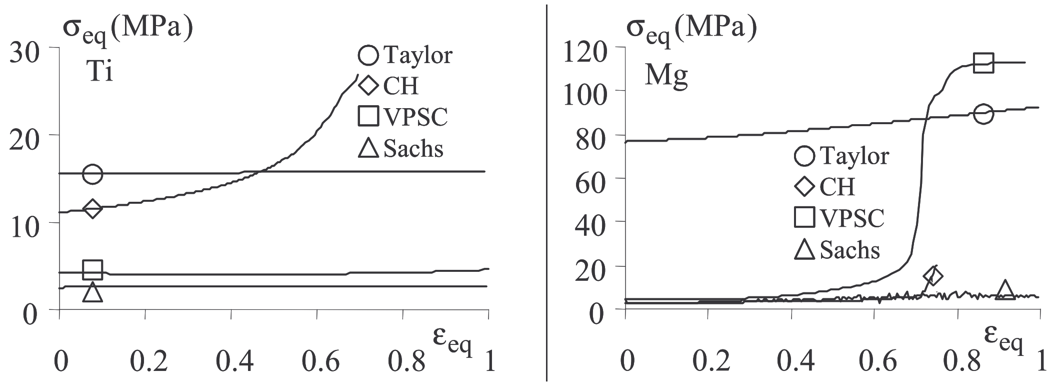

Figure 1. Stress–strain response using different models for Titanium and Magnesium

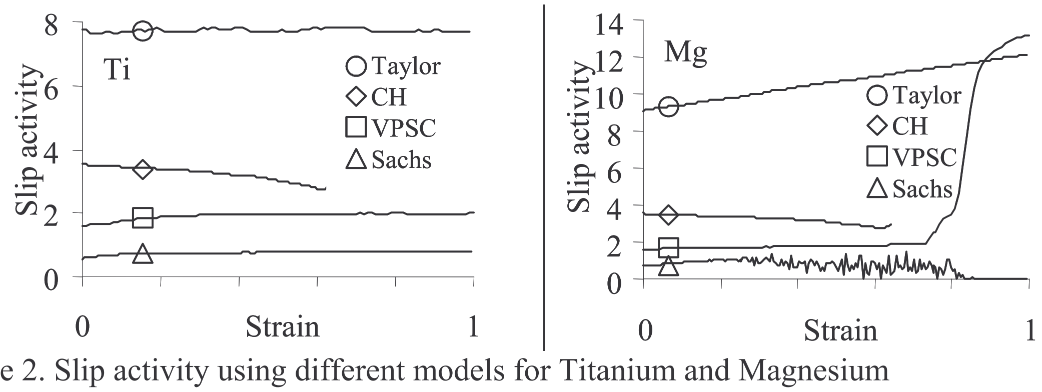

Figure 2. Slip activity using different models for Titanium and Magnesium

4. Conclusion

Our results are in agreements with the results in the literature. The results show that even though all 18 slip systems (basal, prismatic and pyramidal <c+a>) are present and potentially active in a material, the soft modes are activated in the case of the Sachs and the VPSC models. The Taylor model activates both the hard and soft modes to fulfil the requirement of five independent slip systems. The CH model accounts for the kinematic deficiencies by eliminating the hard modes. The results shows here illustrate the differences between the models in terms of stress-strain response, slip activity and texture development. A more detailed comparison with the experimental results is needed to clearly identify the predictive capability of each of the proposed models for hexagonal deforming by crystallographic slip. Twinning must also be included for the cases where it contributes significantly to plastic deformation

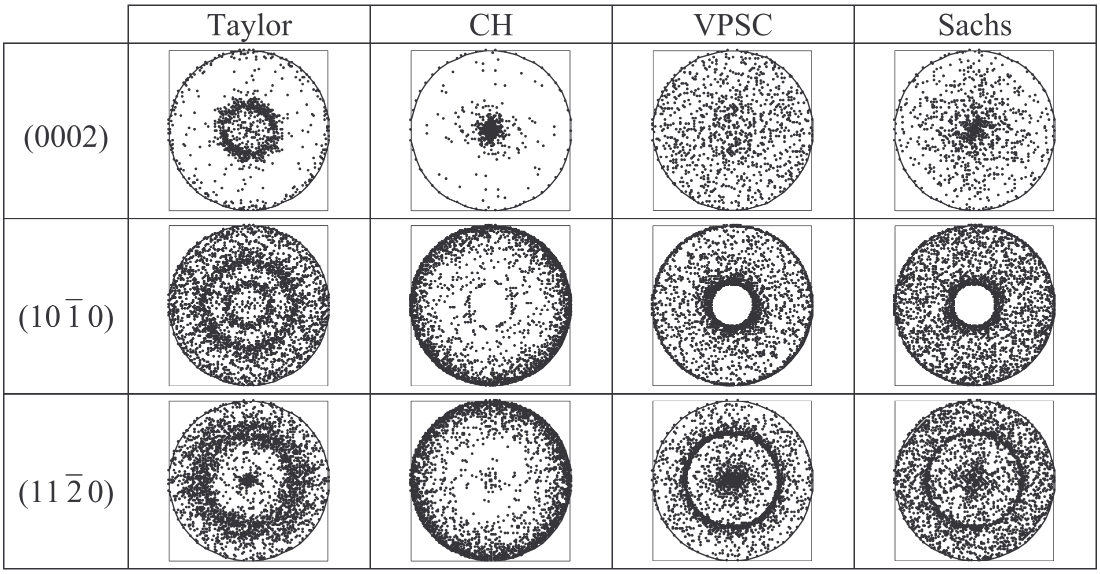

Figure 3. Pole figures using different models for Titanium under compression at ε=-0.6

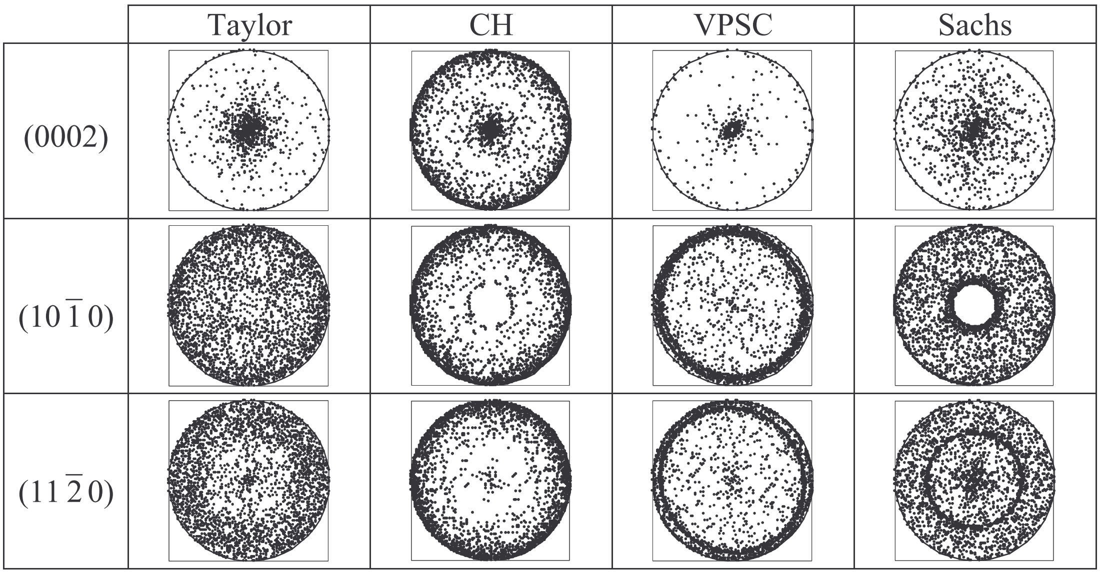

Figure 4. Pole figures using different models for Magnesium under compression at ε=-0.6

References

[1] D.M. Parks and S. Ahzi, *Polycrystalline plastic deformation and texture evolution for crystals lacking five independent slip systems,* J. Mech. Phys. Solids, **38,** 701 (1990)

[2] S.E. Schoenfeld, S. Ahzi and R.J. Asaro, *Elastic-plastic crystal mechanics for low symmetry crystals,* J. Mech. Phys. Solids, **43**, 415 (1995)

[3] S. Ahzi, R. Asaro and D.M. Parks, *Application of crystal plasticity theory for mechanically processed BSCCO super conductors,* Mechanics of Materials, **15**, 201 (1993)

[4] A. Molinari, G.R. Canova and S. Ahzi, *A self-consistent approach of the large deformation polycrystal viscoplasticity,* Acta Metal., **35**, 2983 (1987)

[5] R.A. Lebensohn and C.N. Tomé*, A self-consistent anisotropic approach for the simulation of plastic deformation and texture development of polycrystals: Application to zirconium alloys,* Acta Metal. Mater., **41**, 2611 (1993)

A Coarse Grain Molecular Dynamics Model of Materials Interface Using SPH and DPD Methods

Ken-ichi Saitoh

Department of Mechanical Engineering, Faculty of Engineering,
Kansai University; HRC, Kansai University
3-3-35 Yamate-cho, Suita-shi, Osaka, 564-8680 Japan
E-mail: saitou@ipcku.kansai-u.ac.jp

ABSTRACT

For the purpose of obtaining the atomistic information of materials interface deforming under macroscopically-defined external loading, a combination method of molecular dynamics (MD) and particle methods with coarse grain nature is developed. The particle methods used here are smoothed particle hydrodynamics (SPH) and dissipative particle dynamics (DPD). The model of nano-sized aluminum crystal containing coincidence site lattice (CSL) low-Sigma grain boundary (GB) is constructed and numerical tests are performed. The combined method succeeds in appearance of GB migration caused by tangential shear. Results of stress and displacement agree well with those obtained by pure MD simulations. It is found that interference for deformation by MD-SPH transition is negligible. Then, discussion is performed on the possibility of DPD which is furnished with intermediate nature between MD and SPH.

1. Introduction

Mechanical behavior of materials interface (bi-material interface, grain boundary, or phase boundary) is important for development of advanced materials. Materials interfaces are usually characterized as micro- or nano-structures, whereas characteristic behavior occurs by the effect of external (i.e. macroscopic) loading or constraint. Thus, atomistic simulation offers much insight concerning the structure of material interface, but evaluating its mechanical response under the external effects is of the same importance. The better approach is that both microscopic and macroscopic dynamics are solved concurrently. Bridging space scale (as well as time scale) in problems of materials science and engineering are paid much attention recently. There are several approaches in which multiple computational methods are unified into one theoretical framework[1], such as coarse-grained molecular dynamics(CGMD)[2], FE-MD, QC-MD, or TB-MD approach. In our study, the focused methods are molecular dynamics, dissipative particle dynamics (DPD), and smoothed particle hydrodynamics(SPH). One point is that, since they are all based on mechanics of particle substance (sometimes it is atom, otherwise it is massive continuum body), strong affinity between these methods is expected.

In this paper, first, aluminum grain boundary (GB) model is constructed on a MD-SPH framework. It is shown that shear loading of GB in the MD region can be carried out with adequate transmission of force or displacement through the SPH particles. Furthermore, we discuss the possibility of constructing MD-DPD-SPH framework, where DPD works as buffered methodology between purely microscopic MD and macroscopic SPH.

2. Methods

2.1 Combined method between MD and SPH by force bridging

Although space scale is usually different in MD and SPH methods [3], SPH can be scaled down to atomistic region so as to match atomic configuration treated in MD. We use a force bridging method, the framework of which is introduced by Liu *et al.* as one of possibilities for combining multiple computational methods [4][5]. The system contains MD atoms and SPH particles at the same time. Equations of motions between particles and atoms are:

$$\text{(for MD atoms)}$$

$$\frac{\mathrm{d}v_i^\alpha}{\mathrm{d}t} = -\frac{1}{m_i}\sum_{j=1}^{N_{md1}} \frac{\partial\phi(r_{ij})}{\partial r_{ij}}\frac{r_{ij}^\alpha}{r_{ij}} + \sum_{j=1}^{N_{sph2}} m_j \left(\frac{\sigma_i^{\alpha\beta}}{\rho_i^2} + \frac{\sigma_j^{\alpha\beta}}{\rho_j^2} - \Pi_{ij}\right)\frac{\partial W_{ij}}{\partial r_i^\beta}, \tag{1}$$

$$\text{(for SPH particles)}$$

$$\frac{\mathrm{d}v_i^\alpha}{\mathrm{d}t} = \sum_{j=1}^{N_{sph1}} m_j \left(\frac{\sigma_i^{\alpha\beta}}{\rho_i^2} + \frac{\sigma_j^{\alpha\beta}}{\rho_j^2} - \Pi_{ij}\right)\frac{\partial W_{ij}}{\partial r_i^\beta} + \sum_{j=1}^{N_{md2}} m_j \left(\frac{\sigma_i^{\alpha\beta}}{\rho_i^2} + \frac{\sigma_j^{\alpha\beta}}{\rho_j^2} - \Pi_{ij}\right)\frac{\partial W_{ij}}{\partial r_i^\beta}, \tag{2}$$

where v_i^α is velocity (superscripts, α, β, indicate components hereafter), t is time, r_i^α is position, r_{ij}, r_{ij}^α are interparticle(interatomic) distance and vector, $\phi(r_{ij})$ is interatomic potential function, m_i is mass, ρ_i is density, and $\sigma_i^{\alpha\beta}$ is stress tensor [6]. SPH method requires Π_{ij} and $W_{ij} \equiv W(r_{ij})$, which denote artificial viscosity and kernel function respectively. N_{md1}, N_{sph2} mean the number of atoms or particles which are interacted by an atom i, whereas N_{sph1} and N_{md2} do the number of particles and atoms which are interacted by a SPH particle i. For instance, if an atom is surrounded solely by atoms, N_{sph2} comes to zero. Second term in each equations means atom-particle interaction, which is constructed so as to fulfill action-reaction principle in pairwise manner. We have confirmed that this cross term should be derived from SPH interaction for solid materials because of structural stability [5].

2.2 Computation model and calculation condition

Interatomic potential for MD region is pairwise Lennard-Jones(LJ) type as:

$$\phi(r) = 4e\left\{\left(\frac{s}{r}\right)^{12} - \left(\frac{s}{r}\right)^{6}\right\}. \tag{3}$$

Potential parameters, s, e, shown in Tab.1 are fitted to experimental data of aluminum crystal. In SPH framework, Young's modulus and Poisson's ratio derived from this LJ potential (which are largely deviated from experimental values) are used and the mechanical response is solved assuming linear isotropic elastic medium. The SPH kernel function used here is conventional cubic spline type.

Computational model is shown in Fig.1. On $y = 0$, there is a grain boundary(GB) plane ($\Sigma = 5$ tilt) and periodic boundary condition is applied in x and z directions. MD region includes the GB in the center and is interposed by two SPH regions. Initially, SPH particles are arranged in the same lattice as aluminum atoms aligned in f.c.c. structure. This is not necessary, but can avoid undesirable mismatch arising in coexistence with MD crystal. After sufficient relaxation of structure, external shear is imposed on the system by moving $\pm y$-terminated regions with constant velocity. Calculation conditions are shown in Tab.1.

3. Results & Discussions

Fig.2 shows the energy change of each regions in equilibrating period. Although in early stage there is large change in energy, fluctuation becomes smaller at the end of equilibrating. It is supposed that a stable structure comprising of particles and atoms is obtained.

The $\Sigma = 5$ GB shows diffusive (including rotational) atomic motions caused by tangential shear. Consequently, GB migration perpendicular to GB plane occurs as shown in Fig.3. Regional shear stress is shown in the figure. No strong mismatch in MD-SPH transition region is observed, for both particle arrangement and shear stress. It is found that transmission of force and displacement between MD and SPH regions is carried out appropriately in the present framework.

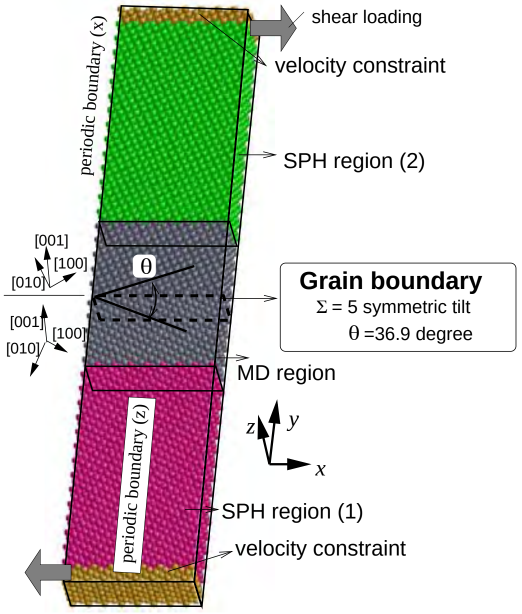

Figure 1: Computation model with grain boundary (MD-SPH combined model).

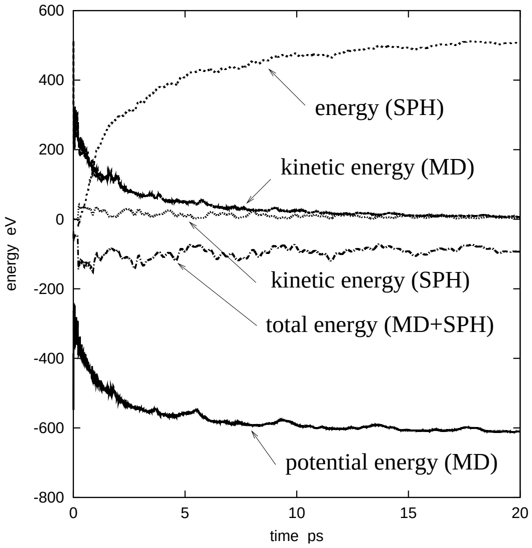

Figure 2: Energy change of MD-SPH system toward equilibrium.

Table 1. Details of calculation model and conditions.

Properties	unit	value
SPH particles	number	11920
MD atoms	number	3960
Particles with constraint	number	800
Cell size (x)	nm	5.123
Cell size (y)	nm	25.61
Cell size (z)	nm	2.025
Shear strain rate	1/s	1.734×10^9
Periodic conditions		on x and z
Numerical integration		Gear's method
Time increment	fs	2.0
Temperature control		no

Properties	unit	value
MD potential parameters		
s	nm	0.2608
e/k_B	K	4948.0
Cutoff length	nm	0.6350
SPH parameters		
Kernel length h	nm	0.2480
Kernel type		cubic spline
Initial density	kg/m^3	2.7×10^3
Young's modulus	GPa	335.2
Poisson's ratio		0.3605

(k_B: Boltzmann constant)

4. Implementation of DPD

The difficulty in performing dissipative particle dynamics (DPD) [7][8] in atomic scale is that there is no obvious information for DPD parameters in the methodology itself. The general expression of DPD is :

$$\frac{\mathrm{d}v_i^\alpha}{\mathrm{d}t} = \frac{1}{m_i}\sum_{j\neq i}(F_{ij}^{C,\alpha} + F_{ij}^{D,\alpha} + F_{ij}^{R,\alpha}), \tag{4}$$

where first, second, and third terms inside parenthesis are conservative force, dissipative force, and random force, respectively. Dissipative term provides particles with mesoscopic viscous nature, and random force leads to thermal fluctuation in finite temperature. A very simple model proposed here is that the conservative force is derived from MD potential (e.g. Eqn.3) by doing $F^{C,\alpha} = -\partial\phi/\partial r^\alpha$. This procedure corresponds to force bridging of MD-SPH combination (Eqn.2). Fig.4 shows the evolving particle configuration of $\Sigma = 5$ GB obtained by solving this DPD equations. Cell-size, total number of particles, and strain rate are identical with Tab.1. It is found that the initial crystalline structure can be kept even in shear loading and GB migration is also produced.

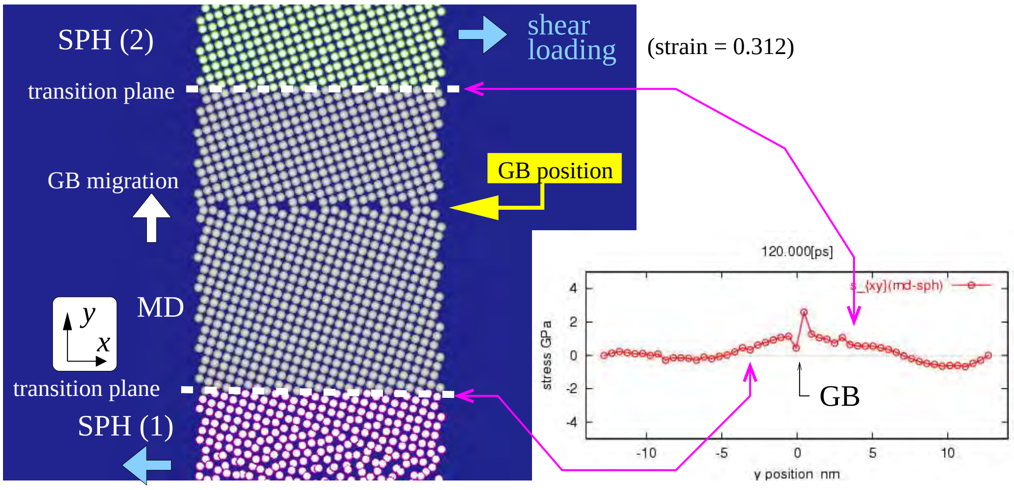

(a) particle (atomic) configuration (b) shear stress distribution (along y)

Figure 3. Atomic configurations during shear loading.

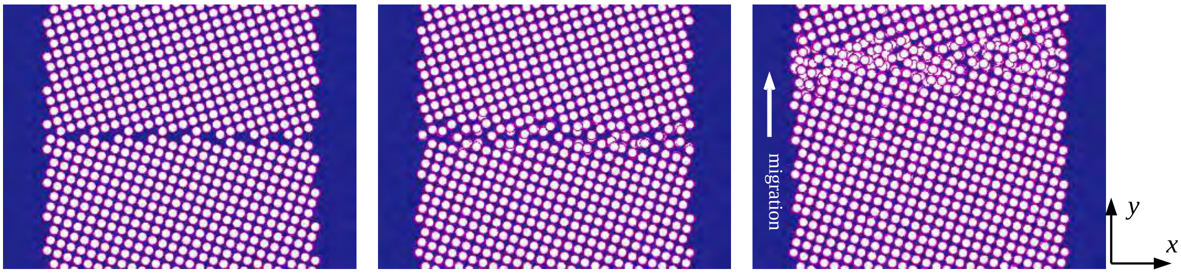

(a) initial state (b) equilibrated (after 20ps relaxation) (c) in shear (strain: 0.42)

Figure 4. An example of DPD results ($\Sigma = 5$ symmetrical tilt grain boundary in shear).

Acknowledgements

This work was partially supported by Ministry of Education, Culture, Sports, Science and Technology, Japan, Grant-in-Aid for Scientific Research on Priority Areas, 18062004, 2006, HRC Kansai University, ORDIST Kansai University, and Grant-in-Aid of Kansai University Jyuten-ryoiki Kenkyu, 2005.

References

[1] *For example:* P.Kohlhoff, P.Gumbsch, and H.F.Fischmeister, Crack Propagation in B.C.C. Crystals Studied with a Combined Finite-Element and Atomistic Model , Philos.Mag., **64**, 851-878, (1992).
[2] R.E.Rudd and J.Q.Broughton, Coarse-grained Molecular Dynamics and the Atomic Limit of Finite Elements, Phys.Rev.,B, **58**, R5893-R5896, (1998).
[3] J.J.Monaghan, Smoothed Particle Hydrodynamics, Annu.Rev.Astron.Astrophys., **30**, 543-574, (1992).
[4] G.R.Liu and M.B.Liu, *Smoothed Particle Hydrodynamics; A Meshless Particle Method*, 341, (2003), World Scientific.
[5] K.Saitoh, Y.Tateoka, and N.Shinke, Dynamics Simulation of Material Interface Using Molecular Dynamics and SPH Methods, *Proceedings of Second International Conference on Multiscale Materials Modeling*, 132-134, (2004).
[6] P.W.Randles and L.D.Libersky, Smoothed Particle Hydrodynamics: Some Recent Improvements and Applications, Comput.Methods Appl.Mech.Engrg., **139**, 375-408, (1996).
[7] P.J.Hoogerbruge and J.M.V.A.Koelman, Simulating Microscopic Hydrodynamic Phenomena with Dissipative Particle Dynamics, Europhys.Lett., **19**, 155-160, (1992).
[8] R.D.Groot and P.B.Warren, Dissipative Particle Dynamics: Bridging the Gap between Atomistic and Mesoscopic Simulation, J.Chem.Phys., **107**, 4423-4435, (1997).

A multiscale model for the cracking resistance of 7000 Al alloys

F.Scheyvaerts[1], **P.R. Onck**[2], **Y. Bréchet**[3], **T. Pardoen**[1]

[1] **Materials Science and Processes Department, Université catholique de Louvain, IMAP, Bâtiment Réaumur, Place Sainte Barbe 2, 1348 Louvain la Neuve, Belgium.**
scheyvaerts@imap.ucl.ac.be, pardoen@imap.ucl.ac.be
[2] **Department of Applied Physics, University of Groningen, Micromechanics of Materials, Nijenborgh 4, 9747 AG Groningen, The Netherlands.**
p.r.onck@rug.nl
[3] **Laboratoire de Thermodynamique et Physico-chimie Métallurgiques, ENSEEG, Institut National Polytechnique de Grenoble, France.**
ybrechet@ltpcm.inpg.fr

ABSTRACT

Fundamental connections between the microstructure and flow properties of a ductile alloy, and its damage have been established. First the competition between an intergranular and/or transgranular mode of fracture is investigated in a heterogeneous representation of the material; next its resistance to the propagation of a pre-existing crack under small-scale yielding conditions is studied. The constitutive description used is an extension of the Gurson model, accounting for void shape effects, void rotation and hardening, including a generalized internal necking condition leading to the loss of the stress carrying capacity.

1. Introduction

In 7000 Al alloys, the microstructure consists of a precipitation-hardened state within the grain, and a precipitate free zone along the gain boundary with large second phase inclusions. Ductile fracture occurs both inside the grains and inside the soft zones along the GB through the nucleation of ellipsoidal voids by precipitate/inclusion cracking or decohesion, their growth and subsequent coalescence. So the same constitutive model is used to simulate damage in both zones, only accounting for the differences in flow properties and microstructural features.

2. Numerical Model

1.1 Void Growth

Pardoen and Hutchinson [1] have developed a Gurson-type void growth model [2] that describes the plastic flow in a continuous porous medium. The model extends the contribution of Gologanu-Leblond-Devaux for the void shape [3] to strain hardening. It is a full constitutive model for a porous elastic-plastic material containing spheroidal voids. In addition, the effect of void rotation due to shear stresses appearing in heterogeneous microstructures is introduced. Due to that, the model contains now ten state variables: the six components of the mesoscopic stress tensor $\mathbf{\Sigma}$, the porosity *f*; the void aspect ratio defined by $S=\ln(W)$ where $W=R_y/R_r$, the void principal axis $\mathbf{n_p}$, and the average yield stress of the matrix material σ_M. The principal axis rotation law is defined thanks to developments made by Kailasam and Ponte Castañeda [4] based on a rigorous homogenization technique [5].

To validate the model for void rotation, its predictions for a pure shear test under plane strain have been compared to 3D unit-cell calculations performed in the finite element commercial code Abaqus. As depicted in Fig. 1, the model is able to capture the fact that the void rotation direction depends on its shape. Indeed, the initially prolate void (W_0=3) rotates clockwise as shear increases, while the oblate void (W_0=1/3) rotates anti-clockwise. In the case of spherical voids (W_0=1), both cell calculation and model confirm that the void starts elongating in the direction of maximum stretching, and corresponds from then to a prolate case.

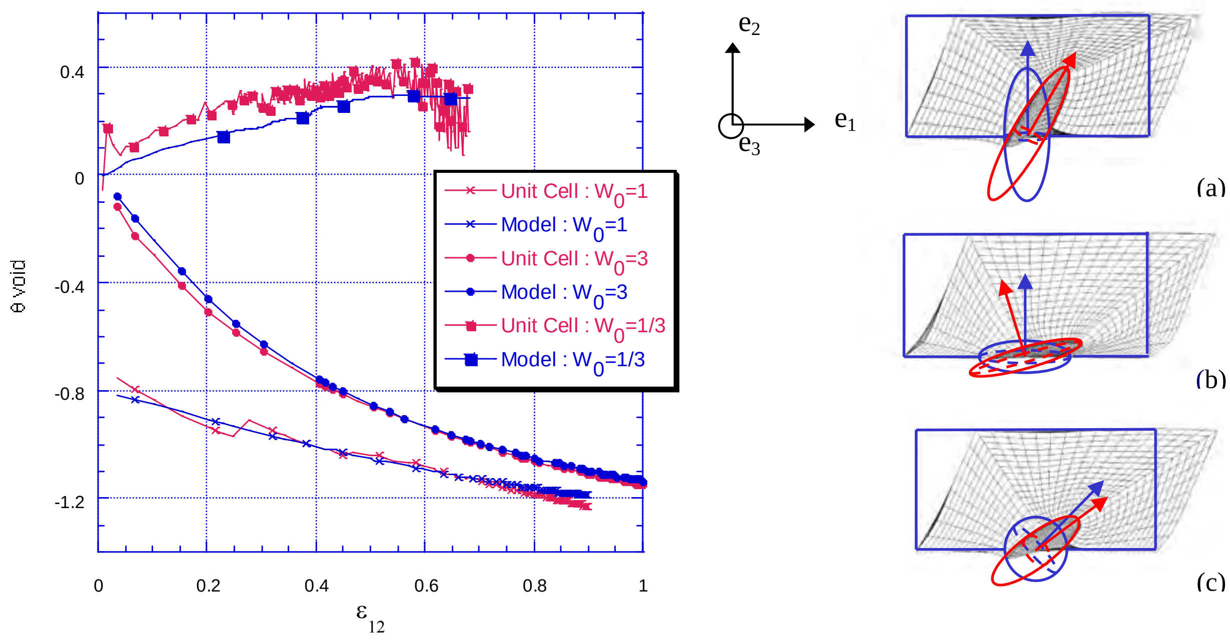

Figure 1. Pure shear test $(\varepsilon_{12}=\gamma\neq 0)$ in plane strain $(\varepsilon_{33}=0)$. Comparison between the model and the unit-cell results for: E/σ_0=100, ν=0.3, n=0.1, f_0=10-2, λ_0=1; and cuts of the deformed 3D unit-cell mesh for (a) W_0=3, (b) W_0=1/3, (c) W_0=1.

1.2 Void Coalescence

The coalescence model directly addresses the mechanism of tensile plastic localization in the ligaments between neighbouring voids, leading to a uniaxial mode of straining. The criterion for the onset of coalescence is based on Thomason's work [6]. According to this criterion, coalescence occurs when the maximum principal stress σ_n reaches a critical value required to initiate the localized internal necking of the intervoid matrix material perpendicular to it. Due to the anisotropy of the present model, this criterion is checked in every direction $\delta\in[-\pi/2,\pi/2]$.

Once the criterion is met (for $\delta=\delta_c$), further straining develops uniaxially in the perpendicular direction to necking with a linear decrease of the normal stress with increasing normal plastic strain, which is consistent with FE void cell calculation results. Finite element void cell calculations are used to tabulate the unloading slopes as a function of the stress triaxiality, the void shape and the relative position of neighbouring voids (e.g. [1]).

3. Competition Between Intergranular and Transgranular Fracture

Cracks propagate preferentially along the GB or through the grains depending on the loading configuration, on the state of hardening and on other microstructural features. We analyze an infinitely large polycrystalline aggregate consisting of hexagonal grains, from which a unit cell can be identified (see Fig. 2(a)). The material is subjected to biaxial loading, with the stress ratio, Σ_{11}/Σ_{22}, remaining constant.

The deformation of the two material parts is described by the constitutive model presented in section 2. The microstructural and micromechanical parameters of the model for typical 7000 aluminium alloys [7] are given in Fig. 2(b). The PFZ is markedly softer than the grain interior, but presenting an enhanced work hardening rate [8]. The PFZ yield stress, specified through the ratio σ_{0g}/σ_{0p}, will take distinct values. Results are presented in Fig. 2(c) in terms of a failure map, i.e. showing the failure mode transition locus in the stress loading Σ_{11}/Σ_{22} ratio versus relative spacing L_{p0}/D_{p0} space.

First the failure map shows that, whatever the flow properties and microstructure, the transgranular failure mechanism is favoured by a low global stress loading as it allows the increase of the stress in the grain without too much void growth within the PFZ. Furthermore, the intergranular mode of fracture is favoured by a high yield stress in the interior of the grains, and a low spacing between second phase inclusions along the PFZ.

(a)

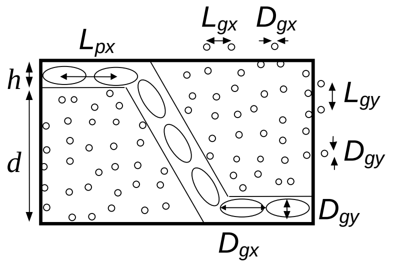

(b)

GRAIN	σ_{0g}/E_g	ν_g	n_g	f_{0g}	W_{0g}	λ_{0g}
	10^{-3}	0.35	0.05	10^{-3}	1	1
PFZ	σ_{0g}/σ_{0p}	ν_p	n_p	f_{0p}	W_{0p}	λ_{0p}
	4-6	0.35	0.3	1.10^{-4}- 8.10^{-2}	1/3	1

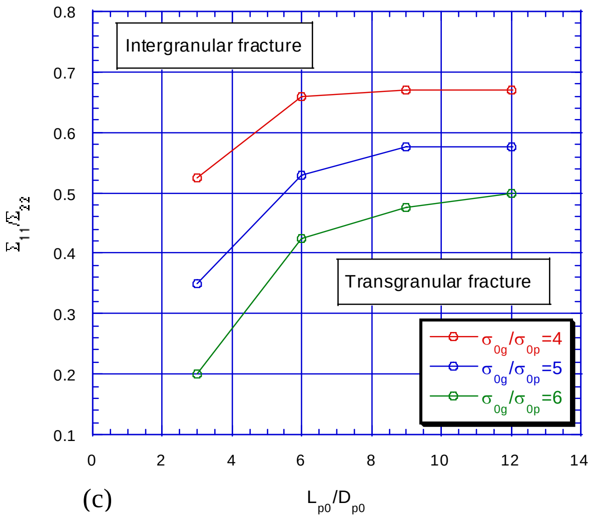

Figure 2. (a) Description of the idealized microstructure and the relative void spacing in the PFZ. (b) Parameters of the model. (c) Effect of the yield stress ratio on the failure mode in a stress loading versus relative particle spacing map

4. Crack Growth Resistance

In the context of material science, the J integral at cracking initiation, J_{Ic}, is usually taken as the relevant parameter for characterizing the toughness of ductile alloys. If J can be measured as a function of the crack extension, it gives the so-called 'J-R curve' of the material. To get it, a small-scale yielding formulation is invoked. The propagation of a macroscopic crack in an infinite elastic-plastic medium loaded remotely by a mode I plane strain elastic crack tip field is simulated (see Fig. 3(a)). The regular mesh designed in the region in front of the crack tip is modelled with the ductile damage model, while the rest is modelled using J_2 flow theory (see Fig. 3(b)). Fig. 3(c) presents computed *J*-R curves for two initial porosities: f_0 =1.71 10^{-3} and f_0 =3.49 10^{-3}, and for three initial void shapes: W_0 = 1/3, 1, 3.

As expected J_{Ic} decreases with increasing f_0. The tearing modulus defined as $T_R = \partial J_R / \partial \Delta a\big|_{small\ a}$ decreases with increasing f_0. Only a small additional void growth is required to fail the following ligaments. Numerically, this means that higher f_0 require smaller process zone to keep the plastic region confined before steady-state crack propagation occurs. The effect of the initial void shape is in accord with intuition. At a given porosity, prolate voids imply a larger intervoid ligament into the fracture plane than oblate shapes. Prolate shapes increase thus $J_{Ic}/\sigma_0 X_0$ while oblate shapes reduce it relative to spherical voids at the same volume fraction. If this is really clear at initiation, the difference tones down with propagation between W_0=3 and W_0=1, while it is maintained with W_0=1/3. This can be explained by considering the void shape evolution for the three cases, but this will not be done here.

The results of Fig. 3 can be used to guide understanding of, as well as to predict the variation of, the fracture toughness as a function of the loading direction for rolled plates with preferential orientation of the second phase.

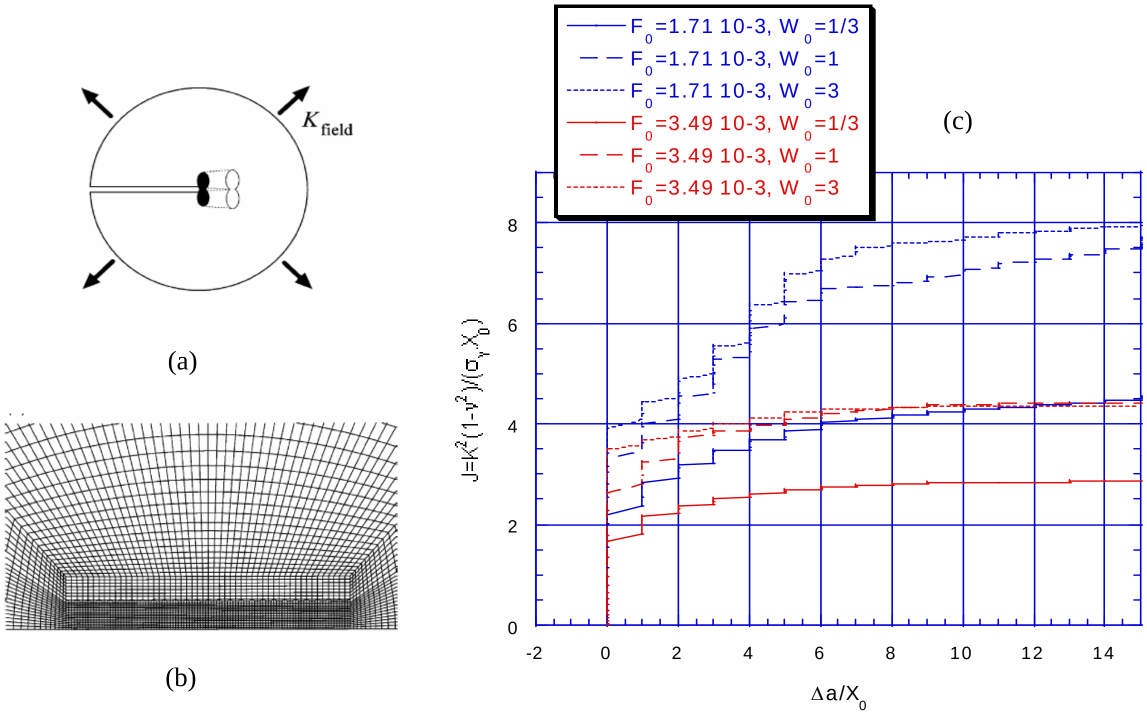

Figure 3. (a) Description of the small scale yielding formulation; (b) zoom of the FE mesh in the near crack tip region; and (c) crack extension curves for σ_0 /E = 0.003, *n* = 0.1, and λ_0= 1.

References

[1] T.Pardoen and J.W.Hutchinson, J. Mech. Phys. Solids, Vol. 48 (2000), 2467-2512.
[2] A.L.Gurson, J. Engng. Mater. Tech. (1977), Vol. 99, 2-15.
[3] M.Gologanu et al., In *Suquet, P. (Ed.) Cont. Micromechanics*, Springer-Verlag (1995).
[4] M.Kailasam and P.Ponte Castañeda, J. Mech. Phys. Solids, Vol. 46 (1998), 427-465.
[5] P.Ponte Castañeda, J. Mech. Phys. Solids, Vol. 39 (1991), 45-71.
[6] P.F.Thomason, *Ductile Fracture of Metals*, Pergamon Press (1990), Oxford.
[7] D.Dumont, A.Deschamps and Y.Brechet, Mater. Sc. Engng., Vol. 356 (2003), 326-336.
[8] T.Pardoen et al., J. Mech. Phys. Solids, Vol. 51 (2003), 637-665.

Atomistic Study of Dislocation Assisted Martensitic Transformation of Cu Precipitate in Fe

Jae-Hyeok Shim[1], **Young Whan Cho**[1], **Sang Chul Kwon**[2], **Whung Whoe Kim**[2]
and Brian D. Wirth[3]

[1]Nano-Materials Research Center, Korea Institute of Science and Technology, Seoul 136-791, Republic of Korea (jhshim@kist.re.kr)
[2]Nuclear Materials Technology Development Division, Korea Atomic Energy Research Institute, Daejon 305-353, Republic of Korea
[3]Department of Nuclear Engineering, University of California, Berkeley, CA 94720, USA

ABSTRACT

Molecular dynamics simulations have been performed to investigate the interaction between a screw dislocation and a coherent, bcc Cu precipitate in bcc Fe. The results indicate that for Cu precipitates of diameter larger than 1.8 nm, the stress field of a screw dislocation assists the martensitic transformation of the Cu precipitate, thereby increasing the precipitate resistance to dislocation motion and a shear bypass interaction. The transformed, close-packed precipitate consists of mixed hcp and fcc stacking and is nucleated from within the precipitate. The observed martensitic transformation mechanism is in agreement with the Nishiyama-Kajiwara model.

1. Introduction

Fe-Cu alloys offer an ideal alloy system to study precipitation hardening due to the very low solubility of Cu in Fe at low temperatures. Therefore, a large number of experimental studies have been devoted to these alloys. Cu precipitates were known to undergo the transformation sequence of bcc→9R→3R→fcc, with increasing size during thermal aging [1]. The 9R structure is close-packed, with a stacking sequence of ABCBCACAB, which can also be thought of as a heavily (stacking-) faulted fcc structure or, alternately as a mixed structure where hexagonal close-packed (hcp) and fcc stacking repeats with a ratio of 2:1. The 3R structure can be regarded as a distorted fcc structure. In addition to experimental investigations, the structural evolution of bcc Cu precipitates in Fe has been studied by theory and modeling, including atomistic simulations. However, the detailed atomistic mechanism for this transformation is not fully known.

In this work, we present large-scale MD simulations of the interaction between a screw dislocation and a bcc Cu precipitate in Fe. These results elucidate the different interaction and detachment mechanism of the screw dislocation from coherent precipitates compared to an edge dislocation, and demonstrates that the stress field of the screw dislocation influences a structural transformation of the precipitate.

2. Simulation methods

The MD simulations use a modified version of the MDCASK code [2] with the Finnis-Sinclair potentials fit by Ackland *et al.* [3] to describe the atomic interactions of Fe-Fe, Cu-Cu and Fe-Cu. The simulation cell consists of a bcc Fe cell, bounded by {112}, {111} and {110} faces in *X*, *Y* and *Z* directions, respectively. The cell dimensions are approximately 14 x 25 x 28 nm (*X*, *Y* and *Z* directions) and contain 840,000 atoms. A coherent bcc Cu precipitate, with diameter 2.5 nm, is placed at the center of the cell about 6 nm away from the screw dislocation, which is introduced based on the continuum elastic displacement field.

Before applying a shear stress, the cell is equilibrated for 50 ps at 10 K. A constant shear stress of 1,000 MPa is applied by superimposing a constant (equal and opposite) force in the [111] direction on the atoms in the outermost $(\bar{1}\bar{1}2)$ and $(11\bar{2})$ surfaces.

3. Results and discussion

Figure 1 presents snapshots in time from an MD simulation of the interaction between a screw dislocation and a 2.5 nm diameter Cu precipitate with an applied shear stress of 1,000 MPa (left side), and the corresponding atomic configurations of the precipitate (right side). After applying the shear stress, the screw dislocation glides toward the precipitate on the $(\bar{1}\bar{1}2)$ plane by kink pair nucleation and propagation along the dislocation line (Fig. 1a). Fig. 1b shows the configuration at 27 ps after applying the shear stress, when the screw dislocation begins to intersect and slightly penetrate the precipitate. However, the screw dislocation is unable to glide further within the precipitate and remains pinned. The dislocation line outside the precipitate continues to glide forward and loops around the precipitate until reaching a critical bowing angle of nearly 0 degrees (Fig. 1c). As the dipole segments of the dislocation surrounding the precipitate strongly interact and annihilate on the departure (left) side of the precipitate, the screw dislocation is able to detach from the precipitate, leaving an Orowan loop (Fig. 1d). For comparison, an MD simulation of the interaction between an edge dislocation and a 2.5 nm diameter bcc Cu precipitate reveals little resistance of the precipitate to the dislocation bypass by the anticipated shear mechanism. Thus the precipitate resistance to the motion of a screw versus an edge dislocation is significantly stronger and responsible for the different interaction and detachment mechanism, i.e. Orowan looping for the screw dislocation and shear for the edge dislocation.

As the screw dislocation approaches the 2.5 nm diameter precipitate, a significant fraction of Cu atoms within the precipitate transform from the original bcc structure. The majority of the transformed Cu atoms have an hcp structure, some Cu atoms in a single $(1\bar{1}0)$ layer transform into an fcc structure, as shown in Fig. 1b. The transformation appears martensitic (or displacive) in nature, because no vacancies are observed inside the precipitate or at the interface and the simulation temperature (10K) is too low to stimulate thermally-activated processes. As the dislocation loops around the precipitate and detaches, many of the transformed Cu atoms revert back to the original structure (Fig. 1c). Then, as the dislocation subsequently continues to glide beyond the precipitate, nearly all of the transformed Cu atoms return to the original structure (Fig. 1d), even as the Orowan glide loop remains. In the case of an edge dislocation interaction with a 2.5 nm diameter Cu precipitate, only a very small fraction of Cu atoms exhibit a similar transformation behavior before the edge dislocation intersects the precipitate. Therefore, it is assumed that the difference in the bypass mechanism observed for the screw and edge dislocation interaction with a 2.5 nm diameter Cu precipitate is associated with the internal structural transformation.

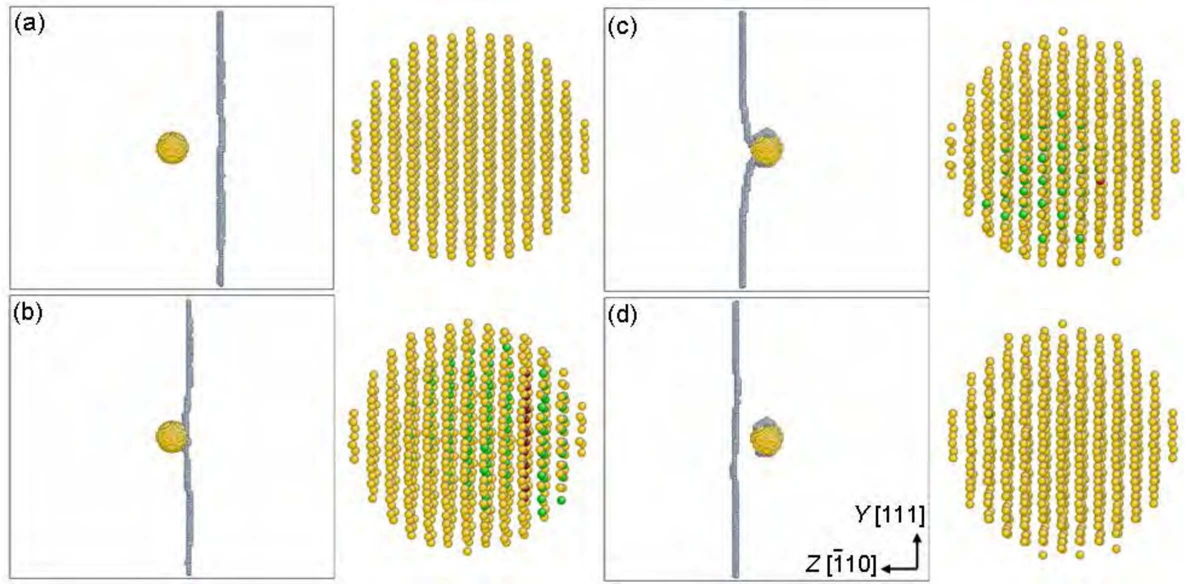

Figure 1. Snapshots in time from the MD simulation of the interaction between a screw dislocation and a 2.5 nm diameter bcc Cu precipitate at 10 K with an applied shear stress of 1,000 MPa at (a) 12, (b) 27, (c) 53, and (d) 60 ps. The gray balls represent atoms in the screw dislocation core, while the yellow, red, and green balls represent Cu atoms in the bcc, fcc and hcp structures, respectively.

The structure and displacement of Cu atoms in the 2.5 nm precipitate shows that the transformation occurs by the shear of $(\bar{1}10)$ planes of Cu atoms in the $[\bar{1}\bar{1}0]$ direction (Fig. 2). Thus the $(\bar{1}10)$ bcc planes become the close-packed planes of the transformed phase, which realizes the Kurdjumov-Sachs orientation relationship between the transformed and untransformed regions of the precipitate (and matrix). This transformation mechanism agrees with that first proposed by Nishiyama and Kajiwara [4] in order to explain the martentistic transformation in a Cu-Al alloy.

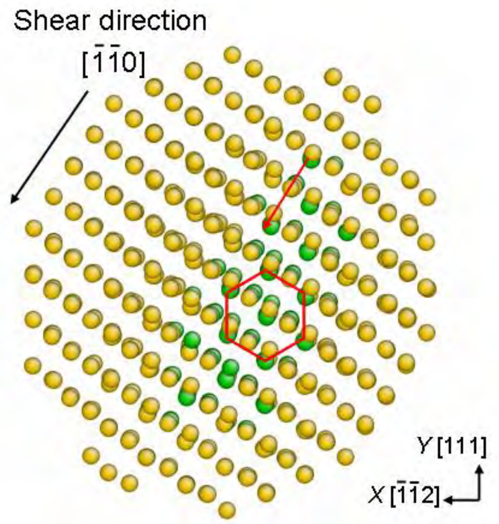

Figure 2. Atomic displacement of Cu atoms within the 2.5 nm diameter precipitate during the transformation at 22 ps after applying a 1000 MPa shear stress to move the screw dislocation. The yellow and green balls represent the Cu atoms in bcc and hcp structures, respectively.

5. Conclusions

The stress field of a screw dislocation assists the reversible transformation of bcc Cu precipitates of 2.5 nm diameter into a close-packed, but incoherent structure in bcc Fe. The transformation mechanism nucleates within the precipitate and is martensitic in nature. The precipitate resistance to screw dislocation glide is significantly larger for transformed precipitates, resulting in screw dislocation bypass by Orowan looping around the precipitate.

Acknowledgements

This study has been sponsored by the Ministry of Science and Technology, Republic of Korea under the Nuclear R&D Program.

References

[1] P.J. Othen, M.L. Jenkins, and G.D.W. Smith, "High-resolution microscopy studies of the structure of Cu precipitates in α-Fe," Philos. Mag. A **70**, 1 (1994).
[2] T. Diaz de la Rubia and M.W. Guinan, "Progress in the development of a molecular dynamics code for high-energy cascade studies," J. Nucl. Mater. **174**, 151 (1990).
[3] G.J. Ackland, D.J. Bacon, A.F. Calder, and T. Harry, "Computer simulation of point defect properties in dilute Fe-Cu alloy using a many-body interatomic potential," Philos. Mag. A **75**, 713 (1997).
[4] Z. Nishiyama and S. Kajiwara, "Electron microscope study of the crystal structure of the martensite in a copper-aluminum alloy," Jpn. J. Appl. Phys. **2**, 478 (1963).

The development of micro deformations theory: the account of polycrystalline material grain sizes

Yuriy A. Chernyakov[1], **Vladimir P. Shneider**[1]

[1] **Theoretical and Applied Mechanics department, Dnepropetrovsk National University, Naukovy, 13, Dnepropetrovsk, Ukraine, 49050, shneider_vova@mail.ru**

ABSTRACT

In the given work the new treatment of the plasticity theory of micro deformation with the purpose of introduction of micro particle sizes is offered. The micro volume is defined by the grain, its yield locus is set by Hall-Petch relationship, and distribution of grain sizes in a sample is set statistically. Such approach allows using physical data on distribution of grain sizes for definition of universal functions of a material.

1. Introduction

Recently the big interest to theories of plastic deformation of polycrystals is shown. The analysis of the results received in this direction allows to draw the conclusion that the micro structural approach is the most perspective. Slip theories like theory of Batdorf and Budiansky, physical theories of Lin type and structural models of type of Masing model concern to such approach.

In due time Novozhilov and Kadashevich [1] had been offered the theory of plasticity considering micro stresses which also concerns to micro structural theory. In this theory heterogeneity of representative macro volume was considered; thus it was supposed, that the micro particles making macro volume, are homogeneous and differ in local yield loci $\tau_k, k = 1..K$. Distinctive feature of the theory was that incompatibility of plastic deformation of micro particles is considered by means of so-called internal micro stresses. The statistics of distribution of yield loci of micro particles in representative macro volume was initially set.

Further this direction was developed by Novozhilov, Kadashevich and Chernyakov [2, 3]. In this variant of the theory which received the name of the theory of micro deformations, micro particles were characterized as well by the certain direction of micro plastic deformation $\hat{\mu}_m \in \Omega,\ m = 1..M$ .The distribution of possible directions of micro plastic deformation is defined by structural features of material. It helped to establish deep connection of the micro deformations theory with slip theories and physical theories of plasticity. The fact that by means of linear relationship at micro level it was possible to describe such complex nonlinear effects at macro level, as modification of yield surface and plastic deformation at complex loading, including cyclic, was demonstrated in the variant of the theory, in which the local yield loci were equal.

The certain lack of micro structural theories is their high degree of phenomenologicalness. Though it is declared the physicalness of basic relationships at the formulation of similar sort of theories, but actually all constants of material or universal functions demand definition from base experiments.

2. New variant of theory of micro deformations

In the given work attempt to give greater physicalness of the theory is undertaken. The new treatment of the theory with the purpose of introduction of the geometrical sizes of micro particles is offered. In the further only originally isotropic materials is accepted and as consequence all possible directions of micro plastic deformation are equivalent in Ω and distribution of local yield loci τ_k is identical to each direction $\hat{\mu}_m$. In the further for numbering a particle we shall use an index $n = k \cdot M + m,\ n = 1..N, N = K \cdot M$. Constitutive relations here are presented for the case of small strains.

While constructing the local law of deformation of *n*-th micro particle, micro strain rate tensor $\dot{\hat{\varepsilon}}_n$ is represented, how it is usual, in the form of the sum of elastic $\dot{\hat{\varepsilon}}_{en}$ and plastic $\dot{\hat{\varepsilon}}_{pn}$ components

$$\dot{\hat{\varepsilon}}_n = \dot{\hat{\varepsilon}}_{en} + \dot{\hat{\varepsilon}}_{pn}. \tag{1}$$

We accept that macro plastic deformation is obtained by averaging of micro plastic deformation throughout representative macro volume

$$\hat{\varepsilon}_p = \sum_{n=1}^{N} \hat{\varepsilon}_{pn} \Delta \nu_n \equiv \left\langle \hat{\varepsilon}_{pn} \right\rangle. \tag{2}$$

Here $\Delta \nu_n \ \left(\sum_{n=1}^{N} \Delta \nu_n = 1 \right)$ is relative volume of *n*-th micro particle in representative macro volume. Distribution of the sizes of micro particles in macro volume is defined by known experimental data on distribution of the sizes of grains in a material.

Micro stress rate tensor $\dot{\hat{\sigma}}_n$ we shall present in the form of

$$\dot{\hat{\sigma}}_n = \dot{\hat{\tau}}_n + \dot{\hat{\rho}}_n, \tag{3}$$

meaning, as well as in [4], under tensors $\dot{\hat{\tau}}_n$ and $\dot{\hat{\rho}}_n$ dissipative and elastic component of rate of resistance to plastic deformations. Such representation is connected to the fact that at closed loop deformation a part of plastic deformation work is always reversible, that is caused by existence of micro elastic forces. The mechanism of occurrence of these micro elastic forces consists of that elastic and plastic deformations don't satisfy the condition of strain compatibility separately, but their sum does. From here non-uniform plastic deformation always is accompanied by non-uniform elastic deformation, which is associated with occurrence of the internal elastic forces. These forces react to plastic deformation (and in some cases, for example at unloading and opposite loading, on the contrary, assist it).

Following [4], tensor of dissipate forces $\hat{\tau}_n$ is specified by the law of plastic flow

$$\hat{\tau}_n = \tau_n \hat{\mu}_n,\ \hat{\mu}_n = \dot{\hat{\varepsilon}}_{pn} / \dot{\lambda}_n, \tag{4}$$

where $\dot{\lambda}_n$ ($\dot{\lambda}_n = \sqrt{\frac{1}{2} \dot{\hat{\varepsilon}}_{pn} : \dot{\hat{\varepsilon}}_{pn}}$) - intensity of micro strain rate, τ_n - particle yield locus, defined by Hall-Patch relationship: $\tau_n = \tau_0 + B d_n^{-1/2} = \tau_0 + B \cdot \nu_0 \cdot \Delta \nu_n^{-1/6}$, where ν_0 - volume of characteristic representative macro volume of the material, defined experimentally. We shall present tensor $\hat{\mu}_n$ in the form of $\hat{\mu}_n = \sqrt{2}\left(\cos(\varphi_n)\hat{\alpha}_n + \frac{1}{\sqrt{3}}\sin(\varphi_n)\hat{i} \right)$, where $\hat{\alpha}_n$ - directing deviator, $\hat{i}$ - identity tensor, $\varphi_n \in \left(0; \frac{\pi}{2} \right)$ - particle dilatation angle. At $\varphi_n = 0$ we receive the theory earlier considered in [5]. Introduction $\varphi_n \neq 0$ allows receiving strain tensor with nonzero trace, so we obtain plastic dilatation and can apply this theory to describing low-cycle fatigue (description of such using is outside of the topic of this paper).

Relationships (4) are valid only for active micro plastic deformation which takes place when

$$\sqrt{\frac{1}{2}\hat{\tau}_n : \hat{\tau}_n} = \tau_n \text{ and } \dot{\lambda}_n > 0 . \tag{5}$$

It is possible to show, that such relationships lead to known condition of plasticity of Schleicher-Mises.

When relationship (4) is not valid, unloading under the elastic law takes place

$$\dot{\hat{\sigma}}_n = \tilde{G} : \dot{\hat{\varepsilon}}_{en} , \tag{6}$$

where $\tilde{G}$ - the fourth rank tensor (a matrix of elastic rigidity) which enters the name so

$$\tilde{G} = \frac{E}{1+\nu}\left[\frac{1}{2}\tilde{I} + \frac{\nu}{1-2\nu}\hat{i}\hat{i} \right], \tag{7}$$

where E and ν - Young's modulus and Poisson's ratio of a particle, identical both at macro and at micro level, $\tilde{I}, \hat{i}$ - identity tensors of fourth and second rank accordingly.

We shall accept internal micro stress rate tensor in the following generalized kind [5]

$$\dot{\hat{\rho}}_n = \begin{cases} R_{1n}\dot{\hat{\varepsilon}}_{pn} + \left(R_{2n} + R_{4n}\sqrt{\hat{\rho}_n : \hat{\rho}_n} \right)\dot{\hat{\varepsilon}}_p : \hat{\mu}_n\hat{\mu}_n + R_{3n}\left\langle \dot{\lambda}_n \right\rangle \hat{\mu}_n & \hat{\mu}_n = \hat{\mu}_{n'} \text{ and } \tau_n = \tau_{n'} , \\ \left(R_{2n} + R_{4n}\sqrt{\hat{\rho}_n : \hat{\rho}_n} \right)\dot{\hat{\varepsilon}}_p : \hat{\mu}_n\hat{\mu}_n + R_{3n}\left\langle \dot{\lambda}_n \right\rangle \hat{\mu}_n & \hat{\mu}_n \neq \hat{\mu}_{n'} \text{ or } \tau_n \neq \tau_{n'} , \\ -\left(R_{1n} + A_n \right)\dot{\hat{\varepsilon}}_{pn} + \left(R_{2n} + R_{4n}\sqrt{\hat{\rho}_n : \hat{\rho}_n} \right)\dot{\hat{\varepsilon}}_p : \hat{\mu}_n\hat{\mu}_n + R_{3n}\left\langle \dot{\lambda}_n \right\rangle \hat{\mu}_n & \hat{\mu}_n = -\hat{\mu}_{n'} \text{ and } \tau_n = \tau_{n'} , \end{cases} \tag{8}$$

where $\hat{\mu}_{n'}$ and $\tau_{n'}$ - deformation direction and yield locus of the particle deformed actively, $R_{1n}, R_{2n}, R_{3n}, R_{4n}$ - material constants.

For establishment of connection of local laws of micro plastic and macroscopical deformation we shall take advantage of Crener relationship

$$\dot{\hat{\sigma}} - \dot{\hat{\sigma}}_n = A_n\left(\dot{\hat{\varepsilon}}_{pn} - \dot{\hat{\varepsilon}}_p \right), \tag{9}$$

where A_n - material constant.

From the foregoing it is possible to obtain

$$\dot{\hat{\varepsilon}}_p = \dot{\hat{\sigma}} : \left(\left\langle \frac{1}{D_{1n}} \hat{\mu}_n \hat{\mu}_n \right\rangle - D_4 \left\langle \frac{D_{3n}}{D_{1n}} \hat{\mu}_n \right\rangle \left\langle \frac{1}{D_{1n}} \hat{\mu}_n \right\rangle \right) : \left(\tilde{I} + \left\langle \frac{D_{2n}}{D_{1n}} \hat{\mu}_n \hat{\mu}_n \right\rangle - D_4 \left\langle \frac{D_{3n}}{D_{1n}} \hat{\mu}_n \right\rangle \left\langle \frac{D_{2n}}{D_{1n}} \hat{\mu}_n \right\rangle \right)^{-1}, \tag{10}$$

where averaging is carrying out only on those particles that are deformed actively and $D_{1n} = R_{1n} + 2A_n, D_{2n} = 2R_{2n} - A - 2R_{4n}\sqrt{\hat{\rho}_n : \hat{\rho}_n}, D_{3n} = 2R_{3n}, D_4 = \left(1 + \left\langle \frac{D_{3n}}{D_{1n}} \right\rangle \right)^{-1}$. The equations (1)-(10) make the closed system of constitutive relations. It is necessary to apply the algorithms in detail described in [4] to reception of numerical results.

3. Conclusions

Authors analyzed experimental data about structure of material and the uniaxial tension-compression diagrams for various materials. The analysis has shown good concurrence of experimental data to theoretical predictions; these results in connection with limitation of volume of given paper are not presented. Thus, the similar approach can be widespread on complex loading also. In particular, we shall note, that application the tensor of general view as tensor of direction of micro plastic deformation allows, first, to simplify the procedure of numerical reception of result due to preliminary integration in tensor space of all averaged variables (see $\langle \ldots \rangle$), secondly, to receive influence of the first invariant of tensor of micro stress on process of deformation and to describe behavior of materials, resisting differently to tension and compression. It can be shown, that within the limits of such model the description of plastic dilatation and construction of low-cycle fatigue theory is possible.

References

1. Kadashevich, Yu.I., and Novozhilov, V.V. (1968). “On the effect of micro pre-stresses in the theory of plasticity.” *Eng.J.Solids Mechanics*, 3, 81-91. (in Russian).
2. Kadashevich, Yu.I., Novozhilov, V.V., Chernyakov, Yu.A. (1985). “Theory of plasticity including micro strains.” *Proc. of USSR AS,* 284(4), 821-823. (in Russian).
3. Kadashevich, Yu.I., Novozhilov, V.V., Chernyakov, Yu.A. (1986). “Theory of plasticity and creep including micro strains.” *Applied Mechanics and Mathematics,* 50(6), 890-897. (in Russian).
4. Kadashevich, Yu.I., and Chernyakov, Yu.A. (1992). “Theory of plasticity, taking into account micro stresses.” *Advances in Mechanics*, 15(3-4), 3-39.
5. Chernyakov, Yu.A., and Shneider, V.P. (2006). “The description of complex cyclic loading in the theory of the plasticity, taking into account micro strains.” *Proc. of AS of Ukraine*, in press. (in Russian).

Development of Representations of Microstructural Information Using Automated Classification and Automated Basis Function Generation Methods

Jeff Simmons[1], *D. Dimiduk*[1], *M DeGraef*[2]

[1]*Air Force Research Laboratory, AFRL/MLLMD, Wright-Patterson AFB, 45433 Dayton, United States of America*
[2]*Department of MS&E, Carnegie Mellon University, 15213 Pittsburgh, USA*

In the past, most materials development efforts were typically data limited, progress being paced by the generation of key experimental information. Computerized data collection of experimental information as well as computer simulation techniques are shifting this limitation from a data limitation to an analysis limitation. It is foreseen that data will be collected in large quantities and stored as analysis techniques are developed that are capable of handling the volumes of information. For this purpose, it is necessary to

develop representation techniques that preserve, as nearly as possible, the full fidelity of the data collected. It is also necessary that these techniques themselves be automated to the degree possible, in order to keep pace with the data collection. To this end, we have worked with developing automated methods of reducing microstructural data to abstract representations, using a basis function approach in which images are represented by superposition of automatically generated basis functions. The problem encountered in this approach is that there is a statistical dependence between the basis functions, significantly increasing the complexity of the representation. Classification techniques promise to reduce this statistical dependence by separating the empirical collection of images into classes that are morphologically similar and to develop separate representations within each class. Additionally, since classification techniques do not rely on averaging, rare events are highlighted and can be detected automatically. This work reviews our efforts on using classifiers and automated basis function generators to develop automated representation methods of the particle coordination information in microstructures.

Phase field coarsening model for Ni-Al-Ti ternary alloys

Gaurav Singh[1], Sundar Amancherla[1], Jiang Liang[2]

[1]GE Global Research, Bangalore, India, Gaurav.Singh2@ge.com,
[2] GE Global Research, Niskayuna NY, USA

ABSTRACT

A phase field model is developed for microstructural evolution of γ/γ' precipitates in a model Ni-Al-Ti ternary alloy. The objective of the study is to develop a multi-component phase-field model to treat γ/γ' in a Ni-Al-Ti alloy. The model is directly linked with the thermo-kinetic databases for the thermodynamic and mobility data. Growth and coarsening kinetics of the γ' precipitates have been investigated in both isothermal and non-isothermal conditions. The results of the model depicting morphological evolution of the two-phase region are in good agreement with experimental observations. The model can be extended to multi-component alloys.

1. Introduction

The development of improved alloys for the aviation industry requires significant time and effort. Typical changes to an existing alloy composition often require a multi-year program. Computer simulation methods can be used to significantly reduce the development cycle by predicting the behavior of the material with out a large experimental effort. However, the computational modeling efforts do need a complimentary experimental effort in order to validate the models. Some of the critical experiments can be used to bridge the gaps in understanding of materials behavior and hence results in improved models.

The microstructure of a material largely determines its various mechanical properties e.g. yield, creep and fatigue strength. Phase field modeling (PFM) has been extensively used for microstructure evolution during phase transformations in Ni-based superalloys [1] by many researchers to date. The majority of the phase field models are constructed to model a binary alloy and they use a free energy functional whose chemical free energy component is obtained by fitting a parabolic form to the experimental data [2,3]. A more realistic microstructural prediction in Ni-based superalloys requires a multi-component model that is linked with the thermodynamic databases to capture the correct form of the chemical free energy. Recently, Phase field models have been developed to simulate multi-component alloys by linking chemical free energy component of the free energy functional in the phase field model to critically assessed databases [4,5,6].

A similar approach has been adopted here to construct the free energy functional for the phase field model for Ni-Al-Ti system. This model demonstrates its capability of being a unified model that is multi-component in nature, and is linked to thermo-kinetics databases and incorporates the strain energy effects on the microstructural evolution.

2. Model

For γ/γ′ two-phase, multicomponent system, a phase parameter (also called order parameter) ϕ(x,t) can be postulated to characterize the phase of the system. ϕ(x,t) is defined to vary continuously from 0 to 1 from γ to γ′ phase with values between 0 and 1 at the interfacial region. In phase field description, a free energy functional F (ϕ, c1, c2…) for multi-component system is a function of order parameter and solute concentrations [7].

$$F = \int_V \left[f(\phi, c_1, c_2, \ldots c_n) + \frac{\varepsilon^2}{2} |\nabla \phi|^2 + e(strain) \right] dV. \tag{1}$$

Where *f* is the free energy density, which may be written as follows

$$f(\phi, c_1, c_2, \ldots c_n) = h(\phi) f^{\gamma}(c_1, c_2, \ldots c_n) + [1 - h(\phi)] f^{\gamma'}(c_1, c_2, \ldots c_n) + \omega g(\phi), \tag{2}$$

where f^{γ} and $f^{\gamma'}$ are the free energy densities of γ and γ′ phases respectively. The interfacial region characterized by the interpolation functions h (ϕ) and g (ϕ) are defined as follows

$$h(\phi) = \phi^3(6\phi^2 - 15\phi + 10), g(\phi) = \phi^2(1-\phi)^2. \tag{3}$$

The diffusion equations for multi-component systems [8] and phase field equation can be written as follows

$$\frac{\partial c_k}{\partial t} = \nabla \sum_{j=1}^{n-1} L''_{kj}(T, c_i, \phi) \nabla \frac{\delta F}{\delta c_j} \tag{4}$$

$$\frac{\partial \phi}{\partial t} = -L \nabla \frac{\delta F}{\delta \phi} = -L\left(\frac{\partial f}{\partial \phi} - \varepsilon^2 \nabla^2 \phi\right) \tag{5}$$

The chemical mobility, L''_{kj}, is modeled as [8]:

$$L''_{kj} = \frac{1}{V_s} \sum_{j=1}^{n} \sum_{r=1}^{n} \left[\delta_{ir} - c_i \left(\frac{V_r}{V_m} \right) \right] \left[\delta_{jk} - c_k \left(\frac{V_k}{V_m} \right) \right] L_{jr} \tag{6}$$

The model parameters ε and ω are related to the interfacial energy and interfacial thickness. The free energy densities for γ and γ′ phases and mobility values have been extracted from TTNi ™ and NIST ™ databases [9]. The strain energy functional is based on the Khachaturyan's theory of structural phase transformation [2].

3. Numerical Simulation

Two-dimensional (simulation size ~1μm^2) simulations have been carried out to characterize the growth and coarsening of γ′ precipitates in isothermal and non-isothermal conditions.
At a temperature of 1273 K, we selected the following two systems from Thermo-Calc ™ [10]:

(A) Al = 0.07 and Ti = 0.07,
(B) Al = 0.078 and Ti = 0.075 mole-fraction,

having 32 and 45 % equilibrium volume fractions of γ′ precipitates respectively. To ensure good statistics for studying coarsening kinetics, few thousand particles (with equilibrium volume fraction) were introduced into the system for microstructure evolution. Circular precipitates of sizes between 10-40 nm were distributed randomly in the starting microstructure. The system is allowed to evolve up to few hundred particles by solving diffusion and phase-field equations. For non-isothermal simulation a constant cooling rate of 1Kτ^{-1} was chosen for system (B) to study the effect of cooling rate on evolution kinetics.

4. Results and Discussions

The particle size distributions (PSD) for system (A) and (B) as functions of time (non-dimensional) are shown in Fig. 1 and Fig. 2, respectively.

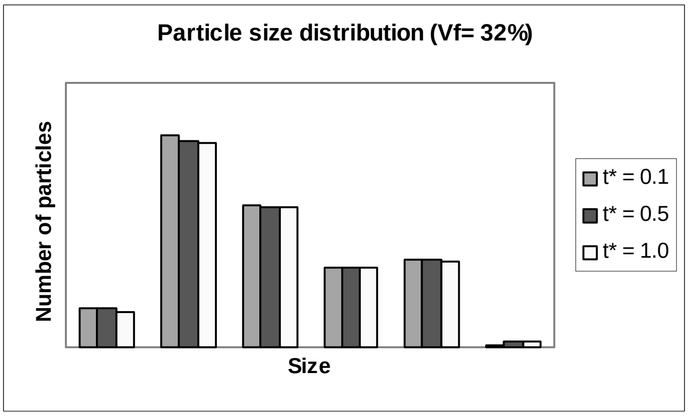

Figure 1. PSD evolution for system (A), (t* is non-dimensional time)

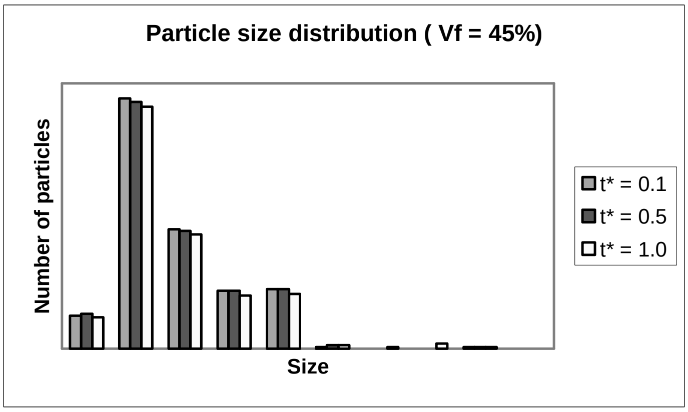

Figure 2. PSD evolution for system (B), (t* is non-dimensional time)

The distributions systematically shift towards the larger γ' precipitates as the microstructure evolves with time, indicating the coarsening of γ' precipitates.

The microstructural development for the non-isothermal case is shown in Fig. 3. We can observe that the growth and coarsening of γ' precipitates takes place simultaneously. The model captures the increasing equilibrium volume fraction of γ' precipitates as the temperature decreases during the slow cooling (see Tab. 1).

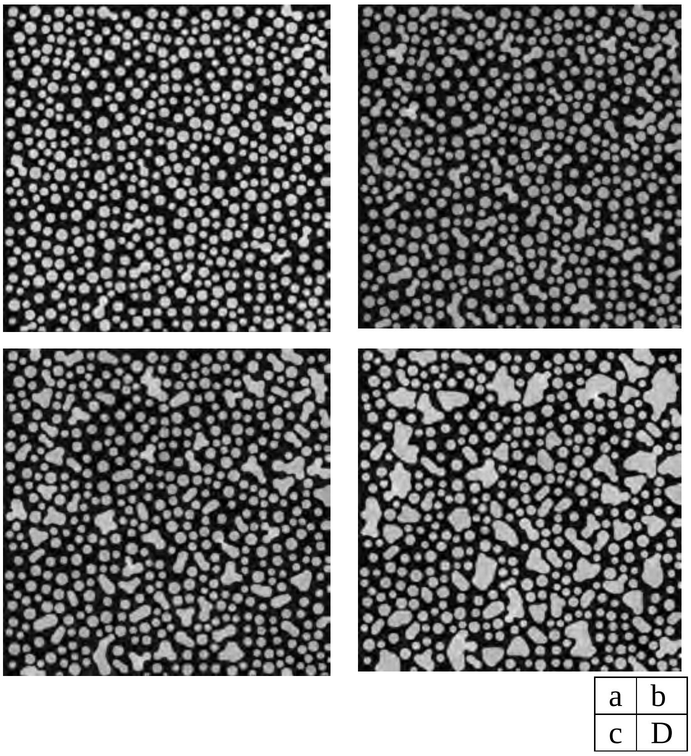

Figure 3 Simulated microstructural development for system (B) upon cooling ($1K\tau^{-1}$). (a)-(d) correspond to the reduced times τ = 1, 5, 10 and 25.

Table 1
Equilibrium volume fractions of γ' precipitates at different temperatures for system (B) when applied a constant cooling rate of $1K\tau^{-1}$.

Temperature (^oC)	Eq. V.f. predicted by Thermo-Calc ™	Eq. V.f. predicted by the model
999	45.38	42.37
995	45.68	43.37
990	46.05	45.32
975	47.11	50.59

The model can be extended to simulate the microstructural development in multicomponent alloys by putting the free energy densities of the gamma and gamma-prime phases in Eqn. 2 as functions of compositions of the alloying elements.

References

[1] L. Q. Chen and Y. Wang, JOM 48, 13 (1996).
[2] Y. Wang, D. Banerjee, C. C. SU and A. G. Khachaturyan, Acta Mater. 46, 2983 (1998).
[3] V. Vaithyanathan and L. Q. Chen, Acta Materialia 50, 4061 (2002).
[4] P. -R. Cha, D. -H. Yeon and J. -K. Yoon, Acta Mater 49, 3295 (2001).
[5] I. Loginova, J. Odqvist, G. Amberg and J. Ågren, Acta Mater. 51, 1327 (2003).
[6] U. Grafe, B. Botteger, J. Tiaden and S. G. Fries, Scripta Mater. 42, 1179 (2000).
[7] S. G. Kim, W. T. Kim and T. Suzuki, Phys. Rev. E, 58, 3316 (1998).
[8] J. Andersson and J. Ågren, J. Appl. Phys. 72(4), 1350 (1992).
[9] TTNi ™ and NIST ™ are registered trademarks of Thermotech Ltd. and National Institute of Standards and Technology.
[10] Thermo-Calc ™ is a registered trademark of Thermo-Calc Software, Inc.

A Monte Carlo Study on the Nucleation and Grain Growth of A Polycrystalline Matrix

P.V. Sivaprasad, K.P.N. Murthy and Baldev Raj
Indira Gandhi Centre for Atomic Research
Kalpakkam - 603 102, Tamilnadu, INDIA
E-mail: prasad@igcar.gov.in

ABSTRACT

In this paper we present the results on the Monte-Carlo simulations of the nucleation and grain growth in a polycrystalline matrix. A Q-state Potts model is considered for simulation. We have investigated a possible Hamiltonian to model preferred orientation in the grain growth by considering crystal orientation effect. The exponent characterising the average grain growth is found to be 0.4 and that characterising the typical grain growth is 0.25. Our studies indicated that the growth exponent is not affected for the modified Hamiltonian and therefore we concluded that orientational effect doesn't influence the growth exponent. We present the results on the grain structure at various stages of evolution with and without considering orientational effects.

1. Introduction

The importance of dynamic recrystallisation (DRX) and the grain size control during hot working operations have stimulated a great deal of basic research [1]. Despite a considerable body of experimental information concerning factors influencing the DRX, the physical mechanisms governing the process have not been understood properly. It is precisely in this context, computer simulation of DRX process would prove useful. Simulations of this kind has earlier been carried out by various researchers [2,3]. We have initiated a computational programme to investigate various aspects of DRX. As a first part of the programme, we have studied the nucleation of grains caused by thermal fluctuations and the subsequent evolution of the grains in the absence of thermal fluctuations. More importantly, we have made an attempt towards investigating explicitly the influence of crystal orientation on the grain growth kinetics.

2. Monte Carlo Simulation

We consider a triangular lattice of size 40 x 40. Each site has six nearest neighbors. To each lattice site *i*, we attach a Potts spin with orientation index that can take any value between 1 and 48. To start with, we systematically assign to each spin a random value of Q chosen independently and uniformly between 1 and 48. In the resulting structure there are no grains and thus it can be considered as the state of the initial material at infinite temperature. Then we quench the system to zero temperature and let it evolve as dictated by the Hamiltonian,

$$H = J \sum_{<i,j>} (1 - \delta_{S_i S_j}) \qquad (1)$$

where J is a positive definite constant; the summation runs over all nearest neighbor pairs and $\delta_{S_i S_j}$ is the usual Kronecker delta that takes value 1 if $S_i = S_j$ and zero otherwise. We employ periodic boundary conditions. The evolution is simulated as follows: We select randomly a site, say *j*, and calculate H_1 considering the interaction of the spin S_j with its six nearest neighbors. We then reassign the value of S_j to any of the values between 1 and 48 with equal probability and calculate the Hamiltonian H_2. If $H_2 < H_1$, we accept the new configuration. Otherwise we reject the new configuration and proceed. A set of N x N attempts constitute one Monte Carlo step. To simulate nucleation, we carry out the evolution *of* structure at a *finite* temperature. This is accomplished as follows: We proceed as before, except where $H_2 > H_1$, we accept the new configuration with a probability given by exp [- $(H2 - H_1) / kT$]. Figure 1 depicts the various stages of evolution after including kT term, with $kT=0.35$. We calculate the average size of the grain as a function of time. We also calculate the typical size [4] of the grain as

$$A_{typ}(t)=exp\ \{\frac{1}{N}\ \sum \underline{l}n\ (A_i)\}. \tag{2}$$

To take into account the crystal orientation effect, we consider the Hamiltonian,

$$H = J_{ij} \sum_{<i,j>} (1 - \delta_{S_i S_j}) \tag{3}$$

The positive constant J_{ij} is proportional to the grain boundary energy per unit length and depends on the orientation of the neighboring site lattice points. If $S_i = S_j$. $J_{ij} = 1.00$ and otherwise, $J_{ij} = 1.00 + (\,|Si - S_j|\,/100)$ so that J_{ij} assumes a value between 1.0 and 1.47 depending upon the orientation of the neighboring lattice points. Even though the value of J_{ij} is assumed to vary between any arbitrarily selected values, in this way, the misorientation between the grains is accounted for in the simulation. Kunaver and Kolar [4] have assumed three different *J* values in their studies for simulating anisotropic grain growth. In contrast, in our study the various

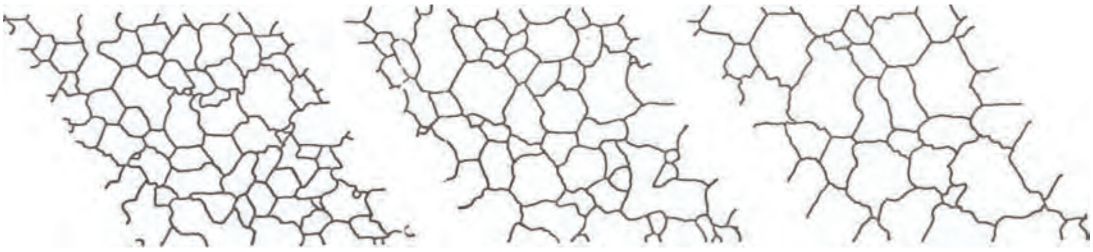

a) 300 MCS *b) 500 MCS* c) *1000 MCS*

Fig. 1. The evolution of microstructure for nucleation and grain growth with constant *J*.

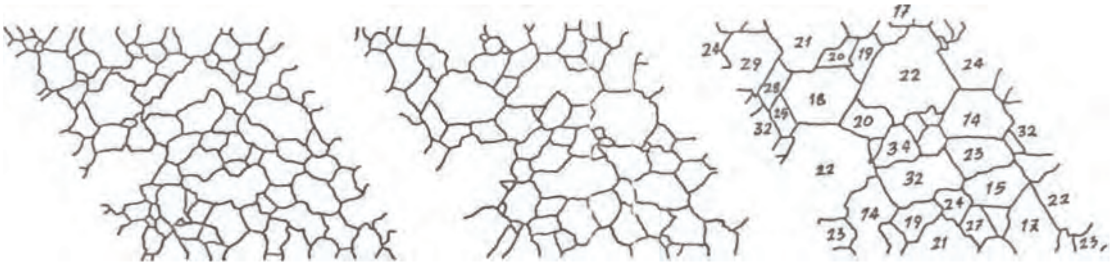

a) *300 MCS* *b) 500 MCS* *c) 1000 MCS*

Fig. 2. The evolution of microstructure for nucleation and grain growth considering orientational effects.

values of J are assumed, to take into account the orientational effect of the neighboring grains on grain growth. Figure 2 depicts the grain structure at various stages of evolution, with orientation effects included. It is seen that the grains of *neighboring* orientation cluster together. The numbers marked inside the grains represent the orientations of the grains for easy visualisation. We calculate the average grain area and typical grain area as a function of time, for both the nucleation and grain growth simulations. All the data presented in this paper represent averages over at least five simulation runs.

3. Results and Discussion

The time dependence of the mean domain size, R is expressed as $R^m - R_0^m = Bt$, where R_0 is the mean domain size at time $t = 0$. When $R \gg Ro$ it can be approximated as $R = C\,t^n$, where the growth exponent, $n = 1/m$. For zero temperature growth kinetics with $Q = 48$, the growth exponent obtained is 0.404. This is in excellent agreement with that reported in literature [2]. We then consider the situation of nucleation and grain growth with constant J. Figure 3(a) depicts the variation of average and typical grain sizes. The growth exponents obtained are 0.39 and 0.29 for average and typical grain areas respectively. Similarly the growth exponents are 0.38 and 0.28 for the simulation considering the orientational effects with $J = J_{ij}$, see Fig. 3(b). The growth exponents of average and typical grain area are nearly equal for the grain growth with and without the orientational effects. This indicates that the growth kinetics are not affected by the orientational effects as has also been found out by Vertex model [6].

Table 1 gives the average and typical grain sizes for the simulations with and without orientational effect. It can be clearly seen from the exponents, the average grain area grows faster than the typical. This suggests a long tail in the distribution of grain size. Such long tail behaviour could be indicative of statistical self similarity of the grain size distribution and a fractal analysis would prove useful. The average as well as typical grain sizes, viz., $A(t)$ and $A_{typ}(t)$, are found to be larger for the simulations without considering the orientational effects. This can be rationalised, because while the orientational effects are considered, the probability for the grains with neighboring orientation is more. Such imposed condition tends to reduce the average and typical grain sizes, although, the kinetics of the growth are not affected. At present we offer no explanation for the specific value of the growth exponents of typical grain area that have been obtained for both the cases.

Table 1 The average and typical grain sizes for nucleation and grain growth with and without considering orientational effects.

MCS	with constant J		with orientational effect	
	$A(t)$	$A_{typ}(t)$	$A(t)$	$A_{typ}(t)$
300	23.85	17.95	17.78	13.05
400	27.12	20.10	20.83	15.07
500	30.11	21.88	23.48	15.36
1000	51.58	40.81	39.02	22.86
1500	64.72	45.67	50.97	28.34
3000	125.00	73.01	94.12	37.96

4. Summary and Conclusions

In summary we have demonstrated the utility of Monte Carlo technique based on Q-state Potts model to simulate a variety of problems in nucleation and grain growth. These studies are being extended to problems associated with DRX. We have also demonstrated that the orientation effects can be included in the Monte Carlo simulation of nucleation and grain growth through the J_{ij} term. Orientation effects do not affect the growth kinetics. The average and typical grain size behaviours suggest a long tail in the grain size distribution.

References

1. T. Sakai and J.J. Jonas, Acta metall. 32 (1984) 189.
2. M.P. Anderson, D.J. Srolovitz, G.S. Grest, and P.S. Sahni, Acta metall. 32 (1984) 783.
3. A.D. Rollett, D.J. Srolovitz, R.D. Doherty and M.P.Anderson, Acta metall. 37 (1989) 627.
4. M.C. Valsakumar and K.P.N. Murthy Pramana-J. Phys. 35 (1990) 461.
5. U. Kunaver and D. Kolar, Acta metall. mater. 41 (1993) 2255.
6. T. Nagai, K. Fuchizaki and K. Kawasaki, Physica A, 204 (1994) 450.

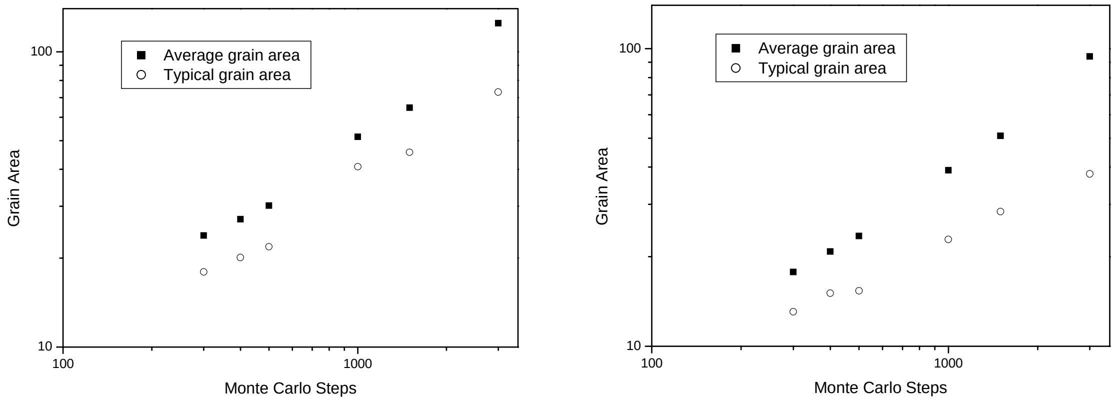

(a) (b)

Fig. 3. The variation of average and typical grain sizes for nucleation and grain growth (a) with constant J and (b) by considering the orientational effects.

Multiscale Physics Of Failure Mechanisms In Power Technology Metallization Under Cyclic Loading

Authors: Tobias Smorodin[1], Jürgen Wilde[2], Matthias Stecher[1]

Affiliations: [1]Infineon Technologies, 81726 München, Germany,
contact: tobias.smorodin@infineon.com;
[2]IMTEK, University of Freiburg, 79110 Freiburg, Germany

ABSTRACT

Engine management electronics in cars are widely supported by smart multi-channel power-DMOS switches that drive the magnetic valves. Due to the dissipation of inductive energy within the power-DMOS a high thermal cycling robustness is required. The mismatch of the thermal expansion coefficient between silicon and metallization system results in a gradual plastic deformation of the metallization. Consequences are the mechanical breakdown of the interlayer dielectric and device failure due to resulting short circuits. The degradation mechanism is observed for DMOS-transistors as well as for thermomechanical test structures. These test structures shift the focus from the whole device to allow power cycling of the metallization system without consequent electromigration phenomena. With this appliance the influence of different stress conditions on mean life is studied. The fatigue mechanisms are accompanied by a change in the metallizations microstructure. This is observed by X-ray diffraction and shows the time-dependent recrystallization behaviour.

1. Introduction

Single-pulse destruction of devices due to one-time excess of the thermal destruction limit was reported in [1]. In this paper we focus on a failure mechanism occurring in devices exposed to a high number (>10000) of power cycles below the thermal destruction limit [2]. After exposure to a high number of cycles devices fail due to electrical short circuits between metallization lines. Analysis by SEM and FIB preparation of power-cycled devices reveals aluminum extruding through cracks in the top passivation layer and cracking of interlayer dielectrics (Fig. 1.1).

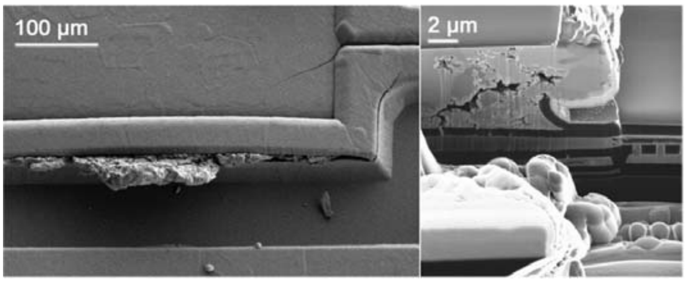

Fig. 1.1 Cracking of passivation layer and interlayer dielectric visualized by SEM and FIB

In order to exclude the influence of electromigration a special test structure suggested by Nguyen [3] is implemented, that allows power-cycling without subsequent electromigration stress. The obtained failure data is well fitted with a Weibull-distribution and provides a linkage between single device failure and the ensemble behavior. With the test structures focus is shifted from power-DMOS in operation to the behavior of the top metallization system under thermomechanical stress. A further zoom into metallizations microstructure is achieved by FIB-preparation and X-Ray diffraction. On this way the impact of the thermomechanical stress on the grain structure and the texture is observed on a microscopic length scale and can be related to the ensemble behavior.

2. Experimental set-up

The test structure consists of a poly-silicon resistor (R ~ 17 Ω), used as heat source by applying a pulsed voltage. Above the heating plate a long meandering aluminum line is located, traversed from both sides by extrusion monitors for the detection of lateral short circuits (Fig. 2.2a). Vertical short circuits are monitored via the covering top metallization plate. As the temperature in the metallization system is of great influence, it is measured by a very narrow aluminum line in the center of the structure. Resistance of this conductor path at room temperature is ~ 900 Ω and the drift after measurement does not exceed 1%.

Our test bench allows testing of ten devices simultaneously with pulses in the range of microseconds to milliseconds. With an electronic detection unit the first short circuit is monitored for each device and the number of cycles to failure is determined by a computational read-out assembly.

The influence of the thermomechanical stress on metallizations microstructure was analyzed by X-ray diffraction. A change in texture depending on the number of load cycles could be observed and is visualized with Chi-scans and pole figures.

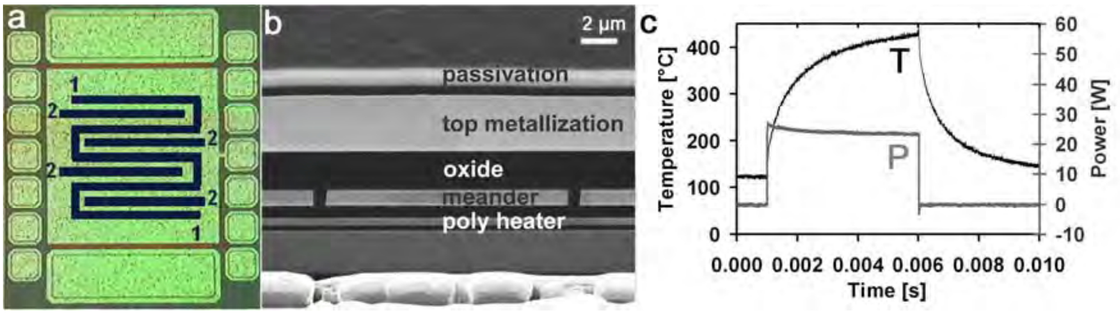

Fig. 2.2a) Top view of test structure, showing the covering top metallization and a sketch of the underlying meander (1) with extrusion monitors (2).
b) FIB-preparation of the initial structure, showing a side view of the poly heater and the overlying metallization.
c) Temperature cycling profile obtained by resistance measurement.

3. Results and discussion

Time-to-failure data for three different temperature cycle conditions are shown in Fig. 3.3a and are well-fitted with a Weibull-distribution. This is applicable in the case of interlayer dielectric breakdown under fast thermal cycling [3].

The momentary state of research on failure mechanisms under thermal cycling builds up on a model suggested by Huang [4] and was extended to power cycling by Nguyen [5]. From this point of view, residual shear stresses at the die surface are primal for failure initiation. However, the stress level is far below the fracture strength of the passivation system. Cracking of passivation occurs, as due to the mismatch in coefficient of thermal expansion with each cycle a plastic deformation of the metallization is accumulated. This reduces shear stresses within the metallization, but increases the stress level on passivation and interlayer dielectrics to a critical value. Considering this approach it is necessary to investigate metallizations microstructure, as the mechanical properties are basic for lifetime modeling.

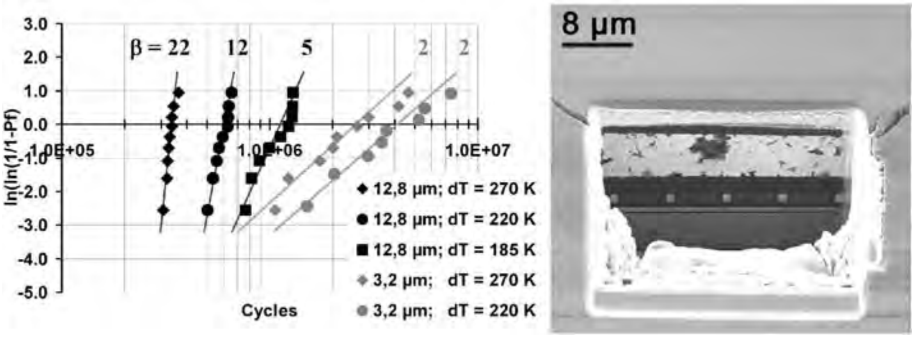

Fig. 3.3a) Weibull-plot of time to failure data for three different temperature cycles and varying conductor path width.

b) FIB cross-section of a device after ~ 1 million power cycles reveals massive void formation.

The influence of the thermomechanical stress on the texture of the metallization system is presented in Fig. 3.4. The initial (111)-fibre texture of the aluminum dissolves during temperature cycling, indicating a stress-induced recrystallization process. The loading time dependent texture formation is shown in Fig. 3.4b, where Chi-Scans are taken on a logarithmically scaled timescale. As the change in texture occurs at a very early point of lifetime it cannot be considered directly as a failure criterion.

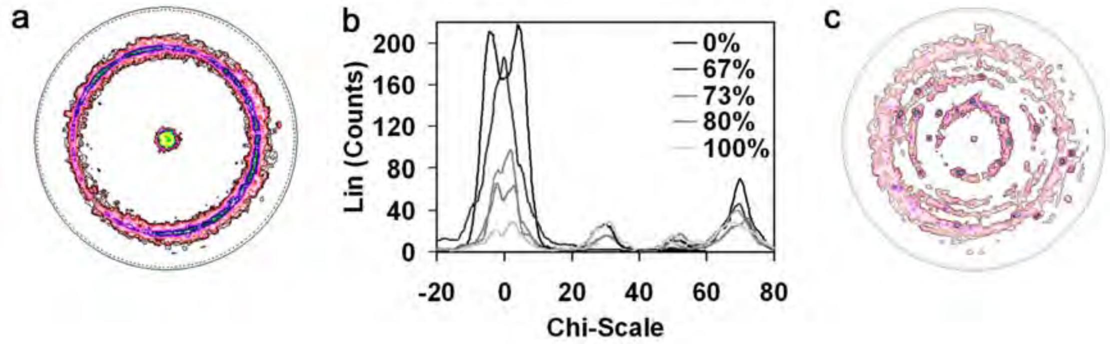

Fig. 3.4 Pole figures on (111)-reflection comparing initial (a) and thermomechanically stressed device after ~ $2{\cdot}10^5$ cycles (c).

b) Chi-Scan on (111)-reflection after different loading time, scaled to percentage of total logarithmic lifetime.

However this finding will be important for simulation-based fatigue life modeling of power cycling in the future, as mechanical properties of the metallization are strongly influenced by materials microstructure.

References

[1] M. Denison *et al.*, "Influence of Inhomogeneous Current Distribution on the Thermal SOA of Integrated DMOS Transistors", ISPSD (2004)

[2] J.M. Bosc *et al.*, "Reliability Characterization of LDMOS Transistors submitted to Multiple Energy Discharges", ISPSD (2000)

[3] H.V. Nguyen *et al.*, "Test Chip for Detecting Thin Film Cracking Induced by Fast Temperature Cycling and Electromigration in Multilevel Interconnect Systems", Proc. of 9th IPFA, 135 (2002)

[4] M. Huang, Z. Suo, Q. Ma, "Metal Film Crawling In Interconnect Structures Caused By Cyclic Temperatures", Acta mater. 49, 3039, (2001)

[5] H.V. Nguyen *et al.*, "Fast temperature and electromigration induced thin film cracking in multilevel interconnection: experiments and modeling", Mic. Rel. 42, 1415, (2002)

Microstructure & Property Modeling in Ni-base Superalloys

Sanjay K. Sondhi [1], Dan Wei [2], Michael F. Henry [3]

[1]GE Global Research Center, Materials Research Laboratory, Bangalore, India
[2]GE Infrastructure – Aviation, Structural Material Development, Lynn, MA, USA
[3]GE Global Research, Structural Materials Laboratory, Niskayuna, NY, USA

ABSTRACT

Two physics based models have been developed, and then employed in tandem, to describe the yield behavior of a nickel-based superalloy over a wide range of heat-treatment conditions. Firstly, a physics based kinetic model has been used to predict the microstructure of René88 as a function of post-homogenization thermal history, including cooling and subsequent aging conditions. The output of this kinetic model provides the vital microstructural input to a physics based yield strength model that is based on interaction of dislocations with ordered precipitates. The predictions of the combined microstructure-strength model are in excellent agreement with literature data, and provide guidelines for optimizing alloy heat-treatment and its microstructure with acceptable quench residual stress.

1. Introduction

Nickel based superalloys form an important class of materials for high-temperature applications in general and gas-turbines in particular. They derive their strength from the presence of coherent and ordered γ' precipitate, having $L1_2$ type crystal structure. The yield strength of these alloys is a strong function of the precipitate sizes and volume fractions, and these in-turn depend on the heat-treatment of the material. Empirical approaches to relate heat-treatment, microstructure and strength are of little use, as these inter-relationships are non-monotonic, highly non-linear, and in some cases even discontinuous. The presence of multi-modal distribution of precipitate, almost ubiquitous in most commercial superalloys, is an added complication. There is a great need for physics based models that can:

- predict the material microstructure as a function of its heat-treatment, and
- predict strength as a function of material microstructure

Clearly this approach requires a quantitative understanding of the physics of the problem, as well as the knowledge of relevant thermo-physical data. In the present study, we have developed physics based models for predicting the evolution of alloy microstructure during heat-treatment and the resultant yield strength. These models have been employed to describe the available literature data for René88 superalloy over a vast range of heat-treatment conditions and microstructures [1]. This approach can be used to optimize the heat-treatment schedule, and hence the material microstructure, for desired levels of strength, and to accelerate the utilization of new alloys.

Table 1: Nominal composition of René88

	Al	B	C	Co	Cr	Mo	Nb	Ti	W	Ni
Wt %	2.1	.016	.05	13	16	4	0.7	3.7	4	Rest

2. Alloy Chemistry & Microstructure

René88 is a powder metallurgically prepared nickel based superalloy used for turbine disk applications. Nominal composition of René88 is given in Tab. 1. Typical heat-treatment involves solution above the γ' solvus temperature, followed by cooling to room temperature and a subsequent aging treatment. Mao et al [1] carried out a detailed study on the variation in yield strength of the René88 for different heat-treatments. The heat-treatment conditions are presented in Tab. 2, and one may refer to the original work for further details. The detailed microstructural data corresponding to each heat-treatment, however, are not reported. In the present work, we have used our microstructure prediction model to bridge this gap by predicting the γ' sizes and volume fractions for all the heat-treatments. As the material was subjected to a super-solvus solution treatment, we have assumed that no primary γ' was present. From the microstructures provided in [1], we have measured the average grain size to be 13 μm using the linear intercept method.

3. Model Details

3.1 Microstructure prediction model

A kinetic model was developed that describes the evolution of ordered γ' precipitate in nickel-based superalloys during quenching from the solution temperature. As the temperature drops during quenching, the model iteratively calculates the level of supersaturation in the γ matrix based on the solute conservation for γ' formers, the precipitate nucleation rate, and the diffusion-driven growth rate. At the end of each iteration, the model generates a revised particle size distribution based on the introduction of nucleated precipitates, precipitate growth, and the application of an isothermal coarsening law to pre-existing particles.

Thermodynamic calculations within the kinetic model used a pseudo-binary approximation in which major γ' formers were lumped together as one component, and the remaining alloy elements comprised the γ solvent. Solubility curve for the γ/γ' pseudo-binary was computed using ThermoCalc™ with Ni-data and validated with of γ' volume fraction measured at temperatures close to the solvus temperature. Volumetric Gibbs free energy functions using ThermoCalc™ were applied to determine the excess Gibbs free energy as a function of solute supersaturation for use in the nucleation rate calculations. These calculations employed classical nucleation formulations that address the counter play among nucleation volumetric free energy, surface energy, and strain energy as well as modifications to treat non-isothermal incubation and the volume exhaustion effect. Following nucleation, particle growth or dissolution was modeled by calculating the diffusive flux across the interface separating the supersaturated matrix and the precipitates and performing a mass balance to determine movement of the interface.

Heat treatment process curves were discretized into short time intervals. The computer model calculates matrix supersaturation, γ' nucleation rate, growth rate, and coarsening rate iteratively for each time step. The model tracks the state of the material as a function of time. Further details on this model can be found elsewhere [2].

3.2 Yield strength prediction model

Nickel based superalloys derive their strength from multiple sources, that include:

- base strength of the solid-solution strengthened γ matrix , σ_{matrix}
- barrier-to-entry of dislocations into the ordered γ' precipitate, σ_{dis}
- Hall-Petch strengthening, σ_{HP}
- lattice parameter mismatch strengthening, and
- cross-slip induced anomalous strengthening

Most aspects of the yield strength model being developed by us have been derived from existing literature, and its structure is similar to the model developed at University of Michigan under the DARPA funded Accelerated Insertion of Materials (AIM) initiative [3]. A detailed description of the concepts borrowed from existing literature, and the modifications made, is beyond the scope of the present paper and will be published elsewhere. For the purpose of the present work, this model has been greatly simplified, without compromising on accuracy, based on the following reasons. The $\gamma - \gamma'$ superalloys usually have very little misfit strengthening contribution, and René88 is reported to have the lowest misfit of any commercial superalloy [4]. Cross-slip induced anomalous strengthening is a thermally activated process with little or no contribution at room temperature. Accordingly the last two strengthening contributions have been ignored in the present study. The yield strength of the superalloy may then be written as: $\sigma_{YS} = \sigma_{matrix} + \sigma_{HP} + \sigma_{dis}$. Furthermore, the grain size was same for all the microstructures in the present study and only microstructural variables were ***different sizes and volume fractions of the strengthening precipitate***. Accordingly, we may express the yield strength corresponding a given microstructure as $\sigma_{YS} = \sigma_0 + \sigma_{dis}$, where σ_0 is the strength of the matrix *including* the Hall-Petch contribution. The magnitude of σ_{dis} depends on the mechanism by which dislocations overcome the strengthening precipitate. This mechanism can be shearing of the γ' by weakly/strongly-coupled pair of dislocations [5, 6], or the Orowan looping process [3, 5]. The equations used for these processes, in the present work are given below, and σ_{dis} is determined by mechanism that requires the *least* amount stress to operate:

$$\sigma_{WPC} = \frac{\overline{M}\Gamma}{2b}\left[A_1\sqrt{\frac{\Gamma f_v d}{T}} - A_2 f_v\right],\ \sigma_{SPC} = \frac{1.72\overline{M}wT\sqrt{f_v}}{2bd}\sqrt{\left[1.28\frac{d\Gamma}{wT} - 1\right]},\ \sigma_{Orowan} = \frac{1.36\,\overline{M}\,Gb}{2\pi\lambda}\ln\left(\frac{\lambda}{b}\right)$$

4. Results

We have used the microstructure prediction model to predict the alloy microstructure for all the heat-treatment conditions listed in Tab 2. The model predicts a multi-modal distribution of precipitate with a wide range of γ' sizes. Experimental data is available on the size of largest γ' as a function of cooling rate [4], and our predictions are in excellent agreement with the literature data. These microstructures have been used as inputs to the yield strength model, and the combined model predictions are presented in Figure 1. Our model predictions are in excellent qualitative and quantitative agreement with the experimental data. The material parameters used are: APB energy $\Gamma = 300 mJ/m^2$; Shear modulus $G = 66GPa$; T is the line tension of a 45° mixed dislocation; $\overline{M} = 3.04$ is the Taylor's factor; $b = 0.254nm$ is the Burger's vector of ½[110] dislocation in Ni-solid solution. d and f_v are the average precipitate size of a population and its effective volume fraction, while λ is the surface-to-surface interparticle spacing. We find that the experimental data is best represented when

Table 2: Heat-treatments applied to René88, subsequent to 5 min super-solvus hold at 1150°C

Set 1: Cooled at different rates (27°C/min - 1083 °C/min)	Set 2: Set 1 aged 24 hrs at 760°C	Set 3: Cooled at 55°C/min and quenched from different *interrupt temperatures*

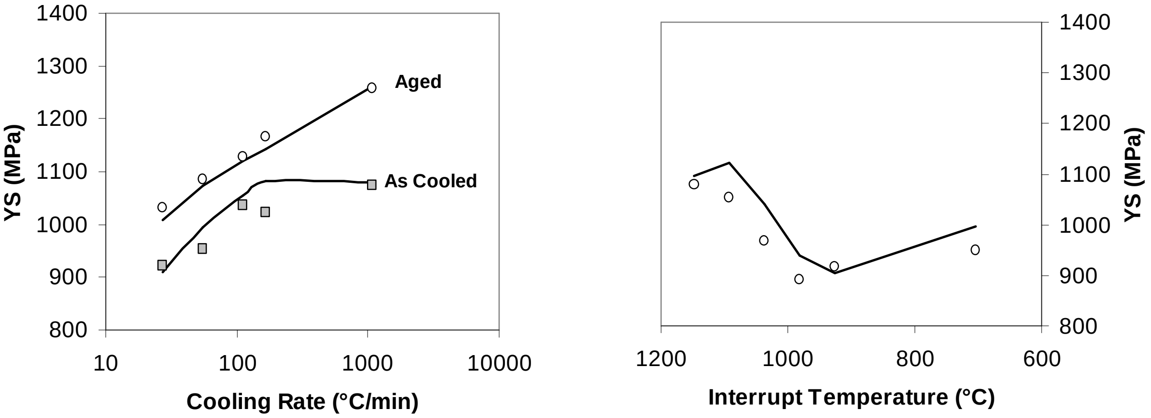

Figure 1: A comparison our combined microstructure-strength model predictions (solid-lines) with of literature data [1] for heat-treatment conditions shown in Figure 1.

$A_2 = 0$ signifying that in the case of weak-pair coupling, the trailing dislocation lies completely outside the precipitate. We find $A_1 = 0.305$ and $w = 1.8$ while σ_0 was taken as 300 MPa. The strengthening contribution from different populations was added linearly. Our analysis indicates that maximum strength is obtained when the precipitates are ~50nm in diameter. Heat-treatments should be tailored to achieve this optimal precipitate size.

5. Conclusions

A combined microstructure-strength prediction model has been developed and applied to explain the literature data on René88. The model predictions are in excellent agreement with experimental data over a wide range of heat-treatments and microstructures. This physics based approach allows us to identify the optimal microstructures for desired yield strength, and the heat-treatments with acceptable quench stress to get there.

References

1. Jian Mao *et al*, Mater. Sci. Eng. **A332** 318 (2002)
2. Timothy P. Gabb *et al* in *Proceedings of Superalloys 2000*, edited by T. M. Pollock et al, TMS, 405 (2000)
3. T. M. Pollock (private communications)
4. S. T. Wlodek, M. Kelly and D. A. Alden in *Proceedings of Superalloys 1996*, edited by R. D. Kissinger et al, 129 (1996)
5. L. M. Brown and R. K. Ham in *Strengthening Methods in Crystals*, edited by A. Kelly and R.B. Nicholson, London, 9 (1971)
6. Bernd Reppich, Acta Metallurgica, **30**, 87 (1982)

The Research of Thermoactivated Changes of the Structure of Antiphase Boundaries in Cu_3Au and Ni_3Al Alloys

Mikhail D. Starostenkov[1], **Evgeniya A. Dudnik**[2]

[1]**Lenin st. 46, Altai State Technical University, Barnaul, 656038, Russia,**
genphys@agtu.secna.ru
[2]**Traktornaya st. 2/6, Rubtzovsk Industrial Institute, Rubtzovsk, 658207, Russia,**
dudnik@rubtsovsk.ru

ABSTRACT

The research of the influence of different types antiphase boundaries in the disordering process was made by a computer experiment on the example of the alloy Cu_3Au and intermetallide Ni_3Al. The distributions of long and short order parameters over the planes parallel to conservative and non-concervative antiphase boundaries were obtained in the dependence on temperature. It was shown, that “washing” effect of the superstructure parameters was observed near relatively high energetical antiphase boundaries of non-concervative type. It is evident that such boundaries can make a definite contribution in the effect of a positive temperature dependence of the yield stress of $L1_2$ superstructure ordered alloys.

1. Introduction

Ordered alloys and intermetallides have being studied by the researchers for more than 50 years because of their unique properties, having an important practical significance. First of all, it is a positive temperature dependence of the yield stress. The alloys of the superstructure $L1_2$-ordering alloy Cu_3Al and intermetallide Ni_3Al have such a peculiarity. There are many suppositions concerning the nature of the above mentioned property of alloys. However, the phenomenon has not been exactly described [1].

One of the first models was based on the supposition that “washing” effects took place near such planar defects as antiphase boundaries (APB) at the increasing of the temperature. The effect was in a local change of short and long order, concentrations of alloy components over the planes, which were parallel to APB. The APB became an insuperable obstacle for the dislocations movement due to that peculiarity. As a result, material strengthening occurred.

It is known that the atomic packing order of the alloy components change step by step at the presence of APB in the superstructure. APB is characterized by the vectors relatively to the shear $\vec{p}$ of the crystal parts. The boundaries with the vector of the relative shear $\vec{p}$, which is parallel to APB plane are called conservative (CAPB). The mentioned defect types can appear as at deformation, so in the result of thermoactivated growth of the ordered domains [3]. The other APB type is noticed only in the systems of planes with changeable components concentration. Such boundary type is called non-conservative (NAPB), it appears only in the process of growth and meetings of the ordered domains. In this case, the vector $\vec{p}$ is directed under some angle to the plane of APB occurrence.

2. The model, the Results and Discussion

The crystal calculated block contained of about $1.87 \cdot 10^5$ atoms. Periodical conditions were applied at the boundaries of the calculated block. The atoms distribution of the alloy components over the sites corresponded to a full stoichiometric $L1_2$ superstructure order. The interaction between different pairs of atoms was taken into account in a discrete model only in three first coordination spheres.

The proper values of the alloy lattice parameter were tabulated using the data on the energy of pair interatomic interactions with the temperature change. It was made in the approximation of Morse potential function according the experimental data presented in [2]. Small concentration of vacancies was introduced in the crystal. The process simulation was made by Monte-Carlo method.

The crystal temperature in every experiment is constantly equal all over the calculated crystal block.

The long order parameter η in Bragg-Williams approximation is used as a parameter controlling the changes in a superstructure.

Structural presentations on a short order are connected with the determination of local distribution of atoms in solid solutions at the presence of heterogeneities. The measure of short order is the relation of the number of atoms *A* and *B* situated at the distances which are equal to the radius of n-th coordination sphere to the number of atoms pairs *A* and *B*, situated at the mentioned distance at their fully chaotic position over the lattice sites.

The computer experiment showed that considerable diffusion jumps of atoms in vacant sites leading to the formation of point substitution defects (PSD) were not observed. The jumps were noticed when atoms introduced into the calculated crystal block formed bivacancy complexes accidentally. They caused a local disturbance of a full order in a crystal even at relatively low temperatures. But the probability of such formations in the limits of the given vacancies concentration appeared to be insignificant.

Let us discussed the results obtained for alloy Cu_3Au during the experiments.

The exchange of places by the atoms over the sublattices Cu and Au with the formation of PSD took place at higher temperatures (500K) in the process of atoms migration by a vacancy mechanism. Such atoms began to form germs and clusters of the disordered phase. The disordering process became stable at a relatively low temperatures at a some level owing to the combination of the PSD formation and annihilation processes.

The disordering process becomes more intensive with the temperature growth and increase of the vacancies concentration and time of a computer experiment. The temperature of phase transition order-disorder also corresponds to an experimental value. In a real experiment, the definite concentration of free vacancies can be seen in the crystal. The part of vacancies in a combined state is preserved in the structures of different types of interphase boundaries.

Two CAPB or NAPB located in the plane [100] were introduced in the crystal block under study. The first type of the boundaries is formed with the relative shear in the calculated block of crystal to the vector ½<110> along the defect plane. The formation of the second type boundaries is simulated by the displacement of one atomic plane in the other place of the calculated crystal block. As a result, one boundary consists of two biatomic planes, the other – two monoatomic planes. Such procedure does not break the stoichiometry of the superstructure.

The picture of the change of long and short order parameters over the planes [100] parallel to the APB is shown in Fig. 1. Fig. 1 shows the changes of short order at the first coordination sphere in the dependence on temperature and types of antiphase boundaries in the ordered alloy. As it follows from the picture, sharp jump of the change of short order is observed near CAPB.

As the pair of CAPB in the complex under study is equivalent, the jumps of the change of short order parameters appear to be identical and they are realized at low temperatures only in the planes forming CAPB. The pictures of the change of short order parameter differ insignificantly, in the planes, forming CAPB from 1 to 0.75. In the other planes which are parallel to CAPB, the order changes from -0.33(3) to -0.27. with some oscillations over the planes.

The other picture of the change of short order parameter is realized near the pair of NAPB. NAPB consisting of biatomic planes are presented by 18 and 19 planes. NAPB consisting of monoatomic planes are presented by 54 and 55 planes. The changes of short order parameter cover four planes near APB formed by monoatomic planes and to 8 planes near biatomic APB. The levels of the maximum of order parameter are different: -0.21 and 0.28.

Washing effects of short order parameter over the planes parallel to NAPB appear to be more significant in comparison with CAPB and include 8 and 16 planes at the crystal heating to 800 K. Maximum levels are equal to 0.03 and 0.21 correspondingly. The maximum of short order parameter near biatomic NAPB increases with the growth of temperature and the change of positive-negative sign. But, the maximum decreases near monoatomic boundary. The effects of washing and oscillation of short order parameters over the planes parallel to APB are more significant in comparison with CAPB. The deviations from an ideal short order parameter at the first coordination sphere of CAPB is observed only near the temperature of phase transition T=800K.

The changes in the distribution of components concentrations over the planes correlate with the above mentioned changes of short order parameters over the planes parallel to NAPB. In the crystal containing two CAPB, the components concentration fluctuates over the planes insignificantly.

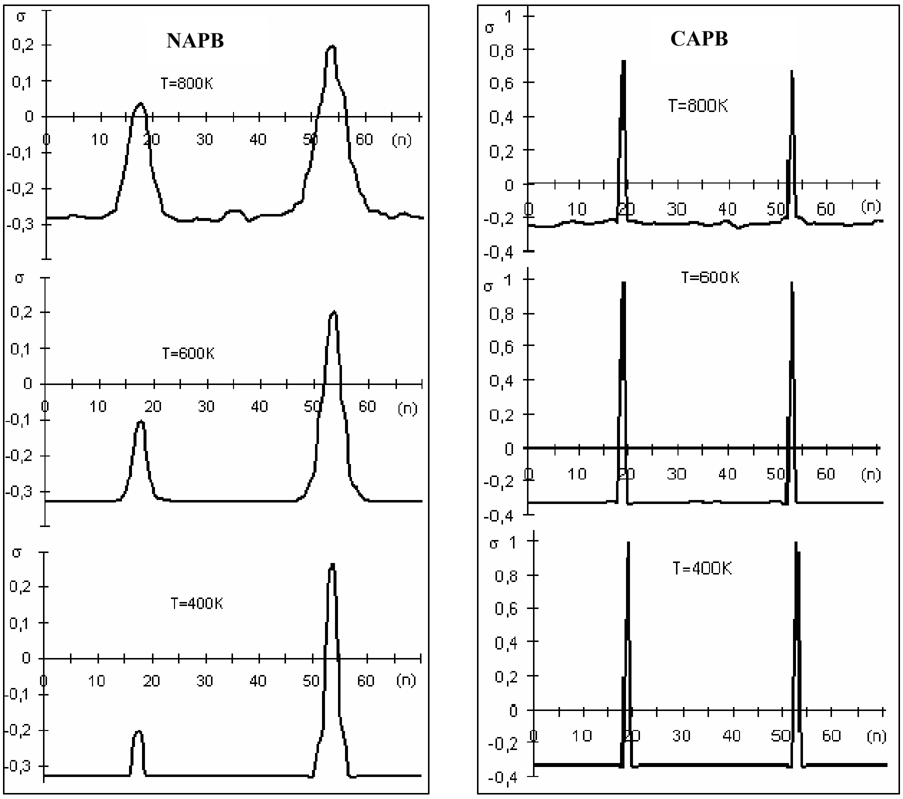

Figure 1. Temperature distribution of short order at the first coordination sphere over the planes parallel CAPB and NAPB, n – the number of planes.

Fig. 2. shows the changes of long order parameter in the dependence on temperature and types of antiphase boundaries in the ordered alloy. Long-order parameter is given with the change of the sign at the transition through APB. In the given case, washing effects of the order parameter are observed more distinct near the pair of NAPB. As it is shown in the figure, the average level of long-order parameter decreases to 0.82.

Washing area according long-order parameter at this temperature includes up to 15 planes at every side relatively biatomic NAPB and up to 12 near monoatomic NAPB. Washing effect according long-order parameter relatively CAPB is less distinct with the growth of temperature. It includes only 3 planes [100] near APB, which are parallel to a defect.

The computer experiments showed that washing effects, i.e. the changes of order characteristics over the planes parallel to the plane of APB location appear to be more distinct near the boundaries of thermal or non-conservative type. That is why it is worth to note that the boundaries types can play a big role in the effect of positive temperature dependence of yield stress in comparison with the boundaries of deformation type (CAPB).

The break of the symmetry elements in an atomic order with the formation of shear boundary near a critical temperature leads to the formation of the ordered phase with it's own symmetry order. The break of the atoms concentration in the plane of the thermal boundary location corresponds to the formation of segregations consisting of one type of atoms. It is evident, that the expenses of energy for a structural reconstruction of the material are big in the last case. That is why, the influence of different APB types having different energies of defect formation on the process of phase transition order-disorder are different type of antiphase boundaries should be different.

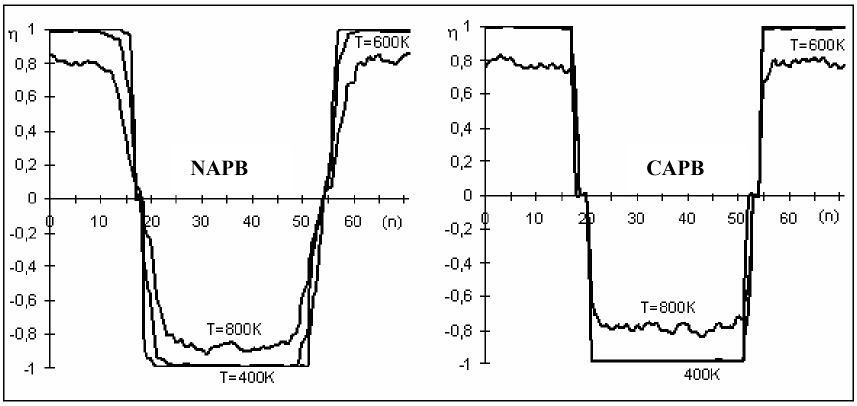

Figure 2. Temperature distribution of long order at the first coordination sphere over the planes parallel CAPB and NAPB, n – the number of planes.

The equilibrium degree of long order in the plane of the location of NAPBs and neighbouring planes decreases at the expense of the segregation of SPSs and their complexes on the boundary. The mechanism of the alloy disordering near shear boundaries have it's own peculiarities. The fractures of CAPB surfaces with the formation of NAPB segments were observed in thermoactivation processes. Faceting of CAPB finally took place. The faceted sections from NAPB segments were transformed in CAPB elements at the expense of thermoactivation processes. As a result, the straightening of CAPB line was noticed, the boundary displaced.

For intermetallide Ni_3Al, temperature interval of the beginning of APB washing process and it's considerable washing covered from 800K to 1400K.

References

1. Popov L.E., Kozlov E.V. Mechanical properties of ordered solid solutions. – M.: Metalurgiya, 1970, 216 p.
2. Poletaev G.M., Starostenkov M.D. // Technical Physics Letters. **29**, 6 (2003).
3. Bragg W.L., Williams E.J. Proc. Roy. Soc. **A151**, 540 (1935); **A152**, 231 (1935).

Atomic-level modelling of dislocation interactions

David Stewart[1], *David Knowles*[2], *Ke-Shen Cheong*[2], *Shaun Hendy*[3], *Yuri Osetsky*[4], *David Bacon*[5]

[1]*Industrial Research Ltd., 69 Gracefield Rd, P. O. Box 31-310, 6009 Lower Hutt, New Zealand*
[2]*MPT Solutions Limited, Gracefield Research Centre, 6009 Lower Hutt, New Zealand*
[3]*Industrial Research Limited, Gracefield Research Centre, 6009 Lower Hutt, New Zealand*
[4]*Oak Ridge National Laboratory, Metal and Ceremics, P. O. Box 2008, TN 37831-6138, Oak Ridge, USA*
[5]*Materials Science and Engineering, Department of Engineering, The University of Liverpool, L69 3GH, Liverpool, United Kingdom*

Metallic thin films deposited on a silicon substrate have a wide range of microelectronic applications, for example in microdevices such as MEMS (micro-electro-mechanical systems) and as interconnects in integrated circuits. Due to differences in thermal expansion coefficients, the temperature changes during manufacture and in service lead to stresses that cause plastic deformation. The system is modelled at the microstructural level using a finite-element model of continuum crystal plasticity. This model requires the dislocation mobility and the distance at which dislocations can annihilate each other, which are currently determined by calibrating against temperature-cycling experiments.

Molecular dynamics (MD) simulations provide a way to determine these quantities based on the physical interactions at the atomic level, increasing the predictive power. MD is used to model dislocation-void and dislocation-dislocation interactions in fcc metals. Atomistic modelling is able to reveal important effects, which are beyond the continuum approach.

The two models are being coupled using multiscale techniques. The continuum model has found localised deformation at the edges of the specimen and at high-angle grain boundaries, so MD will only be used in these regions. The key areas will provide statistics of the MD result to the finite-element model, which will manage the rest of the specimen. Progress to date will be presented.

A Three-Dimensional Computer Modeling on the Development of Bubbles in Polycrystalline Materials

Tomoaki. Suzudo[1], Mitsuhiro Itakura[1], Yuka Fukuda[2], Hideo Kaburaki[1]

[1]Center for Computational Science and e-Systems, Japan Atomic Energy Agency, 2-4 Shirane Shirakata Tokai-mura 319-1195 Japan, E-mail:suzudo.tomoaki@jaea.go.jp;
[2]NS Solusions Corporation, 20-1 Shintomi Futtsu-shi 293-8511, Japan.

ABSTRACT

A new meso-scale computer model is proposed for the simulation of UO_2 fuel microstructural change during its burnup. For this purpose, interface dynamics using a Monte-Carlo simulation method is used. Although the qualitative reproduction of the bubble development is successful, that of the UO_2 grain sub-division is still difficult, and more improvement of the model is necessary to complete the modeling.

1. Introduction

The thermal and mechanical properties of Uranium-dioxide (UO_2) fuel have been studied in order to seek safer and more economic operation of nuclear power plants. An important safety-related requirement is to confine the highly-radioactive fission products within the fuel pellet. It is, however, known that a typical microstructural change occurs at the peripheral region of fuel pellets over some critical value of the burnup ~60 MWd/kgU (e.g. [1,2]), that is, nano-sized bubbles containing fission-gas atoms such as Xe atoms aggregate and form large bubbles with the diameter of ~2μm. At the same time, the original grains become subdivided. See the SEM micrograph shown in Fig. 1. These changes might promote the swelling of the pellet and the gas-release, both of which are not desirable to the safe operation.

The bubble formation and the grain sub-division occur almost at the same time, it is therefore considered that the both phenomena are closely related. Because the sub-divided grains have few defects, the UO_2 crystal undergoes a kind of “restructuring”, and the inert gas atoms aggregate during the “restructuring” process. A clear view of the mechanism of these changes has been sought for more than 20 years, but there is no definite consensus among the researchers.

The authors are trying to reproduce this microstructural change using meso-scale computer modeling approach hoping it can lead to understanding the mechanism. It is commonly known that the q-state Potts model can simulate grain growth processes, but the simulation of grain sub-division processes does not seem to be attained by a simple application of the Potts model. A recent study by Sonada et al. [3] indicated that the sub-divided grains have low angle boundaries. This result suggests that the grain boundary dynamics using the information of misorientation should be necessary for the simulation of the grain sub-division. Note that the Potts model does not usually concern the magnitude of misorientation.

We, in this paper, discuss the development of gas bubbles and the grain sub-division at the same time, using a newly-devised meso-scale computer model. We accordingly use both of the bubble and grain boundary migration dynamics, and the grain boundary migration dynamics dependent on the magnitude of misorientation is introduced.

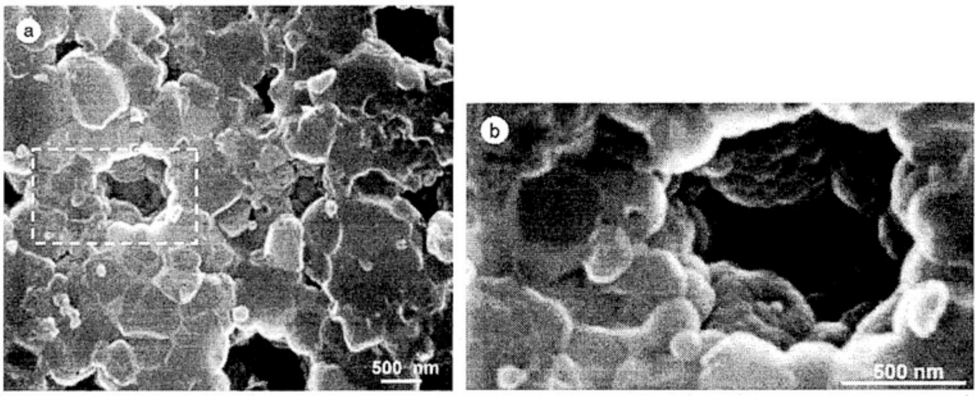

Figure 1. SEM micrographs of the sample of 75 MWd/kgU, 1000 ºC, showing (a) polyhedral grains away from the pore inner surface and (b) high magnification image of the area surrounded by the white dashed line in (a), showing rounded grains inside a pore. After [3].

2. Numerical Methods

This section explains the computer model used in this study. This model utilizes a Monte-Carlo simulation method that adopts a three-dimensional lattice system for the physical space. Each small lattice element carries variables that determine its state. The state of each element assumes either a bubble or a matrix state. A calculation element with the bubble state represent a cluster composed of vacancies and inert gas atoms. The inert gas we consider here is Xe. A calculation element with the matrix state carries also the state of its crystallographic orientation.

The dynamics of the model is determined by a series of Monte-Carlo steps, for which the Metropolis algorithm was adopted. The Hamiltonian used for the algorithm is composed of two kinds of energy: the grain boundary energy (E_{gb}) and bubble/matrix interface energy (E_{bm}). For E_{gb}, the Read-Shockley function [4] is used:

$$E_{gb} = \begin{cases} E_1(\theta/\theta_1)[1-\ln(\theta/\theta_1)] & \theta < \theta_1 \\ E_1 & \theta \geq \theta_1 \end{cases}, \tag{1}$$

where θ=15º. The relative values of the two kinds of energy were fixed throughout the present study as they satisfy E_{bm}: E_1=2:1. Their absolute values can be controlled by changing the Monte-Carlo temperature. The flips used in the Monte-Carlo algorithm include the following two kinds: (a) the migration of a bubble element; (b) replacing the orientation of a matrix element with a neighboring one. Therefore, the total number of bubble elements is conserved throughout the calculation.

3. Results

A typical results started from a random configuration is shown in Fig. 2, where 5% of elements were selected as a bubble element, and the remaining elements as matrix elements. The orientation of the matrix elements was randomly selected.

From Fig. 2 we notice that the black dots become gathered; the bubble growth is successfully simulated in this case study. However, the result also indicates that the grains grow indefinitely, and it does not produce stable small grains. The temperature parameter in the Metropolis algorithm was altered to stop this grain growth, but this tuning did not change significantly the results. In addition to the above calculation, where a three-dimensional hexagonal lattice used, a cubic lattice was also tried. The results, however, were not significantly different from those for the three-dimensional hexagonal lattice.

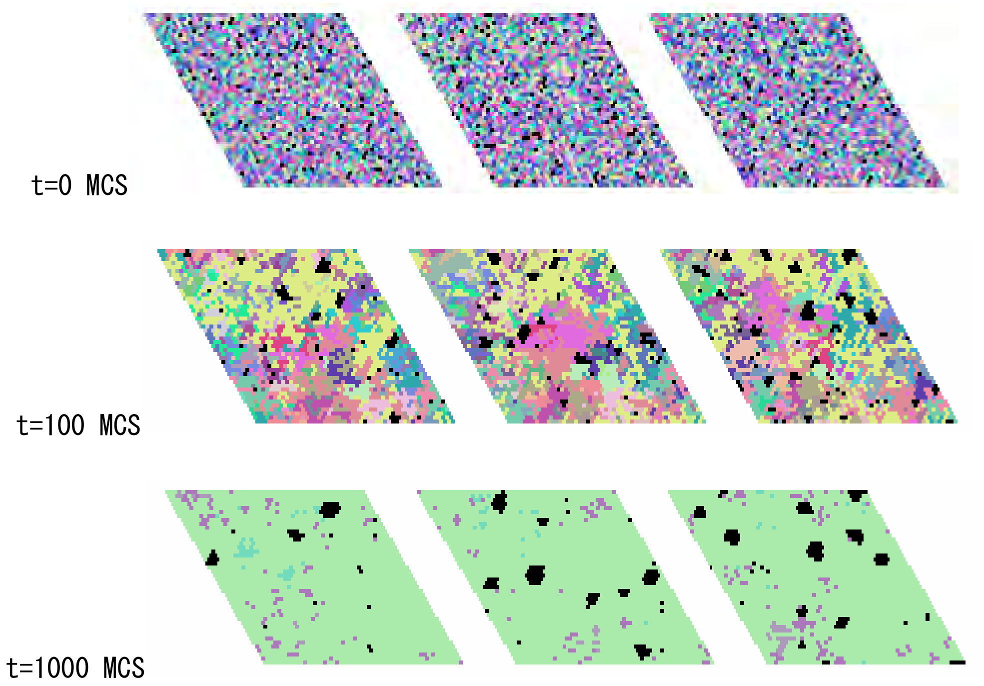

Figure 2. A calculation result started from a random configuration; each snapshot shows the result at the different Monte-Carlo step (MCS) and at the different z-axis position; black dots denote bubble elements and other colors indicate the crystallographic orientation of matrix elements.

4. Discussion

So far we have not succeeded to reproduce the grain subdivision phenomena yet. The cause of this problem seems that the mobility of grain boundaries with small misorientation is too large. Possible improvement may be the introduction of the grain boundary mobility dependent on the misorientation, that is,

$$P = \begin{cases} P_0[1 - \exp\{-n(\theta/\theta_1)^d\}] & \theta < \theta_1 \\ P_0 & \theta \geq \theta_1 \end{cases} \tag{2}$$

where P is the probability for grain boundary with the misorientation θ to be selected for a flip (b) [5]; n and d are integer parameters. This improvement is expected to reduce the mobility of grain boundaries with small misorientation and may lead to stable small grains

Acknowledgements

This study was financially supported by the Budget for Nuclear Research of the Ministry of Education, Culture, Sports, Science and Technology of Japan, based on the screening and counseling by the Atomic Energy Commission of Japan.

References

[1] Hj. Matzke, J. Nucl. Mat. 189, 141(1992).
[2] K. Nogita, K. Une, J. Nucl. Mat. **226**, 302(1995).
[3] T. Sonoda et al., Nucl. Inst. and Meth. In Phys. Res. B **191**, 622(2002).
[4] W. T. Read, W. Shockley, Phys. Rev. **78**, 275(1950).
[5] F. J. Humphreys, Acta Mater. **45**, 5031(1997).

Experimental investigation and multiscale modeling of orientation fields in mesocrystals

Bob Svendsen[1], *Vladislav Levkovitch*[2], *Mark Henning*[3], *Horst Vehoff*[3]

[1]*University of Dortmund, Chair of Mechanics, Department of Mechanical Engineering, 44221 Dortmund, Germany*
[2]*Chair of Mechanics, University of Dortmund, 44227 Dortmund, Germany*
[3]*Chair of Material Science, University of Saarland, 66041 Saarbrücken, Germany*

As has been documented by many experimental investigations, sustained loading of polycrystalline metals results in deformation localization, deformation heterogeneity and deformation/dislocationbased microstructural development. This is particularly true at grain boundaries and triple-junctions in such systems, and leads to complex local stress-field variations driving further deformation-based microstructural development. Among other things, such processes affect the local lattice orientation and its distribution within grains and across their boundaries in the system. In the last few years, a number of studies [e.g., 1, 2] have shown that experimental methods such as electron backscattering diffraction and orientation imaging microscopy (OIM) can be used to determine crystal lattice orientation distributions on the sample surface as a function of position in the sample with a resolution of down to 1 μm. Using these and related methods, one can determine in particular orientation gradients and relate these to lattice curvature. In turn, this curvature can be related in a model-dependent fashionto the density of geometrically-necessary dislocations (GNDs) in the sense of Nye [3] and Ashby [4]. The purpose of the current work is the modeling and simulation of orientation gradient development in mesocrystals subject to tension and bending with the help of recent extensions [e.g., 5, 6] of standard crystal plasticity to include the effects of GNDs on the material and in particular on the hardening behaviour. In particular, this is based on additional energy storage resulting in kinematic-like additional hardening and lengthscale-dependent material behaviour. Comparison of the simulation results with the experimental results of [2] will be carried out.

References

[1] Sun, S., Adams, B. L., Shet, C., Saigal, S., King, W., Mesoscale field investigation of the deformation of an aluminum bicrystal, Scripta Materialia, 39, 501–508, 1998.

[2] Henning, M., Vehoff, H., Local mechanical behavior and slip band formation of thin sheets with large grains, Acta Materialia, in press, 2006.

[3] Nye, J. F., Some geometric relations in dislocated crystals, Acta Metall., , 153–162, 1953.

[4] Ashby, M. F., The deformation of plastically non-homogeneous materials, Phil. Mag., 21, 399–424, 1970.

[5] Svendsen, B., Continuum thermodynamic models for crystal plasticity including the effects of geometrically-necessary dislocations, Journal of the Mechanics and Physics of Solids, 50, 1279-1329, 2002.

[6] Levkovitch, V., Sievert, R. Svendsen, B., Comparison of models for additional hardening in single and polycrystals due to deformation incompatibility, International Journal of Solids and Structures, in press, 2006.

Static Recrystallization Simulation Using Phase-Field Model Based on Crystal Plasticity Theory

Tomohiro Takaki[1], **Akinori Yamanaka**[2], **Yoshikazu Higa**[3], **Yoshihiro Tomita**[2]

[1]**Faculty of Maritime Sciences, Kobe University, 5-1-1, Fukaeminami, Higashinada,**
Kobe 658-0022, Japan, takaki@maritime.kobe-u.ac.jp;
[2]**Graduate School of Science and Technology, Kobe University,**
1-1, Rokkodai, Nada, Kobe 657-8501, Japan;
[3]**Department of Mechanical System Engineering, Okinawa National College of**
Technology, 905, Henoko, Nago 905-2192, Japan.

ABSTRACT

A numerical model and computational procedure for static recrystallization are developed using a phase-field model coupled with crystal plasticity theory. The microstructure and accumulated dislocation density during deformation of a polycrystalline metal are simulated using finite element method based on the strain gradient crystal plasticity theory. Phase-field simulation of the nucleation and growth of recrystallized grain is performed using the crystallographic orientation and stored energy calculated by crystal plasticity finite element simulation. Through this computational procedure, we can get the final recrystallization microstructure taking the deformation microstructure into consideration.

1. Introduction

The microstructures formed during annealing are significantly affected by the pre-deformation microstructures, since the recrystallization originates from dislocation cells or subgrains which appear after deformation and subsequently the recrystallized grain growth occurs driven by the stored energy resulted from the dislocation accumulated during deformation. Recently, the numerical studies using Monte Carlo Potts model [1] and cellular automata model [2] based on the data measured by EBSD analysis are made on static recrystallization. However, to enable more systematic investigations for recrystallization texture, it is key to develop the computational procedure without using experimental data.

In this study, we develop a phase-field model which can simulate the nucleation and growth of recrystallized grain. Here, the crystallographic orientation and dislocation density at the deformation of polycrystalline metal are simulated using finite element method based on the strain gradient crystal plasticity theory [3].

2. Numerical Procedure

The numerical procedure developed here consists of following three steps:
< Step. 1> The crystallographic orientation and dislocation density after deformation of polycrystalline metals are calculated by crystal plasticity finite element simulation.
< Step. 2 > The calculated data are mapped onto a regular lattice used in phase-field simulation. The stored energies calculated from dislocation density are smoothed on the lattice, because phase-field method requires the continuous driving forces.

< Step. 3 > Phase-field simulation during recrystallization is performed in which the nucleation and growth of recrystallized grain are reproduced.

3. Models and Results

By following the procedure shown in previous chapter, crystal plasticity theory, data mapping method and phase-field method employed in this study are briefly explained together with numerical results.

3.1 Strain gradient crystal plasticity

The crystal plasticity finite element method based on a strain gradient theory of rate dependent plasticity [3] is used to examine the microstructure and dislocation distribution during deformation of polycrystalline metals. Here, the critical resolved shear stress on slip system (a) is assumed to be a Bailey-Hirsch type function:

$$g^{(a)} = g_0^{(a)} + a\mu\tilde{b}\sum_{(b)}\varpi_{ab}\sqrt{\rho^{(b)}} \tag{1}$$

where, $g_0^{(a)}$ initial value of $g^{(a)}$, a constant, m elastic shear modulus, $\tilde{b}$ the magnitude of Burgers vector, ϖ_{ab} interaction matrix, and $\rho^{(b)}$ accumulated dislocation density. The accumulated dislocation density is the sum of the densities of SSD and GND. The evolution of SSD is expressed by the balance between the production rate of dislocations and the annihilation by dynamic recovery. The density of GND is calculated from the gradient of shear strain on slip system (a). Since the hardening equation, Eqn. 1, includes the strain gradient term through the dislocation density, it is possible to express the grain size effects.

Figure 1(a) shows the polycrystal model with 23 grains where the average grain diameter is 115.5 μm. This model is divided into 64x64 regular crossed-triangle elements and is compressed at a strain rate 10^{-3} s^{-1} as a 2-slip plane strain problem. Figure 1(b) and (c) illustrate the crystallographic orientation and stored energy after 50% compression, respectively. The stored energy E_{store} is calculated by $E_{store} = 0.5\rho\mu\tilde{b}^2$, where ρ is the total dislocation density of all slip systems.

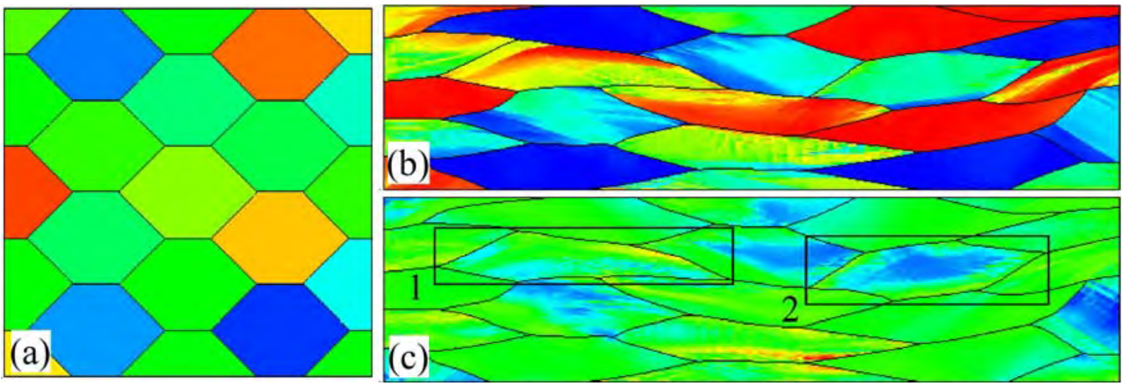

Figure 1. Crystallographic orientation (a) before deformation and (b) at 50% compression, and (c) stored energy. Solid lines indicate initial grain boundaries.

3.2 Data mapping

The data computed by crystal plasticity finite element simulation, i.e. crystallographic orientation and stored energy, are mapped onto the regular lattice of phase-field simulation. The relationship between triangle elements used in finite element simulation and lattice used in phase-field simulation is shown in Fig. 2. The regular lattice size is 0.4 μm and triangle elements are a part of Fig. 1 (b). First, the crystallographic orientation and stored energy on lattice are determined as a value inside an element. In other words, the values of lattice located inside a triangle element are all identical. Next, the misorientation on lattice is determined as a maximum value among the four misorientations between the two neighboring lattices, i.e., $\Delta\theta_1$, $\Delta\theta_2$, $\Delta\theta_3$, and $\Delta\theta_4$, represented in Fig.2. Then, the stored energies mapped onto the regular lattice are smoothed using Winslow's smoothing method:

$$E_{store} = \sum_{j=1}^{m} E_j w_j \Big/ \sum_{j=1}^{m} w_j \qquad (2)$$

where, E_{store} smoothed stored energy on lattice i, E_j stored energy before smoothing on lattice j, w_j weight represented as an inverse of distance between lattice i and lattice j, and m the number of lattice inside a considering circle with radius r. In this study, $r = 3\Delta x$ is selected where Δx is lattice size. Finally, the crystallographic orientation, misorientation and smoothed stored energies on all regular lattices are determined. Figures 3 (a) and (b) show the distributions of smoothed stored energy and misorientation, respectively, for the regions 1 (332.8 x 64 μm^2) and 2 (268.8 x 76.8 μm^2) illustrated in Fig.1.

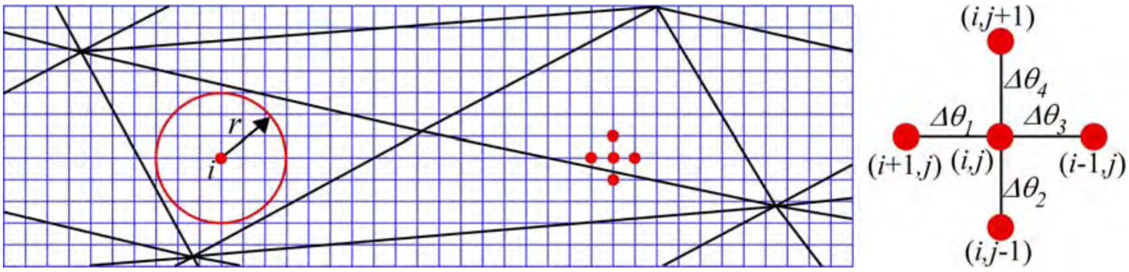

Figure 2. Triangle elements for crystal plasticity finite element simulation and regular lattice for phase-field simulation.

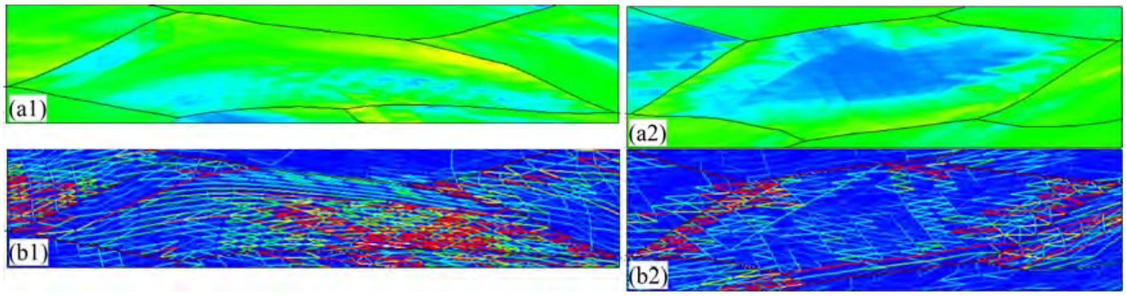

Figure 3. (a) smoothed stored energy and (b) misorientation. 1 and 2 indicates region 1 and 2 of Fig.1, respectively.

3.3 Phase-field simulation

By using the data mapped onto regular lattice, the nucleation and growth of recrystallized grain are simulated using phase-field method. In the present phase-field model, two order parameters, i.e., phase field ϕ which equals zero in the deformed matrix and unity in recrystallized grain and crystallographic orientation θ, are employed. The time evolved equations for the order parameters are as following:

$$\frac{\partial\phi}{\partial t}=M_\phi\left[\alpha^2\nabla^2\phi-\frac{\partial f(\phi)}{\partial\phi}-2\phi s|\nabla\theta|\right] \qquad (3) \qquad\qquad \frac{\partial\theta}{\partial t}=M_\theta\frac{1}{\phi^2}\nabla\cdot\left(\phi^2 s\frac{\nabla\theta}{|\nabla\theta|}\right) \qquad (4)$$

where, $f(\phi)$ a free energy density expressed by double well type function: $f(\phi)=(1-p(\phi))E_{store}+Wq(\phi)$ with $p(\phi)=\phi^3(10-15\phi+6\phi^2)$ and $q(\phi)=\phi^2(1-\phi)^2$, $W=6\sigma/\delta$ energy wall height related to interface energy σ and interface thickness δ, $\alpha=\sqrt{3\delta\sigma}$ gradient coefficient, $s=\alpha\sqrt{2W}/\pi$, $M_\phi=m\sqrt{2W}/6\alpha$ mobility for ϕ where m is a mobility of grain boundary migration, and $M_\theta=(1-p(\phi))M_\phi$ mobility for θ. Equations (3) and (4) are solved by an adaptive finite element method [4].

Figure 4 shows the initial nucleus sits, the growth process, and final recrystallization microstructure. The site saturated nucleation model is used, in which the following nucleation criteria are assumed: (1) the high angle grain boundary of more than 15 degree, (2) the stored energy of more than 0.6 MPa, (3) the orientation of the nucleus is presented in the deformed structure, and (4) the minimum distance between the two neighboring nuclei is $10\Delta x$. The initial radius of nucleus is set to $3\Delta x$. From Fig.4, it is observed that, in region 1, the nucleation and growth of recrystallized grains occur inside the grain before deformation, while, in region 2, the recrystallized grains originate only from grain boundary.

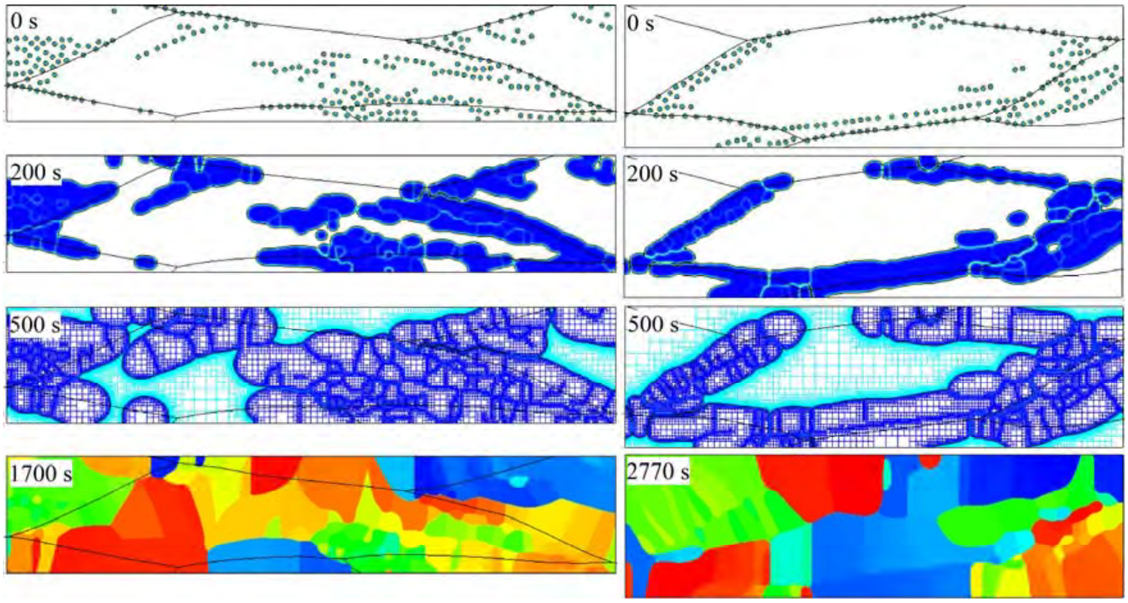

Figure 4. Time evolutions of recrystallized grain growth and final recrystallization microstructures. Adaptive meshes are illustrated only for results at 500s.

References

[1] S. Choi and J. H. Cho, “Primary recrystallization modelling for interstitial free steels”, Mater. Sci. Eng. A405, 86, (2005).

[2] D. Raabe and L. Hntcherli, “2D cellular automaton simulation of the recrystallization texture of an IF sheet steel”, Compu. Mater. Sci. 34, 299, (2005).

[3] Y. Higa, Y. Sawada and Y. Tomita, “Computational simulation of characteristic length dependent deformation behavior of polycrystalline metals”, Tran. JSME 69, 523, (2003).

[4] T. Takaki, T. Fukuoka and Y. Tomita, “Phase-field simulation during directional solidification of a binary alloy using adaptive finite element method”, J. Crystal Growth 283, 263, (2005).

Laser Post-Treatment of Plasma-Sprayed Yttrium-Stabilized Zirconia Coatings

Daniel Tolksdorf[1], *Hannes Weckmann*[2]

[1]*Institute for Industrial Manufacturing and Management (IFF), Universität Stuttgart, Nobelstrasse 12, 70569 Stuttgart, Germany*

[2]*BMW Group, 80788, Muenchen, Germany*

Laser post-treatment has become a common procedure to modify properties of thermal sprayed coatings for a wide range of materials. Using this procedure has the advantage that even minor quality of the base coatings is mostly sufficient to achieve good coating results after post treatment. Moreover there is only low impact, i.e. thermal load on the substrate during laser process. Comprehensive surveys about effects of the laser process on the possible microstructure and coating property are still rare. To investigate different factors of influence in the laser process and to characterize their effects on the coating is focus of the present paper.

Ceramic layers obtained by vacuum plasma spraying (VPS) were used as base material. Therefore yttrium stabilised zirconia powder was deposited on ferritic steel plates using standard VPS-parameter. Afterwards the surface of the plasma sprayed coatings was post-treated by laser-remelting process, carried out with a CO2-laser system running in continuous wave mode. Laser energy, scan velocity and line spacing were varied as main factors of influence in the laser process using a D-optimal design of experiments (DoE). To characterise and to quantify the effects of the factors on the coating properties a multiple regression was done utilizing micro hardness, depth of penetration and surface roughness as response for the DoE. Additional micro structural investigations, i.e. SEM, X-ray diffraction were carried out. Starting with the typical lamellar structure received by thermal spray processes, laser treated coatings varied from melted block-shaped to columnar texture. Possibly crystalline formations and even nanostructured top coats deposited from gas phase have been observed depending on process settings.

Slip System Based Model for Work Hardening and Softening of Aluminium Including Strain Path Change Effects

Steven Van Boxel, **Marc Seefeldt, Bert Verlinden and Paul Van Houtte**

Department of Metallurgy and Materials Engineering, Katholieke Universiteit Leuven,
Kasteelpark Arenberg 44, B-3001, Leuven, Belgium
Email: Steven.VanBoxel@mtm.kuleuven.be.

ABSTRACT

A new phenomenological multiscale model is proposed for single phase aluminium alloys, which is able to predict the hardening and softening transition effects that take place during strain path changes. At the mesoscopic level the critical resolved shear stresses (τ_{CRSS}) of each slip system will be updated separately, depending on the current slip activity of all slip systems and the microstructure remaining form the prior strain mode. The resulting stress-strain curves display the transient behaviour during imposed strain path changes.

1. Introduction to the multiscale model

Three levels of homogenisation are present in the model. The highest (macroscopic) level incorporates texture information by selecting a representative set of discrete orientations out of an orientation distribution function (ODF). The transition to the mesoscopic level is done by the classical full constraint (FC) Taylor model, assuming the same velocity gradient for all individual orientations. At the mesoscopic level, shear rates of the individual slip systems are obtained with the generalised Schmid law and the Taylor assumption. Other than in the FC Tayler model, the critical resolved shear stresses (τ_{CRSS}) can differ for each slip system and for the slip direction. The evolution equations for the τ_{CRSS} will be explained in detail in section 2.

At the microscopic level the interaction of dislocations with the dislocation substructure, in single phase alloys the main contribution to work hardening, is modelled by the Alflow model of Nes [1]. The homogenisation is at the level of the hardening rate of an active slip system which will be integrated in the evolution equations of the τ_{CRSS}'s.

The model is, regarding its setup, similar to models of Peeters et al. [2] and Holmedal et al. [3]. Compared to the latter, the difference lies only in the evolution equations of the τ_{CRSS}'s.

2. Model for the critical resolved shear stresses

The critical resolved shear stresses are updated for each slip system α by integrating a classical hardening law which will be modified to take into account the effects during strain path changes. The basic law is taken from Kocks et al. [4] which is of the form

$$\dot{\tau}^{\alpha} = \theta_1 \sum_{\beta} \left(\frac{\tau^{\beta}}{\tau^{\alpha}} H^{\alpha\beta} \left| \dot{\gamma}^{\beta} \right| \right). \tag{1}$$

θ_1 is the hardening rate of an individual slip system which will be calculated with the Alflow model. $H^{\alpha\beta}$ is the classical hardening matrix to account for interactions between slip systems. Here unity is taken if slips are coplanar and 1.4 otherwise. The shear rates $\dot{\gamma}^{\beta}$ are coming from the FC Taylor model and taken constant during a strain increment.

This evolution equation enables one to model latent hardening effects and therefore the overall anisotropy, but the transient behaviour experimentally observed during abrupt changes of the strain path (previous latent hardened slip systems soften initially during cross load, the reverse of an active slip system hardens during a reversal of strain) can not be predicted. This behaviour can be attributed to the suddenly modified dislocation activity in the microstructural configuration of the previous straining mode. The partial dissolving of the existing microstructure is often thought to cause the softening in cross tests [5], while differences in the storage of pre-existing and newly formed dislocations are thought to cause the hardening in a strain reversal test [6].

To introduce the deformation history of previous deformation steps, two variables λ and π are introduced for each slip system having the following rate equations:

$$\dot{\lambda}^{\alpha} = b_1\left|\dot{\gamma}^{\alpha}\right| - b_2\lambda^{\alpha} \qquad \text{and} \qquad \dot{\pi}^{\alpha} = c_1\dot{\gamma}^{\alpha} - c_2\pi^{\alpha}\,. \tag{2,3}$$

During a strain path change, the ratios $b_2/b_1 \cdot \lambda^{\alpha}$ and $c_2/c_1 \cdot \pi^{\alpha}$ will both evolve exponentially from the shear rate $\dot{\gamma}^{\alpha}$ in the former deformation mode to the shear rate of the current one, with the difference that π^{α} also reflects the directionality of the slip (when a slip is reversed, $\dot{\gamma}^{\alpha}$ becomes negative and π^{α} will exponentially evolve towards this new negative value, while λ^{α} does not change, e.g. the second slip system in fig. 1).

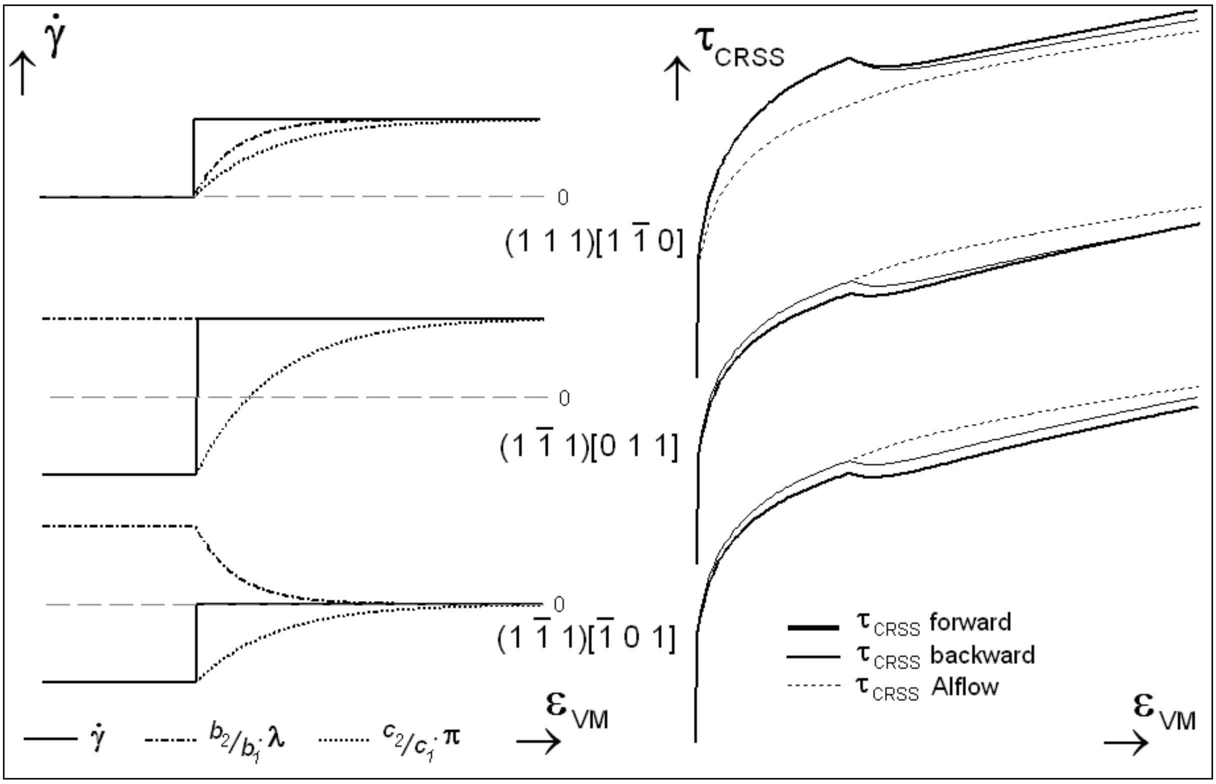

Figure 1. Left: imposed shear rates for the three slip systems and the corresponding responses of λ and π. Right: critical resolve shear stresses for the three slip systems in both slip directions calculated with of mesoscopic model.

In fig. 1 an example is displayed concerning three slip systems. The first slip system is initially inactive but becomes active when an abrupt change of strain path occurs. The two others are active in the first strain path. The second reverses the direction of slip in the strain path change, while the third one becomes inactive. The imposed shear rates $\dot{\gamma}$ and the responses of λ and π (scaled with the ratio of the modelling parameters to make them comparable to $\dot{\gamma}$) are shown on the left side.

The change of the τ_{CRSS} (eqn (1)) is now made dependent of the exisiting microstructure, built up in the previous strain mode, by introducing λ and π under certain conditions. If the activity on a slip system δ abruptly lowers or becomes zero then $b_2/b_1 \cdot \lambda^\delta > \left|\dot{\gamma}^\delta\right|$ (e.g. the third slip systems in fig 1.). If this condition holds, the $\left|\dot{\gamma}^\delta\right|$ for slip system δ in eqn 1 is replaced by $\dot{\lambda}^\delta$, making eqn (1):

$$\dot{\tau}^\alpha = \theta_1 \sum_{\beta \neq \delta} \left(\frac{\tau^\beta}{\tau^\alpha} H^{\alpha\beta} \left|\dot{\gamma}^\beta\right| \right) + \theta_1 \frac{\tau^\delta}{\tau^\alpha} H^{\alpha\delta} \left(b_1 \left|\dot{\gamma}^\delta\right| - b_2 \lambda^\delta \right) \tag{4}$$

The hardening of all the slip systems due to prior activity of slip system δ gets reversed to a certain extend ($b_1\left|\dot{\gamma}^\delta\right| - b_2\lambda^\delta < 0$) with an exponential decay (all slip systems in fig 1 are softened by this effect) . The magnitude of the decay is controlled by b_1 while the rate of the decay is controlled by b_2. These two parameters can be seen as characteristics for the strength and sustainability of the microstructure built up during the previous straining mode, which is characterised by the set of λ^α's. Eqn (4) can model the transient effects during cross tests.

The initial softening and subsequent extra hardening during a strain reversal test are modelled in a similar way. For this reason it is necessary to differentiate between the τ_{CRSS} in the forward and backward direction of a slip system. Whenever a slip system is active it will soften the slip resistance in its reverse direction in the following way:

$$\dot{\tau}^{-\alpha} = \theta_1 \sum_{\beta \neq \alpha} \left(\frac{\tau^\beta}{\tau^\alpha} H^{\alpha\beta} \left|\dot{\gamma}^\beta\right| \right) + \theta_1 H_{inv} \left|\dot{\gamma}^\alpha\right| \quad \text{with} \quad H_{inv} < H^{\alpha\alpha} \tag{5}$$

The reverse slip direction will harden less than the active slip direction due to a lower selfhardening coefficient (e.g. slip systems 2 and 3 before the strain path change in fig 1.). If a slip system δ is active and $\left|\dot{\pi}^\delta\right| = \text{abs}\left(c_1\dot{\gamma}^\delta - c_2\pi^\delta\right) > 0$ (meaning that the activity was reversed), extra hardening due to the storage of the pre-existing and reversed dislocations is modelled by

$$\dot{\tau}^\alpha = \theta_1 \sum_{\beta} \left(\frac{\tau^\beta}{\tau^\alpha} H^{\alpha\beta} \left|\dot{\gamma}^\beta\right| \right) + \theta_1 \text{abs}\left(c_1\dot{\gamma}^\delta - c_2\pi^\delta\right) \tag{6}$$

This extra hardening also has an exponential decay of which the magnitude and the rate are controlled by c_1 and c_2 (e.g. the forward slip of the second system in fig. 1 after the strain path change).

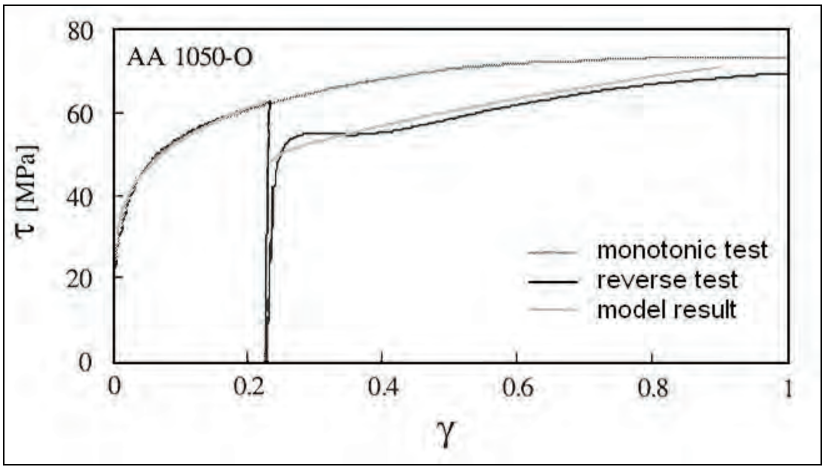

Figure 2. Experimental stress-strain curve of a simple shear test with strain reversal (from [6]) compared with model result

3. Results and discussion

In fig. 2 an experimental stress-strain curve of a simple shear test at room temperature of a AA1050-O sheet sample is shown [6]. After 22% of shearing the strain path is reversed. The model is capable of capturing the transient behaviour after the strain path change to a reasonable extend. However, the hardening behaviour is too complex to be described by eqn. 2 and 3. A more advanced model (e.g. the model of Peeters et al. [2]) is needed to capture all the characteristics of the transition.

Acknowledgements

The authors would like to thank B. Holmedal from the NTNU in Trondheim for inspiring discussions and for providing the Alflow code. The authors are grateful for the funding provided by the Fund for Scientific Research-Flanders, FWO-project G.0521.04. M.S. gratefully acknowledges his postdoctoral fellowship from the FWO-Vlaanderen.

References

1. **Nes E**. Modelling of Work Hardening and Stress Saturation in FCC Metals. *Prog. Mater. Sci.* 41: 129-193, 1998
2. **Peeters B, Seefeldt M, Teodosiu C, Kalidindi SR, Van Houtte P and Aernoudt E.** Work-Hardening/Softening behaviour of BCC Polycrystals during Changing Strain Paths: I. An Integrated Model based on Substructure and Texture Evolution, and its Prediction of the Stress-Strain behaviour of an IF Steel during Two-stage Strain Paths. *Acta Mater.* 49: 1607-1619, 2001
3. **Holmedal B, Van Houtte P, An Y, Pedersen K, Furu T, Court S, Daniel D and Nes E.** Strain Path Changes in Aluminium Alloys. *Aluminium* 80: 738-742, 2004
4. **Kocks UF, Franciosi P and Kawai M**. A Forest Model of Latent Hardening and its Application to Polycrystal Deformation. *Textures Microstr.* 14-18: 1103-1114, 1991
5. **Li F and Bate PS.** Strain Path Change Effects in Cube Textured Aluminium Sheet. *Acta Metall. Mater.* 39:2639-2650, 1991
6. **Vincze G, Rauch EF, Gracio JJ, Barlat F and Lopes AB.** A Comparison of the Mechanical behaviour of an AA1050 and a Low carbon Steel Deformed upon Strain Reversal. *Acta Mater.* 53: 1005-1013, 2005

Effect of Non-Glide Stresses on Deformation of BCC Metals at Finite Temperatures

Roman Gröger and Vaclav Vitek

Department of Materials Science and Engineering, University of Pennsylvania,
3231 Walnut Street, Philadelphia, PA 19104-6272, U.S.A.

ABSTRACT

In this paper, we show that plastic flow of bcc metals at finite temperatures and strain rates can be captured by a model in which the underlying physics enters via the results of single-dislocation atomistic studies at 0 K. The Peierls potential is constructed solely from the results of atomic-level calculations and accounts for both the crystal symmetry and the effect of non-glide stresses. This potential is then employed in calculations of the stress dependence of the enthalpy to nucleate a pair of kinks, which is used subsequently to evaluate the temperature and strain rate dependence of the yield stress. Results of these calculations are shown to be in excellent agreement with experimental data.

1. Introduction

The plastic deformation of all bcc metals is controlled by $1/2\langle 111\rangle$ screw dislocations that have non-planar cores and, therefore, possess a very high Peierls stress. This leads to a strong temperature dependence of the flow stress at low temperatures. In addition, the non-planar core also induces a pronounced tension-compression asymmetry [1] that has commonly been interpreted in terms of the twinning-antitwinning asymmetry of the sense of shearing in the slip direction. However, detailed atomistic calculations [2, 3] have disclosed that the situation is more complex and that the Peierls stress is also a strong function of the shear stress perpendicular to the slip direction. These studies, which employed molecular statics and thus correspond to 0 K, have ascertained the dependence of the critical resolved shear stress (CRSS) for glide, i.e. the Peierls stress, of the 1/2[111] screw dislocation as a function of: (i) the angle χ between the maximum resolved shear stress plane (MRSSP) and the $(\bar{1}01)$ plane and (ii) the shear stress τ perpendicular to the slip direction. These results have then been utilized to construct an effective yield criterion that correctly captures the effect of non-glide stresses [3, 4]. When formulating such criterion we define an effective stress τ^* as a linear combination of shear stresses parallel and perpendicular to the slip direction in two different {110} planes:

$$\tau^* = \sigma\left[\cos\chi + a_1\cos(\chi+\pi/3)\right] + \tau\left[a_2\sin 2\chi + a_3\cos(2\chi+\pi/6)\right]. \tag{1}$$

Here σ is the shear stress parallel to the slip direction acting in the MRSSP and the yield criterion is then $\tau^* \le \tau^*_{\mathrm{cr}}$ where τ^*_{cr} is an effective yield stress. a_1, a_2, a_3 and τ^*_{cr} are parameters determined by fitting the $\mathrm{CRSS}-\chi$ and $\mathrm{CRSS}-\tau$ dependencies obtained from atomistic calculations. In the case of molybdenum, $a_1 = 0.24$, $a_2 = 0$, $a_3 = 0.35$, $\tau^*_{\mathrm{cr}}/C_{44} = 0.027$.

At finite temperatures, a moving dislocation surmounts the Peierls barrier at stresses lower than the Peierls stress via the formation of pairs of kinks and with the aid of thermal activation. However, 0 K calculations do not determine the Peierls barrier but merely its maximum slope along a transition coordinate ξ defined as the minimum-energy path between two adjacent equivalent potential minima. The Peierls stress σ_P and the Peierls barrier $V(\xi)$ are related by

$$\sigma_P b = \max\left(dV/d\xi\right). \tag{2}$$

For a given angle χ of the MRSSP and angle ψ, which the slip plane makes with the $(\bar{1}01)$ plane, the Peierls stress can be expressed as $\sigma_P = \mathrm{CRSS}\cos(\chi - \psi)$. Since screw dislocations do not have well-defined slip planes, it is necessary to consider a two-dimensional Peierls potential, $V(x, y)$, defined in the plane perpendicular to the dislocation line. The height and shape of this potential and, most importantly, its dependence on the applied stress tensor, are crucial information for the development of a theory of the thermally activated motion of screw dislocations.

In this paper, we first show how the Peierls potential and its dependence on the stress tensor can be extracted from the data obtained in atomistic studies at 0 K. Using this information we then develop a model of the formation of pairs of kinks following the approach of Dorn and Rajnak [5]. We then employ this model in the analysis of the temperature and orientation dependence of the yield stress in molybdenum the results of which are compared with experimental observations [6-8]. In the following, the yield stress is always expressed as the shear stress parallel to the slip direction resolved in the $(\bar{1}01)$ plane.

2. Construction of the Peierls potential

The shape of the effective Peierls potential, $V(x, y)$, is based on a mapping function, $m(x, y)$, that is defined in the plane perpendicular to the dislocation line, i.e. (111) plane in the case of the 1/2[111] screw dislocation. This function captures periodicities and symmetries in this plane, in particular the symmetry-dictated positions of potential minima, maxima and saddle points. It is shown in Fig. 1 as a contour plot where dark regions are potential minima and bright regions potential maxima; the maximum height of $m(x, y)$ is one.

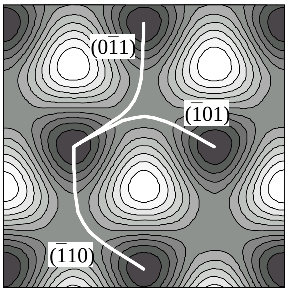

Figure 1: Mapping function m(x,y). The white curves depict the three equivalent minimum energy paths between the potential minima.

We begin the construction of the effective Peierls potential by capturing the fundamental symmetries in the (111) plane. This can be accomplished by writing $V(x, y) = \Delta V\, m(x, y)$, where ΔV is a currently unknown potential height. To determine ΔV, we investigate loading by pure shear, σ, parallel to the slip direction for χ=0. For this loading, atomistic studies show that the dislocation moves along the $(\bar{1}01)$ plane, i.e. ψ=0, and thus $\sigma_P = \mathrm{CRSS}$ in (2). The shape of the Peierls barrier, $V(\xi)$, experienced by the dislocation is obtained as a cross-section of $V(x, y)$ along the transition coordinate ξ defined above that, in the present case, connects two adjacent potential minima on the $(\bar{1}01)$ slip plane. This minimum-energy path has been determined numerically using the Nudged Elastic Band method. The potential height, ΔV, is then obtained to satisfy (2).

In order to incorporate the effect of non-glide stresses, we first generalize the Peierls potential within each repeat cell of the (111) plane to $V(x, y) = [\Delta V + V_\sigma(\theta)]\, m(x, y)$, where θ is a polar angle in the (111) plane measured in the same sense as χ and ψ, and the term $V_\sigma(\theta)$ represents an angular distortion of the three-fold symmetric basis of the potential by the non-glide stress σ applied in a plane *different* than $(\bar{1}01)$. The functional form of the added term is written as $V_\sigma(\theta) = K_\sigma(\chi)\, \sigma b^2 \cos\theta$ which obeys the symmetry of the shear stress parallel to the slip direction and assures that the largest distortion is always applied in the $(\bar{1}01)$ plane. In this equation, the function $K_\sigma(\chi)$ is determined from the requirement that (2) reproduces the $\mathrm{CRSS} - \chi$ dependence obtained from atomistic studies. Since in these calculations the glide is always along the $(\bar{1}01)$ plane and thus ψ=0 for any orientation of the MRSSP, the Peierls stress in (2) becomes $\sigma_P = \mathrm{CRSS}\cos\chi$ and the corresponding value of $K_\sigma(\chi)$ can be found by numerically solving (2) when ΔV has already been fixed.

Finally, the effect of the shear stress perpendicular to the slip direction, τ, is incorporated by writing $V(x,y)=[\Delta V+V_\sigma(\theta)+V_\tau(\theta)]\,m(x,y)$, where $V_\tau(\theta)$ represents an angular distortion of the Peierls potential by τ. The functional form of $V_\tau(\theta)$ is now chosen such that it reproduces the symmetry of the shear stress perpendicular to the slip direction and, simultaneously, is a linear function of τ. One of the simplest forms that satisfies both these requirements is $V_\tau(\theta)=K_\tau(\chi)\,\tau b^2\cos(2\theta+\pi/3)$. In order to keep the evaluation of $K_\tau(\chi)$ relatively simple, we consider $\chi\in(-\pi/6,+\pi/6)$ and shear stresses $\tau/C_{44}=\pm0.01$ for which the dislocation glides on the $(\bar{1}01)$ plane. The Peierls stress in (2) is thus again $\sigma_P=\mathrm{CRSS}\cos\chi$ and the values of $K_\tau(\chi)$ for a given χ can be found by numerically solving (2). Very importantly, the Peierls potential has been constructed only from the data corresponding to the $(\bar{1}01)$ slip and the change of the slip plane at large negative τ, observed in atomistic studies, is not included *a priori*. The contour plots of the distorted Peierls potential for two different values of τ and $\chi=0$ are shown in Fig. 2.

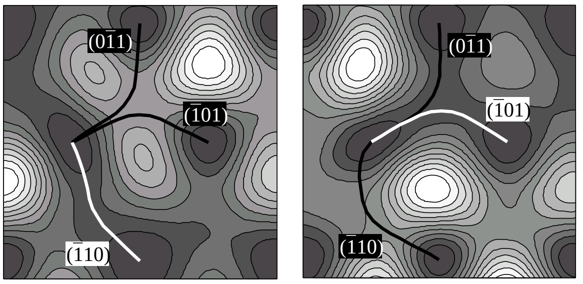

a) τ/C_{44}=-0.05 b) τ/C_{44}=+0.05

Figure 2: Effect of the shear stress perpendicular to the slip direction, τ, on the shape of the effective Peierls potential V(x,y). The curves define the minimum energy paths for the dislocation glide along the three different {110} planes. The white path has the lowest Peierls barrier.

The effective Peierls potential, $V(x,y)$, developed as described above, reproduces correctly both the twinning-antitwinning asymmetry of the shear stress parallel to the slip direction and the effect of the shear stress perpendicular to the slip direction. It is seen from Fig. 2b that for positive τ the Peierls potential displays a low-energy path along the most-highly stressed $(\bar{1}01)$ plane, which thus leads to a low Peierls barrier for slip on this plane. However, this slip is suppressed at negative τ (Fig. 2a) where the lowest Peierls barrier corresponds to the glide along the $(\bar{1}10)$ plane. For other orientations of the MRSSP and negative τ, the low-energy path typically develops either on the $(\bar{1}10)$ or on the $(0\bar{1}1)$ plane. The Schmid stress in these planes is much lower than in the $(\bar{1}01)$ plane and the slip can thus be classified as anomalous. This finding is in excellent agreement not only with 0 K atomistic studies [2, 3] but also with experiments [6]. Interestingly, since the possibility of slip on other planes than $(\bar{1}01)$ has not been assumed in the construction of the Peierls potential, the anomalous slip at negative τ follows *naturally* from the chosen shape of the term $V_\tau(\theta)$.

3. Activation enthalpy and the temperature dependence of the yield stress

At stresses lower than the Peierls stress, the dislocation moves towards the top of the Peierls barrier and, simultaneously, the originally three-fold symmetric basis of the Peierls potential gets distorted by the action of σ and τ. The activation enthalpy ΔH for nucleation of a pair of kinks, which depends on the shape of the Peierls potential, can be evaluated using the model of Dorn and Rajnak [5]. The plastic strain rate $\dot{\gamma}$ is then given by the standard relation of the reaction rate theory

$$\dot{\gamma}=\dot{\gamma}_0\sum_\alpha \exp[-\Delta H^\alpha(\sigma,\tau)/kT]. \tag{3}$$

where ΔH^α is the stress-dependent activation enthalpy for the slip system α. When considering only the most operative slip system with the lowest ΔH and setting $\dot{\gamma}_0$ to comply with an effective density of mobile dislocations, the temperature dependence of the yield stress can be obtained for a given strain rate from the relation $\Delta H(\sigma,\tau)=kT\ln(\dot{\gamma}_0/\dot{\gamma})$.

The symbols in Fig. 3 show the temperature dependence of the yield stress measured by Hollang *et al* [7] for single crystals of Mo under loading in tension along $[\bar{1}49]$ and two plastic strain rates. Since this loading leads to the single slip on the $(\bar{1}01)[111]$ system, the temperature dependence of the yield stress can be readily calculated and it is depicted in Fig. 3 by solid lines. At stresses lower than 115 MPa, the slip occurs by nucleating two interacting kinks and the activation enthalpy is determined by the elastic interaction of kinks [9] (dashed lines in Fig. 3). An excellent agreement between the theory and experiments is obvious.

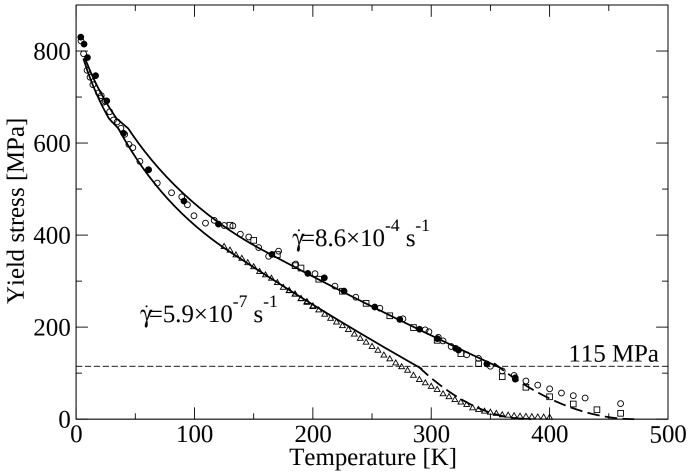

Figure 3: Temperature dependence of the yield stress for tension along $[\bar{1}49]$. The experimental data are from [7].

For loading along $[\bar{1}49]$ the MRSSP is the $(\bar{1}01)$ plane (χ=0) and no twinning-antitwinning asymmetry is present. However, the calculated yield stress in compression is higher than in tension. This significant tension-compression asymmetry, caused by the shear stress perpendicular to the slip direction, is in good qualitative agreement with experimental observations [8]. Interestingly, if the loading axis deviates toward the [011] corner of the stereographic triangle, the tension-compression asymmetry changes its character and the yield stress in tension becomes larger than that in compression. This trend is again in agreement with the experiments in [8].

4. Conclusion

This paper shows how the results of single-dislocation atomistic studies at 0 K can be used to develop a mesoscopic theory of thermally activated dislocation motion and to finally attain the theoretical description of the temperature, strain rate and orientation dependence of the yield stress. This multiscale sequential combination of atomistic modeling with the dislocation theory results in the physically based multislip yield criteria for plastic flow of bcc metals at finite temperatures and strain rates.

References

1. J. W. Christian, *Metall. Trans. A, 14* (1983) 1237.
2. K. Ito and V. Vitek, *Philos. Mag. A, 81* (2001) 1387.
3. R. Gröger and V. Vitek, *Materials Science Forum, 482* (2005) 123.
4. V. Vitek, M. Mrovec and J. L. Bassani, *Mat. Sci. Eng. A, 365* (2004) 31.
5. J. E. Dorn and S. Rajnak, *Trans. TMS-AIME, 230* (1964) 1052.
6. P. J. Jeffcoat, B. L. Mordike and K. D. Rogausch, *Philos. Mag., 34* (1976) 583.
7. L. Hollang, M. Hommel and A. Seeger, *Phys. Stat. Sol. (a), 160* (1997) 329.
8. L. Hollang and A. Seeger, *Materials Transactions, JIM, 40* (2000) 141.
9. A. Seeger, *J Phys IV, 5* (1995) 45.

Size effects on micro-twinning in NiTi shape memory alloys

Martin Franz-Xaver Wagner

The Ohio State University, Department of Materials Science and Engineering, 441A Watts Hall, 2041 College Road, 43210 Columbus, United States of America

In contrast to classical continuum mechanics predictions, the mechanical properties of materials depend on specimen size as external lengths decrease to micro-meter scales or even below. Characterization of the fundamental material behavior at small scales is a necessary prerequisite for modeling of microstructure-property relationships. And size effects are of particular interest for micro engineering applications, where NiTi shape memory alloys are potential candidates for future MEMS devices.

Recent experimental studies established focused ion beam (FIB) milling to prepare micro-pillars for compression testing, and uncovered novel size effects on plasticity of several material systems. In comparison, deformation of NiTi adds an additional level of complexity, because it is characterized by an interaction of three micro structural processes: plastic deformation by dislocation slip; stress-induced martensitic phase transformation (formation several possible twin variants); and subsequent detwinning. While it is well-known from macroscopic compression testing of single crystalline NiTi that different orientations of a specimen with respect to external loads may favor one process over the other, size effects on the deformation behavior of NiTi have not been reported to date.

In this contribution, we present first results from ongoing micro-pillar testing of single crystalline NiTi. We study the load-deformation data and discuss competing microstructural processes for different orientations and sample sizes (pillar diameters) at the micron-scale. We consider an energy minimization theory for martensitic twinning to rationalize the relationship between sample orientation and dominating deformation mechanism, and we assess two underlying hypotheses: On the one hand, a change from multi-variant to single mode twinning may well occur with decreasing specimen size as constraints from surrounding bulk material are removed. Conversely, even in the absence a size effect on twinning, there is the opportunity that plasticity will be suppressed in favor of shape memory at smaller size scale.

Dislocation dynamics simulations of high strain rate deformation of FCC Cu

Zhiqiang Wang[1], *Richard LeSar*[1]

[1]*Los Alamos National Lab, Theoretical Division, T-12, MS B268, Los Alamos National Lab, 87544 Los Alamos, USA*

The detailed understanding of high-rate deformation of engineering materials is crucial to many applications. We apply a novel Parametric Dislocation Dynamics (PDD) method, along with the use of high performance computing, to simulate material behaviour under high- rate loadings. With careful analysis of the simulations, we can provide a detailed picture of microstructural changes, exploring the connection between these changes and the macroscopic response for diferent rates of deformation. Simulation results are compared with experimental observations.

Development of precipitate strengthening model for Cu-Co Alloys

Brian Wirth

University of California, Berkeley, Nuclear Engineering Department, 94720-1730 Berkeley, United States of America

Recent molecular dynamics simulations of the interaction between gliding edge or screw dislocations and coherent cobalt precipitates in Cu-Co alloys have revealed a new interaction and detachment mechanism, which involves the combined shear and Orowan loop bypass of the leading and trailing Shockley partials, respectively. The Orwan looping of the trailing Shockley partial is caused by the energy decrease (strengthening) associated with the reversible crystallographic transformation of the cobalt precipitate from fcc to hcp stacking on the dislocation glide plane, which is temperature dependent. This presentation describes a precipitate strengthening model under development which accounts for this mechanism and is able to reliably predict the observed temperature dependence observed in the molecular dynamics simulations. The model predictions are also compared to the available experimental data on the anomalous temperature dependence of the critical resolved shear stress reported for Cu-Co alloys. The comparison indicates that the relatively low temperature of the maximum resolved shear stress may result from a transition in the dislocation interaction mechanism.

Anisotropic Liquid Phase Sintering Investigated by Means of Micromechanical and Discrete Element Modeling

Authors: A. Wonisch[1], K. Korn[1], T. Kraft[1], H. Riedel[1]

Affiliations: [1]Fraunhofer Institute for Mechanics of Materials, Woehlerstr. 11, 79108 Freiburg, Germany; e-mail: andreas.wonisch@iwm.fraunhofer.de

ABSTRACT

Sintering green bodies made by typical industrial production processes like uniaxial compaction, tape casting or extrusion may exhibit a significant anisotropic microstructure which in turn leads to anisotropic sintering behavior. By applying the Discrete Element Method (DEM) we are able to investigate the sintering process on the grain scale and show how anisotropic grain arrangements lead to anisotropy in macroscopic quantities like the strain rate. These DEM simulations are compared to a micromechanical, anisotropic liquid-phase sintering model. By implementing the model into a finite element program simulating anisotropic sintering of complex shaped 3D parts becomes possible.

1. Introduction

Sintering theory developed continuously from the late 1940s onwards. Current investigations deal often with numerical modelling in a more or less detailed manner. In most of these approaches continuum mechanical models have been used [1]. By implementing an adequate constitutive sintering model into a finite element program, it is possible to predict distortions due to gravity or an inhomogeneous green density even for complex shaped 3D parts. However, a mechanism that is still poorly understood is anisotropic shrinkage due to an anisotropic microstructure of the green body [2]. Thus, to improve modelling of such systems a better understanding of the fundamental reasons for anisotropic behaviour is necessary.

2. Discrete Element Method applied to Liquid Phase Sintering

The Discrete Element Method is a general simulation scheme that allows simulating processes in powder technology like die filling, compaction or sintering on a grain-scale [3,4]. Thus, effects caused by rearrangement or anisotropic configurations are considered by design. Between particles appropriate forces must be derived to properly describe the desired process.

Each particle is represented by its position vector $\mathbf{r}_i$, velocity $\mathbf{v}_i$ and mass m_i. The time evolution is determined by Newton’s equations of motion. These equations of motions are integrated in discrete time intervals Δt by means of a Velocity-Verlet propagation scheme Boundary conditions allowing to specify a desired stress state (e.g. $\sigma = 0$ for free sintering) are used. This is achieved by employing a proportional controller which computes the macroscopic strain rate $\dot{\varepsilon}_{ij}$ on the simulation box needed to obtain the prescribed stress. Each face of the simulation box and all particles are displaced in every time step by $\Delta x_i = \dot{\varepsilon}_{ij} x_j \Delta t$. For affine movement (no rearrangement) the propagation scheme is deactivated.

The force laws used for the DEM sintering simulations are based on the liquid phase sintering model derived by Svoboda et al. [5]. The attractive sintering force can be written as the sum of a contribution caused by the effective liquid pressure and the solid-liquid interface energy

$$F_s = F_l + F_{sl} = -2\pi\gamma_l R + 2\pi\gamma_{sl} c^2 / R \tag{1}$$

where γ_l is the specific surface energy of the liquid, γ_{sl} the specific surface energy of the solid-liquid interface, c the radius of the contact area and R the particle radius.

Additionally, a viscous force arises due to diffusion

$$F_v = \pi c^2 \left(\frac{1}{L\Omega} + \frac{k_B T c^2}{4 C_l \Omega \delta_b D_b} \right) R\dot{\delta} \tag{2}$$

with L being the reaction constant for solution or precipitation, k_B the Boltzmann constant, T the temperature, C_l the concentration in the liquid collar, Ω the atomic volume of the dissolving species, $\delta_b D_b$ the grain boundary thickness times the diffusions coefficient of the solid atoms in the liquid grain boundary.

These forces are contact forces which only act when two particles touch each other. A long-range capillary force F_b caused by liquid bridges between particle pairs is also considered [6]

$$F_b = 2\pi\gamma_l R\, \mathrm{e}^{-C_2 d / R} \tag{3}$$

Here d is the separation between two particles and C_2 a material constant associated with the surface tension of the liquid. A break-up distance of 0.4 R for the liquid bridge is assumed.

3. Micromechanical modeling

To derive the analytical constitutive equation for the deformation of a powder aggregate due to liquid phase sintering, macroscopic tensors of sintering stress and viscosity are formulated in terms of the previously described contact forces (the form is similar to the quantities of [7])

$$C_{ijkl} = \frac{3D}{4\pi} \int_\Omega z(n)\eta(n) n_i n_j n_k n_l \, d\Omega \quad , \quad \sigma_{ij}^s = \frac{3D}{4\pi} \int_\Omega z(n) F^s(n) n_i n_j \, d\Omega \tag{4}$$

C_{ijkl} is the viscosity tensor, σ_{ij}^s is the stress tensor, n the unit vector, D the relative density and z the contact density. The integration is performed over the unit sphere Ω. η results from the viscous force and F^s contains the other forces. Both tensors have an anisotropic nature. They describe the material behaviour in a linear viscous law with

$$\dot{\varepsilon}_{ij} = C_{ijkl} (\sigma_{ij} - \sigma_{ij}^s) \tag{5}$$

In the isotropic case, the tensor quantities reduce to the equations used in [5]. The orientation distributions of contacts and contact area yield an anisotropic material behaviour. The inner variables, relative density and contact area distribution, are updated similar to Ref. [8].

4. Simulation results

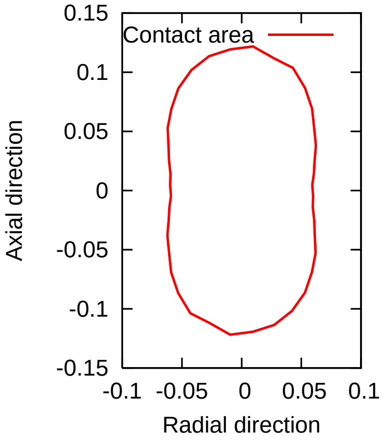

Figure 1. Initial contact area distribution after DEM compaction simulation used for all sintering simulations.

For the following simulations a periodic cell consisting of about 15,000 spherical particles is used. To generate a particle arrangement that exhibits significant anisotropy the initial configuration is first uniaxially compacted to a relative density of 70% by employing a DEM cold compaction simulation [4]. The initial anisotropy in the contact area distribution is shown in Fig. 1. In this graph the distance to the origin corresponds to the size of the contact area in the specific direction. Because of radial isotropy a 2D representation is sufficient. Starting from this configuration free sintering simulations are performed. For better comparison with the micromechanical model particle rearrangement is deactivated. The initial contact area distribution depicted in Fig. 1 is also used as the starting point for the micromechanical simulations. The contact number distribution (i.e. particles directly touching each other) shows a similar, albeit notably smaller anisotropy.

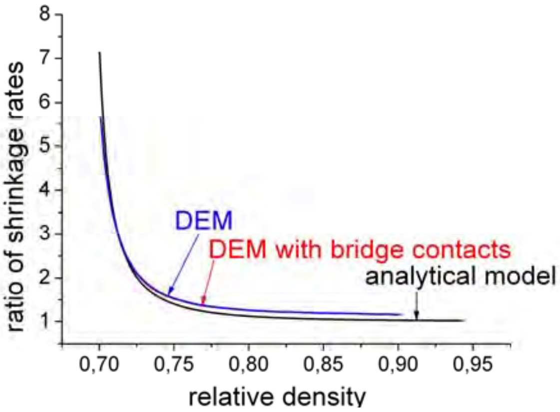

Figure 2. Ratio of shrinkage rates (radial to axial direction) for different models.

Important quantities describing the anisotropic sintering behavior of the sintering body are the shrinkage rates in radial and axial direction. Because of the initial anisotropy the shrinkage rates significantly differ at first. At the beginning of free sintering (D = 70%) the shrinkage rate in radial direction is almost 7 times higher than in axial direction (see Fig. 2). This can be explained by that fact that the viscous force from Eq. (2) has a quadratic dependence on the contact area which means that a larger contact area corresponds to a lower sintering rate. Because the initial configuration has significantly larger contact areas on average in axial direction this leads to a lower shrinkage rate in that direction. However, because of the lower shrinkage rates the contact areas in axial direction also develop more slowly, which means that the anisotropy is reduced over time.

Both the DEM simulation and the micromechanical model show similar trends with the shape of the shrinkage ratio curves being almost identical. This is independent of the use of long-range capillary forces. However, for higher densities there is a slight difference: While the analytic curve tends to 1.0 (corresponding to isotropic sintering), the DEM based simulations show a final strain rate ratio of about 1.1. This trend is also visible when looking at the ratio of average contact areas in radial and axial direction. Again, the analytic model shows a convergence towards 1.0 while for particle simulations a small anisotropy is left.

This difference in the two models indicates that while in this case anisotropic behaviour is largely determined by the anisotropy in the contact area distribution there might be other factors not captured in the micromechanical model which have an additional (albeit small) influence. One contributing factor might be the initial anisotropy in the number of contacts which is also reduced over time but at a faster pace than the contact area. In the analytic model this influence is only considered by a linear evolution equation while in the DEM based simulations the contact number increases for lower densities strongly non-linear.

+5. Continuum Mechanical Implementation

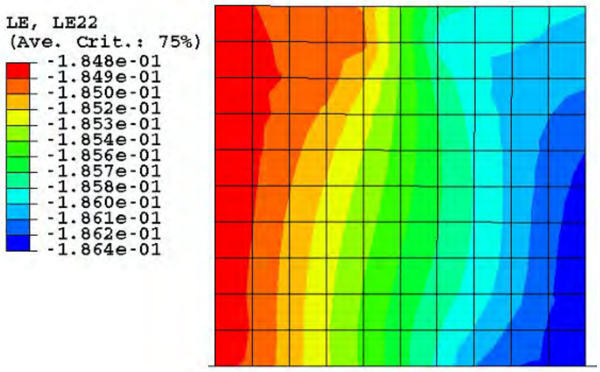

Figure 3. Finite Element Simulations of Anisotropic Sintering Behaviour (highlighted by strain rate in y direction).

The micromechanical model was implemented as a material subroutine for the finite element program ABAQUS/Standard. This allows the simulation of complex shaped 3D parts on a macroscopic scale. Fig. 3 shows a demonstration example of such a continuum mechanical simulation. Here a pre-compacted 3D part (uniaxial in z direction) is sintering with a load being applied during sintering from the middle to the right side of the component in y direction. Accordingly higher strains can be observed in the right side of the part although in this case the differences are very small.

6. Conclusions

By applying the Discrete Element Method to the simulation of liquid-phase sintering it was shown that this method is well-suited to describe anisotropic behavior. The leading mechanisms for anisotropy during sintering were identified to be an anisotropic initial configuration in the distribution of contact areas throughout the green body and the way particles are arranged. It was also shown that anisotropy is reduced over time. The simulations results are in good agreement with a corresponding micromechanical model although some open questions remain. This offers the possibility to further improve the analytical model and its finite element implementation which in turn could lead to even better model prediction.

References

[1] H. Riedel, and T. Kraft, *Continuum Scales Simulation of Engineering Materials: Fundamentals – Microstructures – Process Applications* (Wiley-VCH, Berlin, 2004)

[2] A. Zavaliangos, and D. Bouvard, Numerical Simulation of Anisotropy in Sintering Due to Prior Compaction, Int. J. Powder Metall. 36, 7 (2000)

[3] C. Bierwisch, B. Henrich, T. Kraft, M. Moseler, and H. Riedel, *3D-Modelling of Die Filling*, in Proceedings Euro PM 2005 Vol. 3 (Shrewsbury, U.K., 2005)

[4] I. Schmidt, A. Wonisch, B. Henrich, M. Moseler, and H. Riedel, *Computation of Macroscopic Yield Surfaces by Particle Methods*, in Proceedings Euro PM Vol. 3 (Shrewsbury, U.K., 2005)

[5] J. Svoboda, H. Riedel, and R. Gaebel, *A Model for Liquid Phase Sintering*, Acta Mater. **44**, 8 (1996)

[6] A. Petersson, and J. Agren, Rearrangement and Pore Size Evolution During WC-Co Sintering Below the Eutectic Temperature, Acta Mat. **53** (2005)

[7] A. Jagota, and P.R. Dawson, *An Anisotropic Continuum Model for the Sintering and Compaction of Powder Packings*, Mech. of Mat. **7** (1998)

[8] N.A. Fleck, *On the Cold Compaction of Powders*, J. Mech. Phys. Sol. **43**, 9 (1995)

Molecular Dynamics Study of Interfacial Dislocation Network at Gamma/Gamma-Prime Interface in Ni-Based Superalloys

Kisaragi Yashiro[1], **Joy Rizki Pangestu**[1] **and Yoshihiro Tomita**[1]

[1] Kobe University, 1-1, Rokkodai, Nada, Kobe 657-8501, JAPAN
yashiro@mech.kobe-u.ac.jp

ABSTRACT

Molecular dynamics simulations are conducted on misfit dislocations at semi-coherent interface between Ni and Ni_3Al single crystals. After the initial relaxation, network-like misfit dislocations are found on the interface along [110] and [$\bar{1}$10] directions, as observed in experiments. An ideal sphere indenter is then plunged into the surface of Ni phase to nucleate dislocations and approach them to the misfit dislocations. It is revealed that the mesh nodes of misfit dislocations attract a prismatic dislocation loop generated under the tip and change their morphology.

1. Introduction

The network-like misfit dislocations are found on the interfaces between gamma matrix and rafted gamma-prime precipitates in Ni-based superalloys [1]. It is also reported that the mesh spacing of the network definitely relates to the creep resistance. Thus we have tried to model the cutting phenomena between the network and mobile dislocations in the gamma matrix by using 3D discrete dislocation dynamics [2]; however, there is so far no study on the short-range interaction between misfit dislocations and actual dislocations gliding in mono-lattice. Thus we have performed molecular dynamics simulations on the laminate structure of Ni and Ni_3Al single crystals with different number of atomic planes, reporting the core structure of misfit dislocations and its motion under the tension/compression normal or parallel to the interface [3]. In the present study, similar semi-coherent interface and misfit dislocations are made in Ni/Ni_3Al laminate plate and an ideal sphere indenter is plunged into the Ni surface, in order to reveal the interaction between the misfit dislocations and mobile ones in mono-lattice.

2. Simlation procedure

The interatomic potential adopted here is the embedded atom method (EAM), of which functions and parameters are proposed by Voter and Chen [4]. Single crystalline plates of Ni and Ni_3Al are attached each other under the periodic boundary conditions in the x and y directions, or [100] and [010], respectively, as shown in Fig. 1(a). The Ni phase (γ) has the dimensions of 50 50 15 fcc lattices while that of the Ni_3Al phase (γ) is changed either 49 49 15 or 48 48 15 $L1_2$ lattices. In order to aboid the misfit concentration at the periodic boundaries, the lattice parameter of γ and γ are adjusted to $49a_{\prime} = 50a$ or $48a_{\prime} = 50a$ in the initial configuration. Then they are relaxed by molecular dynamics simulation of 15000 fs, changing the cell size in the x and y directions to cancel the normal stress. Figures 1 (b) and (c) show the misfit dislocations on the γ and γ interface after the initial relaxation. The dislocation core is visualized by the common neighbor analysis (CNA) [5] and the upper γ atoms are eliminated in the figures. Then an spherical indenter of 5 nm radius is plunged into the γ surface, as schematically illustrated in Fig. 1 (a). The atoms receive repulsive force from the center of indenter tip according to the potential $V(r) = A\theta(R \quad r)(R \quad r)^3$,

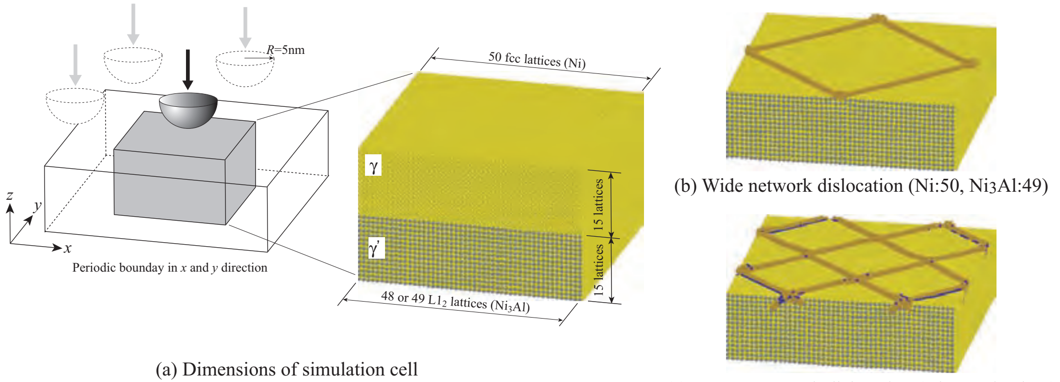

(a) Dimensions of simulation cell

(b) Wide network dislocation (Ni:50, Ni3Al:49)

(c) Narrow network dislocation (Ni:50, Ni3Al:48)

Fig. 1 Simulation models.

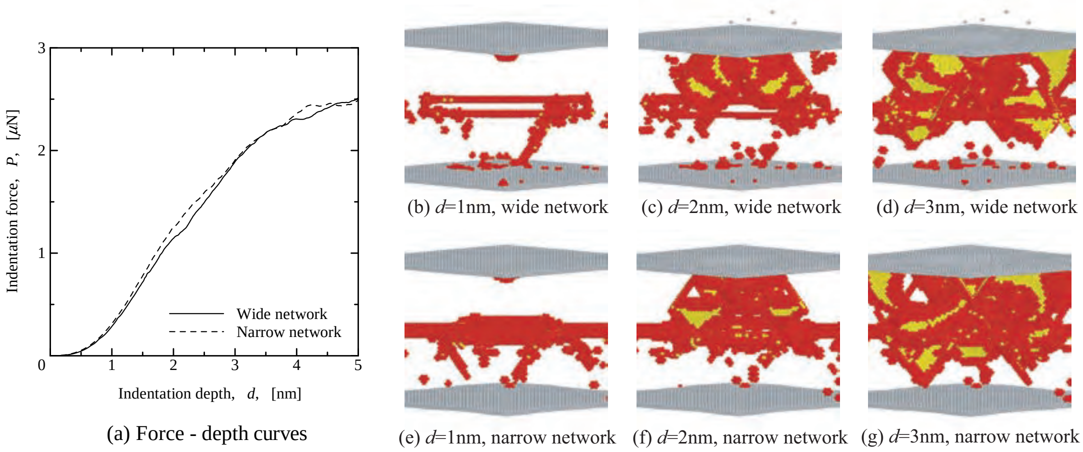

(a) Force - depth curves

(b) d=1nm, wide network (c) d=2nm, wide network (d) d=3nm, wide network

(e) d=1nm, narrow network (f) d=2nm, narrow network (g) d=3nm, narrow network

Fig. 2 Indentation force–depth behavior and dislocation motion.

where A is a force constant, $\theta(R - r)$ is the step function, R the indenter radius and r is distance between atom and the tip center [6]. In the present study, the force constant of $A = 5.0 \times 10^2\,\mathrm{nN/nm^2}$, the constant tip speed of $10^{-4}\,\mathrm{nm/fs}$ and the the maximum depth of 5 nm are adopted. The temperature is controlled at 10 K during the simulations.

3. Results and discussion

Figure 2(a) indicates the indentation depth–force curves. There is slight difference in the repulsive force acting on the tip, despite of the network spacing. Figs. 2(b)–(g) shows the motion of dislocation and other defects visualized by CNA. The dark shaded circles are the defect or dislocation core, while the light shaded ones, except the upper and lower surface, are the hcp atoms or stacking faults between Shockley partials. Dislocation burst emerges beneath the tip around the indentation depth of $d = 1.5\,\mathrm{nm}$, which is the flexion point in the depth–force curve. Before the burst, we can find some defects from the dislocation network into the γ′ phase. We have already reported that the network dislocation could be a source of dislocation under external loading [3]; however, the defects don't grow as a loop but a line in the present simulation. This might be an embryo of screw dislocation between the mesh node and the lower surface. After the burst, it is difficult to find out the difference in the growth and emission of prismatic dislocation with these 3D view.

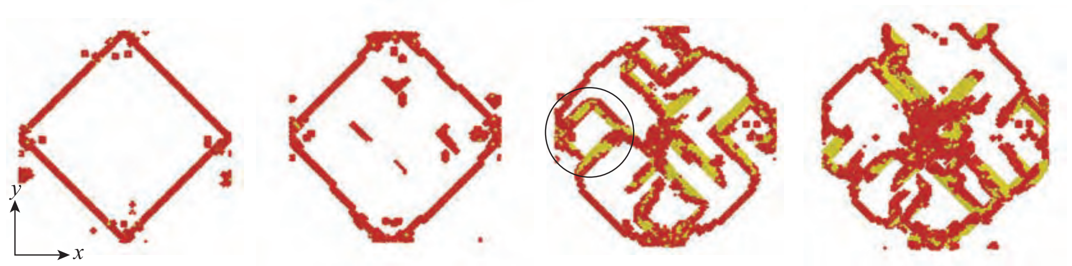

(a) *d*=1nm, wide network (b) *d*=2nm, wide network (c) *d*=3nm, wide network (d) *d*=4nm, wide network

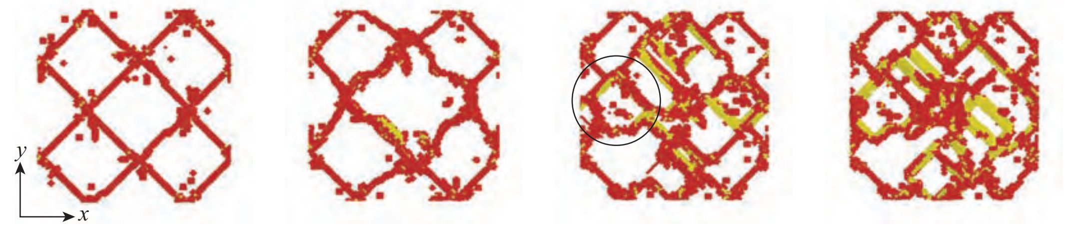

(e) *d*=1nm, narrow network (f) *d*=2nm, narrow network (g) *d*=3nm, narrow network (h) *d*=4nm, narrow network

Fig. 3 Morphology of dislocations at the interface.

In order to reveal the morphology change in the network dislocation, Fig. 3 shows the CNA defects within the slab region of 1 nm thickness at the γ γ interface. In Fig. 3(f), the center mesh of narrow network is already distorted at the indentation of $d = 2$ nm since the leading edge of prismatic loop is comparable with the mesh. It is of interest that the mesh becomes concave inward despite the atoms are pushed-out by the indentation. On the other hand, the change in the wide network is relatively small and we can find the cross-sectional lines of prismatic loops in the mesh (Fig. 3(b)). At the depth of $d = 3$ nm, the gliding dislocations definitely interact with misfit dislocations. Each intersection of dislocation network attract a prismatic loop, resulting in the morphology change at the mesh node as indicated with the circle in Figs. 3(c) and (g). The leading edge of prismatic loop keeps glinding into the γ phase even after changing the morphology of mesh node; however, the trailing edge tends to stay on the interface.

References

[1] Zhang, J. X, Murakumo, T., Harada, H. and Koizumi, Y. (2003): "Dependence of Creep Strength on the Interfacial Dislocations in a Fourth Generation SC Superalloy TMS-138", *Scripta Materialia*, Vol.48, pp.287–293.

[2] Yashiro, K, Nakashima, Y. and Tomita, Y. (2006): "Discrete Dislocation Dynamics Simulation of Interfacial Dislocation Network in Gamma/Gamma-Prime Microstructure of Ni-based Superalloys", *Computer Modeling in Engineering and Sciences*, Vol.11, No.2, pp.73–80.

[3] Yashiro, K., Pangestu, J. R. and Tomita, Y. (2006): "Structure and Motion of Misfit Dislocations at Ni/Ni$_3$Al Interface: Molecular Dynamics Study", *Journal of The Society of Materials Science, Japan*, submitted.

[4] Voter, A. F. and Chen, S. P. (1987): "Accurate Interatomic Potentials for Ni, Al and Ni$_3$Al", *Materials Research Society Symposium Proceedings*, Vol.82, pp.175–180.

[5] Honeycutt, J. D. and Andersen, H. C. (1987): "Molecular Dynamics Study of Melting and Freezing of Small Lennard-Jones Clusters", *The Journal of Physical Chemistry*, Vol.91, No.19, pp 4950–4963.

[6] Kelchner, C. L., Plimpton, S. J., Hamilton, J. C. (1998): "Dislocation Nucleation and Defect Structure During Surface Indentation", *Physical Review B*, Vol.58, pp.11085–11088.

A Study of Deformation and Texture Evolution during Nanoindentation in a Cu Single Crystal Using Phenomological and Physically-Based Crystal Plasticity FE Models

Nader N. Zaafarani[1], Franz Roters, Dierk Raabe

Department of Microstructure Physics and Metal Forming, Max-Planck-Institut für Eisenforschung, Max-Planck-Str. 1, 40237 Düsseldorf, Germany
[1] nader@mpie.de

ABSTRACT

The microstructure and texture changes underneath a conical nanoindent in Cu (111) single crystals are investigated. The theoretical investigation is carried out by introducing the problem into a 3D crystal plasticity based finite element simulation where two different constitutive material models are used. The theoretical findings are compared with experimental observations revealed form a 3D experiment which uses sets of subsequent (11 -2) planes conducted in serial sectioning by a focused ion beam (FIB) system in the form of a cross-beam 3D crystal orientation microscope (3D EBSD). The used elastic-viscoplastic crystal plasticity model predicts a pronounced deformation-induced 3D patterning of the lattice rotations below the indent. This is characterized by an outer tangent zone with large absolute values of the rotations and an inner zone closer to the indenter axis with small rotations. Yet it fails to predict the fine details of the rotation patterning with the frequent changes in sign observed in the experiment and over-emphasizes the magnitude of the rotation field compared with the experiments. These differences between simulation and experiment encouraged the implementation of a physically-based crystal plasticity model for FCC materials into the crystal plasticity FEM. The model adopts the evolution of the dislocation density as a source of material hardening. A dependency of the six pile-up pattern around the indent on the crystallographic orientation could be established.

1. Introduction

With the Nanoindentation testing method the mechanical properties of materials at the microstructural scales can be determined. This could be very useful for studying local mechanical response of modern miniaturized electronic and engineering devices, micro-mechanical systems and material thin coatings. Beside the commonly extracted force-displacement curves from the nanoindentation test an enhanced understanding of indentation mechanics might enable one to extract and address a larger spectrum of constitutive material parameters than before. A few previous works [1-4] could be found dealing with the microstructural analysis in small-scale indentation testing. This could be due to the complicated boundary and kinematic conditions, microstructural size effects, anisotropy, and heterogeneity of the deformation and stress fields around the indent. In that context this study addresses as one particular aspect of nanoindentation the formation of the crystallographic texture evolution caused by the applicationof tha nanoindent in a Cu single crystal and the corresponding deformation zone around the indent. The crystal plasticity finite element simulations are essential for the interpretation of the observed rotation fields. They allow us not only to establish the relationship between crystallographic shear and texture but provide also information about the spatial 3D distribution of the individual shear rates on the active slip systems that entail the observed lattice rotations.

2. Modeling and Simulation

2.1 Constitutive Models

Two different material models are introduced to the FE code in order to simulate the nanoindentation of a {111} single crystal copper with a conical indent of 1.5 μm tip radius. The depth of the indentation is 1μm. The constitutive laws for the phenomenological model are based on power law relations. The elasto-visco plastic model introduced by Kalidindi et al. [5] is based on a crystal plasticity model. The model is designed for the prediction of the evolution of the crystallographic texture based on the phenomenology of the face centered cubic (FCC) lattice. The hardening law on a slip system α is given by

$$\dot{\gamma}_\alpha = \dot{\gamma}_0 \left| \frac{\tau_\alpha}{s_\alpha} \right|^{1/m} \operatorname{sign}(\tau_\alpha) \tag{1}$$

where $\dot{\gamma}_\alpha$ is the shear rate on the slip system subjected to the resolved shear stress τ_α having a slip resistance of s_α . $\dot{\gamma}_o$ and m are material parameters and stand for the reference shearing rate and the rate sensitivity of slip. The physically-based model [6] adopts Orowan equation as a base for the flow rule and the evolution of the statistically stored dislocations (ρ_{SSD}) as the source of the material hardening

$$\sigma = f\,(\rho_{SSD}) \tag{2}$$

where (σ) represents the stress state of the material.
The behavior of the governing equations of the two models is influenced by the choice of the material fitting parameters integrated in them. In order to determine proper values for them a compression test is performed on a copper single crystal. The experimental stress-strain curve is used through fitting in determining the materials parameters. As shown in Fig.1. a very good agreement between models and experiment characteristics could be achieved. For detailed information about the parameter values refer to [6] and [7].

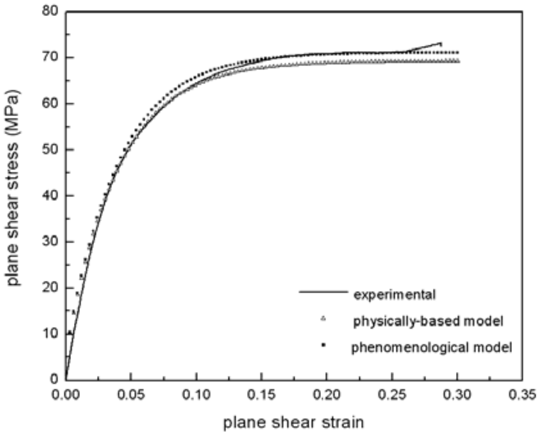

Figure 1. Stress-strain curves used for fitting the parameters contained in the two models

2.2 Finite element models

The constitutive models mentioned above were implemented in the finite element code MARC via user-defined subroutine HYPELA2 for the simulation of the indentation of the Cu single crystal. The mesh consisted of 4312 elements and 5224 nodes. The elements are of 3D-hexahedral type with 8 integration points. Near the center of the indented area, special care was taken when meshing the sample due to the high probability to obtain heavily distorted elements. The indenter is treated as a rigid body. As a boundary condition the lower face of the cylinder is kept fixed. Otherwise, each node possesses three translational and three rotational degrees of freedom. The friction between the indenter and the sample was assumed to be zero.

3. Results and Discussion

Comparison of the simulated crystal rotations with the experimental data underneath the indent shows that the physically-based model -Fig.2c- predicts the frequent changes in sign of the rotation patterning about the [11-2] crystal direction obtained experimentally -Fig.2b- better than the simulations with the elasto-visco plastic model shown in Fig.2a.

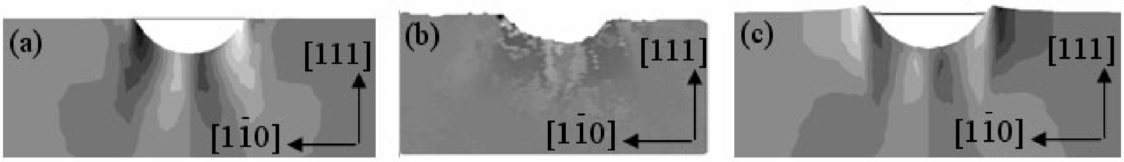

Figure 2. The crystal rotation pattern underneath the indent around [11-2] direction for a) phenomenological model , b) EBSD measurement and c) physically-based model (light color = ccw rotation, dark color = cw rotation)

Figs. 3a and 3b represent the pile-up pattern around the indent for the two models. The experimental results are compared with an AFM scan of the surface surrounding the scan. A sixfold pile-up pattern could be detected around the indent in the simulation using both models. However some descrepencies of the material pile-up could be observed between the phenomenological findings and the experiment. A better agreement with the measured topography could be detected with the physically-based model. This is to be expected, as the fitted values assigned for the parameters in the latter model are based on the physics of the movement of the deformed material. Thus they would give a better representation of the behaviour of the material.

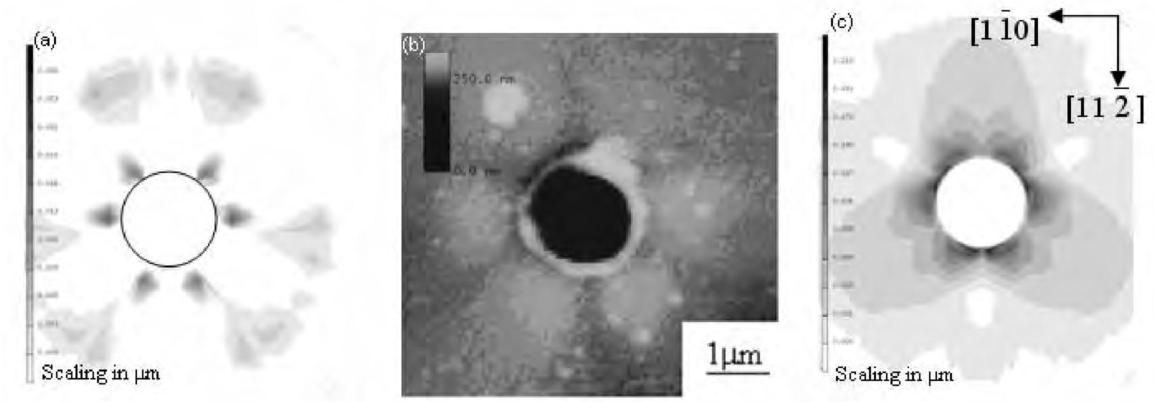

Figure 3. Pile-up pattern around the indent on (111) surface resulting from a) phenomenological model , b) AFM measurement and c) physically-based model

On the other hand, an investigation of the active slip systems on the surface of the sample and around the indent shows that beside some secondry slip system a sixfold pattern of different slip systems is dominating, as shown in Fig. 4. This suggests that the pile-up patterning around the indent might be a consequence of the activation of a small set of slip systems carrying most of the material translation. This slip motion does not interact with the secondary slip systems, which results in small strain hardening. Consequently, a significant amount of parallel dislocations will glide along a small volume, leading to the initiation of the pile-up pattern.

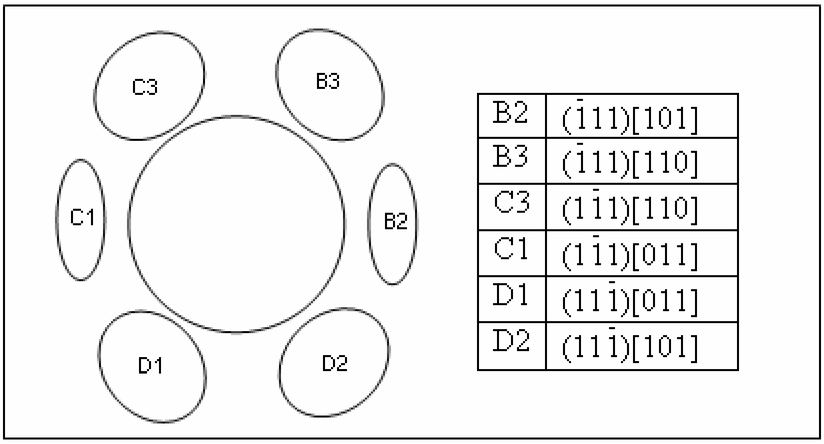

B2	$(\bar{1}11)[101]$
B3	$(\bar{1}11)[110]$
C3	$(1\bar{1}1)[110]$
C1	$(1\bar{1}1)[011]$
D1	$(11\bar{1})[011]$
D2	$(11\bar{1})[101]$

Figure 4. Schematic representation showing the active slip systems acting in regions around the surface of a 1μm deep nanoindent in {111} Cu single crystal

In general, the physically-based crystal plasticity model enhances the prediction of the material properties. It also allows us to obtain better results by implementing the effect of strain gradients induced in the indented region.

References

[1] Y.Wang, D.Raabe, C.Klüber, F. Roters, "Orientation dependence of nanoindentation pile-up patterns and of nanoindentation microtextures in copper single crystals", Acta Materialia **52**, 2229 (2004).

[2] Y.Liu et al. "Combined numerical simulation and nanoindentation for determining mechanical properties of single crystal copper at mesoscale", Journal of the Mechanics and Physics of solids **53**, 2718 (2005).

[3] K.K.Mclaughlin et al., "Measurement of crystal lattice rotations under nanoindents in copper", Mater. Res. Soc. Symp. Proc. **841**, 3 (2005).

[4] D.Kiener et al., "Microstructural evolution of the deformed volume beneath microindents in tungsten and copper", Acta Materialia **54,** 2801 (2006).

[5] S.R.Kalidindi, C.A.Bronkhorst, L.Anand, "Crystallographic texture evolution in bulk deformation processing of fcc metals", Journal of the Mechanics and Physics of solids Vol. **40**, 537 (1992).

[6] A.Ma, F.Roters, "A constitutive model for fcc single crystals based on dislocation densities and its application to uniaxial compression f aluminium single crystals", Acta Materialia **52,** 3603 (2004)

[7] N.Zaafarani et al. "Three dimensional investigation of the texture and microstructure below a nanoindent in a Cu single crystal using 3D EBSD and crystal plasticity finite element simulations", Acta Materialia **54**, 1863 (2006).

Modeling the influence of grain boundaries on deformation resistance by statistical dislocation theory

X.H. Zeng[1], P. Eisenlohr[1], W. Blum[1]

Institut für Werkstoffwissenschaften, LS 1, Universität Erlangen-Nürnberg,
Martensstaße 5, 91058 Erlangen, Germany, xiaohui.zeng@ww.uni-erlangen.de

ABSTRACT

A statistical one-parameter dislocation model is proposed to explain the influence of high-angle grain boundaries on the deformation with emphasis on the steady state. The evolution of dislocation density is modeled from the rates of generation and annihilation of dislocations. At low homologous temperatures where spontaneous dislocation annihilation prevails, the deformation resistance increases with decreasing grain size according to the Hall-Petch relation. At elevated temperatures fast thermally activated (climb controlled) annihilation of dislocations at grain boundaries leads to a relative minimum of steady-state deformation resistance as function of grain size.

1. Introduction

There is now little doubt that the deformation resistance is controlled by dislocation mechanisms down to grain sizes $d \approx 20$ nm [1]. The behavior of ultrafine-grained (ufg) and nanocrystalline (nc) materials differs distinctly from that of materials with conventional grain size (cg). The limitation of the dislocation mean free path by the high-angle grain boundaries enhances the rate at which dislocations are generated. On the other hand, the grain boundaries with their relatively open atomic structure facilitate loss of dislocations by thermally activated processes. The superposition of both effects explains the strengthening as well as the softening in the steady state of deformation due to fine grains.

2. Model

Lattice dislocations arriving at high-angle grain boundaries generally keep their character as linear defects. This is illustrated by the fact that these extrinsic grain boundary dislocations can be made visible by transmission electron microscopy.

A lattice edge dislocation entering a high-angle boundary from one of the two neighboring crystallites forms a step at the surface of that crystal while the surface of the neighboring crystal remains unchanged (Fig. 1a). Analogous single-sided steps result from glide in the second crystallite. Even though the two steps in Fig. 1a differ due to differences in slip systems of the two grains, they can react by diffusive processes in the boundary to form a ledge with reduced stress field (Fig. 1c). In an approximative manner we treat this process of ledge formation from two single-sided steps as dissolution of a dislocation

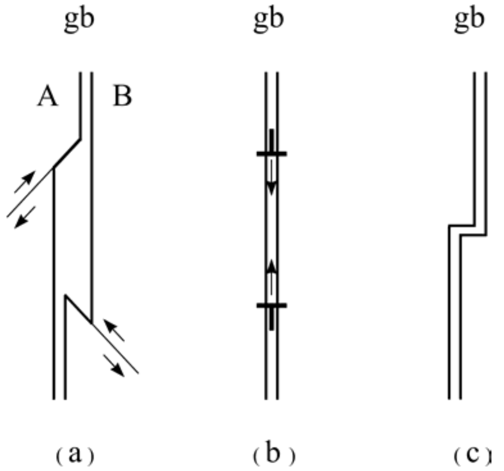

Figure 1: Recombination of dislocations at high-angle grain boundaries (gb). (a) single-side steps due to extrinsic edge dislocation, (b) schematic dislocation picture of (a), (c) stress-free grain boundary ledge after recombination of steps by climb in grain boundary.

dipole (Fig. 1b). The steady state of the grain boundary structure then results from the dynamic equilibrium of generation of extrinsic boundary dislocations by glide within the grains and their recombination in the grain boundaries.

The basic equations of the model are as follows. The flow stress σ is related to the dislocation length ρ per volume [2]:

$$\sigma = \alpha\, M\, G\, b\, \sqrt{\rho_\mathrm{f} + f\, \rho_\mathrm{gb}} \tag{1}$$

(M: Taylor factor, G: shear modulus, b: Burgers vector length). α is the interaction constant for lattice dislocations; subscripts f and gb refer to free and grain boundary dislocations, respectively. $f \leq 1$ is a weighting factor. The thermal component of flow stress has been neglected in (1). The geometrical relation between ρ_gb and dislocation length per grain boundary area is:

$$\rho_\mathrm{gb} = N_\mathrm{gb} \cdot \frac{2}{d}\,. \tag{2}$$

Free dislocations are generated at a rate

$$\dot{\rho}_\mathrm{f}^{+} = \frac{M}{b\, k_\mathrm{f}\, \rho_\mathrm{f}^{-0.5}} \cdot \dot{\epsilon} \qquad\qquad k_\mathrm{f} = 33.6 + 60\,(d/\mathrm{\mu m}\,)^{-1}\,. \tag{3}$$

It varies in inverse proportion to the average spacing of free dislocations $\rho_\mathrm{f}^{-0.5}$ and in direct proportion to the (plastic) strain rate $\dot{\epsilon}$. The d-dependence of k_f captures the reduction in the rate of dislocation storage within the grain interior occurring when the mean free path of dislocations approaches the grain size d. The length of extrinsic boundary dislocations per boundary area increases at the rate

$$\dot{N}_\mathrm{gb}^{+} = \frac{k_\mathrm{gb}\, M}{b} \cdot \dot{\epsilon}\,, \tag{4}$$

where k_{gb} is a constant according to simple geometry [3]. The rates at which free and boundary dislocations disappear from the material are the sum of spontaneous (spon) and thermally activated (therm) processes:

$$\dot{\rho}^{-} = \dot{\rho}^{-,\mathrm{spon}} + \dot{\rho}^{-,\mathrm{therm}} \,. \tag{5}$$

The spontaneous annihilation rates are of the form [4, 5]:

$$\dot{\rho}^{-,\mathrm{spon}} = \frac{M}{b}\,\dot{\epsilon}\,2d_{\mathrm{spon}} \times \frac{\rho}{n_{\mathrm{g}}} \,, \tag{6}$$

where d_{spon} is the capture distance for spontaneous annihilation and n_{g} is the number of dominant slips systems. The expressions for dislocation loss by climb read:

$$\dot{\rho}_{\mathrm{f}}^{-,\mathrm{therm}} = \frac{2}{\xi^2\,\pi\,(1-\nu)}\,\frac{G\,\Omega}{k_{\mathrm{B}}\,T}\,D_{\mathrm{v}}\,\rho_{\mathrm{f}}^2 \tag{7}$$

$$\dot{N}_{\mathrm{gb}}^{-,\mathrm{therm}} = \frac{1}{\pi\,(1-\nu)}\,\frac{G\,\Omega}{k_{\mathrm{B}}\,T}\,\delta_{\mathrm{gb}}D_{\mathrm{gb}}\,N_{\mathrm{gb}}^4 \,. \tag{8}$$

An important difference between (7) and (8) is that climb is controlled by the coefficient of lattice diffusion D_{v} and of grain boundary diffusion D_{gb}, respectively (Ω: atomic volume, δ: grain boundary width, ν: Poisson's ratio, k_{B}: Boltzmann constant, $\xi = 0.5$).

The steady state solution for the deformation resistance is obtained by equating the rates of generation and annihilation of dislocations [6].

3. Result

The model was applied to pure Cu taking existing material data and estimating unknown model parameters. The results obtained for the steady state deformation resistance at ambient temperature are displayed in Fig. 2 as function of grain size. At normal rates of deformation above $10^{-5}\ \mathrm{s}^{-1}$ the flow stress is athermal due to control of dislocation loss by spontaneous annihilation. The flow stress increases monotonically with decreasing grain size in proportion to $d^{-0.5}$. At low rates of deformation, however, thermally activated climb becomes important. This leads the flow stress to become dependent on plastic strain rate $\dot{\epsilon}$. Due to the differences in the dislocation loss processes inside the grains and at the boundaries, a decrease in grain size from conventional size of 50 µm to ultrafine size of 0.35 µm makes the material softer. This result is in reasonable agreement with experimental data [3, 5]. Note that the softening relates only to the steady state of deformation and not to the yield stress which is lower for cg Cu compared to ufg Cu. With d decreasing further into the nc range there is a further enhancement of the rate at which extrinsic dislocations are generated at the boundaries. In consequence of that the curves shift to the right in Fig. 2. This is also consistent with experimental data [6]. The shift means that softening is no longer observed in the steady state of deformation.

4. Concluding remarks

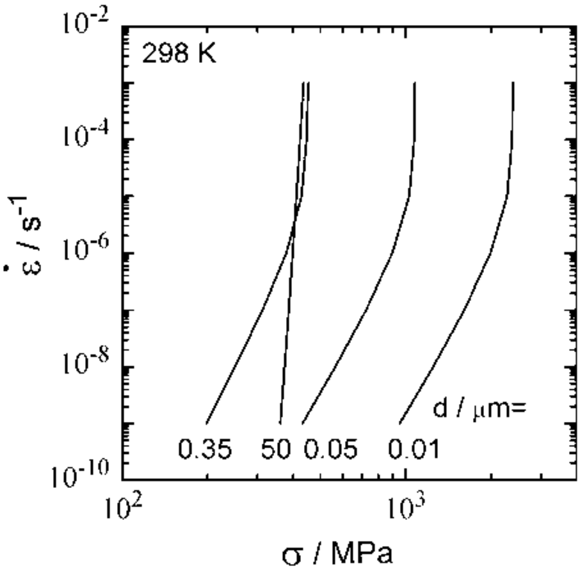

Figure 2: Steady state deformation resistance $\dot{\epsilon}$-σ of pure Cu at room temperature calculated from the model as function of grain size.

The model presented above is certainly oversimplified. However, the quantitative consideration of generation and loss of dislocations in the grains and at the grain boundaries yields a simple qualitative picture of how the deformation resistance depends on grain size. It should be noted that direct contributions of grain boundaries to deformation by sliding and diffusive flow were not necessary to explain the material behavior. However, such processes will certainly occur and modify the deformation resistance established by the dislocation processes considered in this work [7].[1]

References

[1] M.A. Meyers, A. Mishra, and D.J. Benson, Mechanical properties of nanocrystalline materials, Prog. Mater. Sci., 51, 427, 2005.

[2] J. C. M. Li and Y. T. Chou, The role of dislocations in the flow stress grain size relationships, Metall. Trans., 1, 1145, 1968.

[3] Y.J. Li, X.H. Zeng, and W. Blum, Transition from strengthening to softening by grain boundaries in ultrafine-grained Cu, Acta Mater., 52(17), 5009, 2004.

[4] W. Blum, P. Eisenlohr, and F. Breutinger. Understanding creep - a review, Metall. Trans., 33A, 291, 2002.

[5] X. H. Zeng, P. Eisenlohr, and W. Blum, Modelling the transition from hardening to softening by high-angle grain boundaries, ICSMA 14, 2006. submitted.

[6] W. Blum, Y.J. Li, J. Chen, X.H. Zeng, and K. Lu, On the Hall-Petch relation between flow stress and grain size, Z. Metallkd., 2006. submitted.

[7] R. Z. Valiev, E. V. Kozlov, Yu. F. Ivanov, J. Lian, A. A. Nazarov, and B. Baudelet, Deformation behaviour of ultra-fine-grained copper, Acta metall. mater., 42(7), 2467, 1994.

---

[1] Financial support of Deutsche Forschungsgemeinschaft under contract BL135/30-2 is gratefully acknowledged.